AD-A149 518

(10)

RESEARCH AND DEVELOPMENT TECHNICAL REPORT
CECOM -81-0136-6

UHF RADIOWAVE PROPAGATION THROUGH FORESTS

PREPARED BY:

R.H. Lang, A. Schneider, F.J. Altman, and Kiet Truong

20000804119

CYBERCOM CORPORATION
4105 NORTH FAIRFAX DRIVE
ARLINGTON, VIRGINIA 22203

**Reproduced From
Best Available Copy**

CYBERCOM TECHNICAL REPORT: CTR-108-06
MAY 1984

Distribution Statement: Approved for Public Release; Distribution Unlimited

CECOM

U S ARMY COMMUNICATIONS-ELECTRONICS COMMAND
FORT MONMOUTH, NEW JERSEY 07703

85 01 08 002

# NOTICES

## Disclaimers

The citation of trade names and names of manufacturers in this report is not to be construed as official Government indorsement or approval of commercial products or services referenced herein.

## Disposition

Destroy this report when it is no longer needed. Do not return it to the originator.

# RESEARCH AND DEVELOPMENT TECHNICAL REPORT
## CECOM -81-0136-6

## UHF RADIOWAVE PROPAGATION THROUGH FORESTS

PREPARED BY:

R.H. Lang, A. Schneider, F.J. Altman, and Kiet Truong

CyberCom Corporation
4105 North Fairfax Drive
Arlington, Virginia 22203

DTIC
SELECTE
JAN 1 5 1985
B

CyberCom Technical Report: CTR-108-06
May 1984

# CECOM

## U S ARMY COMMUNICATIONS-ELECTRONICS COMMAND
## FORT MONMOUTH, NEW JERSEY 07703

# NOTICES

## Disclaimers

The citation of trade names and names of manufacturers in this report is not to be construed ar official Government indorsement or approval of commercial products or services referenced herein.

## Disposition

Destroy this report when it is no longer needed. Do not return it to the originator.

# REPORT DOCUMENTATION PAGE

**READ INSTRUCTIONS BEFORE COMPLETING FORM**

| 1. REPORT NUMBER | 2. GOVT ACCESSION NO. | 3. RECIPIENT'S CATALOG NUMBER |
|---|---|---|
| CECOM-81-0136-6 | AD-A149518 | |

| 4. TITLE (and Subtitle) | 5. TYPE OF REPORT & PERIOD COVERED |
|---|---|
| UHF RADIOWAVE PROPAGATION THROUGH FORESTS | Annual Report<br>April 83 - April 84 |
| | 6. PERFORMING ORG. REPORT NUMBER<br>CTR-108-06 |

| 7. AUTHOR(s) | 8. CONTRACT OR GRANT NUMBER(s) |
|---|---|
| R.H. Lang, A. Schneider, F.J. Altman, and Kiet Truong | DAAK80-81-C-0136 |

| 9. PERFORMING ORGANIZATION NAME AND ADDRESS | 10. PROGRAM ELEMENT, PROJECT, TASK AREA & WORK UNIT NUMBERS |
|---|---|
| Cybercom Corporation<br>4105 North Fairfax Drive<br>Arlington, Virginia 22203 | 1L1.61102.AH48.PF.01 |

| 11. CONTROLLING OFFICE NAME AND ADDRESS | 12. REPORT DATE |
|---|---|
| US Army Communications-Electronics Command | May 1984 |
| Center for Communications Systems | 13. NUMBER OF PAGES |
| Fort Monmouth, NJ 07703 | 235 |

| 14. MONITORING AGENCY NAME & ADDRESS(if different from Controlling Office) | 15. SECURITY CLASS. (of this report) |
|---|---|
| | Unclassified |
| | 15a. DECLASSIFICATION/DOWNGRADING SCHEDULE |

16. DISTRIBUTION STATEMENT (of this Report)

Approved for public release; distribution unlimited.

17. DISTRIBUTION STATEMENT (of the abstract entered in Block 20, if different from Report)

18. SUPPLEMENTARY NOTES

19. KEY WORDS (Continue on reverse side if necessary and identify by block number)

UHF Radiowave Propagation, Forests, Foliage, Vegetation, Trees, Attenuation, Transmission Loss, Channel Characterization, Pulse Response, Lateral Waves, Multiple Scattering

ultrahigh frequency

20. ABSTRACT (Continue on reverse side if necessary and identify by block number)

A model for ~~UHF~~ radiowave propagation through a forest of tree trunks, branches, and leaves which had been first described in ~~report~~ CECOM-81-0136-4 has been extended. Forest characterization includes the dielectric properties of green wood and leaves, tree trunk diameter distributions, branch orientation, and canopy structure. Plots of the effective dyadic susceptibility and specific attenuation for homogeneous and non-homoge-

DD, FORM 1473 EDITION OF 1 NOV 65 IS OBSOLETE

a previous report        i

neous forests of tree trunks are presented. The theory of the anisotropic forest slab model is extended to include the forest floor and multiply-reflected space and lateral waves. Basic transmission losses versus frequency for various radio-link geometries are plotted, as are the responses to five-nanosecond pulses at 600 MHz.

Incoherent multiple scattering in a two-dimensional forest of tree trunks, small or large with respect to the wavelength, is studied. Plots are shown for single-tree scatterer patterns, albedos, and total cross-sections versus frequency, as well as normalized specific intensity versus scattering angle, normalized coherent and incoherent scattering intensities versus distance, and normalized frequency- and space-correlation functions.

| Accession For | |
|---|---|
| NTIS GRA&I | ☑ |
| DTIC TAB | ☐ |
| Unannounced | ☐ |
| Justification | |
| By | |
| Distribution/ | |
| Availability Codes | |
| Dist | Avail and/or Special |
| A-1 | |

CONTENTS

FIGURES

TABLES

[This page intentionally left blank]

## 1.0 Introduction

This report describes a stochastic radiowave propagation model useful for assessing the effects of forests upon wide-bandwidth digital radio communication systems operating in the 200-2000 MHz band. It represents an extension of the model first reported in CyberCom Technical Report CTR-108-01 [42]. The theoretical basis for this model was first developed by Foldy [23] and later extended by Lax [45], Twersky [68] and others. According to this model, the forest is represented as a time-invariant, stratified configuration of randomly-positioned and randomly-oriented discrete canonical scatterers. Tree trunks are modeled as infinitely-long circular dielectric cylinders; branches as finitely-long circular dielectric cylinders; and leaves as flat dielectric discs. The propagating radiowave is considered to consist of two parts: a mean (coherent) component derived by averaging statistically over an ensemble of forest configurations, and a residual random (non-coherent, diffuse, or fluctuant) component uniquely determined by a specific forest configuration.

## 1.1 The Coherent Radiowave

Initially, the emphasis in model development was directed toward characterization of the mean (coherent) component of the propagating radiowave. A physically appealing representation for the mean component was obtained by postulating that the mean field components satisfy Maxwell's equations "in the mean" and that the ensemble of discrete scatterers can be replaced by an equivalent continuous medium described by an effective dyadic permittivity $\underline{\varepsilon}$. However, in contradistinction to earlier models wherein the effective permittivity was either postulated or deduced from measurement, the CyberCom model directly related $\underline{\varepsilon}$ to such salient biophysical forest parameters as the tree trunk number density, the tree trunk diameter probability density function, and leaf area index.

The forest model was refined by assuming the trees to be bounded below by a smooth forest floor and bounded above by air. Earlier efforts [15,62,64] had suggested, however, that the introduction of the ground complicates the model significantly. In the earlier model [42], these complications were avoided by allowing the forest floor to recede to infinity thereby reducing the stratified forest model to a half-space representation; the newer, more general model described in this report, however, incorporates a forest floor of arbitrary permittivity. The electromagnetic boundary value problems involved in both models were solved using the classical approach first described by Sommerfeld and later extended by Brekhovskikh [5].

The stratified forest models described above are time-harmonic models in the sense that the signal radiated by the transmitting antenna is a sinusoidal waveform of angular frequency $\omega$. However, because the equivalent forest continuum characterized by the effective dyadic permittivity $\underline{\varepsilon}$ is linear, Fourier transform techniques have been employed to generalize the model so that it accommodates arbitrarily modulated waveforms. Using this approach it has been possible to determine the mean pulse distortion and differential pulse delay associated with radiowave propagation through a stratified forest.

## 1.2  The Incoherent Radiowave

As the propagating radiowave penetrates deeper and deeper into the forest, the relative contribution of the random (incoherent) component becomes progressively more important. This trend, anticipated from experiments [51,52], was first predicted theoretically using a two-dimensional, unbounded forest consisting solely of tree trunks [42]. The application of this early model, however, is limited to tree trunk diameters that scatter in the low-frequency (Rayleigh) regime; for the 200-2000 MHz band the model proves valid only for tree trunks less than 1 centimeter in diameter.

The early low-frequency, Rayleigh-scattering model [42, Section 7] has been improved and is now no longer restricted to

small-diameter trees. Further, the model, in addition to describing the intensity (power) of both the coherent and non-coherent components, can also be used to determine the space correlation function and frequency correlation function of the propagating radiowave. Fourier transformation of the former describes the angular spectrum of radiowaves arriving at a point; Fourier transformation of the latter describes the delay spread of the forest scatter path.

## 1.3  Scope

This report describes a stochastic radiowave propagation model useful for assessing the effects of forests on wide-band digital communication systems. In Section 2 the forest is characterized, first as to the permittivity of constituent woody material, then as to the geometries of trunks, branches and leaves. Finally it is recognized that forests, in general, have canopies supported by trunks, and some overall models are proposed. Section 3 presents the susceptibilities and attenuations for an unbounded forest of tree trunks having uniform or exponentially-distributed diameter distributions. Section 4 considers a more realistic forest, bounded not only above by the air interface but also below by the ground. The theory is developed; intra-forest multipath propagation is evaluated; the concept of basic transmission loss is introduced; and Doppler shift is considered. Section 5 presents detailed basic transmission losses and pulse responses for direct, reflected, direct-plus-reflected, lateral and total waves in semi-infinite leaf and trunk forests. Section 6 uses an integro-differential equation for the space-frequency correlation function to evaluate the properties of the incoherent field, which becomes important at the higher frequencies of interest here. A two-dimensional forest of circular, fixed-diameter, randomly-positioned trunks is studied. From the general space-frequency correlation function are derived the frequency correlation function for thin trunks (yielding coherence bandwidth) and the space correlation function

for arbitrary diameters. The coherent and incoherent intensities are also found for this general case, removing the size limitations of the earlier report [42].

## 2.0 Biophysical Forest Characterization

The characterization of a forest will be undertaken at several levels. It is first found in Section 2.1 to be supported by many sources that the basic materials of green wood and leaves (consisting largely of water) have similar dielectric properties. A CyberCom model is established for current work, although it may be refined after further study. The second level of consideration is basically geometrical, but quite complex in its specification, and even more so in its electromagnetic implications. This level involves the detailed description of trunks, branches, and leaves. The required parameters include densities, sizes, and orientations, considered in Section 2.2. The third level requires standing back from the parts of trees, and even from the trees themselves, to see the forest, not as a whole it turns out, but as a canopy, consisting mostly of branches and leaves, supported above the ground by the trunks. This view is considered in Section 2.3. Finally, forest models are synthesized by quantifying the above concepts in practical cases. Section 2.4 indicates sources of numerical data and proposes several CyberCom forest models.

## 2.1 Electrical Properties of Green Wood and Leaves

The electrical properties of green wood and leaves can be specified in terms of their relative permittivity $\varepsilon_\ell$ and permeability $\mu_\ell$. As with most biological materials, the relative permeability $\mu_\ell$ is close to unity. The relative permittivity $\varepsilon_\ell$ is complex and, for the complex exponential time dependence $\exp[j\omega t]$, can be written in the form

$$\varepsilon_\ell = \varepsilon_\ell' - j\varepsilon_\ell'' \qquad (2\text{-}1\text{-}1)$$

where $\varepsilon_\ell'$ and $\varepsilon_\ell''$ represent, respectively, the real and imaginary parts of the permittivity $\varepsilon_\ell$. The imaginary part is proportional, of course, to the conductivity $\sigma$ through the relation

$$\varepsilon_\ell'' = \sigma/\omega\varepsilon_0 \qquad (2\text{-}1\text{-}2)$$

where $\varepsilon_o$ is the permittivity of free space. The real part $\varepsilon_\ell'$ is often called the dielectric constant; the imaginary part $\varepsilon_\ell''$, the loss factor.

Although the electrical properties of wood have been the subject of numerous studies [10,30,37], relatively few measured data pertain to green wood and leaves, and fewer still to frequencies above 100 MHz [38,66]. The most appropriate appear to be those of Broadhurst [6]. These studies suggest that, firstly, the permittivity of green wood is not strongly species-dependent, although, taken as a class, coniferous (needle-bearing, tree wood and needles appear to have somewhat smaller permittivities than those of deciduous (leaf-bearing) tree wood and leaves. Secondly, although the importance of intrinsic water content for the relative permittivity of wood has been substantiated by many studies, because green wood nearly always has a high intrinsic water content (approximately 75% by volume), the permittivity of green wood is relatively independent of water content. Thirdly, Broadhurst's measurements on Tulip trees (L1, D3 of Fig. 2-1) and Bamboo (his Fig. 3) suggest very little difference between the permittivity of green wood and leaves.

Broadhurst's data for Tulip tree and Maple (L2 of Fig. 2-1) suggest that above 10 MHz the dielectric constant $\varepsilon_\ell'$ is only weakly dependent upon frequency and that over the band 200-2000 MHz $\varepsilon_\ell'$ is approximately equal to 40. For frequencies below 1000 MHz, the imaginary part $\varepsilon_\ell''$ appears to be dominated by conduction losses and so decreases linearly with increasing frequency. Above 1000 MHz, however, relaxation losses associated with molecular polarization begin to dominate and, in this frequency region, $\varepsilon_\ell''$ begins to increase with increasing frequency. Accordingly, in this study of UHF radiowave propagation through forests, the relative complex permittivity of green wood and leaves has been modeled using the relation

$$\varepsilon_\ell = 40.0 - j \left[ \frac{1.5}{f_{GHz}} + \frac{2.0 f_{GHz}}{[1 + (f_{GHz}/20.0)^2]} \right] \qquad (2-1-3)$$

where $f_{GHz}$ is the radiowave frequency expressed in GHz.

2-2

Table 2-1 summarizes the sources used to determine the dielectric properties of the forest constituents, that is, green wood and leaves, at 50 MHz and above. Most of the data are in the form of dielectric constant $\varepsilon'_\ell$ and loss tangent $\delta$. From these, the real and imaginary parts of susceptibility ($X'_\ell$ and $X''_\ell$, respectively) have been found using the relations $X'_\ell = \varepsilon'_\ell - 1$ and $X''_\ell = \varepsilon'_\ell \tan\delta$. The results are plotted in Figures 2-1 and 2-2. The CyberCom model is seen to be a reasonable approximation, but it may be noted that, in general, the deciduous and leaf (D&L) curves lie above those for coniferous and needles (C&N). It seems likely, therefore, that there may be a requirement for specializing the CyberCom model to deciduous and coniferous trees. These newer, improved models may turn out to be continuous functions of wood density, moisture content, and/or other parameters.

## 2.2  Physical Properties of Trunks, Branches, and Leaves

The electromagnetic properties of the forest constituents (trunks, branches, and leaves) depend not only on the electrical properties of the damp, woody material considered above, but also on the geometrical factors of size, shape, and orientation. The tree trunks are the largest forest scatterers and so, are considered in greatest detail. In the 1983 CyberCom Report [42], a forest of uniform trunk diameter was studied. Here, two major forest types of non-uniform trunk diameter are considered: the homogeneous forest, characterized by an even-aged stand with a normal (gaussian) distribution of trunk diameters, and the inhomogeneous forest, characterized by an uneven-aged stand with an exponential (inverse J-shaped) diameter distribution. The latter is characterized by a slope defined by a diameter $D_{av}$ which may not be the true average diameter because of tree trunk thinning by man or natural causes. Branch orientation statistics for conifers have been found and are presented. Branch diameter and length will be considered in a subsequent report. Leaves are discussed in some detail because they may be of interest at the higher frequencies.

2-3

Table 2-1 <u>Sources of Dielectric Properties of Forest Constituents</u>

| Material | Location | Cut | Moisture Content % | Frequency Range, MHz | Key | Authors | Y |
|----------|----------|-----|--------------------|----------------------|-----|---------|---|
| Oak | Trunk | England | | 75 | to 60 | D1 | Hearmon & Burcham [30] | 1 |
| Wych Elm | Trunk | | | 70 | to 60 | D2 | | |
| Pine | Trunk | Germany | R | 65 | to 5000 | C1 | Trapp and Pungs [66] | 1 |
| | | | | 95 | to 5000 | C2 | | |
| Douglas Fir | Trunk | Wisconsin | A | 75 | 1000,3000 | C3 | James and Hamill [38] | 1 |
| Spruce | Needles | Ohio | | 60 | 8500 | N1 | Carlson [10] | 1 |
| Yew | Needles | | | 60 | | N2 | | |
| Tulip Tree | Leaf | US-NBS | | 77 | to 4500 | L1 | Broadhurst [6] | 1 |
| Maple | Leaf | | | | | L2 | | |
| Tulip Tree | Branch | | R | 58 | | D3 | | |
| Douglas Fir | Trunk | Wisconsin | R | soaked | to 50 MHz | C4 | James [37] | 1 |
| White Oak | Trunk | | R | soaked | | D4 | | |

Note: D = deciduous    R = radial
A = axial    C = coniferous    N = needles    L = leaves

2-4
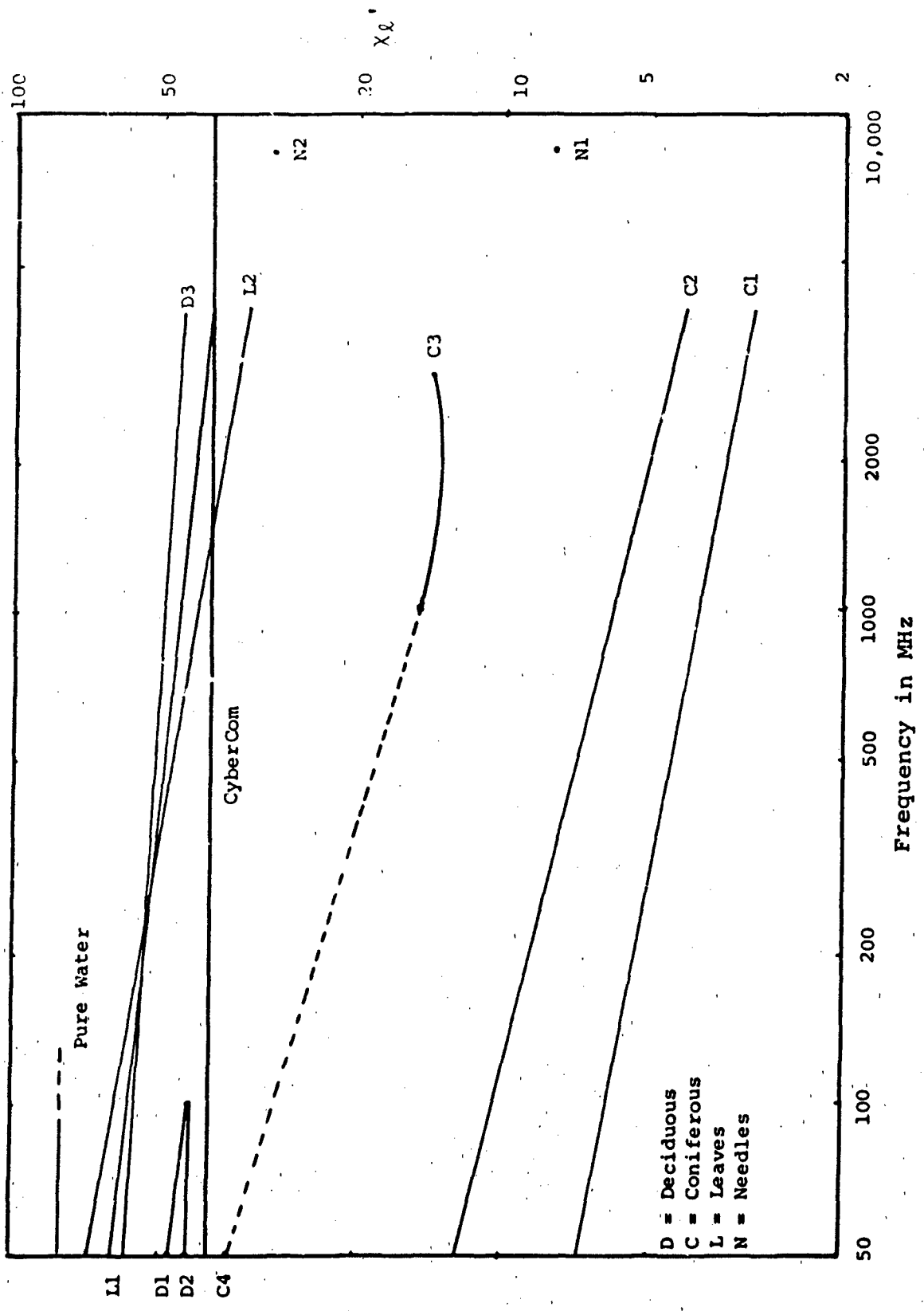
Figure 2-1: Susceptibility of Forest Constituents ($\chi_\ell'$)

D = Deciduous
C = Coniferous
L = Leaves
N = Needles

Pure Water

CyberCom

Frequency in MHz

$\chi_\ell'$

Figure 2-2: Susceptibility of Forest Constituents ($\chi_\ell''$).

D = Deciduous
C = Coniferous
L = Leaves
N = Needles

Frequency in MHz
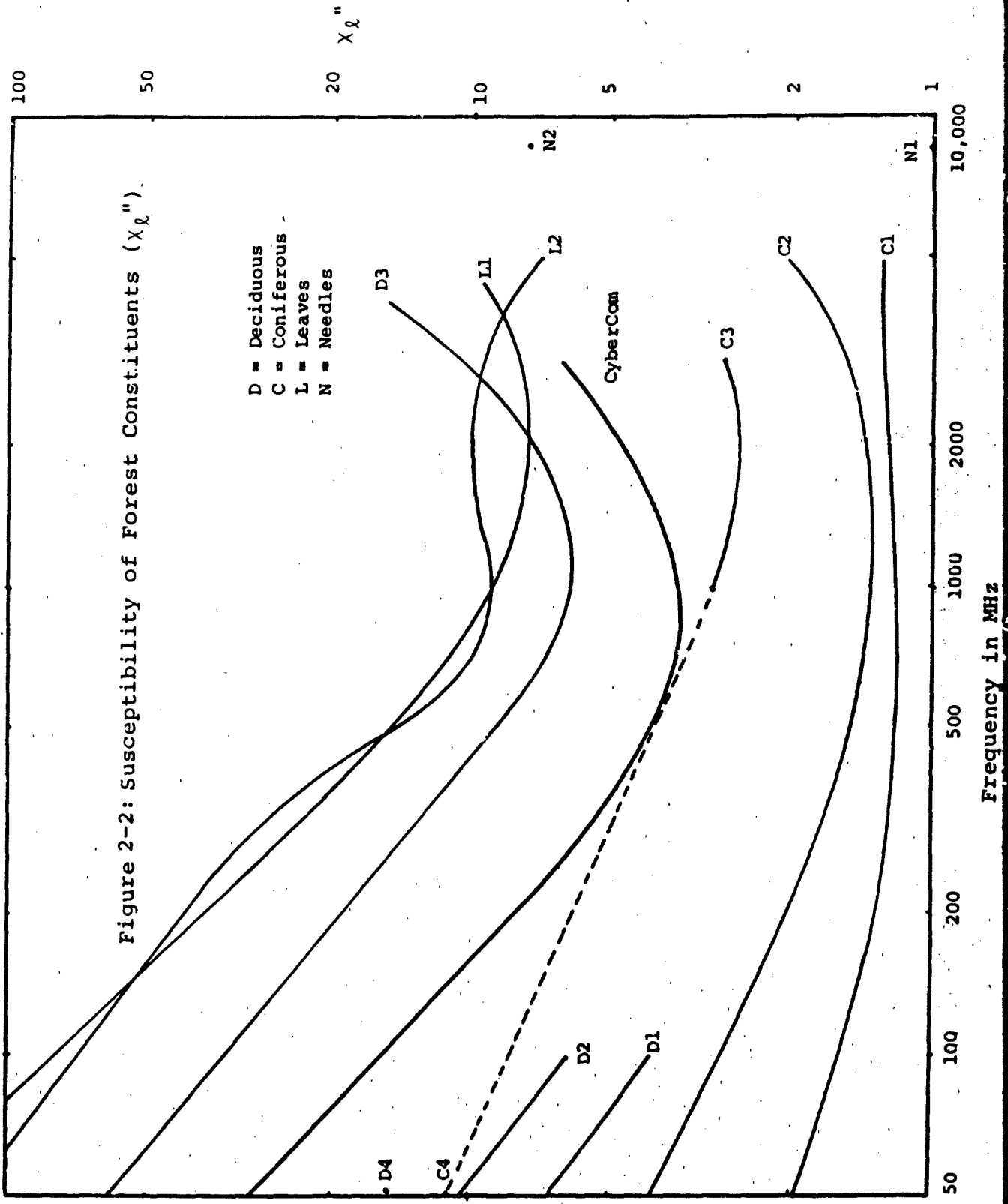
### 2.2.1  Trunk Diameter Distributions

The equations presented in Sections 4.1 and 4.2 of CyberCom Technical Report CTR-108-01 [42] for the effective dyadic susceptibility ($\chi$) and specific attenuation ($\alpha$) of tree trunks are predicated upon a fixed tree trunk diameter and are, therefore, applicable only to homogeneous forests. To calculate a weighted average of $\chi$ and $\alpha$ for a non-homogeneous forest the tree trunk diameter probability density function (or stand structure) must be known.

In general, the trunk diameter probability density function of an even-aged stand or plantation is nominally normal (gaussian) [28,54,76]. Expressed mathematically as

$$p(D) = (\sqrt{2\pi}\sigma)^{-1} \exp\{-(D-\bar{D})^2/2\sigma^2\} \qquad (2-2-1)$$

the normal probability density function is uniquely specified by two parameters - the mean tree trunk diameter ($\bar{D}$) and the standard deviation ($\sigma$). The mean trunk diameter of an even-aged stand depends upon the age of the stand - older stands having larger diameters, and the species composition - certain species grow faster than others. The projected average trunk diameters at 30, 60, and 90 years for several upland deciduous species are shown in Table 2-2 [28]. The standard deviation of the trunk diameters about the mean also depends upon the age and composition of the stand, although composition appears to be the more important parameter. Trunk diameter data taken from 87 half-acre plots used by the USDA Forest Service in Ohio, Kentucky, Missouri and Iowa suggest that the coefficient of variation (the ratio of $\sigma/\bar{D}$) ranges from about 0.7 (young, irregular stands) to about 0.1 (old, uniform stands) [refer to Table 6 of Gingrich [28]].

The similarity of nearly-normal empirical probability density functions of trunk diameter to the normal probability density function can be measured in terms of "skewness" and "kurtosis." Skewness is a measure of lack of symmetry; a density function with a longer tail to the right of the mean has positive skewness. Kurtosis is a measure of the extent to which the height of the

Table 2-2:  Projected Average Trunk Diameter (inches)

| Species | 30 years | 60 years | 90 years |
|---|---|---|---|
| Yellow poplar | 6.9 | 14.3 | 21.9 |
| Black walnut | 6.1 | 12.6 | 18.8 |
| Scarlet oak | 5.0 | 11.0 | 17.9 |
| Red oak | 4.6 | 10.1 | 16.8 |
| White ash | 4.7 | 10.0 | 16.1 |
| Black oak | 4.8 | 10.1 | 15.9 |
| Sugar maple | 3.9 | 8.4 | 13.5 |
| Beech | 3.4 | 7.4 | 12.1 |
| White oak | 3.6 | 7.5 | 11.8 |
| Hickory | 3.5 | 7.1 | 11.0 |
| Chestnut oak | 2.8 | 5.8 | 9.7 |

Table 2-3:  Trunk Diameter Distributions [Uneven-Aged Stands]

| Author | Region | Trees | Diameter | $\bar{D}$ | $r^2$ |
|---|---|---|---|---|---|
| Frank et al [24] | Northeast US | Spruce-Fir | 1-12" | 2.44" | 1.00 |
| Roach [54] | Allegheny | hardwoods | 1-12" | 2.27" | 0.99 |
| Wiant [76] | Appalachian | hardwoods | 4-15" | 2.44" | 0.99 |

empirical density function exceeds that of the normal density function; an empirical density function with a sharper, higher peak than the normal has positive kurtosis. All even-aged stands have some positive skewness, although skewness decreases with age [2 ,28]. Kurtosis, usually positive for very young stands, becomes negative as the stand ages. Nevertheless, both Gingrich [28] and Roach [54] have concluded that the coefficients of variation, skewness, and kurtosis are more closely related to tree average diameter than to stand site or age. This conclusion could prove especially helpful in developing forest models suitable for radiowave propagation prediction from forest stand data. Nearly-normal probability density functions for three even-aged stands are shown in Figure 2-3.

The Weibull probability density function has also been suggested as a probabilistic model for tree trunk diameters. In [15] an example is given for a 20-year old shortleaf pine (Pinus echinata) plantation having 800 trees per acre (1980 trees per hectare). The approximating Weibull probability density function, however, corresponds closely to a normal probability density function having a mean trunk diameter of 15.3 centimeters and a standard deviation of 3.8 centimeters.

The probability density function of an uneven-aged stand is nominally exponential (sometimes called inverse J-shaped in forestry). Expressed mathematically as

$$p(D) = (1/\overline{D})\exp\{-D/\overline{D}\} \qquad (2\text{-}2\text{-}2)$$

the exponential probability density function is uniquely specified by a single parameter - the mean tree trunk diameter ($\overline{D}$). In contradistinction to an even-aged forest, the mean trunk diameter of a mature uneven-aged stand does not depend upon its age - only upon its species composition. Table 2-3 shows several sources of uneven-aged forest data ( one of which is plotted in Figure 2-4 ) from the northeastern United States, and the mean trunk diameters derived by fitting exponential probability density functions to the data using a least-squares method. The mean trunk diameters are all close to 2.5 inches (6.35 cm);
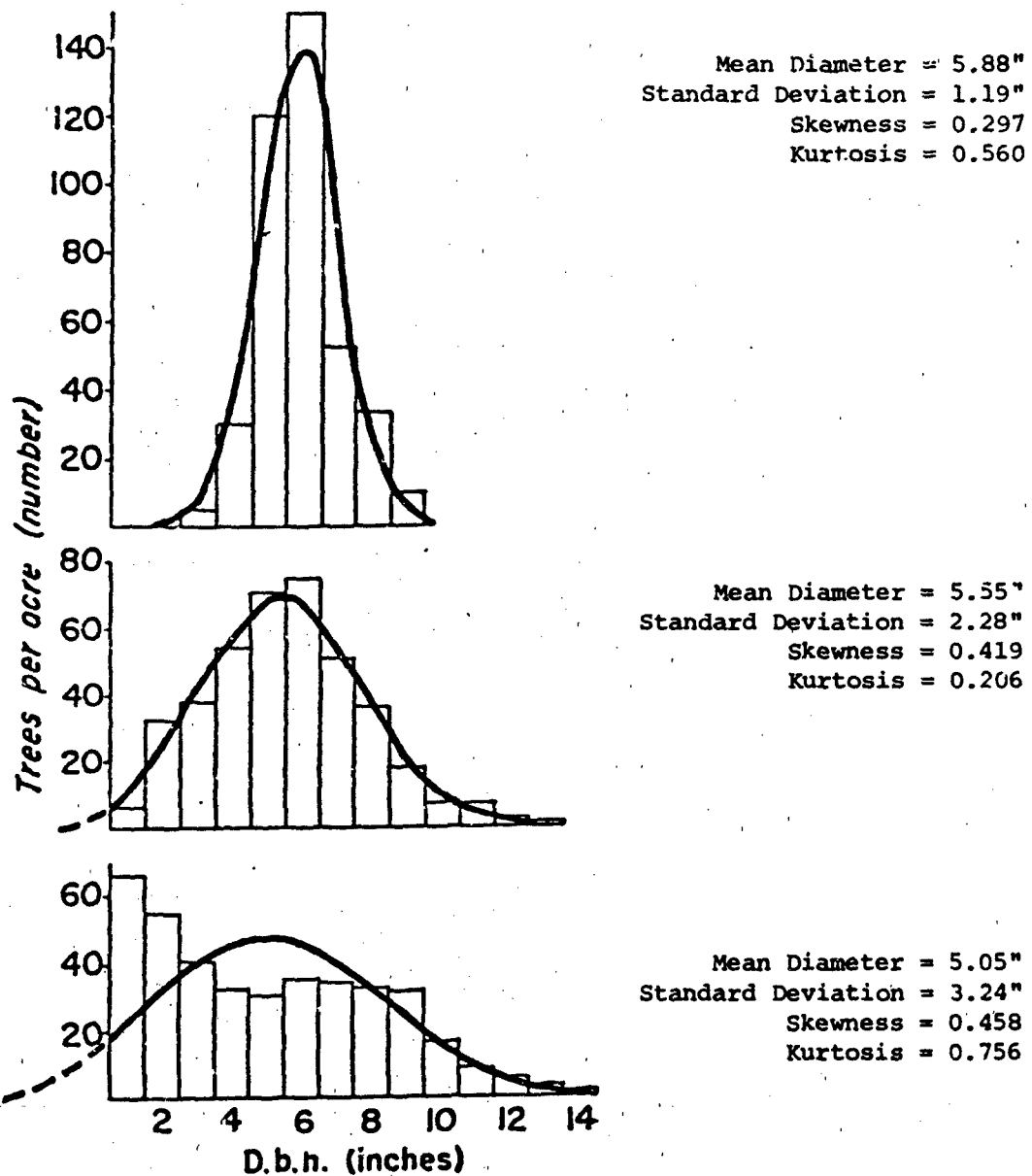
Figure 2-3: Trunk Diameter Probability Density Functions [Even-aged Stands] [28]
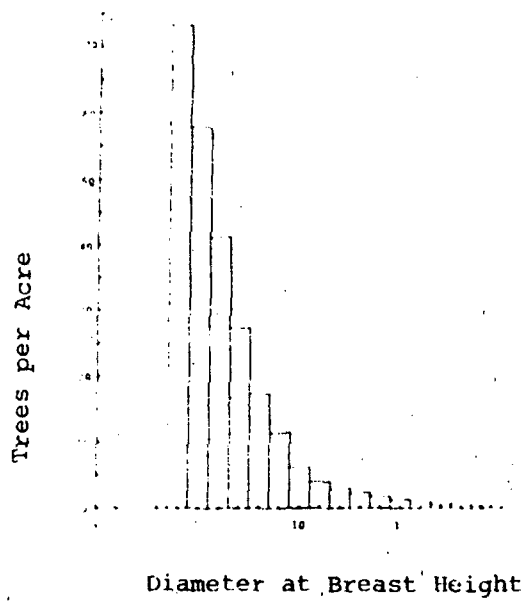
Figure 2-4:  Trunk Diameter Probability Density Function
[Uneven-aged Stand] [76]

the corresponding correlation coefficients of the least-squares fit are all near unity and suggest a very good fit.

It should be realized, however, that the parameter, mean tree trunk diameter ($\overline{D}$), as used above in Equation (2-2-2) is strictly a mathematical measure for the slope of the exponential probability density function and that the mean tree trunk diameter as measured in the field may be considerably larger, especially if the smaller trees are not well represented because of thinning and/or competition by the larger trees.

The previous paragraphs underscore the importance of mean trunk diameter in characterizing the trunk diameter probability density function. Other factors bearing on the density function, while not so important as mean trunk diameter, are the type of stand (even-aged or uneven-aged) and, if even-aged, its age and species composition (especially the latter). In addition to the trunk diameter probability density function, the trunk number density is also required to estimate the mean effective dyadic susceptibility and specific attenuation of non-homogeneous forests. A potentially useful aid in characterizing forests for radiowave propagation prediction may be the forester's "stocking guide." These guides relate trunk (stem) number density, trunk basal area, mean trunk diameter in the manner exemplified by Figure 2-5. Silviculturists use these guides to manage forest yield. As noted by Roach [54], "the guide has a rational biological basis; it is generally independent of the influence of site, age, or stand structure; and the measurements that are needed for its application can be easily and quickly obtained in the field." The trunk number density and basal area have been summarized by Cannell [9] for many forests of the world; the corresponding mean trunk diameter and, perhaps, species composition can be inferred from stocking guides; and from these data the trunk probability density function can be estimated.

2.2.2  Branch Orientation

The equations presented in Sections 4.1 and 4.2 of CyberCom Technical Report CTR-108-01 for the effective dyadic

DIAMETER OF TREE OF AVERAGE BASAL AREA — INCHES

BASAL AREA PER ACRE — SQUARE FEET

TREES PER ACRE — HUNDRED
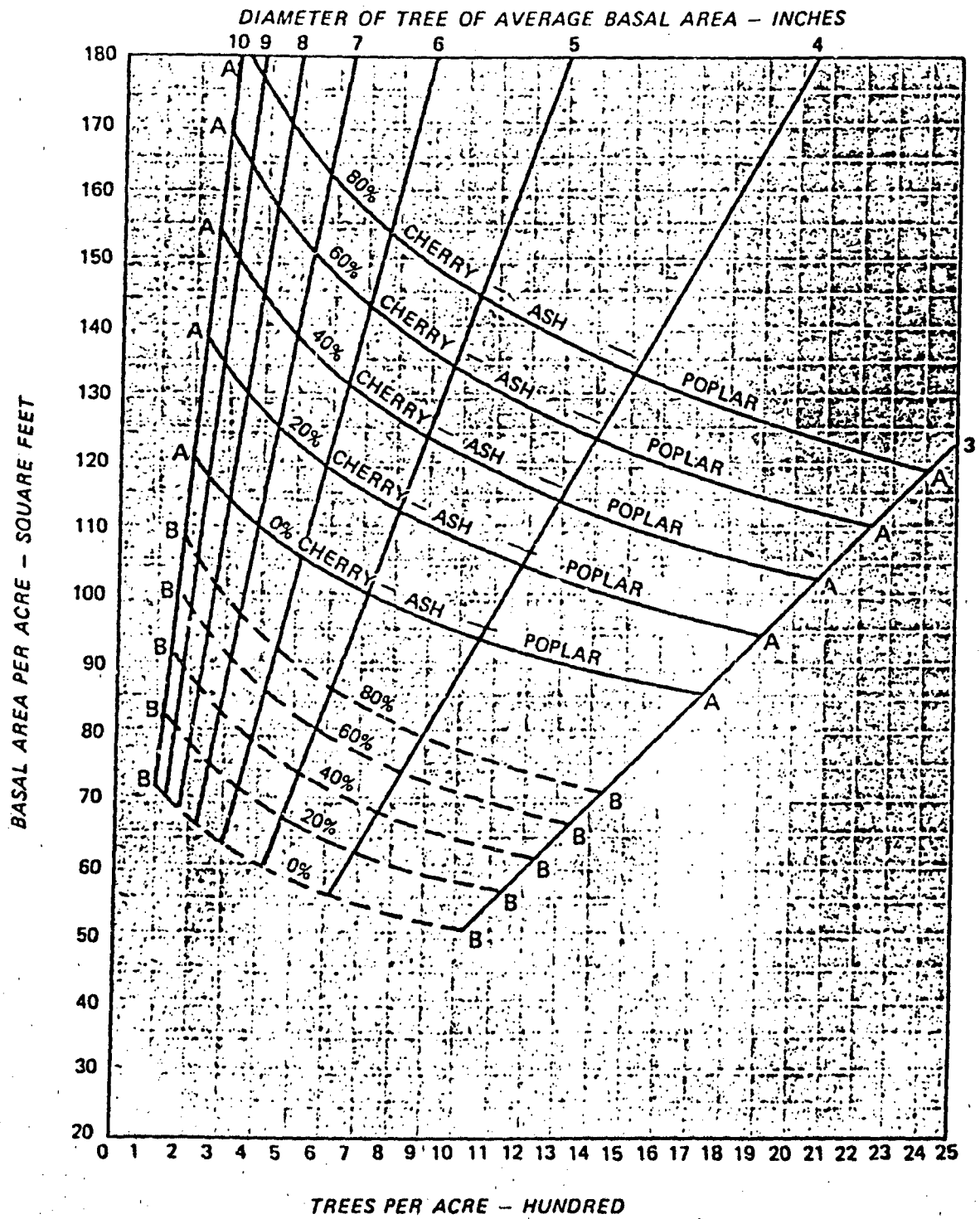
Figure 2-5:  Stocking Guide for Allegheny Hardwoods.

susceptibility and specific attenuation of branches and leaves involve the probability density functions of their inclination angles. Probability density functions for the branch inclination angles of 80-year old Lodgepole pine in Wyoming were measured by Gary [27] and are presented here in Figure 2-6(a). It is apparent from this figure that the inclination angles of the younger branches in the upper crown are steeper than those of the older branches in the lower crown. This trend is confirmed by Ford [24] and by Kimes et al [39]. The negative angles indicate that some branches pointed downward. Gary [27] also reported that there was no significant departure from azimuthal symmetry. Linear fits to these data have been made by CyberCom and are presented in Figure 2-6(b). These linear models for the probability density function of the branch inclination angle will be employed by CyberCom in subsequent numerical evaluations of the effective dyadic susceptibility and specific attenuation of coniferous forests. Analogous data for the branch inclination angles of deciduous trees have not yet been located.

## 2.2.3  Leaf Properties

Because leaf sizes approach the wavelength only at the higher frequencies of interest ($\lambda$ at 2000 MHz = 6"), it appears that the only leaf parameter of real importance in the present model is the fractional volume occupied. This is considered in the overall forest characterization of Section 2.4. However because of the previous concentration on leaf parameters in CyberCom Technical Report CTR-108-01 and because of possible future interest (at higher frequencies for the applications), the results of a study of leaf parameters is included below.

### 2.2.3.1  Leaf Diameter and Thickness

Two good sources for the area and thickness of leaves of southeastern deciduous trees were found. The data from Rothacher [56] are summarized in Table 2-4. The composition by species for the Tennessee Valley shows, in the weight column and in the numbers of trees larger than 11 inches diameter at
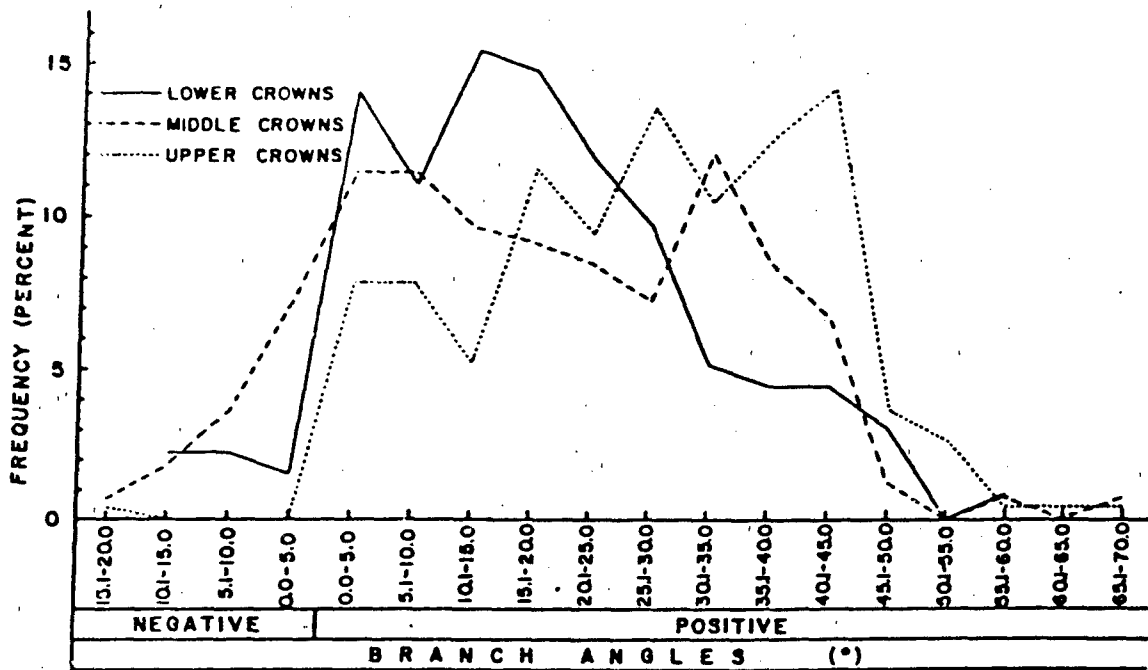
Figure 2-6(a):  Branch Inclination Angles (measured)
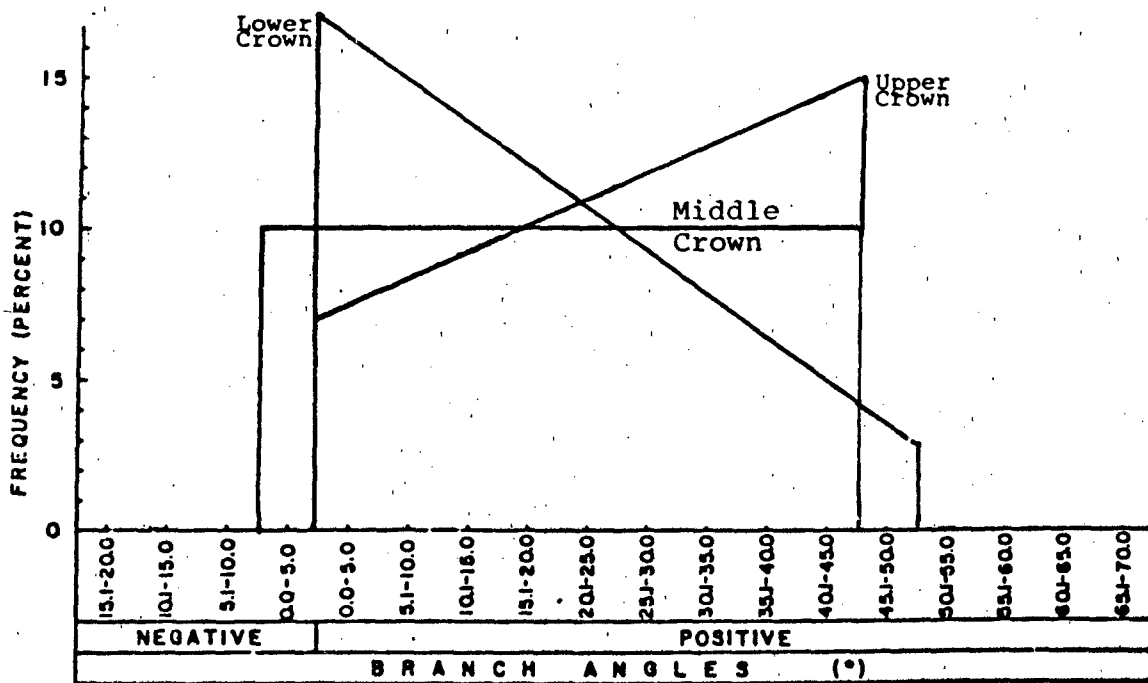


Figure 2-6(b):  Branch Inclination Angles (CyberCom)

Table 2-4 Biophysical Parameters of Clear Creek Forest Experimental Acre (1954) [56]

| Species | Number of Trunks by dbh class | | | | Trunk Basal Area ft² | Leaves/acre | | | Per Leaf | | | |
|---|---|---|---|---|---|---|---|---|---|---|---|---|
| | 0.5"-4.9" | 5.0"-10.9" | 11.0" plus | All | | Num. 1000 | Area m² | Dry Weight Kg | Area cm² | Thick. mm | Volume cm³ | Spec. Grav. g/cc |
| Quercus alba<br>White Oak | 85 | 13 | 2 | 100 | 7.71 | 840 | 3,240 | 212 | 39 | .24 | .9 | .27 |
| Quercus velutina<br>Black Oak | 79 | 3 | 5 | 87 | 7.60 | 284 | 2,414 | 195 | 85 | .18 | 1.5 | .45 |
| Quercus coccinea<br>Scarlet Oak | 14 | 6 | 8 | 28 | 13.54 | 787 | 3,833 | 327 | 47 | .15 | .7 | .57 |
| Quercus prinus<br>Chestnut Oak | 17 | 3 | - | 20 | 1.78 | 131 | 721 | 47 | 55 | .24 | 1.3 | .27 |
| Quercus falcata<br>Southern Red Oak | 9 | 1 | 2 | 12 | 3.20 | 214 | 975 | 94 | 46 | - | - | - |
| Quercus stellata<br>Post Oak | 4 | 1 | 1 | 6 | 1.54 | 38 | 209 | 9 | 55 | .31 | 1.7 | .29 |
| Quercus marylandica<br>Blackjack Oak | - | - | 1 | 1 | .72 | 26 | 114 | 13 | 44 | - | - | - |
| Carya tomentosa<br>Mockernut Hickory | 78 | 1 | - | 79 | 1.52 | 34 | 541 | 48 | 159 | .18 | 2.9 | .49 |
| Carya Glabra<br>Red Hickory | 65 | - | - | 65 | .72 | 21 | 243 | 17 | 116 | - | - | - |
| Acer rubrum<br>Red Maple | 30 | 1 | - | 31 | .60 | 103 | 258 | 16 | 25 | .20 | .5 | .31 |
| Liriodendron tulip.<br>Yellow Poplar | 9 | - | - | 9 | .34 | 48 | 279 | 19 | 58 | .20 | 1.2 | .34 |
| Prunus serotina<br>Black Cherry | 9 | - | - | 9 | .09 | 12 | 14 | 1 | 12 | .17 | .2 | .42 |
| Oxydendrum arboreum<br>Sourwood | 339 | 26 | - | 365 | 12.26 | 1082 | 3317 | 140 | 31 | .16 | .5 | .26 |

Table 2-4 Biophysical Parameters of Clear Creek Forest Experimental Acre (cont.)

| | Number of trunks by dbh class | | | | Trunk Basal Area ft² | Leaves/acre | | | Per Leaf | | | |
|---|---|---|---|---|---|---|---|---|---|---|---|---|
| | 0.5"-4.9" | 5.0"-10.9" | 11.0" plus | All | | Num. 1000 | Area m² | Dry Weight Kg | Area cm² | Thick. mm | Volume cm³ | Spec. Grav. g/cc |
| Nyssa sylvatica — Blackgum | 187 | 1 | – | 188 | 2.35 | 277 | 650 | 36 | 23 | – | – | – |
| Cornus florida — Dogwood | 98 | 2 | – | 100 | 2.07 | 294 | 859 | 37 | 29 | .30 | .9 | .14 |
| Sassafras albidum — Sassafras | 27 | – | – | 27 | .20 | 13 | 39 | 2 | 30 | .21 | .6 | .24 |
| Castanea dentata — Chestnut | 7 | – | – | 7 | .04 | 7 | 49 | 2 | 70 | .17 | 1.2 | .24 |
| Rhus Copallina — Flameleaf Sumac | 5 | – | – | 5 | .03 | 1 | 6 | 1 | 6 | – | – | – |
| Pinus echinata — Shortleaf Pine | 5 | 7 | – | 12 | 3.26 | 4533 | 1398 | 113 | 3 | – | – | – |
| Pinus virginiana — Virginia Pine | 2 | 1 | – | 3 | .53 | 322 | 81 | 6 | 2.5 | – | – | – |
| Trees-Number | 1069 | 66 | 19 | 1154 | | | | | | | | |
| Basal Area ft²: | 19.01 | 18.25 | 22.84 | | 60.10 | | | | | | | |
| Leaves-1,0 | 2089 | 5804 | 1174 | | | 9057 | | | | | | |
| Area-m² | 7180 | 5889 | 6171 | | | | 19240 | | | | | |
| Weight-Kg | 427 | 399 | 519 | | | | | 1345 | | | | |

2-17

breast height (dbh), the predominance of oaks. The numerous small sourwoods form an understory following a heavy cut 15 years before data acquisition. Dividing the total leaf areas by the numbers of leaves according to species, the area per leaf column is obtained with areas ranging from 2.5 $cm^2$ for pine needles to 159 $cm^2$ for hickory leaves. Catalpa leaf areas up to 750 $cm^2$ have been reported [1], but the more representative values of about 55 for Scarlet Oak and Yellow Poplar give a typical equivalent circular diameter of about 8 cm. The average leaf thicknesses, from Carpenter and Smith [11], are for shade leaves in Lexington, Kentucky. They range from 0.15 mm to 0.30 mm, with a typical value of 0.2 mm. The volumes per leaf range from 0.2 to 2.9 cc. The specific gravities are derived by dividing the total leaf weights in grams by the total volumes in cubic centimeters. The values range from 0.14 g/cc to 0.57 g/cc with a typical figure of about 0.35 g/cc.

The data for conifers provided in Table 2-5 are from the Biological Handbook [1] except the first two items from Rothacher [56]. Needle lengths have been added from Little [46]. An effective cylinder diameter for the short-leaf pine needle may be obtained as 0.5 mm using a length of 20 cm to account for two-leaf fascicles per Rothacher.

## 2.2.3.2 Foliage Inclination Angles

Probability density functions for the needle inclination angles of Lodgepole pine were measured by Kimes et al [39] and found to be relatively invariant with height. CyberCom has found that these density functions can be approximated by

$$p(\theta) = \begin{cases} 1/60, & (0° \leq \theta \leq 30°) \\ (90-\theta)/3600, & (30° \leq \theta \leq 90°) \end{cases} \qquad (2-2-3-2-1)$$

Subsequent measurements on Douglas fir by Smith et al [60] substantiate these results. Smith et al also considered the leaf inclination angles in a deciduous oak-hickory canopy. Here, only the lower-third of the canopy agreed with the coniferous probability density; the two upper-thirds had probability density

Table 2-5 Total Surface Areas of Conifer Needles [1]

| Species (P. = Pinus) | Location | Surface Area | | Length | Notes |
|---|---|---|---|---|---|
| | | cm²/leaf | cm²/plant | cm | |
| P. echinata Short Leaf Pine | Tennessee | 2.5 | 1.2 x 10 | 6-13 | Avg. of exp'tal acre (12 trees) |
| P. virginiana Virginia Pine | Tennessee | 3.0 | 270,000 | 5-7.5 | Avg. of exp'tal acre (3 trees) |
| P. strobus Eastern White Pine | Vermont | 1.2 | 149,000 | 6-13 | 27 years old 2' x 2' spacing |
| P. resinosa Red Pine | Vermont | 4.0 | 78,000 | 13-15 | 27 years old 2' x 2' spacing |
| P. banksiana Jack Pine | Minnesota | 5.0 | | 2-4 | 6000'-7000' alt. |
| P. contorta Lodgepole Pine | Wyoming | 1.3 | | 2.5-7.5 | 6000'-7000' alt. |
| Picea engelmannii Engelmann Spruce | Wyoming | .5 | | 1.5-2.8 | 6000'-7000' alt. |
| Abies lasiocarpa Alpine Fir | Wyoming | .6 | | 2.5-4.5 | 6000'-7000' alt. |

functions that were essentially uniform for inclination angles between 0 and 33 degrees from the horizontal.

## 2.3 Forest Canopy Structure

The most obvious structural feature of a forest is not just that it consists of trunks, branches and leaves, but that these are formed into a canopy of branches and leaves, supported by the trunks. (For isolated or widely-spaced trees, the continuous canopy reduces to an ensemble of crowns). This simple concept, with importance for electromagnetic modelling, is not well covered in the literature. The lumberman pays for wood without regard to its source and the business expert cares no more about the growing heights of leaves or branches. Only academic sources, sometimes in support of the above economically-oriented workers, were found for canopy structure, largely coniferous. Some items considered below include foliage distribution and canopy thickness.

The distribution of foliage weight with height in the canopy of an even-aged stand (e.g., a plantation of trees planted at the same time) can be reasonably well described by a normal (gaussian) probability density function [24,27,63,73]. Nevertheless, as might be expected, not all even-aged stands show good agreement. For example, although Waring et al [67] showed this model to be valid for Ponderosa pine, they found Douglas fir and Grand fir had modal peaks well below mid-canopy height. Further, although Stephens [63] found this model suitable for Red pine and Japanese cedar, he also found the weight distributions for three species of deciduous trees from Japan to have modal peaks well above mid-canopy. This upward skew of the weight distribution for deciduous trees is also supported by Figure 65 of Assmann [2] and by Table 2-6 from Smith et al [60].

Although canopy thickness data are scarce, Ford's curve [24] for a stand of Sitka spruce suggests a ratio of canopy thickness to forest height of about 0.6. Gary [27], too, suggests a ratio close to 0.6 for Lodgepole pine; Kinerson and Fritschen

Table 2-6: Canopy Layer Heights and Leaf Area Index (LAI)

| | Douglas Fir | | Oak-Hickory | |
| Canopy Layer | Median Height (m) | LAI | Median Height (m) | LAI |
|---|---|---|---|---|
| Upper | 23.2 | 1.5 | 18.3 | 3.4 |
| Middle | 14.0 | 5.3 | 11.0 | 0.8 |
| Lower | 4.7 | 1.0 | 3.7 | 0.4 |

Note: LAI = Total one-sided leaf area / projected area under canopy

Table 2-7: Total Green Weight of Above-Ground Tree Biomass (millions of metric tons) (excluding foliage) [48]

| Softwoods (Coniferous) | | | Hardwoods (Deciduous) | | |
|---|---|---|---|---|---|
| Southern Pines | 2175 | 35.0% | Oaks | 1543 | 25% |
| Loblolly | 923 | 15.0% | Soft Hardwoods | 1542 | 25% |
| Slash | 461 | 7.5% | | | |
| Other Pines | 791 | 12.5% | | | |
| Other Softwoods | 281 | 4.0% | Other Hardwoods | 717 | 11% |
| Total Softwoods | 2455 | 39.0% | Total Hardwoods | 3803 | 61% |

[40] about 0.5 for Douglas fir; and Assmann [2] about 0.4 for Norway spruce and 0.3 for Scots pine. All are, obviously, conifers. For deciduous trees, Hutchinson and Matt [33] give a relative canopy thickness of 0.5 for Yellow Poplar at Oak Ridge, Tennessee, and Assmann [2] gives a value of 0.5 for Common beech. In view of these data, CyberCom will employ a value of 0.5 for the ratio of canopy thickness to forest height for all forest models, coniferous and deciduous.

## 2.4 Forest Models

Although models of all forests of the world may ultimately be of interest, it seems best to start with a region of high interest and high data availability, such as the southeastern United States. Recently empirical test data were acquired in Florida and Tennessee in areas dominated by oaks and pines. Table 2-7, which refers to commercial forest land in the seaboard states from Virginia to Florida shows that pines comprise 35% and oaks 25% of the above ground forest biomass.

The best forest data base available - broadest in both geographical coverage and in parameters considered - appears to be a 1982 compilation of "World Forest Biomass and Primary Production Data" by M.G.R. Cannell [9]. The first half of Table 2-8 summarizes 12 pages of this book, including most of the relatively complete data from the southeastern United States, largely from the Great Smoky Mountains. From these data are derived the fractional volumes in the right hand columns and several representative parameters.

The first numerical column of Table 2-8 gives the number of trees generally larger than 2 cm in diameter at breast height (dbh) per hectare ($10^4 m^2$) of forest. A typical figure of 2500 corresponds to an average trunk density $\rho_t$ of 0.25 trunks/$m^2$ or an average spacing between trunks of about 2 meters. The average tree heights presented in the second column are used in establishing the height of the forest and estimating leaf and branch fractional volumes. In the third column, basal area gives the total of the cross-sectional areas of all the trees

Table 2-8  Southeastern United States Forest Parameters

| Species | Locale | Num. Dens. N/ha | Avg. Ht. m | Basal area m²/ha | Stem Vol. m³/ha | Dry Mass in t/ha Stem& Bark | Brchs | Lvs | Spec Grav. g/cc | Fractional Vol. in % Stem& Bark | Brchs | Lvs | Leaf Area Index |
|---|---|---|---|---|---|---|---|---|---|---|---|---|---|
| Acer saccharum (Sugar Maple) | Gt. Sm. | 1210 | 33 | 64 | 890 | ←606→ | | 3.5 | .56 | ←1.3→ | | .008 | - |
| Aesculus octandra (Yellow Buckeye) | Gt. Sm. | 1450 | 34 | 54 | 720 | 422 | 74 | 4.0 | .35 | 1.4 | .25 | .013 | 6.2 |
| Fagus grandifolia (American Beech) | Gt. Sm. | 2170 | 13 | 22 | 120 | 93 | 35 | 3.0 | .56 | .51 | .19 | .016 | 7.4 |
| Liriodendron tul. (Yellow-Poplar) | Gt. Sm. | 1820 | 22 | 34 | 310 | 167 | 49 | 4.7 | .40 | .76 | .22 | .021 | - |
| Liriodendron tul. (Yellow-Poplar) | Tenn. | - | 20 | 19 | - | 84 | 21 | 3.9 | .40 | .42 | .11 | .020 | - |
| Populus deltoides (E. Cottonwood) | Ala. | 8056 | 15 | 20 | 131 | 56 | 7 | 3.6 | .37 | .40 | .05 | .026 | - |
| Quercus alba (White Oak) | Gt. Sm. | 660 | 29 | 31 | 350 | ←366→ | | 3.5 | .60 | ←.84→ | | .008 | - |
| Quercus prinus (Chestnut Oak) | Gt. Sm. | 2130 | 30 | 36 | 402 | ←416→ | | 4.2 | .65e | ←.85→ | | .009 | 6.3 |
| Abies fraseri (Fraser Fir) | Gt. Sm. | 1410 | 26 | 50 | 488 | ←310→ | | | .39 | ←1.22→ | | | - |
| Picea rubens (Red Spruce) | Gt. Sm. | 640 | 23 | 51 | 514 | ←300→ | | | .38 | ←1.37→ | | | - |
| Pinus taeda (Loblolly Pine) | N.C. | 2243 | 15 | 49 | - | 125 | 15 | 8.0 | .47 | .71 | .09 | .045 | - |

e = estimated from similar species

(d≥2cm) per hectare. A typical basal area of 45 m²/ha with 1500 trees/ha gives a cross-sectional area per tree of 0.03 m², corresponding to an average tree diameter of about 20 cm. The fourth column, stem volume, is the total of all trunk volumes independent of dbh.

Dry masses are shown next in columns five, six and seven for stem wood and bark combined, branches, and leaves. An arrow indicates that a figure includes that for the adjacent column. It is of interest to note that the maximum/minimum ratio for trunks and branches runs near 11, but for leaves only 1.5. This may reflect a basic requirement for efficient capture of radiation by the canopy. Specific gravities (green vol./dry wt.) from the Wood Handbook [70] are listed next in column eight. These are used to estimate fractional volumes for use in equations for specific attenuation. Several of these values, notably those for maple and the oaks, differ significantly from those calculated in Table 2-4 for dry leaves. The difference may arise from the use of green leaf thicknesses in the calculations, but it is not understood in that case why the values for Yellow Poplar are not equally far off.

The weights per hectare divided by the specific gravities give the volume per hectare, but to convert this to fractional volume requires the "canopy volume", that is, its effective thickness over the hectare. Although illustrations in tree manuals suggest that the leaves are confined to about eight-tenths of the average tree height, pictures taken within forests reveal that leaves or needles may be confined to much smaller fractional height and so one-half was used. These results are expressed in percent for compactness, and show high variability.

The leaf area index is the total one-sided leaf area divided by the projected area under the leaves. Thus, the total number of leaves per hectare is the product of the leaf area index and the projected area, $10^4 m^2$, divided by the one-sided area of a single leaf. The leaf number density $\rho_\ell$ can be obtained by dividing the number of leaves per hectare by the "canopy volume", which is projected area times effective canopy thickness.

For example, for a forest with a leaf area index of 6, an effective canopy thickness of 16 meters and a per-leaf area of 50 cm$^2$, $\rho_\ell$ is about 75 leaves per cubic meter.

[This page intentionally left blank]

## 3.0  Unbounded Forest Susceptibility and Specific Attenuation

This section of this report will investigate the effects of changing forest parameters on the effective susceptibility and specific attenuation of the forest considered as a uniform dielectric medium. Three main types of forest are considered. Homogeneous (even-aged) forests of tree trunks of different diameters from 1 to 16 inches diameter are covered in Section 3.1. Non-homogeneous (uneven-aged) forests of trunks with diameters following the exponential distribution are covered in Section 3.2. Finally, forests of leaves are covered in Section 3.3.

## 3.1  Homogeneous Forest of Tree Trunks

The sensitivity to tree trunk diameter of the effective dyadic susceptibility ($\underline{\underline{\chi}}$) and the specific attenuation ($\alpha$) of an unbounded, homogeneous forest of parallel trees is shown in Figures 3A-1 to 3A-18. These results, which encompass a range of trunk radii extending from 0.0125 meter to 0.20 meter, have been calculated using Equation (4-1-1-1) and (4-2-1-3) of CyberCom Technical Report CTR-108-01. Because of the relatively weak dependence of $\epsilon_\ell$ on frequency, both $\underline{\underline{\chi}}$ and $\alpha$ are sensitive to frequency and trunk radius primarily through the parameter $k_o a$. As a consequence, the curves presented in these figures are very nearly frequency-shifted replicas of each other, although they are displaced in magnitude by an amount proportional to a power of a. In the case of $\underline{\underline{\chi}}$, the displacement is proportional to $a^2$; in the case of $\alpha$, the displacement is proportional to $a^2$ in the low-frequency (Rayleigh) region and to $a^{3/4}$ in the resonant region. At the higher resonant frequencies, the resonant <u>maxima</u> of $(\chi'_t, \chi'_z)$ decrease roughly as the square of the frequency; conversely, the resonant <u>minima</u> of $(\chi''_t, \chi''_z)$ decrease roughly linearly with increasing frequency. The first null in $\chi'_z$ is due to a change in sign of $\chi'_z$ occurring as a consequence of resonance when the circumference of the tree equals the wavelength within it ($300/f_{MHz}\sqrt{\epsilon}$). This resonant behavior may be attributed to circumferential surface waves

that reinforce themselves after successive trips around the perimeter [49,50]. It is apparent from Figures 3B-3 through 3B-5 that the specific attenuations for both horizontally and vertically polarized radiowaves have nearly the same high-frequency asymptote.

## 3.2 Non-homogeneous Forest of Tree Trunks

In order to determine the effective dyadic susceptibility and specific attenuation in a non-homogeneous forest, wherein the tree trunk radius a is a random variable described only statistically by some probability density function p(a), it is necessary to effect a weighted average of the $\underline{\underline{X}}$ and $\alpha$ attributable to some particular radius a. In a non-homogeneous forest the mean effective dyadic susceptibility $\overline{\underline{\underline{X}}}$ and the mean specific attenuation $\overline{\alpha}$ can be determined from the following relations:

$$\overline{\underline{\underline{X}}} = \int \underline{\underline{X}}(a)p(a)da \qquad (3\text{-}1\text{-}1)$$

$$\overline{\alpha} = \int \alpha(a)p(a)da \qquad (3\text{-}1\text{-}2)$$

where,

$\underline{\underline{X}}(a)$ = effective dyadic susceptibility for trunk of radius a

$\alpha(a)$ = specific attenuation for trunk of radius a

$p(a)$ = probability density function of trunk radii.

The probability density function of the trunk radii (diameters) has been discussed and described in Subsection 2.2.1 and found to be nearly normal (gaussian) for even-aged forests and exponential for uneven-aged forests. However, in th remainder of this subsection, only uneven-aged, non-homogeneous forests will be considered. In consonance with Section 2.2.1 and Table 2-4 it will be assumed that

$$p(a) = (1/\overline{a})\exp[-a/\overline{a}] \qquad (3\text{-}1\text{-}3)$$

where $\overline{a}$ = 3.2 cm is the mean tree trunk radius.

The mean effective dyadic susceptibility and mean specific attenuation in an unbounded, uneven-aged, non-homogeneous, trunk-

3-2

dominated forest, wherein tree trunk radii are described statistically by the exponential probability density function of Equation (3-1-3), has been evaluated using the approximations

$$\bar{\bar{X}} \simeq \sum_{i}^{N} \underline{X}(a_i) p(a_i) \Delta a_i \qquad (3\text{-}1\text{-}4)$$

$$\bar{\alpha} \simeq \sum_{i}^{N} \alpha(a_i) p(a_i) \Delta a_i \qquad (3\text{-}1\text{-}5)$$

and plotted in Figures 3-1 and 3-2. In effecting these calculations N was set equal to 12 and the $a_i$ assumed the values from 1 to 12 inches. For convenience, these results have been normalized to a tree trunk number density of $\rho = 0.1$ tree trunk per square meter. The usual smoothing effect of integration is very apparent.

In any real forest, the exponential probability density function proves valid only over a range of a bounded by, say, $a_{min}$ to $a_{max}$. Outside of this range, the exponential probability density function usually over-estimates the relative number of tree trunks. Recognizing this, the validity of Equations (3-1-4) and (3-1-5) if the limits of integration are restricted to the range $[a_{min}, a_{max}]$ can be assessed by considering the normalized distribution function

$$F(a_{max}) = \int_{0}^{a_{max}} f(a) p(a) da \Big/ \int_{0}^{\infty} f(a) p(a) da \qquad (3\text{-}1\text{-}6)$$

where $f(a)$ assumes the role of either $\underline{X}$ or $\alpha$. More specifically, if $f(a) = \underline{X}$ or if $f(a) = \alpha$ and attention is restricted to the low-frequency (Rayleigh) region, then $f(a) \propto a^2$ and

$$F(a_{max}) = [1 - (1 + a_{max}/\bar{a} + a_{max}^2/2\bar{a}^2) \exp\{-a_{max}/\bar{a}\}] \qquad (3\text{-}1\text{-}7)$$

If $f(a) = \alpha$ and attention is restricted to the resonant region, then $f(a) \propto a^{3/4}$ and

$$F(a_{max}) = \gamma(1.75, a_{max}/\bar{a})/\Gamma(1.75) \qquad (3\text{-}1\text{-}8)$$

where $\gamma(x,y)$ is the incomplete gamma-function defined by

EFFECTIVE DYADIC SUSCEPTIBILITY

FREQUENCY IN MHZ

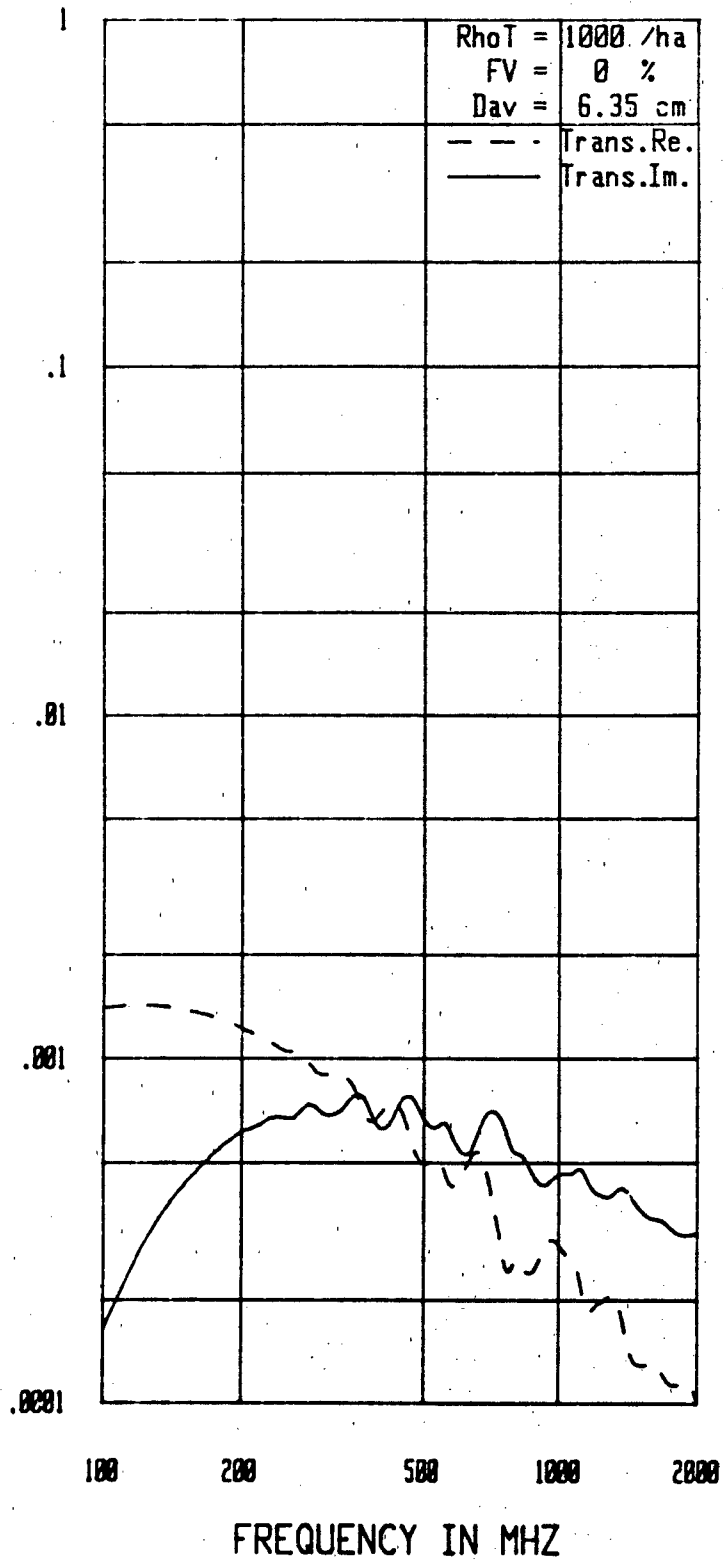| RhoT = | 1000 /ha |
| FV = | 0 % |
| Dav = | 6.35 cm |
| — — · | Trans.Re. |
| ——— | Trans.Im. |

Figure 3-1(a):   Effective Dyadic Susceptibility - $X_t$
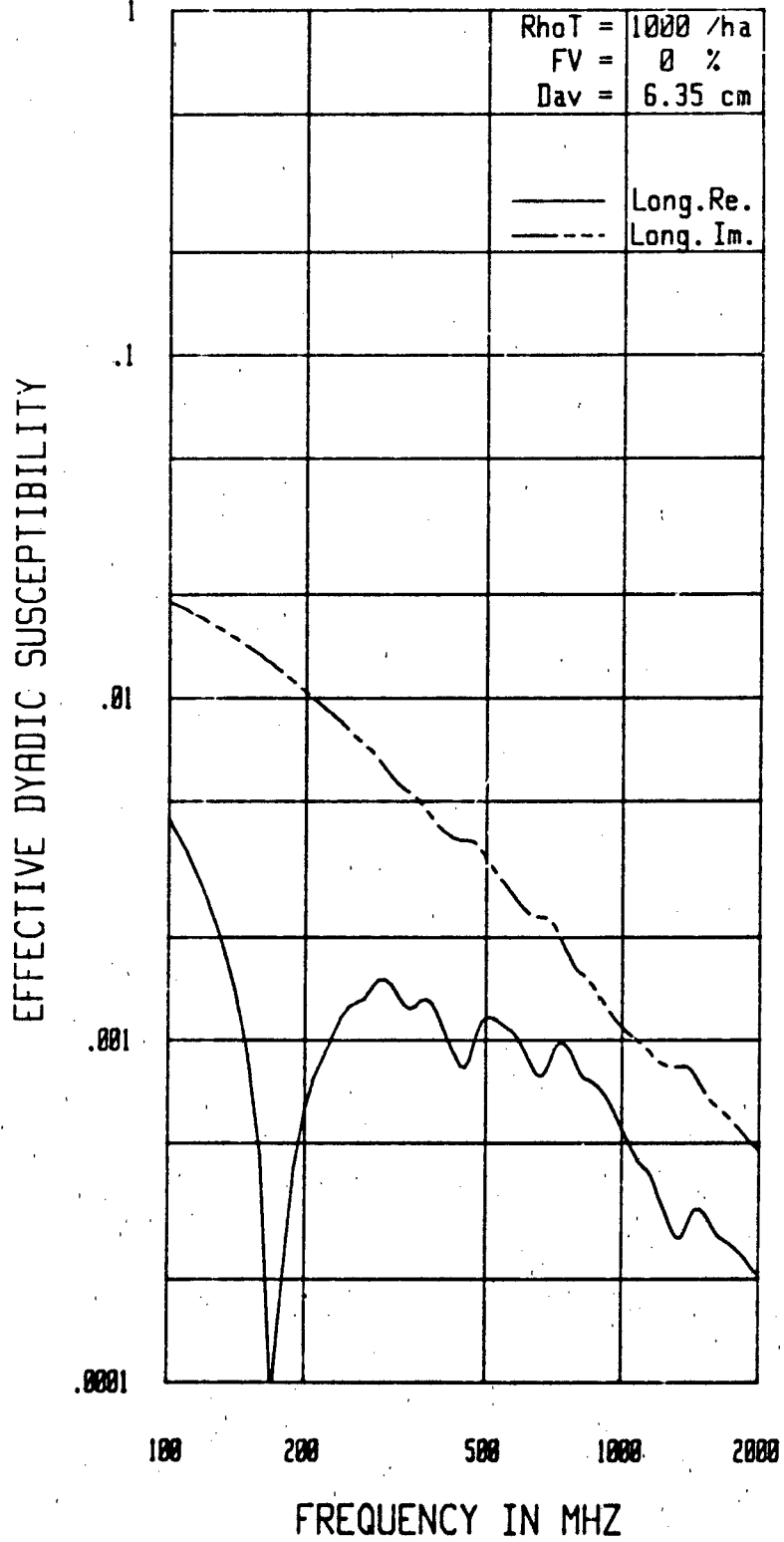(Trunks, Uneven-aged, $\bar{a}$ = .031m)

Figure 3-1(b): Effective Dyadic Susceptibility - $\chi_z$
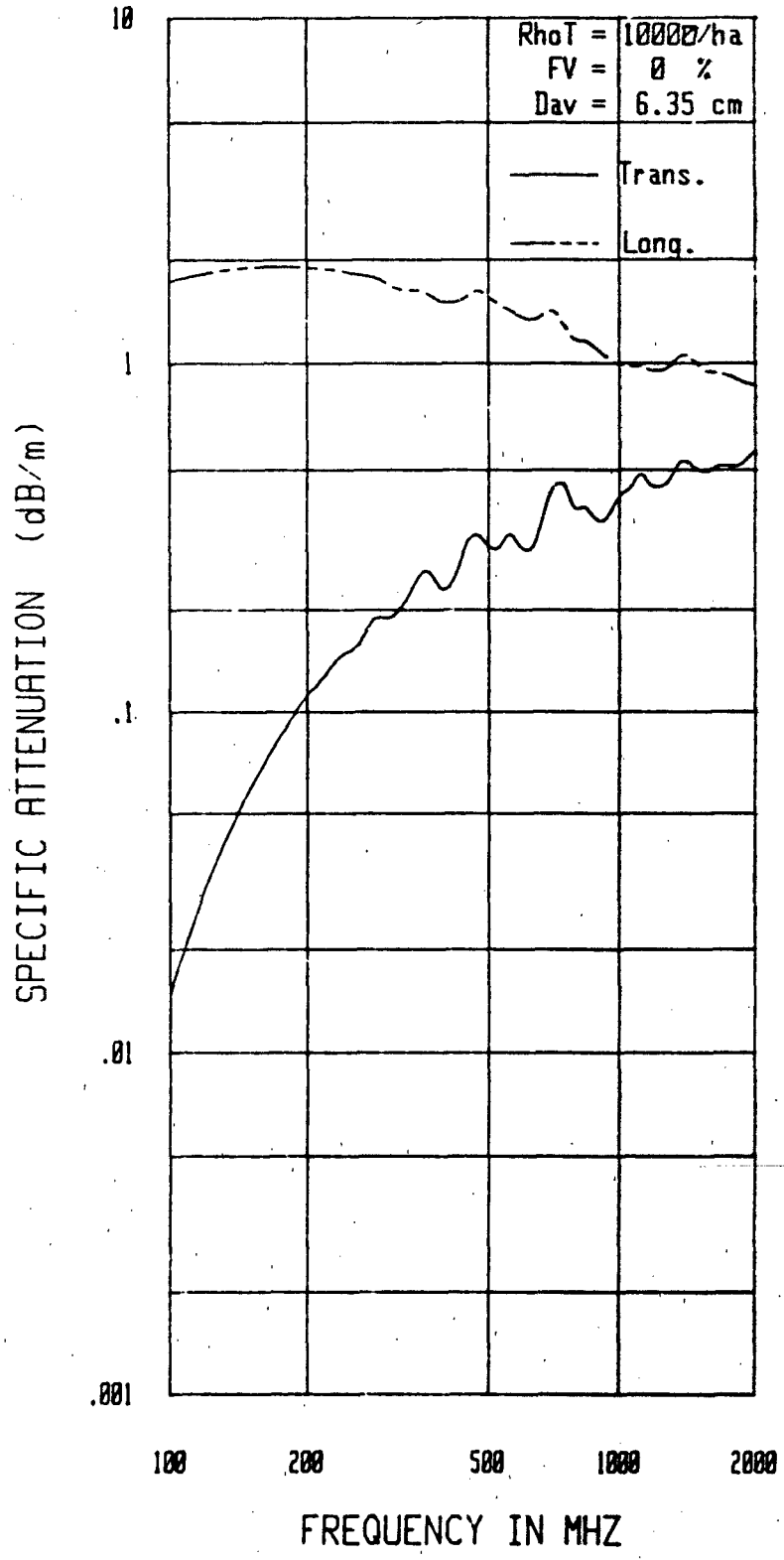(Trunks, Uneven-aged, $\bar{a} = .031m$)

3-5

Figure 3-2:  Specific Attenuation (Trunks, Uneven-aged, $\bar{a} = .031$m)

$$\gamma(x,y) = \int_0^Y t^{x-1}\exp\{-t\}dt \qquad (3-1-9)$$

and $\Gamma(x)$ is the complete gamma-function defined by

$$\Gamma(x) = \int_0^\infty t^{x-1}\exp\{-t\}dt \qquad (3-1-10)$$

The normalized distribution function $F(a_{max})$ has been evaluated in both the Rayleigh and resonant regions using Equations (3-1-7) and (3-1-8), respectively, and plotted in Figure 3-3. It is apparent from this figure that in an uneven-aged forest typical of the northeastern United States about 80% of the mean effective dyadic susceptibility or the mean specific attenuation in the Rayleigh region can be attributed to trees having trunk radii in the range 4-16 centimeters (diameter at breast height in the range 3-13 inches). About 80% of the specific attenuation in the resonant region can be attributed to trees having trunk radii in the range 1-11 centimeters (diameter at breast height in the range 1-9 inches). In the frequency range 200-2000 MHz where all trees having trunk radii greater than about 1 centimeter (2 inch diameter at breast height) are resonant, the mean specific attenuation is primarily attributable to tree trunk radii in the range 1-11 centimeters (1-9 inches at breast height).

3.3 Forest of Leaves

Figures 3-4 and 3-5 show similar $\underline{\chi}$ and $\alpha$ plots for the leaf forest considered in CyberCom Technical Report CTR-108-01 in order to make this report complete in itself and to present comparisons between leaf and trunk forest characteristics*. Because the leaves are small compared to the wavelength (Rayleigh or non-resonant) the plots are relatively smooth. The plots for large diameter trees are fairly smooth due to averaging resulting from the large number of wavelengths on a circumference. Because the trunks are all vertical and the leaves are largely horizontal (0° to 30° tilt), $\chi_t > \chi_\ell$ for leaves and vice versa

*Figures 4-1, 2, 4, 6, and 9 of CyberCom Technical Report CTR-108-01 are shown as Figures 3A-4, 3-4, 3B-4, and 3-5.
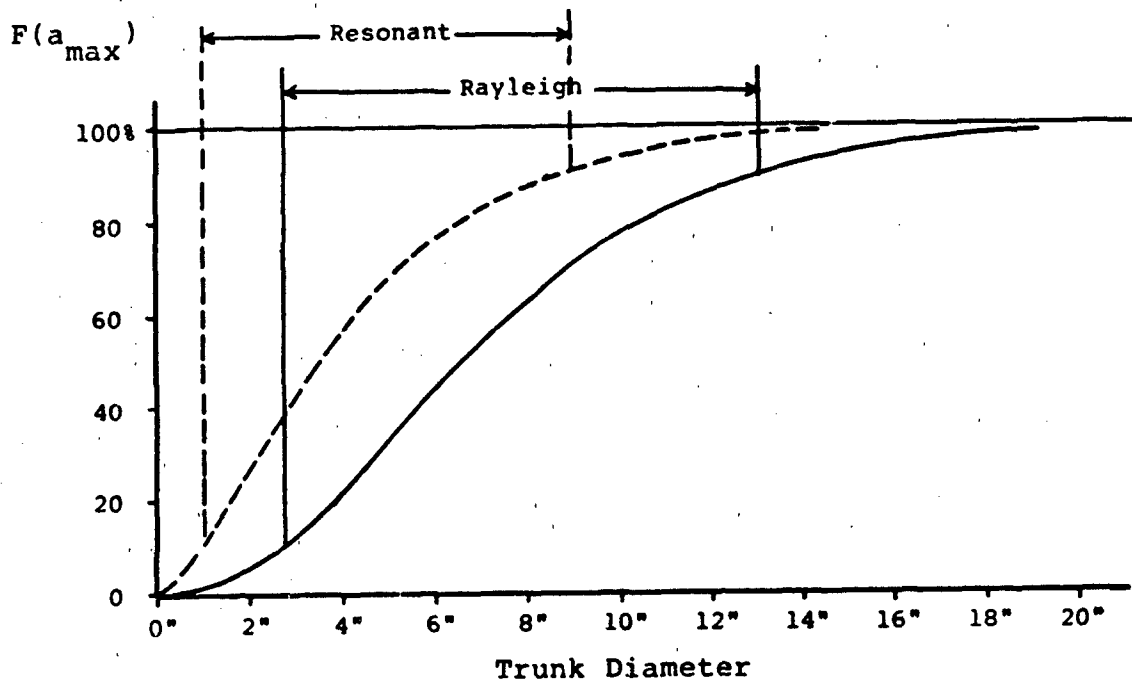
Figure 3-3:  Normalized Distribution Function $F(a_{max})$

Figure 3-4: Effective Dyadic Susceptibility (Leaves, FV = .1%)
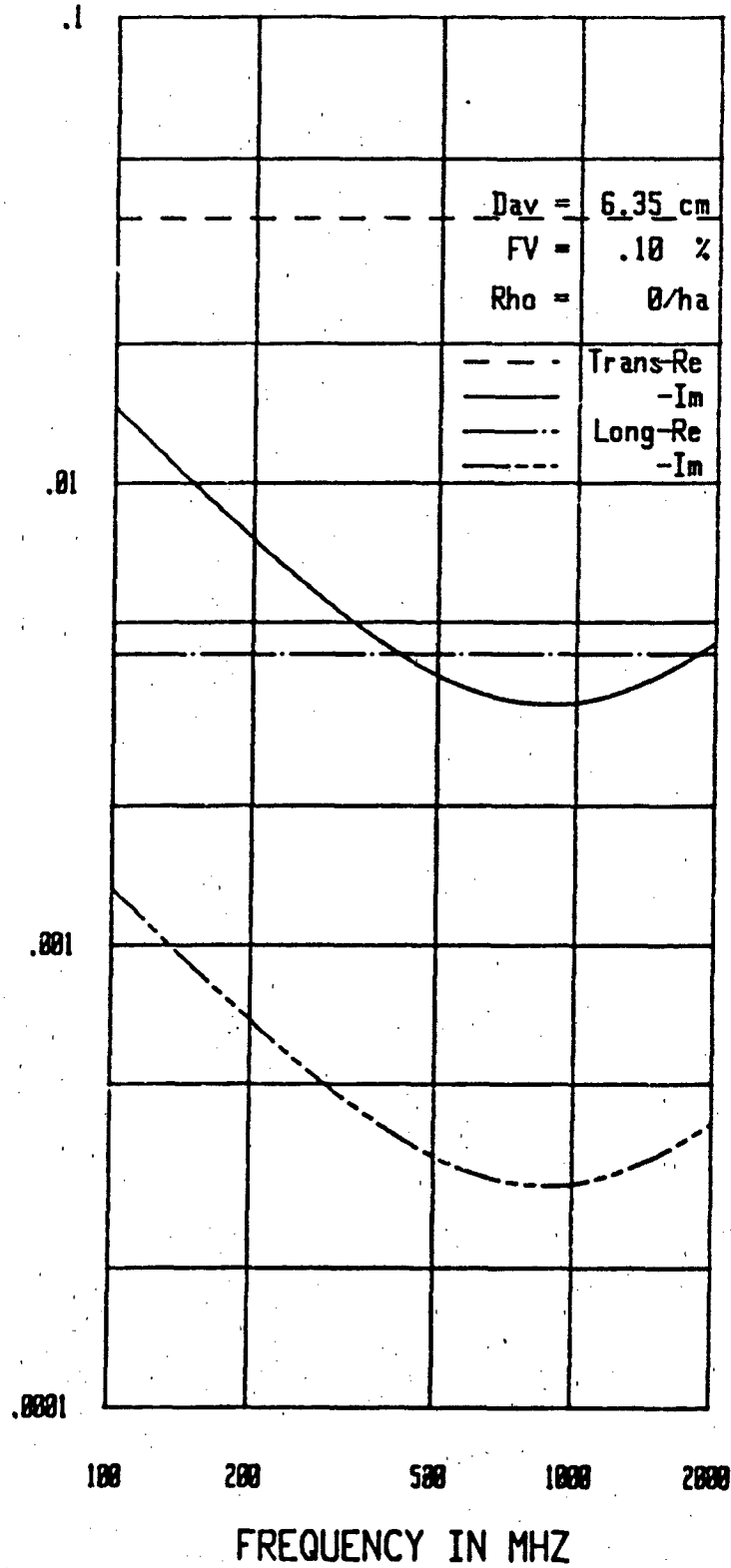
SPECIFIC ATTENUATION (dB/m)

10

Dav = 6.35 cm
FV = .10 %
Rho = 0/ha

Trans
———— Long
——·——

1

.1

.01

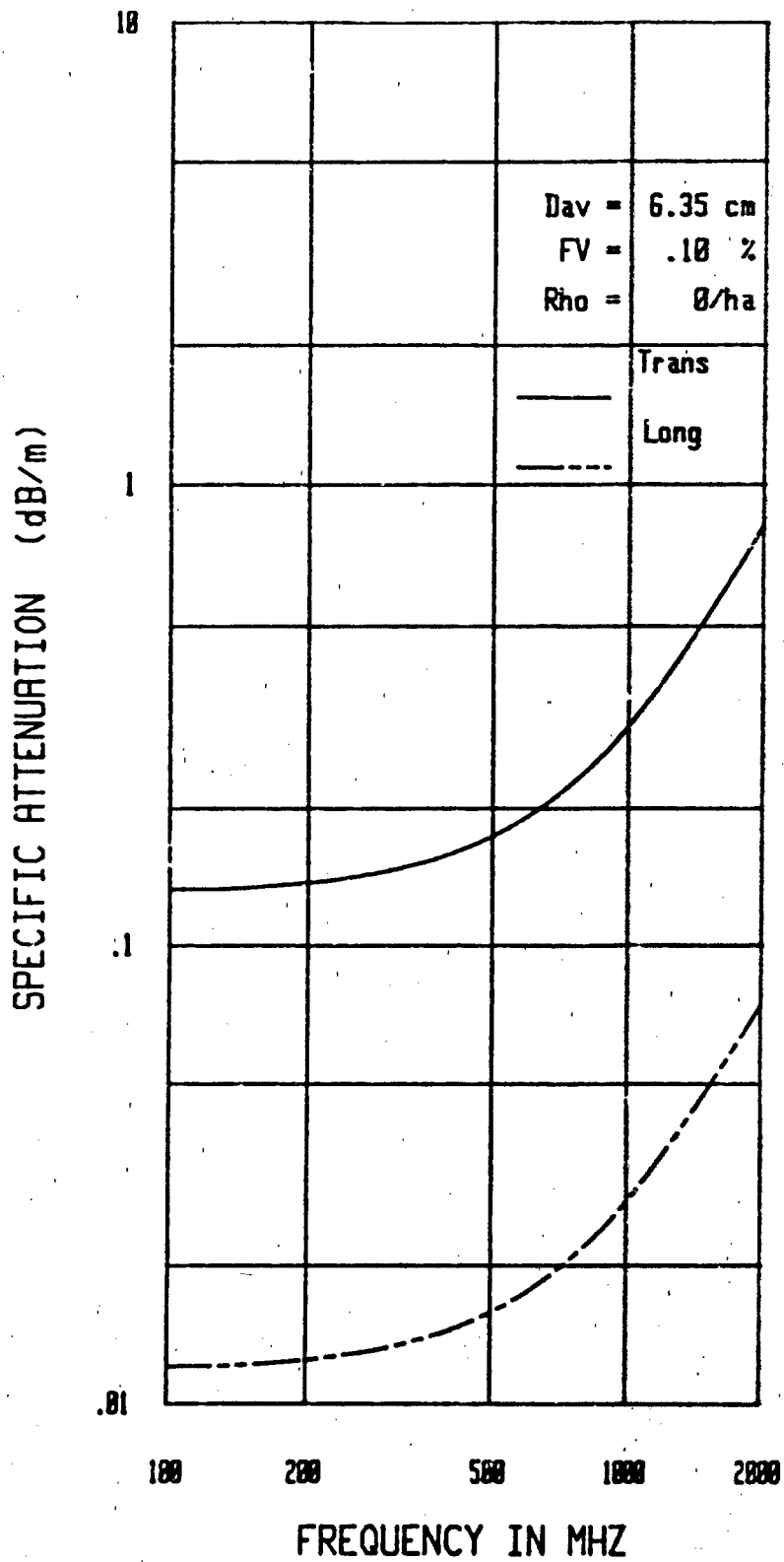100    200       500   1000    2000

FREQUENCY IN MHZ

Figure 3-5:   Specific Attenuation (Leaves, FV = .1%)

3-10

for trunks. It may be seen, of course, that the α curves are closely related to those for $\underline{X}"$ (imaginary plot of susceptibility).

The sensitivity of $\underline{X}"$ for a non-homogeneous forest (1-12-1) to addition of leaves was briefly investigated. For the most interesting case with vertical antennas, $X_z"$ showed only a small change at highest frequencies upon addition of 0.1% fractional volume of leaves, as in CyberCom Technical Report CTR-108-01. In the other case, $X_t"$ showed small changes at low frequencies with a leaf fractional volume of 0.003%.

[This page intentionally left blank]

## ANNEX 3A

### Effective Dyadic Susceptibility
### of Homogeneous Trunk Forests

| Radius (meters) | Diameter (inches) | Figure Number |
|---|---|---|
| 0.0125 | 1 | 3A-1 |
| 0.025 | 2 | 3A-2 |
| 0.05 | 4 | 3A-3 |
| 0.10 | 8 | 3A-4 |
| 0.15 | 12 | 3A-5 |
| 0.20 | 16 | 3A-6 |

## ANNEX 3B

### Specific Attenuation
### of Homogeneous Trunk Forests

| Radius (meters) | Diameter (inches) | Figure Number |
|---|---|---|
| 0.0125 | 1 | 3B-1 |
| 0.025 | 2 | 3B-2 |
| 0.05 | 4 | 3B-3 |
| 0.10 | 8 | 3B-4 |
| 0.15 | 12 | 3B-5 |
| 0.20 | 16 | 3B-6 |

EFFECTIVE DYADIC SUSCEPTIBILITY

FREQUENCY IN MHZ

| RhoT = | 10000/ha |
| Diam = | 2.5 cm |
| FVL = | 0 % |

- - - Trans.Re.
——— Trans.Im.

.1

.01

.001

.0001

$X_t'$

$X_t''$

100    200    500    1000    2000
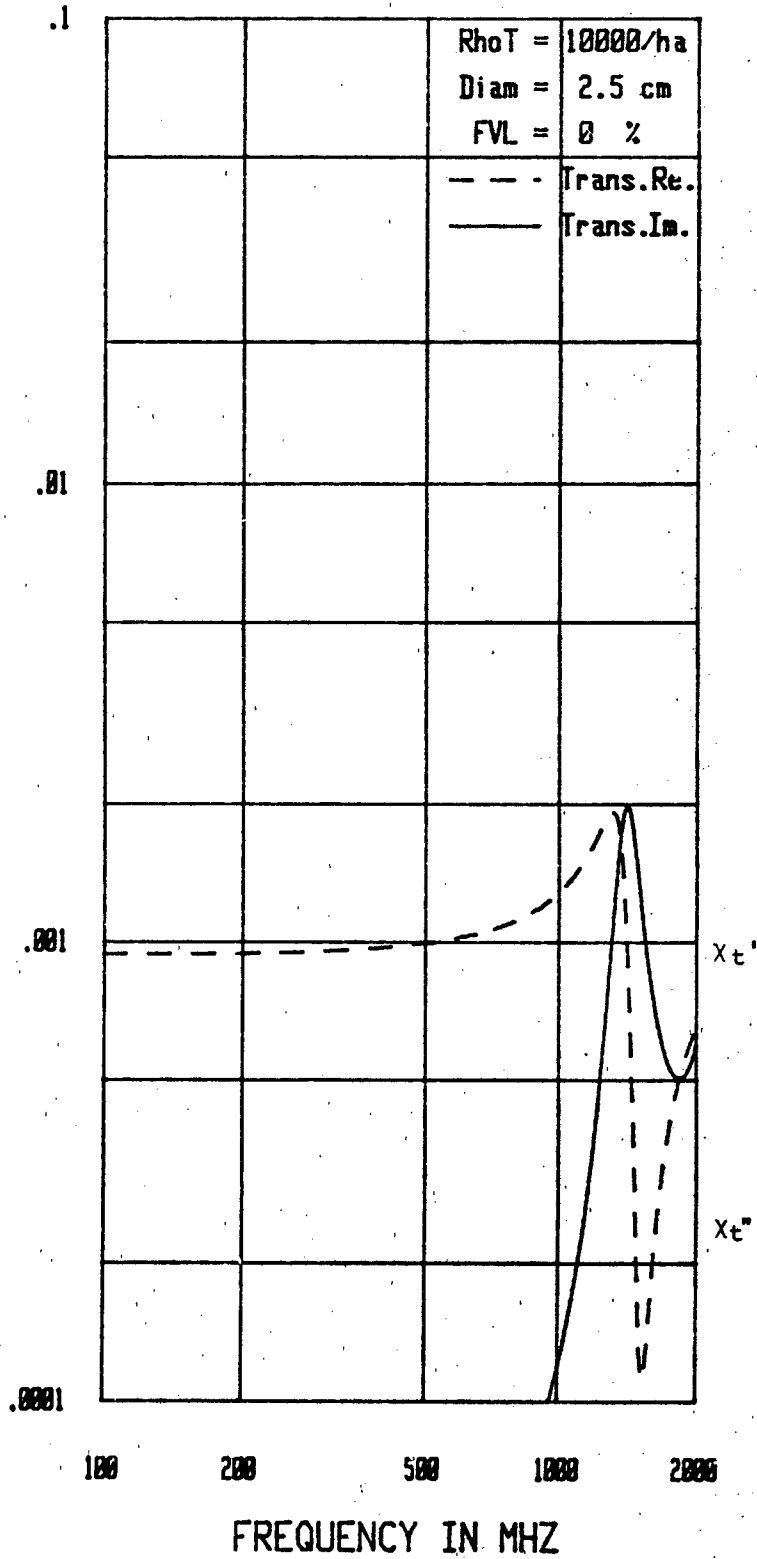
Figure 3A-1(a):   Effective Dyadic Susceptibility
[Trunks, a = .0125m]

3A-1
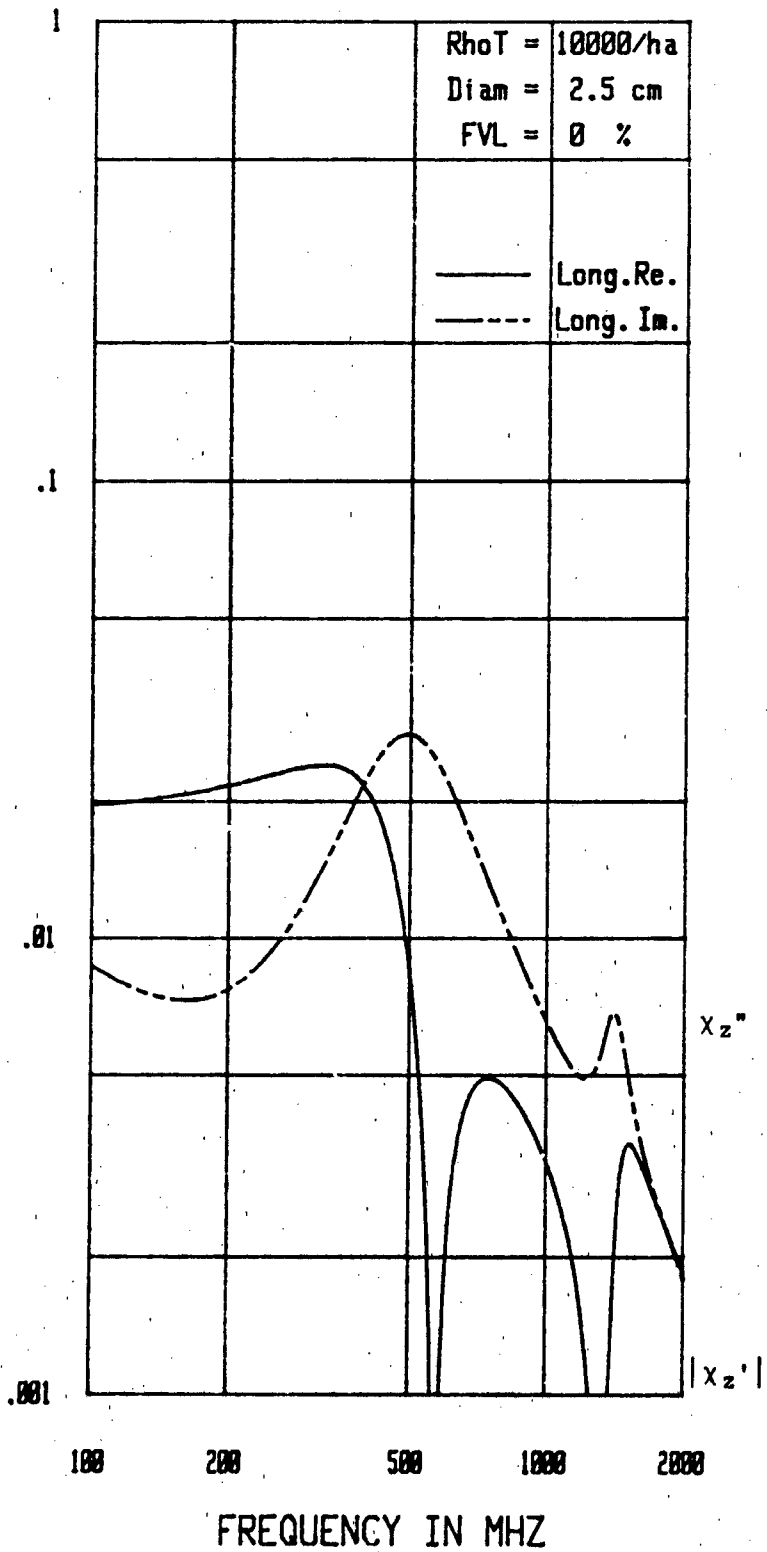
Figure 3A-1(b):  Effective Dyadic Susceptibility
[Trunks, a = .0125m]

3A-2

Figure 3A-2(a):   Effective Dyadic Susceptibility
[Trunks, a = .025m]
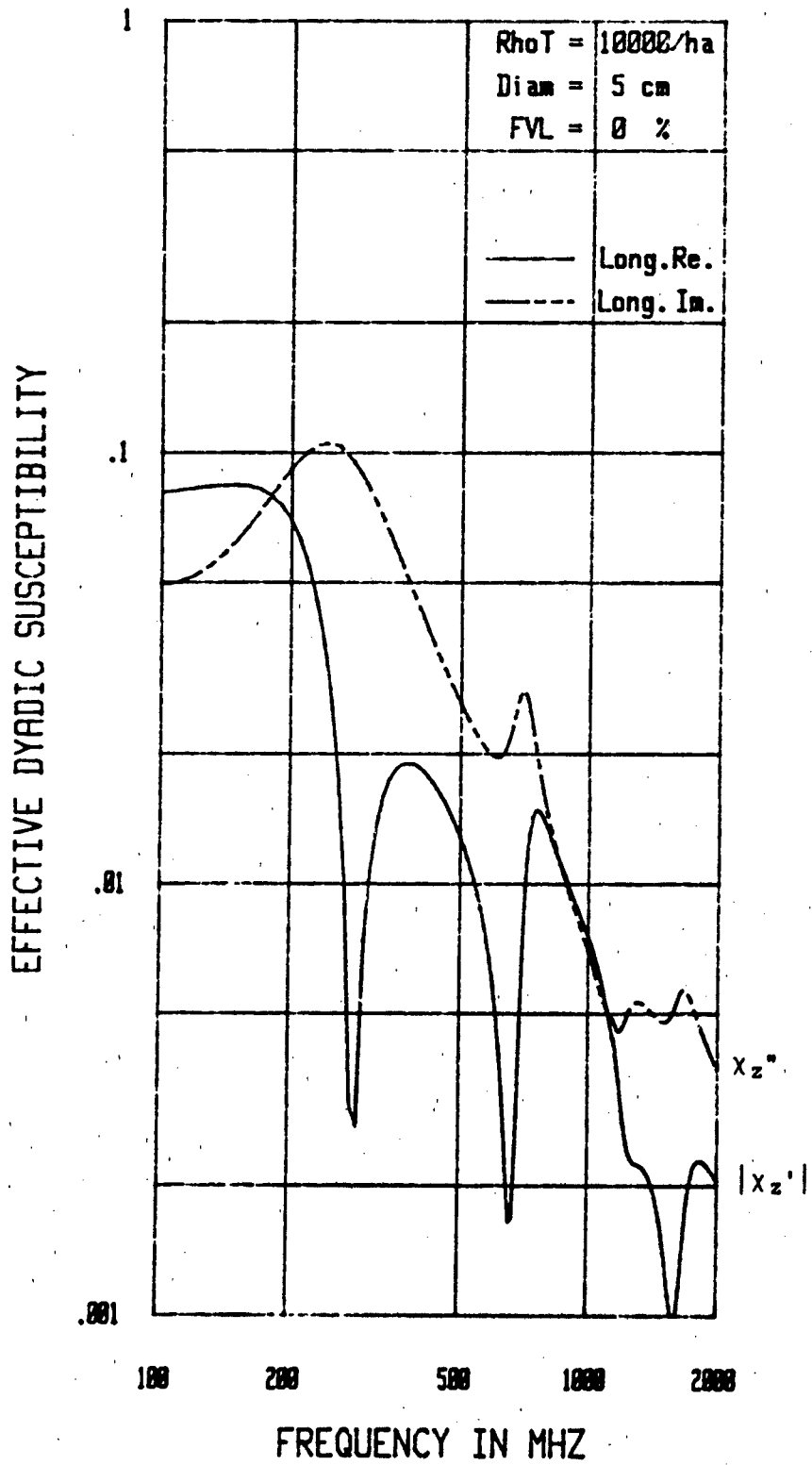
Figure 3A-2(b):  Effective Dyadic Susceptibility
[Trunks, a = .025m]
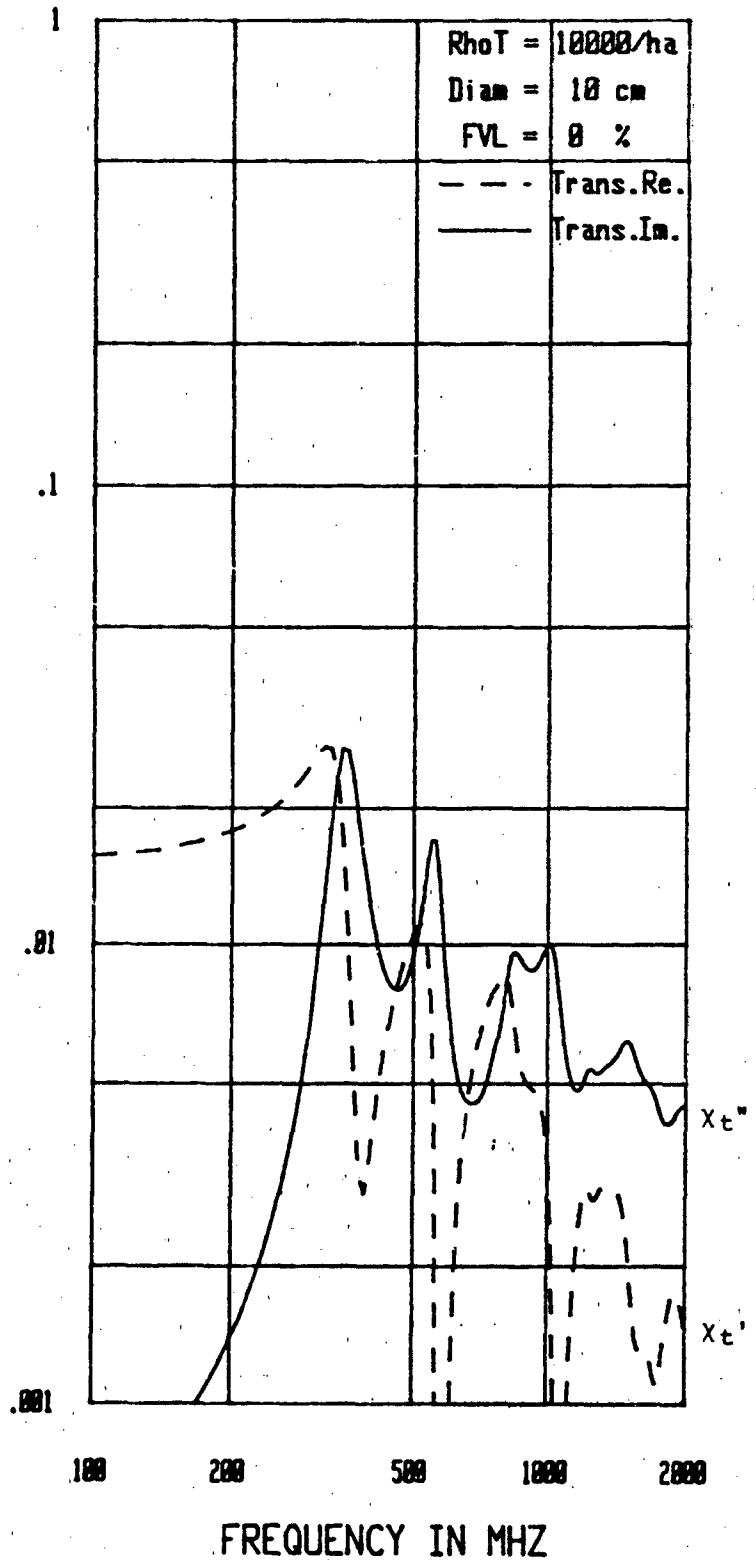
Figure 3A-3(a): Effective Dyadic Susceptibility
[Trunks, a = 0.05m]
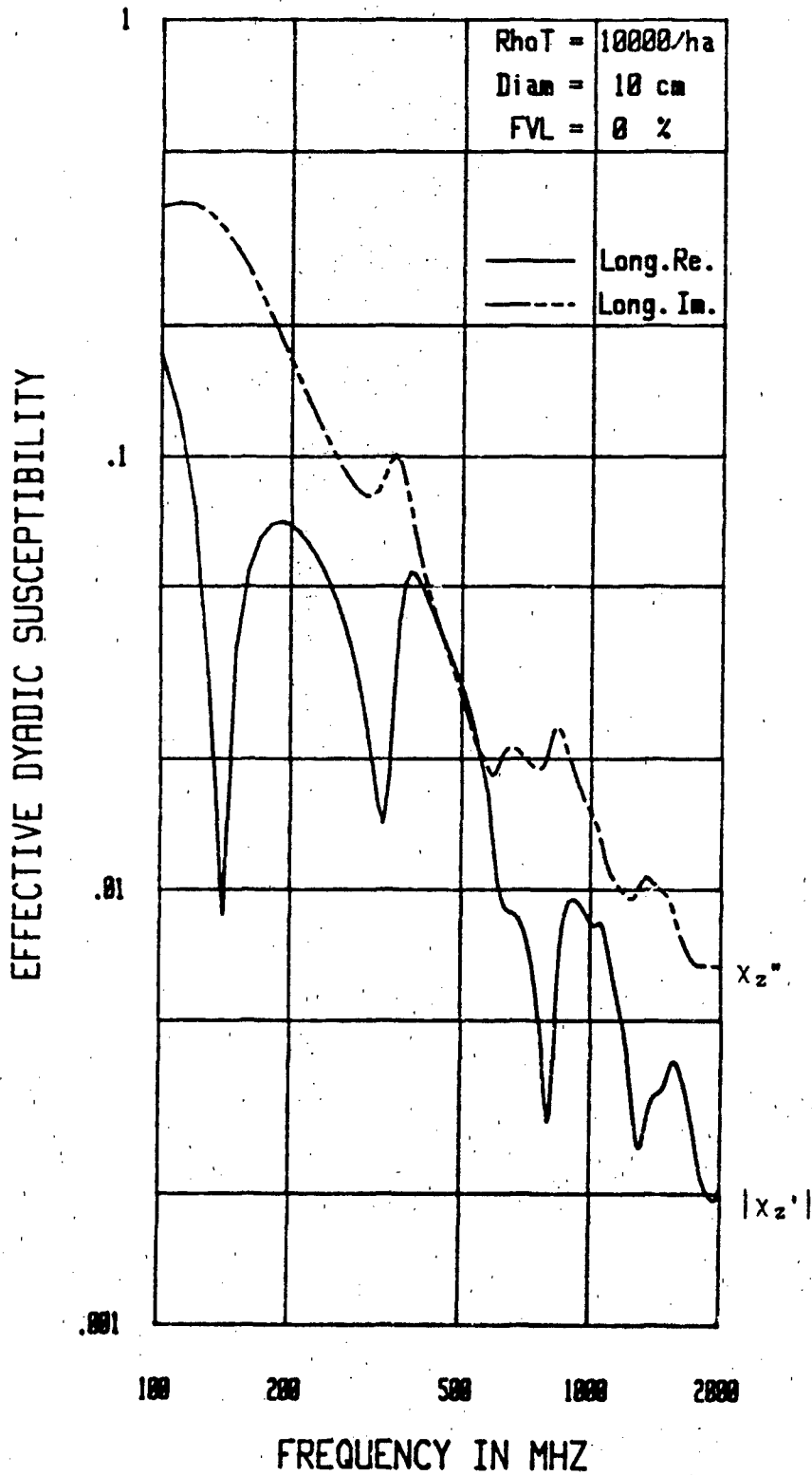
Figure 3A-3(b): Effective Dyadic Susceptibility
[Trunks, a = 0.05m]
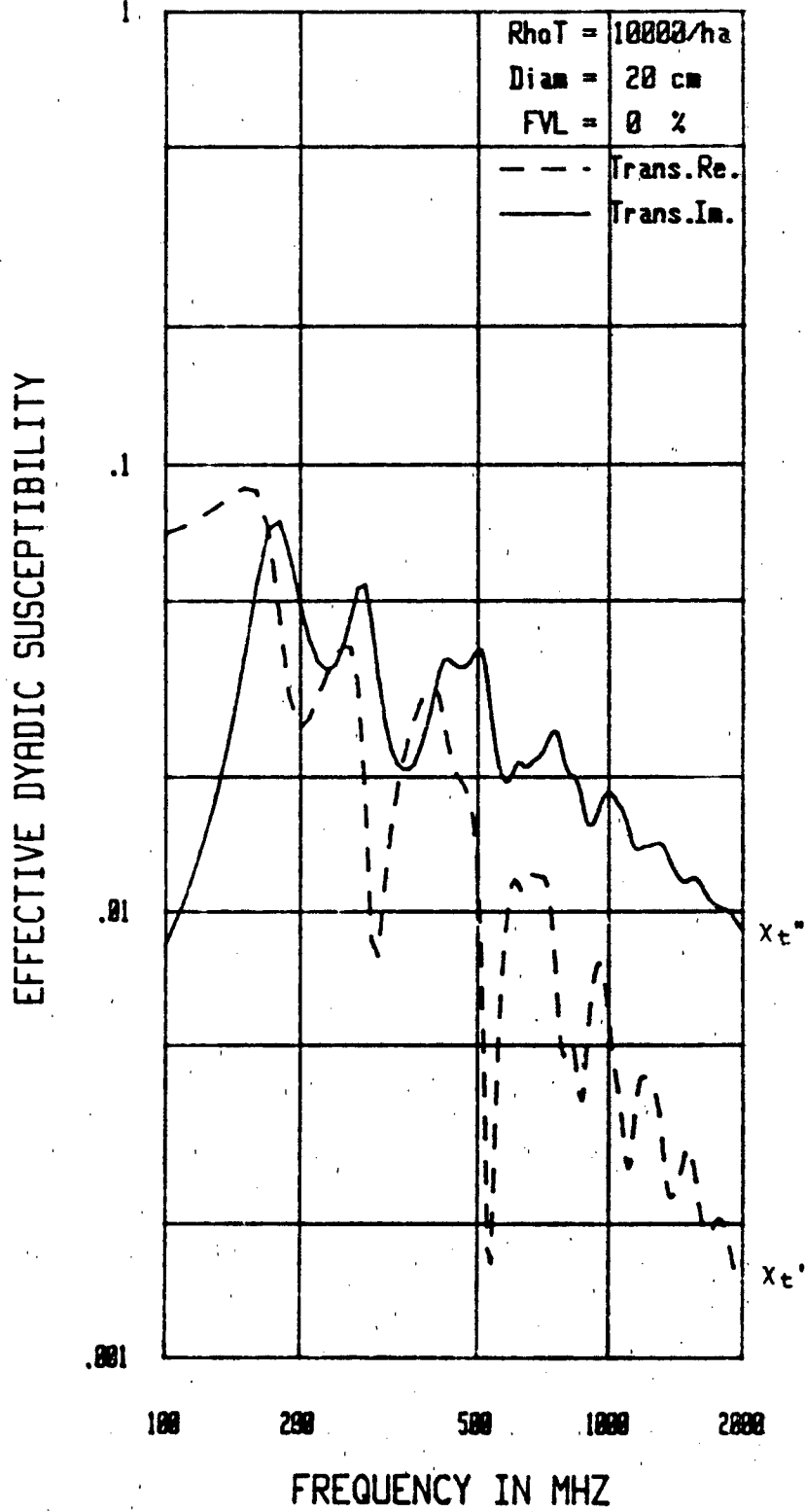
Figure 3A-4(a):  Effective Dyadic Susceptibility
[Trunks, a = 0.10m]

3A-7
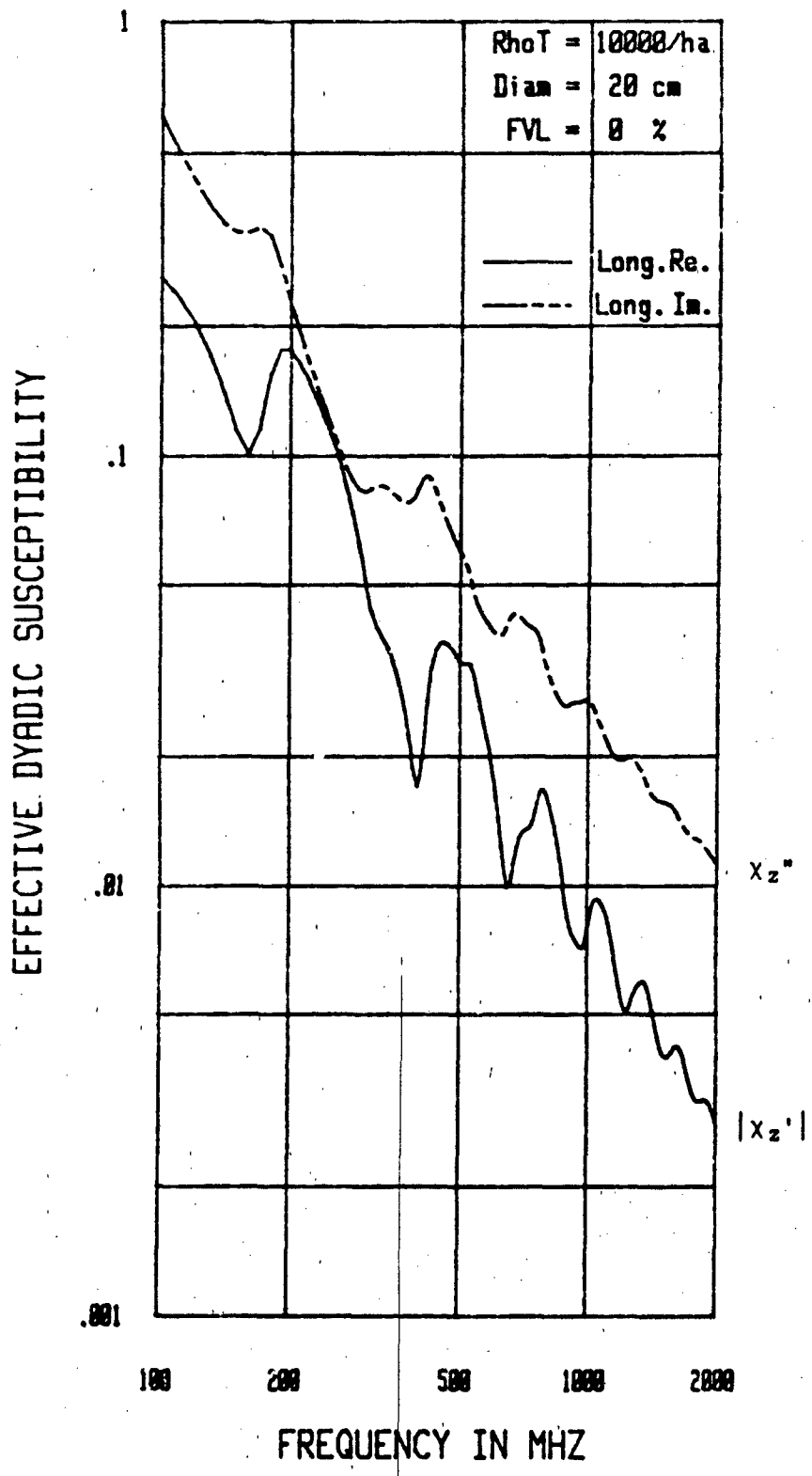
Figure 3A-4(b):  Effective Dyadic Susceptibility
[Trunks, a = 0.10m]
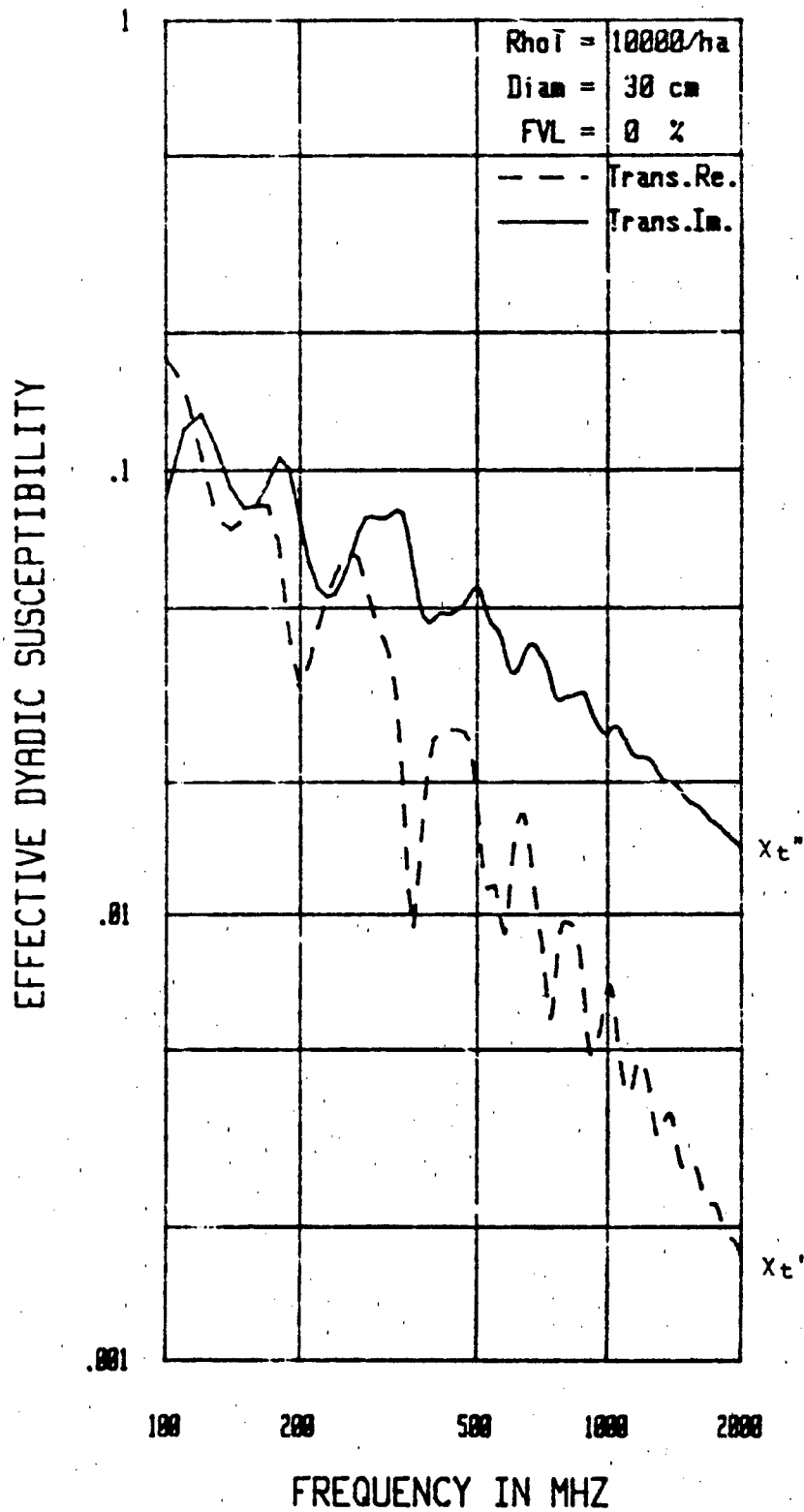
Figure 3A-5(a):   Effective Dyadic Susceptibility
[Trunks, a = 0.15m]
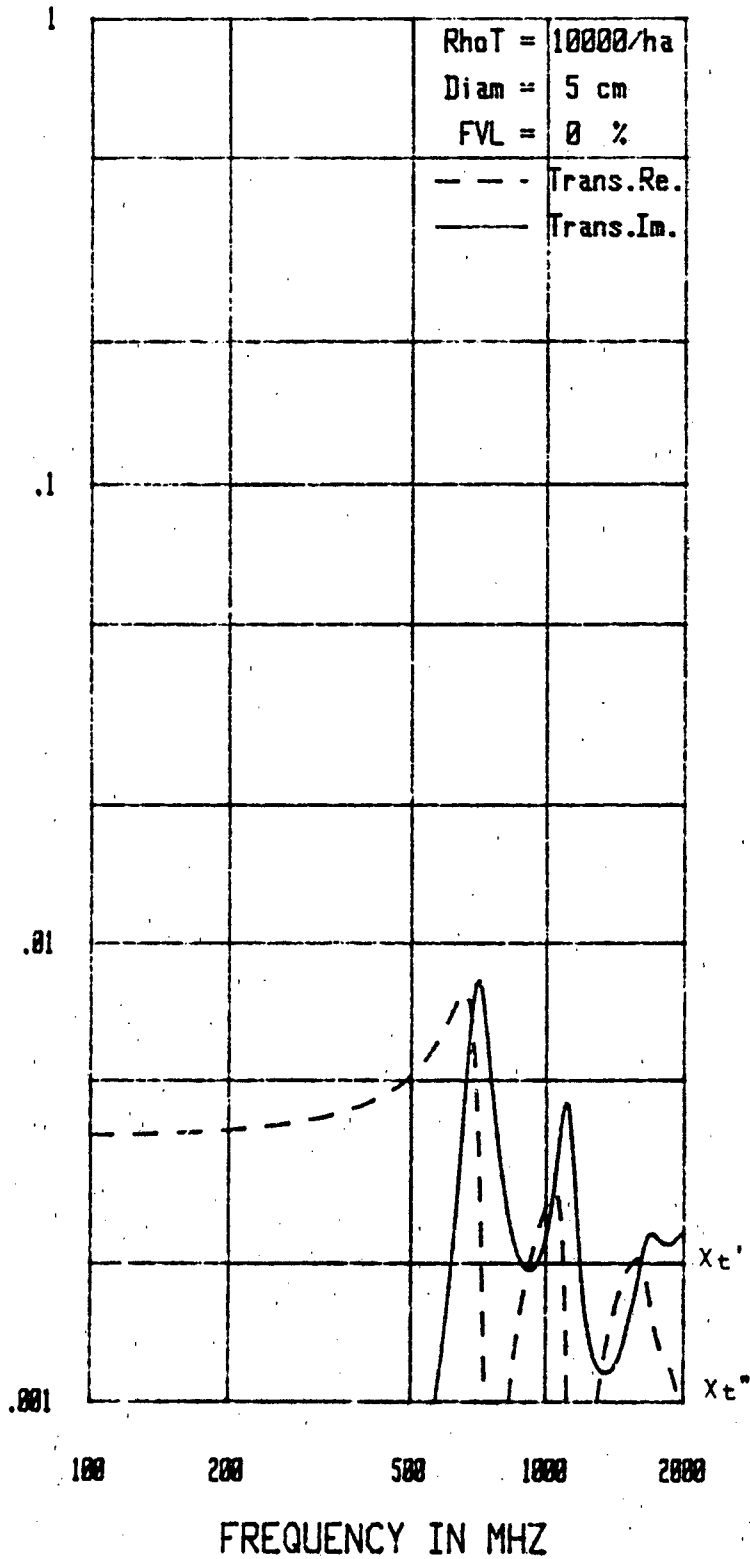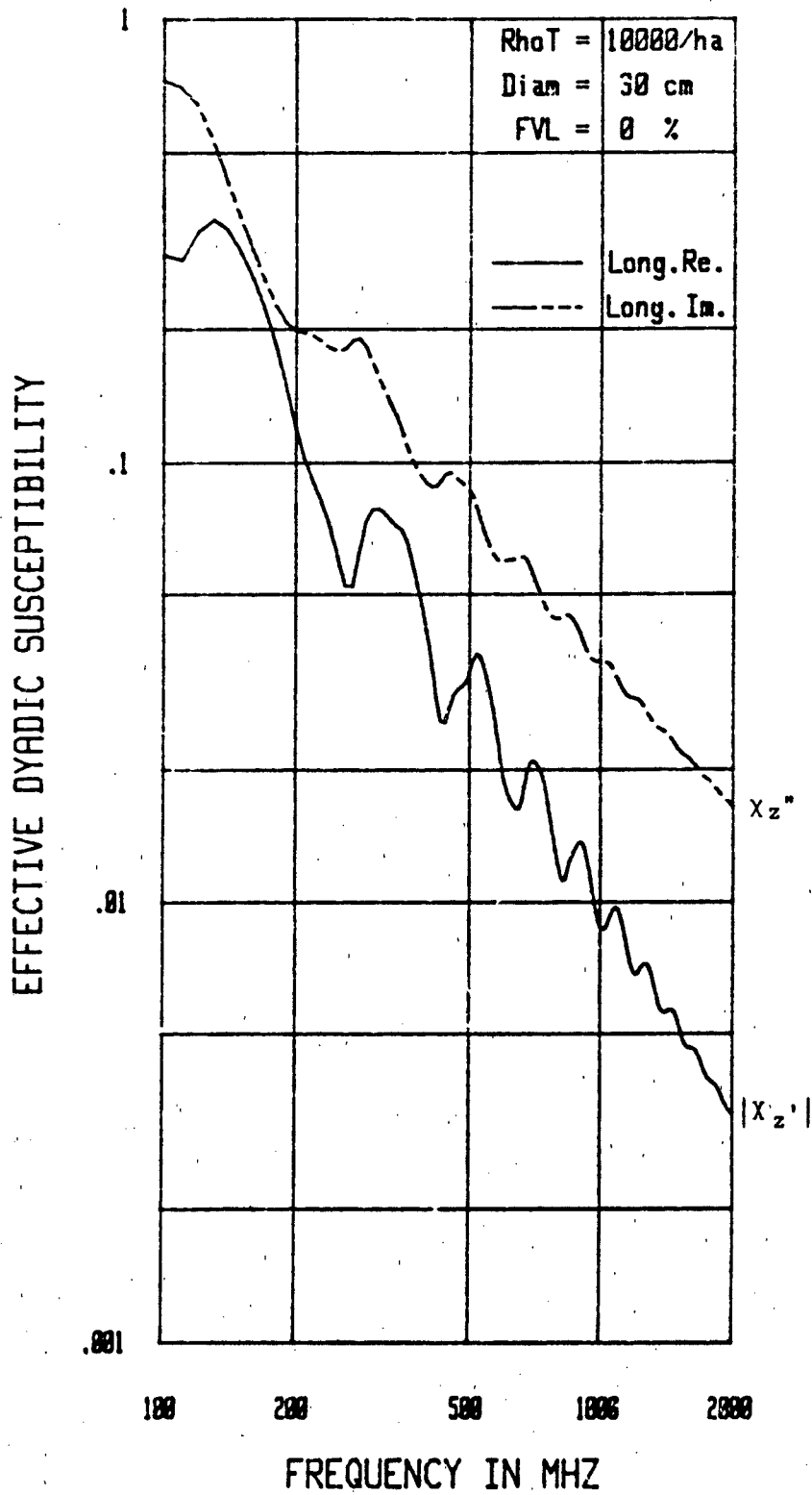
Figure 3A-5(b):   Effective Dyadic Susceptibility
[Trunks, a = 0.15m]
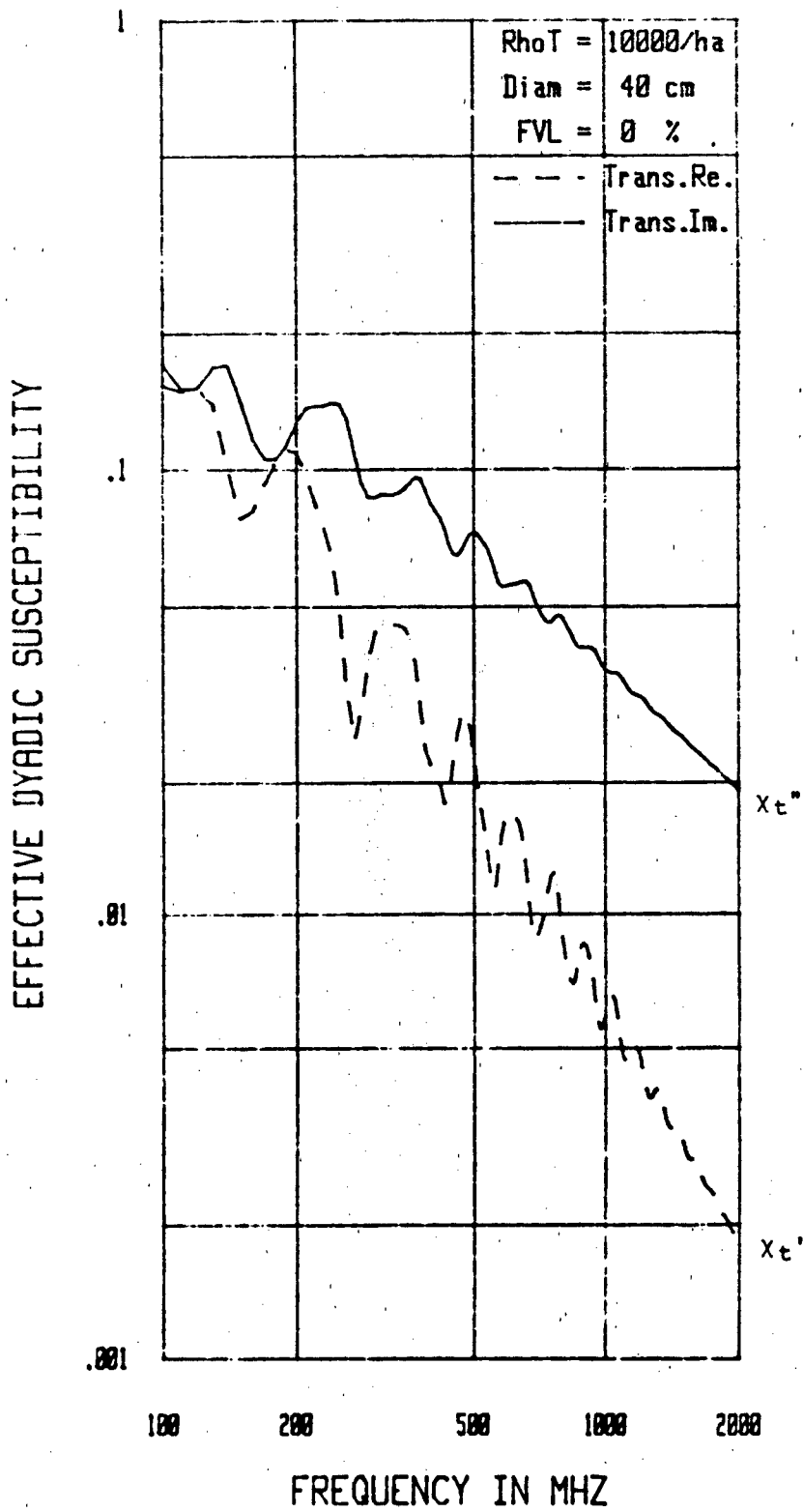
Figure 3A-6(a):   Effective Dyadic Susceptibility
[Trunks, a = 0.20m]

3A-11
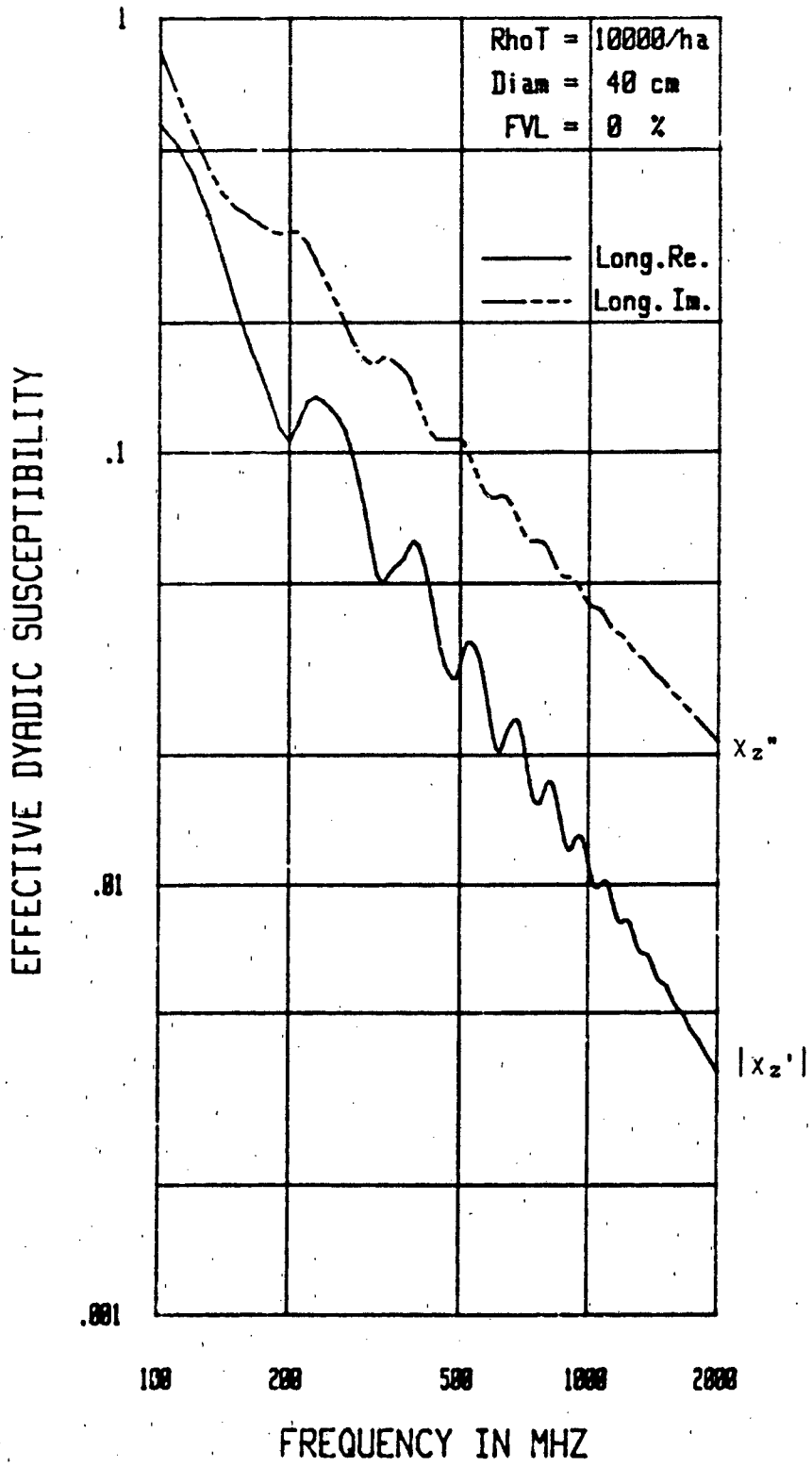
Figure 3A-6(b): Effective Dyadic Susceptibility
[Trunks, a = 0.20m]
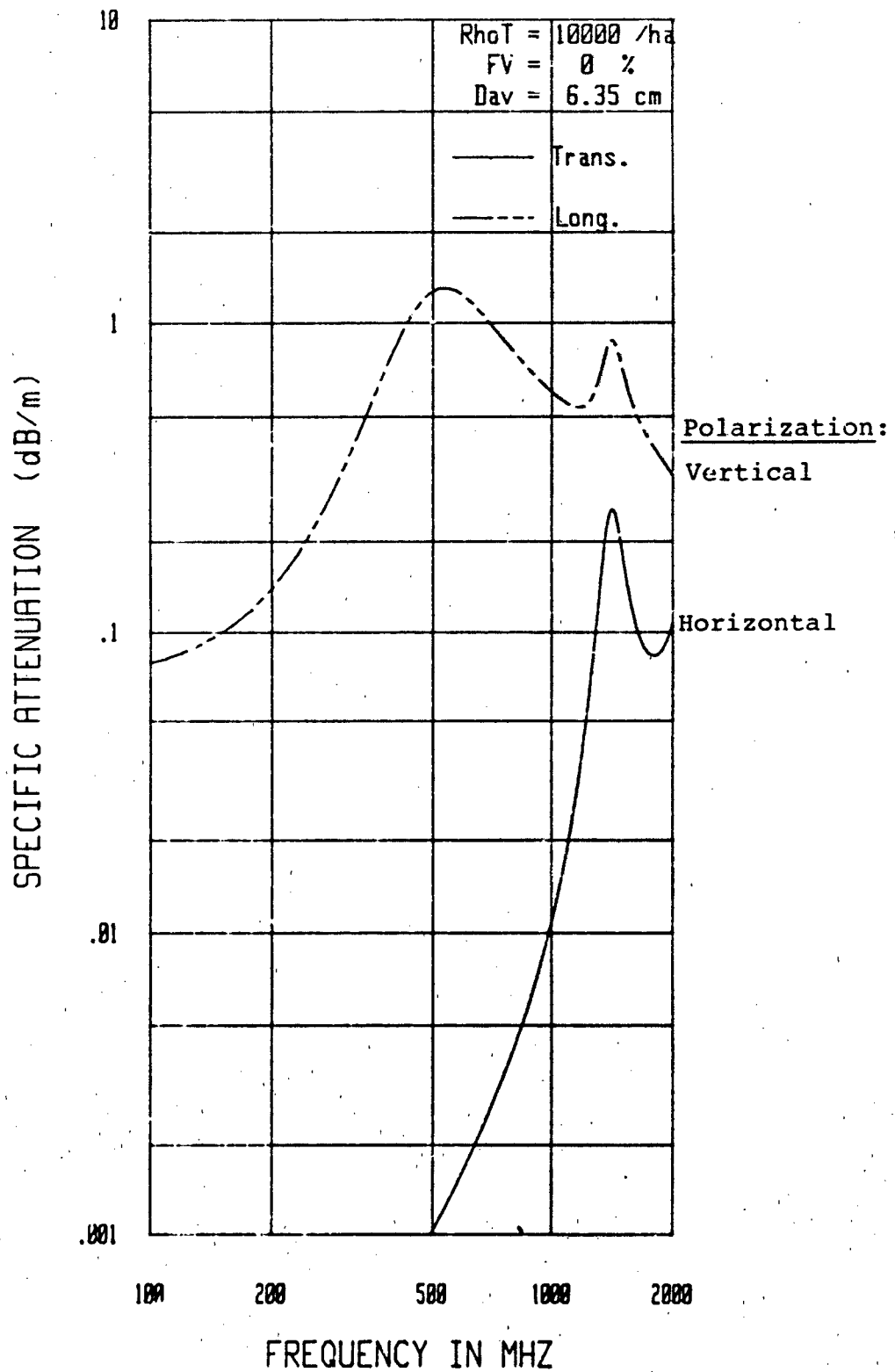
Figure 3B-1: Specific Attenuation [Trunks, a = .0125m]
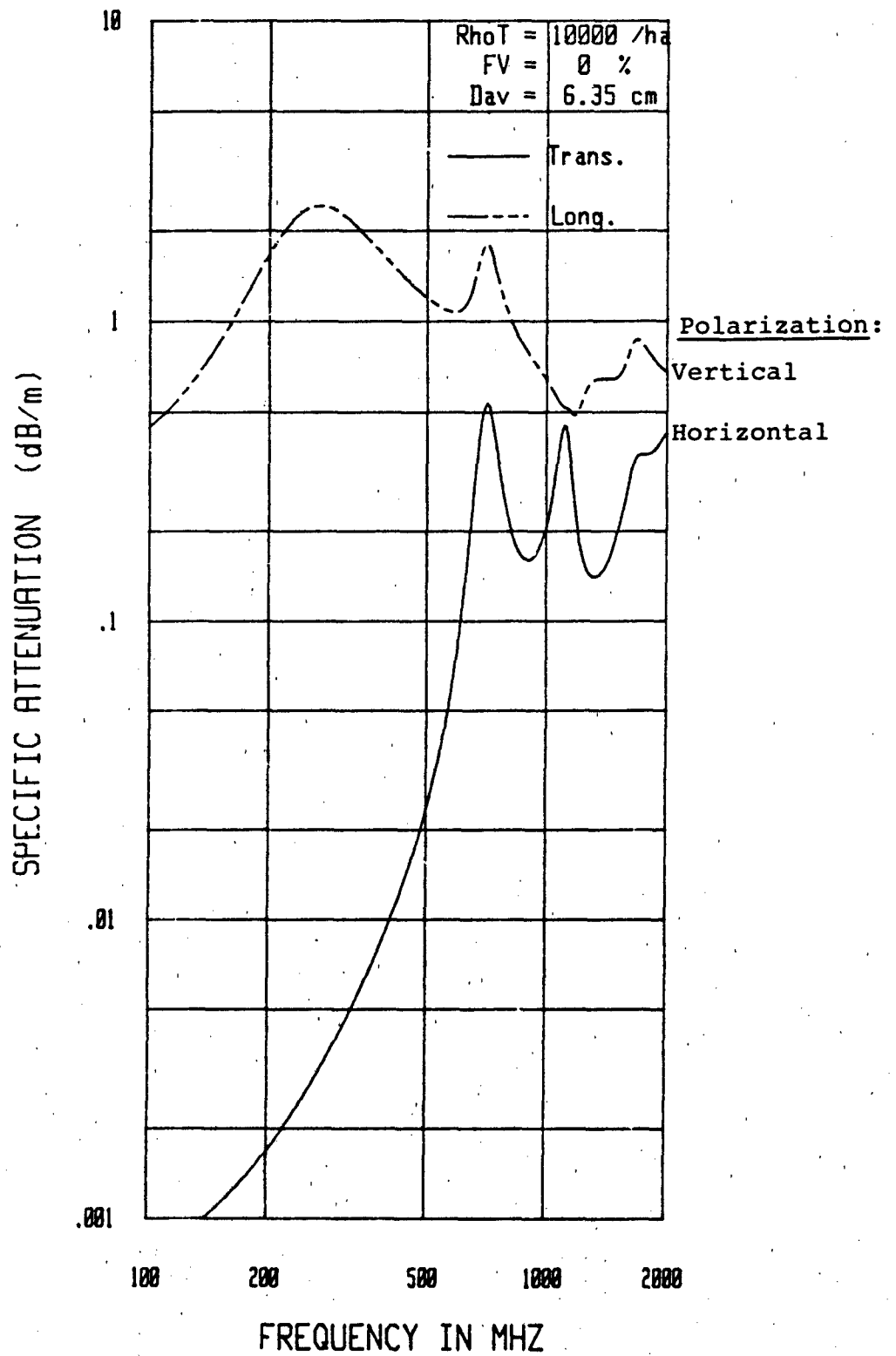
Figure 3B-2:   Specific Attenuation   [Trunks, a = .025]
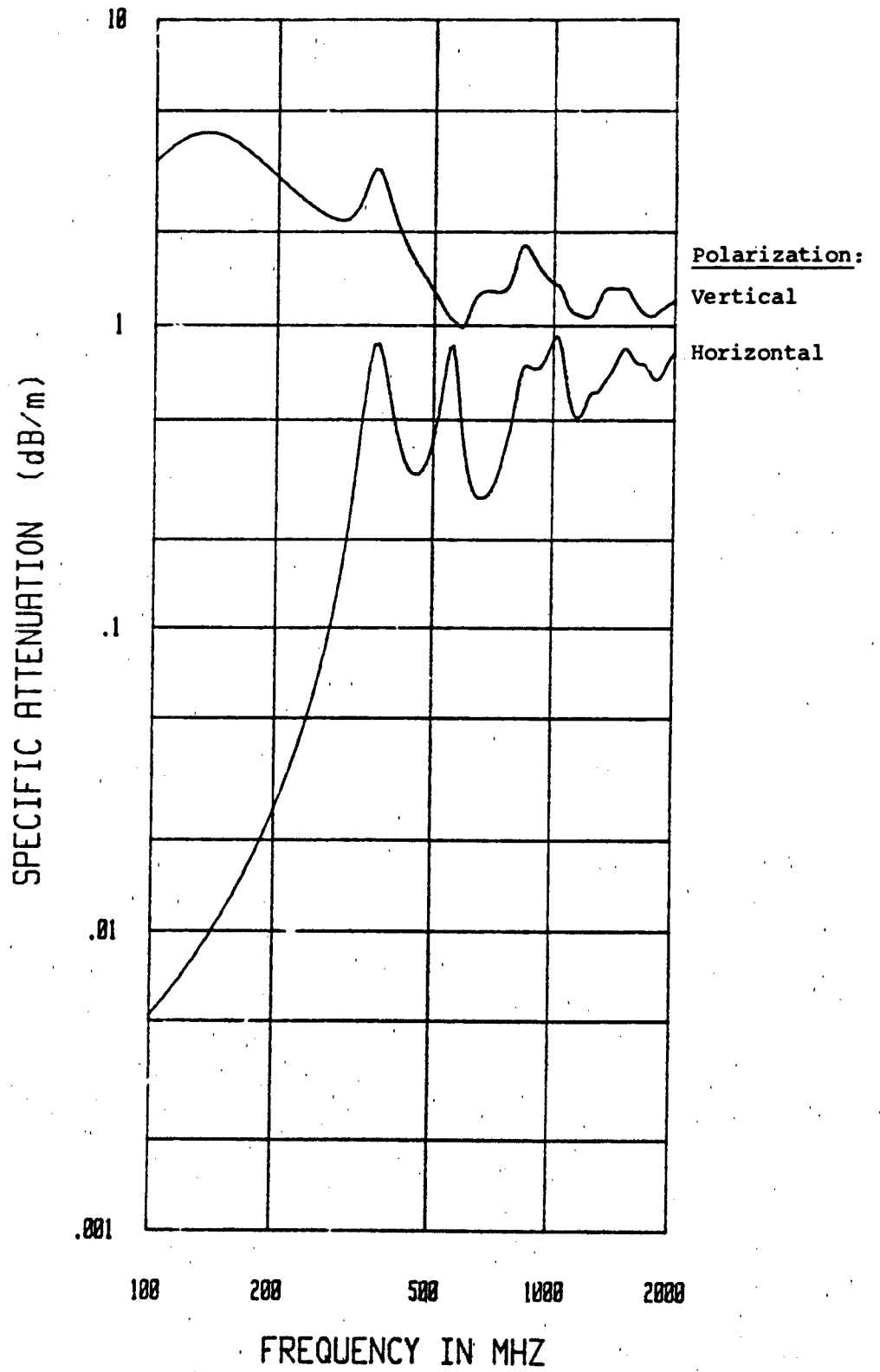
Figure 3B-3:  Specific Attenuation   [Trunks,  a = 0.05m]

3B-3
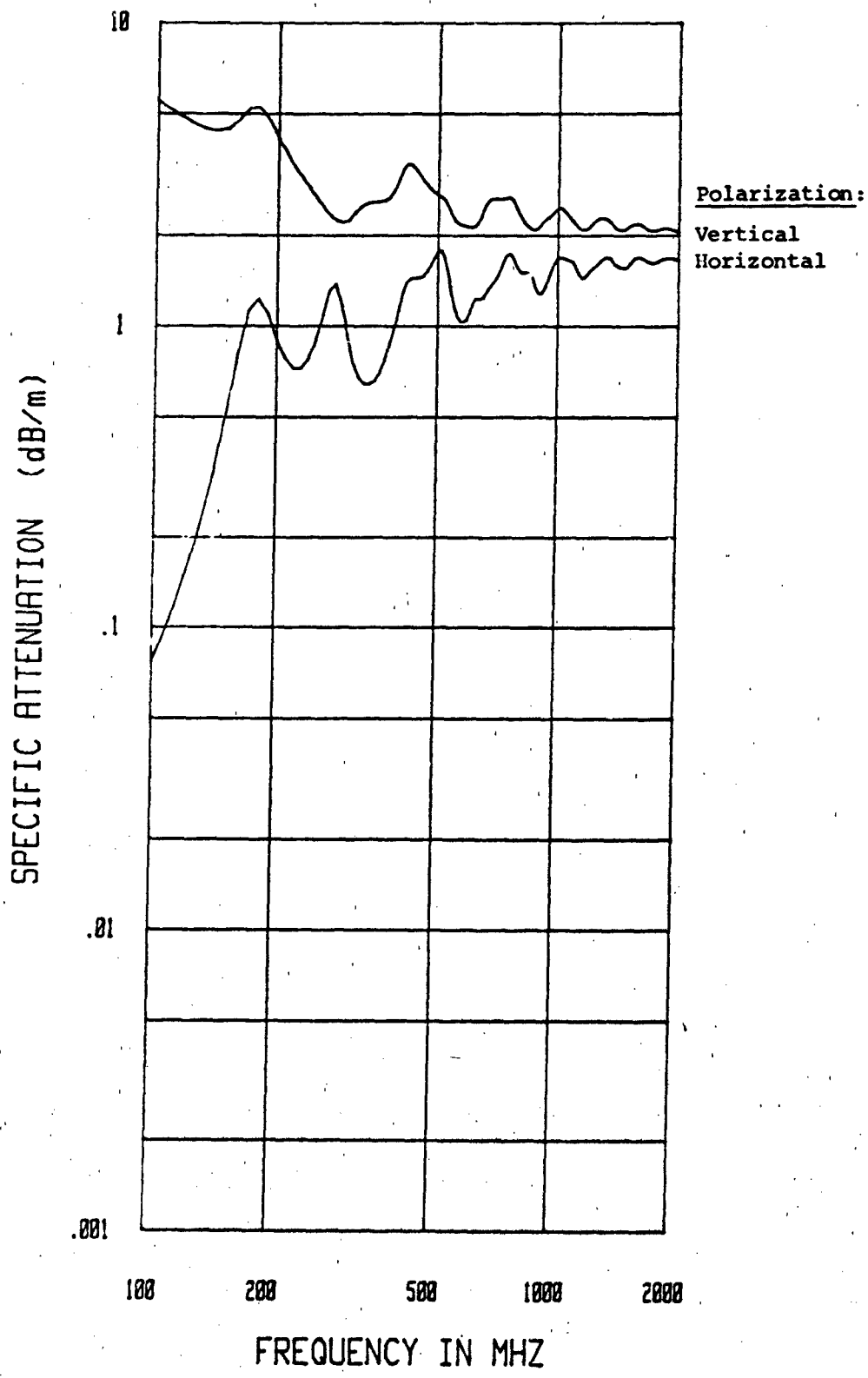
Figure 3B-4:  Specific Attenuation   [Trunks,  a = 0.10m]
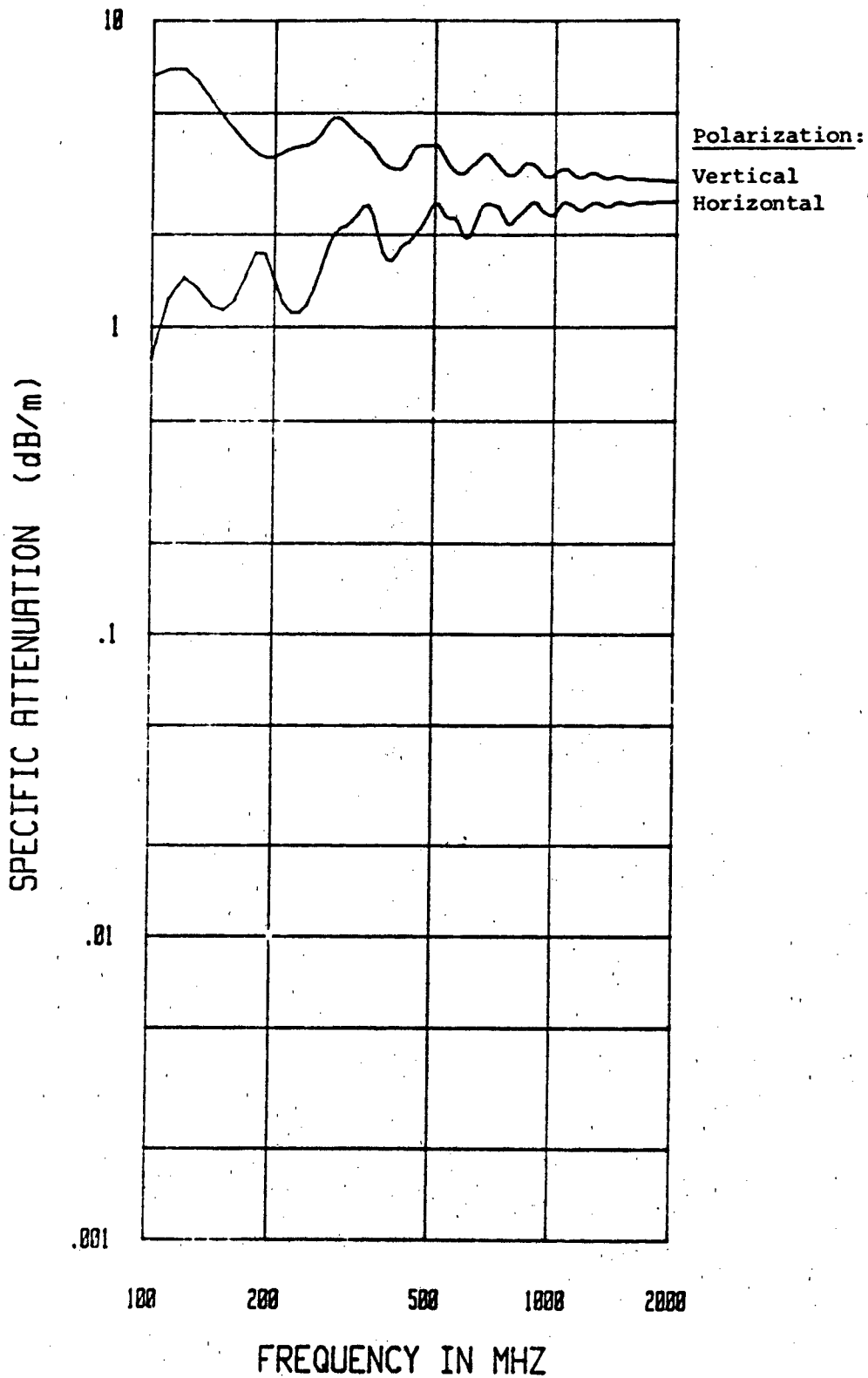
Figure 3B-5:  Specific Attenuation  [Trunks, a = 0.15m]
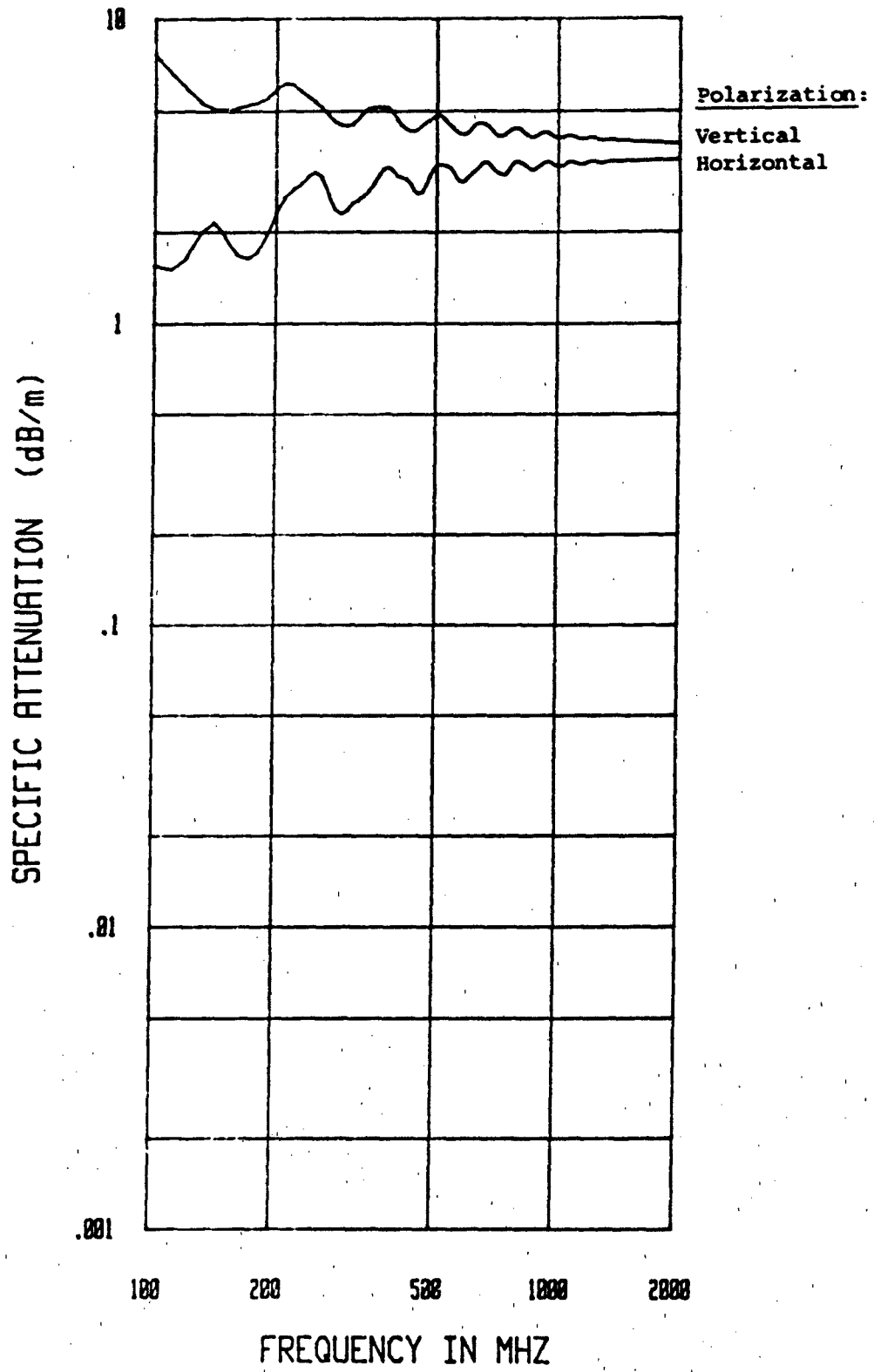
Figure 3B-6:  Specific Attenuation  [Trunks, a = 0.20m]

[This page intentionally left blank]

## 4.0 Anisotropic Forest Slab Model

In this section the medium will be bounded to represent the forest. In [42] the upper air-forest interface was introduced to produce the half-space model, shown in Figure 4-1(a). Although relatively simple, it gives rise to the lateral-wave which is essential to long-range transmission. The slab model to be considered here adds the lower ground interface as in Figure 4-1(b). Further possible model refinements are the multi-slab model, representing the canopy as in Figure 4-1(c), and the inclusion of height-dependent properties as in Figure 4-1(d).

Section 4.1 formulates the problem, introducing the reflection coefficient at the ground as well as at the air interface. Section 4.2 performs the asymptotic (approximate) evaluation of the equation just developed using methods of [42], but these are complicated by multiple reflection of both space and lateral waves at the upper and lower forest boundaries. This multipath nature is treated in detail in Section 4.3. Curves of reflection coefficient versus distance for the media of interest are shown. Interference of direct and reflected waves is expanded to include the many possible cases of multiple reflection above and below the forest. Then the lateral wave is included. This may be excited after, or received after, multiple reflections. Section 4.4 introduces the concept of basic transmission loss, the normal tool of radio link design. It is useful in the broad-band application to spread-spectrum transmission of interest here. Finally Section 4-5 finds that terminal motion produces negligible Doppler shifts.

## 4.1 Model Formulation

The anisotropic slab model for UHF radiowave propagation through forests is shown in Figure 4-2. The electrically anisotropic forest slab, sandwiched between the electrically isotropic air and ground, is characterized by the effective dyadic permittivity $\underline{\varepsilon}\varepsilon_o$ (at least so far as the mean fields are concerned). The scalar permittivities of the air and the ground are denoted by $\varepsilon_o$ and $\varepsilon_g\varepsilon_o$, respectively. All three media are
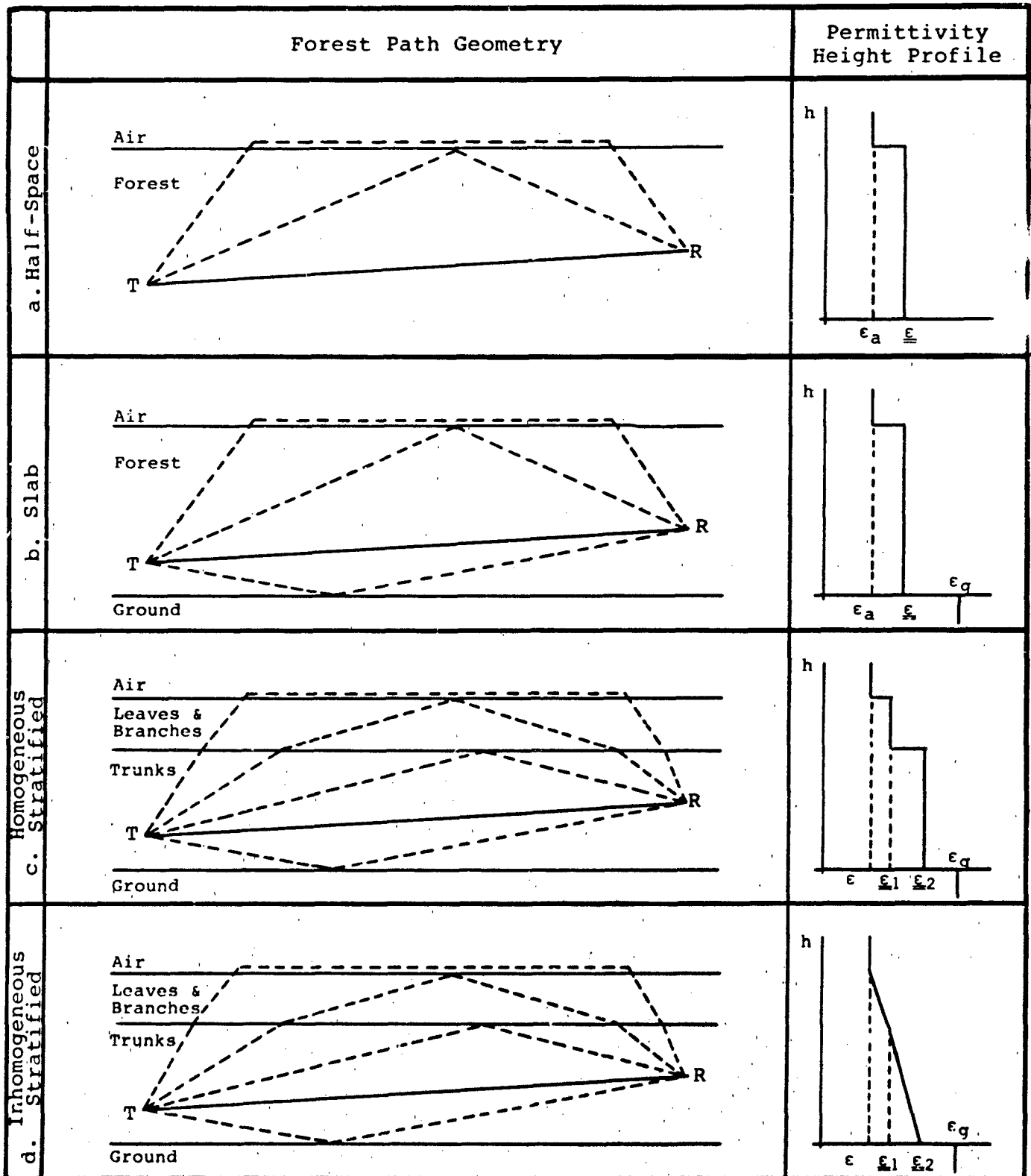
Figure 4-1: Stratified Forest Models
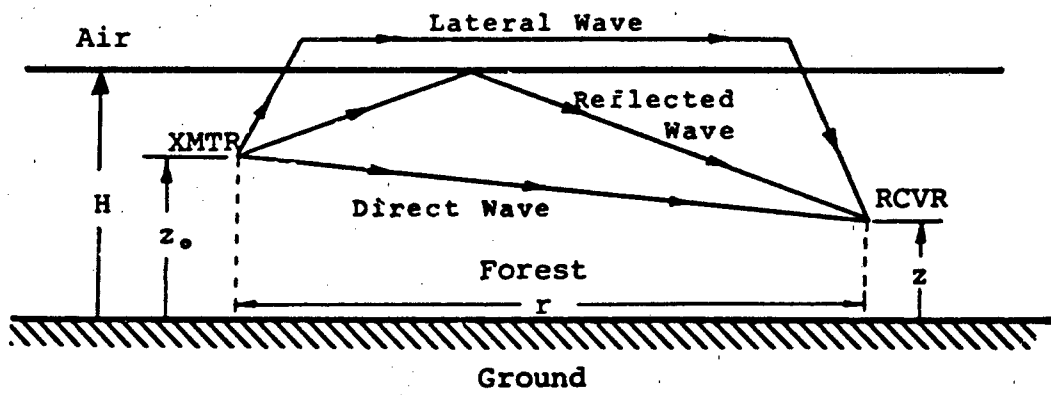
Figure 4-2: Slab Model for the Forest

assumed to be magnetically isotropic and characterized by the free-space permeability $\mu_o$. The transmitting antenna is represented as a vertical electric (Hertzian) dipole having a time-harmonic current moment $Id\ell \cdot \exp\{j\omega t\}$ located at height $z_o$ above the ground.

In an unbounded, anisotropic forest characterized by a uniaxial effective dyadic permittivity

$$\underline{\underline{\varepsilon}} = \varepsilon_t \underline{x}^\circ \underline{x}^\circ + \varepsilon_t \underline{y}^\circ \underline{y}^\circ + \varepsilon_z \underline{z}^\circ \underline{z}^\circ \qquad (4\text{-}1\text{-}1)$$

the mean electromagnetic fields associated with a z-directed (vertical) Hertzian dipole can be derived from a Hertz vector potential $\underline{A}$ that has only a z-directed component, viz.

$$A_z(\underline{r}, z) = \frac{-Id\ell}{8\pi^2 \omega \varepsilon_o \varepsilon_z} \int \frac{\exp\{-j(\underline{\beta}_t \cdot \underline{r} + \tau |z - z_o|)\}}{\tau} d\underline{\beta}_t \qquad (4\text{-}1\text{-}2)$$

where

$$\tau = \tau^1 - j|\tau''| = \sqrt{\varepsilon_t/\varepsilon_z} \sqrt{k_\bullet^2 \varepsilon_z - \beta_t^2} \qquad (4\text{-}1\text{-}3)$$

The electromagnetic fields can be derived from the vector potential $\underline{A}$ using the relations

$$\underline{E} = \nabla(\nabla \cdot \underline{A}) + k_\bullet^2 \varepsilon_t \underline{A} \qquad (4\text{-}1\text{-}4)$$

$$\underline{H} = j\omega \varepsilon_o \varepsilon_t (\nabla \times \underline{A}) \qquad (4\text{-}1\text{-}5)$$

For the anisotropic forest slab model, the tangential components of the electromagnetic fields must be continuous across the air-forest and the forest-ground interfaces. If the source of these fields is a z-directed (vertical) Hertzian dipole, the boundary conditions can be succinctly summarized in terms of a Hertz vector potential having only a z-directed component by writing

$$A_z^I(\underline{r}, H) = \varepsilon_t A_z^{II}(\underline{r}, H) \qquad (4\text{-}1\text{-}6)$$

$$\varepsilon_t A_z^{II}(\underline{r}, 0) = \varepsilon_g A_z^{III}(\underline{r}, 0) \qquad (4\text{-}1\text{-}7)$$

$$\partial[A_z^I(\underline{r},H)]/\partial z = \partial[A_z^{II}(\underline{r},H)]/\partial z \qquad (4\text{-}1\text{-}8)$$

$$\partial[A_z^{II}(\underline{r},0)]/\partial z = \partial[A_z^{III}(\underline{r},0)]/\partial z \qquad (4\text{-}1\text{-}9)$$

where the superscripts I, II, III identify, respectively, the Hertz potentials intrinsic to the air, forest, and ground.

As a consequence of these boundary conditions, the radiation condition and Equation (4-1-2), CyberCom has found the Hertz potential within the anisotropic forest slab to be[*]

$$A_z^{II}(\underline{r},z) = \frac{-Id\ell}{8\pi^2\omega\varepsilon_o\varepsilon_z} \int \frac{[1+R_g\exp\{-j2\tau_2 z_o\}]\ [1+R_a\exp\{-j2\tau_2(H-z)\}]}{[1-R_aR_g\exp\{-j2\tau_2 H\}]}$$

$$\times \frac{\exp\{-j(\underline{\beta}_t\cdot\underline{r}+\tau_2|z-z_o|)\}}{\tau_2}\ d\underline{\beta}_t \qquad (4\text{-}1\text{-}10)$$

where,

$$R_a(\underline{\beta}_t) = \frac{\tau_2 - \varepsilon_t\tau_1}{\tau_2 + \varepsilon_t\tau_1} \qquad (4\text{-}1\text{-}11)$$

$$R_g(\underline{\beta}_t) = \frac{\varepsilon_g\tau_2 - \varepsilon_t\tau_3}{\varepsilon_g\tau_2 + \varepsilon_t\tau_3} \qquad (4\text{-}1\text{-}12)$$

are, respectively, the Fresnel reflection coefficients associated with the air-forest and forest-ground interfaces, and where

$$\tau_1 = \tau_1' - j|\tau_1''| = \sqrt{k_o^2 - \beta_t^2} \qquad (4\text{-}1\text{-}13)$$

$$\tau_2 = \tau_2' - j|\tau_2''| = \sqrt{\varepsilon_t/\varepsilon_g}\ \sqrt{k_o^2\varepsilon_z - \beta_t^2} \qquad (4\text{-}1\text{-}14)$$

$$\tau_3 = \tau_3' - j|\tau_3''| = \sqrt{k_o^2\varepsilon_g - \beta_t^2} \qquad (4\text{-}1\text{-}15)$$

are the dispersion relations. The electromagnetic fields within the anisotropic forest slab can be derived by substituting Equation (4-1-10) into Equations (4-1-4) and (4-1-5).

Equations (4-1-5), (4-1-6) and (4-1-10) constitute the formal solution for the electromagnetic fields of a vertical electric (Hertzian) dipole in an anisotropic forest slab.

---

[*]Strictly speaking, Equation (4-1-10) is valid only when $z>z_o$. If $z<z_o$, then z and $z_o$ must be interchanged.

## 4.2  Asymptotic Evaluation

The integral representation afforded by Equation (4-1-10) for the Hertz potential within the anisotropic forest slab is not amenable to exact analytic evaluation. However, analytic asymptotic approximations have been derived based upon CyberCom's earlier development of an anisotropic forest half-space model [42] and the pioneering efforts of Sachs and Wyatt [57], Tamir [65,64,19], and others on the isotropic forest slab model.

Before proceeding with the development of these asymptotic approximations, it will prove expedient to recast the expression for the Hertz potential within an anisotropic forest half-space [42, Equation (5-2-39)] in geometric terms consistent with Fig. 4-1. Thus, introducing the following correspondences apparent by comparison of Fig. 4-2 and Fig. 5-2 of [42],

$$d \rightarrow (H - z_o) \tag{4-2-1}$$

$$z \rightarrow -(H - z) \tag{4-2-2}$$

into the equation previously cited, the Hertz potential within the anisotropic forest slab $A_z^{II}\big|_{\infty/2}$ may be written in the form[*]

$$A_z^{II}(\underline{r},z)\Big|_{\infty/2} = \frac{-Id\ell}{8\pi^2\omega\varepsilon_o\varepsilon_z} \left\{ \int \left[ \frac{\exp\{-j\tau_2|z - z_o|\}}{\tau_2} \right.\right.$$

$$\left.\left. + R_a(\underline{\overset{o}{t}}) \frac{\exp\{-j\tau_2(2H-z-z_o)\}}{\tau_2} \right] \exp\{-j\underline{\beta}_t \cdot \underline{r}\} d\underline{\beta}_t \right. \tag{4-2-3}$$

The first integral corresponds to the Hertz potential of a Hertzian dipole within an unbounded, anisotropic medium, the second integral represents the effect of the air-forest interface. These integrals were evaluated in [42]: the first integral describes a direct wave propagating through the forest to the receiving location; the second integral describes a wave reflected from the air-forest interface and, possibly, a lateral wave propagating along the air-forest interface.

---

[*]Valid for arbitrary z and $z_o$ within the slab.

Consider, now, the Hertz potential within the anisotropic forest slab [Equation (4-1-10)]. If the denominator of the integrand is expanded in a power series using the relation

$$(1 - z)^{-1} = 1 + z + z^2 + \ldots \qquad (|z|<1) \qquad (4\text{-}2\text{-}4)$$

Equation (4-1-10) may, upon interchanging the order of integration and summation, be recast into the form

$$A_z^{II}(\underline{r},z) = \frac{-Id\ell}{8\pi^2 \omega \varepsilon_o \varepsilon_z} \sum_{j=1}^{4} S_j \qquad (4\text{-}2\text{-}5)$$

where

$$S_j = \sum_{m=0}^{\infty} I_{jm} \qquad (4\text{-}2\text{-}6)$$

and

$$I_{1m} = \int R_a^m(\beta_t) R_g^m(\beta_t) \frac{\exp\{-j\tau_2[2mH+|z-z_o|]\}}{\tau_2}$$

$$\cdot \exp\{-j\underline{\beta}_t \cdot \underline{r}\}d\underline{\beta}_t \qquad (4\text{-}2\text{-}7)$$

$$I_{2m} = \int R_a^{m+1}(\beta_t) R_g^m(\beta_t) \frac{\exp\{-j\tau_2[2(m+1)H-(z+z_o)]\}}{\tau_2}$$

$$\cdot \exp\{-j\underline{\beta}_t \cdot \underline{\beta}\}d\underline{\beta}_t \qquad (4\text{-}2\text{-}8)$$

$$I_{3m} = \int R_a^m(\beta_t) R_g^{m+1}(\beta_t) \frac{\exp\{-j\tau_2[2mH+(z+z_o)]\}}{\tau_2}$$

$$\cdot \exp\{-j\underline{\beta}_t \cdot \underline{r}\}d\underline{\beta}_t \qquad (4\text{-}2\text{-}9)$$

$$I_{4m} = \int R_a^{m+1}(\beta_t) R_g^{m+1}(\beta_t) \frac{\exp\{-j\tau_2[2(m+1)H-|z-z_o|]\}}{\tau_2}$$

$$\cdot \exp\{-j\underline{\beta}_t \cdot \underline{r}\}d\underline{\beta}_t \qquad (4\text{-}2\text{-}10)$$

It can be inferred by analogy with Equation (4-2-3) that the integral

$$I_{10} = \int \frac{\exp\{-j\tau_2 |z-z_\circ|\}}{\tau_2} \exp\{-j\underline{\beta}_t \cdot \underline{r}\} d\underline{\beta}_t \qquad (4\text{-}2\text{-}11)$$

describes a direct wave propagating through the forest slab; the integral

$$I_{20} = \int R_a(\underline{\beta}_t) \frac{\exp\{-j\tau_2(2H-z-z_\circ)\}}{\tau_2} \exp\{-j\underline{\beta}_t \cdot \underline{r}\} d\underline{\beta}_t \qquad (4\text{-}2\text{-}12)$$

describes a wave reflected from the air-forest interface and, possibly, a lateral wave propagating above the air-forest interface as well. Further analogy with Equation (4-2-12) suggests that the integral

$$I_{30} = \int R_a(\underline{\beta}_t) \frac{\exp\{-j\tau_2(z+z_\circ)\}}{\tau_2} \exp\{-j\underline{\beta}_t \cdot \underline{r}\} d\underline{\beta}_t \qquad (4\text{-}2\text{-}13)$$

describes a wave reflected from the forest-ground interface; any lateral wave that might be propagated below this interface, however, would be highly attenuated by ground losses and so may be neglected.

More generally, the integrals $I_{jm}$ can be evaluated asymptotically using the method of steepest descents, just as Equation (4-2-12) was evaluated in [1, Section 5.3]. This method leads to a saddle-point result for each integral as well as a branch-cut contribution if a branch-cut is crossed by the steepest descent path. The saddle-point results for the $I_{jm}$ integrals are

$$I_{1m}^{(r)} \sim -2\pi R_a^m(\theta_{1m}) R_g^m(\theta_{1m}) \frac{\exp\{-jk_\circ \sqrt{\epsilon_z} R_{1m}\}}{aR_{1m}} \qquad (4\text{-}2\text{-}14)$$

$$I_{2m}^{(r)} \sim -2\pi R_a^{m+1}(\theta_{2m}) R_g^m(\theta_{2m}) \frac{\exp\{-jk_\circ \sqrt{\epsilon_z} R_{2m}\}}{aR_{2m}} \qquad (4\text{-}2\text{-}15)$$

$$I_{3m}^{(r)} \sim -2\pi R_a^m(\theta_{3m}) R_g^{m+1}(\theta_{3m}) \frac{\exp\{-jk_\circ R\sqrt{\epsilon_z} R_{3m}\}}{aR_{3m}} \qquad (4\text{-}2\text{-}16)$$

4-8

$$I_{4m}^{(r)} \sim -2\pi R_a^{m+1}(\theta_{4m}) R_g^{m+1}(\theta_{4m}) \frac{\exp\{-jk_oR\sqrt{\epsilon_z}\ R_{4m}}{aR_{4m}} \qquad (4\text{-}2\text{-}17)$$

where

$$R_a(\theta) = \frac{\cos\theta - \sqrt{\epsilon_t}(1 - \epsilon_z\sin^2\theta)^{\frac{1}{2}}}{\cos\theta + \sqrt{\epsilon_t}(1 - \epsilon_z\sin^2\theta)^{\frac{1}{2}}} \qquad (4\text{-}2\text{-}18)$$

$$R_g(\theta) = \frac{\epsilon_g\cos\theta - \sqrt{\epsilon_t}(1 - \epsilon_z\sin^2\theta)^{\frac{1}{2}}}{\epsilon_g\cos\theta + \sqrt{\epsilon_t}(1 - \epsilon_z\sin^2\theta)^{\frac{1}{2}}} \qquad (4\text{-}2\text{-}19)$$

are the Fresnel reflection coefficients at the air-forest and ground-forest interfaces, respectively, and

$$\theta_{1m} = \text{Arctan}\{r/a[2mH+|z-z_o|]\} \qquad (4\text{-}2\text{-}20)$$

$$\theta_{2m} = \text{Arctan}\{r/a[2(m+1)H-(z+z_o)]\} \qquad (4\text{-}2\text{-}21)$$

$$\theta_{3m} = \text{Arctan}\{r/a[2mH+(z+z_o)]\} \qquad (4\text{-}2\text{-}22)$$

$$\theta_{4m} = \text{Arctan}\{r/a[2(m+1)H-|z-z_o|]\} \qquad (4\text{-}2\text{-}23)$$

and

$$R_{1m} = \{r^2 + a^2[2mH+|z-z_o|]\}^{\frac{1}{2}} \qquad (4\text{-}2\text{-}24)$$

$$R_{2m} = \{r^2 + a^2[2(m+1)H-(z+z_o)]\}^{\frac{1}{2}} \qquad (4\text{-}2\text{-}25)$$

$$R_{3m} = \{r^2 + a^2[2mH+(z+z_o)]\}^{\frac{1}{2}} \qquad (4\text{-}2\text{-}26)$$

$$R_{4m} = \{r^2 + a^2[2(m+1)H-|z-z_o|]\}^{\frac{1}{2}} \qquad (4\text{-}2\text{-}27)$$

Branch-cut contributions to the $I_{jm}$ integrals must also be included whenever the $\theta_{jm}$ exceed the so-called critical angle

$$\theta_c = \text{Arcsin}(1/\sqrt{\epsilon_z}) \qquad (4\text{-}2\text{-}28)$$

4-9

The branch-cut contributions to the $I_{jm}$ integrals are

$$I_{1m}^{(b)} \sim -4\pi\varepsilon_z mR_g^m(\theta_c)$$

$$\cdot \frac{\exp\{-jk_o[r+a(\varepsilon_z-1)^{\frac{1}{2}}[2mH+|z-z_o|]]\}}{k_o(\varepsilon_z-1)r^2} \qquad (4-2-29)$$

$$I_{2m}^{(b)} \sim -4\pi\varepsilon_z(m+1)R_g^m(\theta_c)$$

$$\cdot \frac{\exp\{-jk_o[r+a(\varepsilon_z-1)^{\frac{1}{2}}[2(m+1)H-(z+z_o)]]\}}{k_o(\varepsilon_z-1)r^2} \qquad (4-2-30)$$

$$I_{3m}^{(b)} \sim -4\pi\varepsilon_z mR_g^{m+1}(\theta_c)$$

$$\cdot \frac{\exp\{-jk_o[r+a(\varepsilon_z-1)^{\frac{1}{2}}[2mH+(z+z_o)]]\}}{k_o(\varepsilon_z-1)r} \qquad (4-2-31)$$

$$I_{4m}^{(b)} \sim -4\pi\varepsilon_z(m+1)R_g^{m+1}(\theta_c)$$

$$\cdot \frac{\exp\{-jk_o[r+a(\varepsilon_z-1)^{\frac{1}{2}}[2(m+1)H-|z-z_o|]]\}}{k_o(\varepsilon_z-1)r} \qquad (4-2-32)$$

More accurate representations for the branch-cut contributions $I_{jm}$ can be inferred by analogy from Equations (5-3-37) and (5-3-40) of [42]. Constraints bearing upon the validity of these results can also be inferred from [42].

Because branch-cut contributions are included only when

$$\theta_{jm} > \theta_c \qquad (4-2-33)$$

the number of branch-cut contributions is finite. As a consequence, Equation (4-2-6) can be re-written in the form

$$S_j = \sum_{m=0}^{\infty} I_{jm}^{(r)} + \sum_{m=0}^{M} I_{jm}^{(b)} \qquad (4-2-34)$$

The electromagnetic fields ($\underline{E}$ and $\underline{H}$) within the anisotropic forest slab can be derived from the Hertz vector potential $A_z^{II}$

4-10

[Equation (4-2-5)] by using Equations (4-1-4) and (4-1-5). For example, the vertically-polarized electric field vector $\underline{E}$ is

$$E_z = E_z^{(d)} + E_z^{(r)} + E_z^{(\ell)} \tag{4-2-35}$$

where

$$E_z^{(d)}(\underline{r},z) = \sqrt{a}\left(\frac{\omega\mu_o}{4\pi}\right)Id\ell\,\sin^2\theta_{10}\,\frac{\exp\{-jk_o\sqrt{\varepsilon_z}\,R_{10}\}}{R_{10}} \tag{4-2-36}$$

$$E_z^{(r)}(\underline{r},z) = \sqrt{a}\left(\frac{\omega\mu_o}{4\pi}\right)Id\ell$$

$$\cdot\left\{\sum_{m=1}^{\infty}\,[R_a^m(\theta_{1m})R_g^m(\theta_{1m})\sin^2\theta_{1m}]\frac{\exp\{-jk_o\sqrt{\varepsilon_z}\,R_{1m}\}}{R_{1m}}\right.$$

$$+\sum_{m=0}^{\infty}\,[R_a^{m+1}(\theta_{2m})R_g^m(\theta_{2m})\sin^2\theta_{2m}]\frac{\exp\{-jk_o\sqrt{\varepsilon_z}\,R_{2m}\}}{R_{2m}}$$

$$+\sum_{m=0}^{\infty}\,[R_a^m(\theta_{3m})R_g^{m+1}(\theta_{3m})\sin^2\theta_{3m}]\frac{\exp\{-jk_o\sqrt{\varepsilon_z}\,R_{3m}\}}{R_{3m}}$$

$$\left.+\sum_{m=0}^{\infty}[R_a^{m+1}(\theta_{4m})R_g^{m+1}(\theta_{4m})\sin^2\theta_{4m}]\frac{\exp\{-jk_o\sqrt{\varepsilon_z}\,R_{4m}\}}{R_{4m}}\right\}$$

$$\tag{4-2-37}$$

$$E_z^{(\ell)}(\underline{r},z) = 60\,Id\ell\,\frac{a}{\varepsilon_z-1}\cdot\frac{\exp\{-jk_o r\}}{r^2}$$

$$\cdot\left\{\sum_{m=1}^{M}\,[mR_g^m(\theta_c)]\exp\{-jk_o a(\varepsilon_z-1)^{\frac{1}{2}}[2mH+|z-z_o|]\}\right.$$

$$+\sum_{m=0}^{M}\,[(m+1)R_g^m(\theta_c)]\exp\{-jk_o a(\varepsilon_z-1)^{\frac{1}{2}}[2(m+1)H-(z+z_o)]\}$$

$$+\sum_{m=1}^{M}\,[mR_g^{m+1}(\theta_c)]\exp\{-jk_o a(\varepsilon_z-1)^{\frac{1}{2}}[2mH+(z+z_o)]\}$$

$$+ \sum_{m=0}^{M} [(m+1) R_g^{m+1} (\theta_c)] \exp\{-jk_0 a (\varepsilon_z - 1)^{\frac{1}{2}} [2(m+1) H - |z - z_0|]\}\Big\}$$

<div align="right">(4-2-38)</div>

In Equation (4-2-35), $E_z^{(d)}$ represents a direct wave propagating through the anisotropic forest slab from the transmitter to the receiver; $E_z^{(r)}$ represents multiply-reflected waves also propagating through the anisotropic forest slab from the transmitter to the receiver [refer to Figure 4-3a]; and $E_z^{(\ell)}$ represents multiply-reflected lateral waves associated with the air-forest interface [refer to Figure 4-3b]. The first summation in Equation (4-2-37) corresponds to waves which experience an even number of reflections in propagating from the transmitter to the receiver and for which the first reflection is from the ground; the second summation corresponds to an odd number of reflections, the first of which is from the air; the third corresponds to an odd number of reflections, the first of which is from the ground; and the fourth summation corresponds to an even number of reflections, the first of which is from the air.

## 4.3 Intra-Forest Multipath

The anisotropic forest slab model differs from the anisotropic forest half-space model by accounting for ground reflections. The principal consequence of ground reflections is the appearance of intra-forest multipath. Two types of intra-forest multipath can be identified: multiply-reflected space waves, described by Equation (4-2-37) and illustrated in Figure 4-3(a); and multiply-reflected lateral waves, described by Equation (4-2-38) and illustrated in Figure 4-3(b). Intra-forest multipath can either enhance or degrade the received signal level according to whether the concomitant phasor interference is constructive or destructive; in addition, intra-forest multipath can lead to pulse distortion and inter-symbol interference.
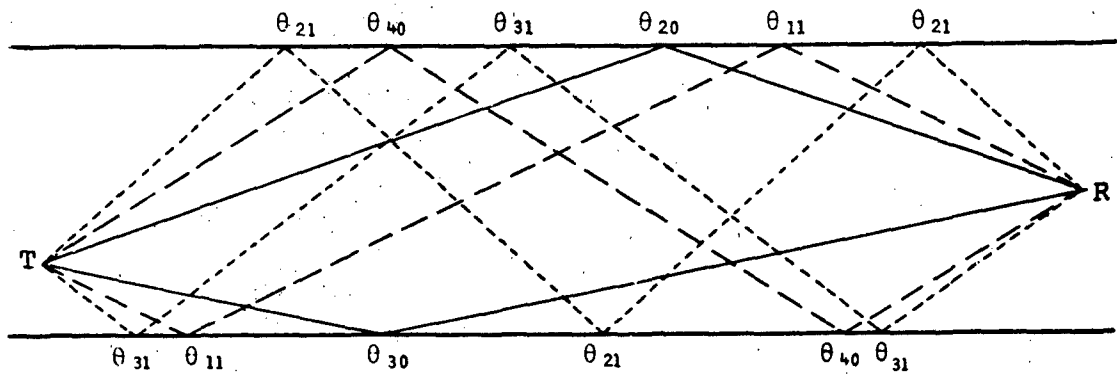
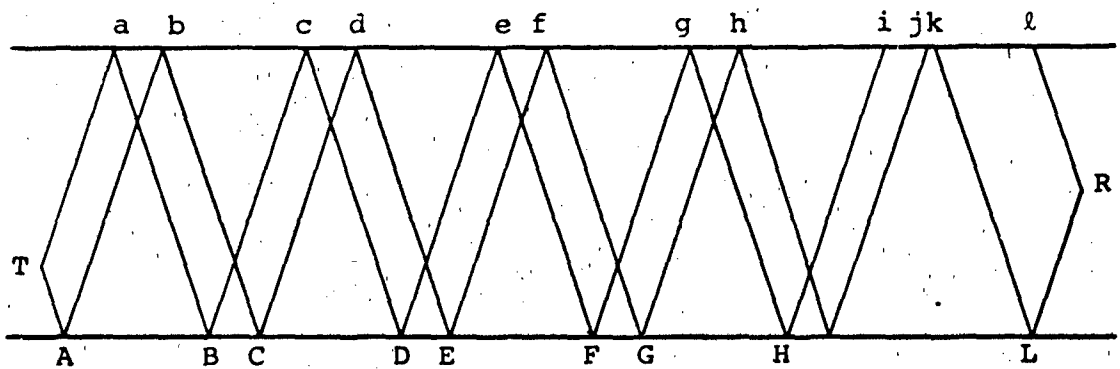Figure 4-3(a): Multiply-Reflected Waves (Space)



Figure 4-3(b): Multiply-Reflected Waves (Lateral)
(e.g. TaBcℓR)

It is apparent from Equation (4-2-37) and (4-2-38) that the Fresnel reflection coefficients at the air-forest and forest-ground interfaces [denoted by $R_a(\theta)$ and by $R_g(\theta)$, respectively] play an important role in determining the relative contributions of the contributing multipath. The behavior of these reflection coefficients is examined in the following sub-section. Successive sub-sections address the intra-forest multipath associated with multiply-reflected space waves and multiply-reflected lateral waves.

### 4.3.1 Fresnel Reflection Coefficients

The Fresnel reflection coefficients associated with the air-forest and forest-ground interfaces are given, respectively, by

$$R_a(\theta) = \frac{\cos\theta - \sqrt{\epsilon_t}(1 - \epsilon_z\sin^2\theta)^{\frac{1}{2}}}{\cos\theta + \sqrt{\epsilon_t}(1 - \epsilon_z\sin^2\theta)^{\frac{1}{2}}} \tag{4-3-1}$$

$$R_g(\theta) = \frac{\epsilon_g\cos\theta - \sqrt{\epsilon_t}(\epsilon_g - \epsilon_z\sin^2\theta)^{\frac{1}{2}}}{\epsilon_g\cos\theta + \sqrt{\epsilon_t}(\epsilon_g - \epsilon_z\sin^2\theta)^{\frac{1}{2}}} \tag{4-3-2}$$

where $\epsilon_t$ and $\epsilon_z$ are, respectively, the transverse and longitudinal components of the uniaxial effective dyadic permittivity of the forest; $\epsilon_g$ is the permittivity of the ground; and $\theta$ is the incidence angle measured relative to the normal.

The magnitude $|R|$ and the phase $|Arg|$ of the Fresnel reflection coefficient for the forest-ground interface $R_g(\theta)$ is shown in Figure 4-4(a) as a function of the glancing angle [complement of the incidence angle] for the case of moist ground ($\epsilon_g' = 30$, $\sigma_g = 0.05$ S/m) and a frequency of 300 MHz. At the Brewster angle, $|R|$ exhibits a pronounced minimum and the phase $|Arg|$ changes by nearly 180 degrees. At grazing incidence (glancing angle equal to zero) $R_g(90°) = -1$. Analogous results are shown in Figure 4-4(b) for the case of dry ground ($\epsilon_g' = 15$, $\sigma_g = 0.005$ S/m). Although Equation (4-3-2) reveals that that $R_g(\theta)$ also depends upon the effective dyadic permittivity

|R|

Moist Ground

f = 300 Mhz
$\varepsilon_g$ = 30
$\sigma_g$ = 0.05 S/m

Glancing Angle  (degrees)

ARG
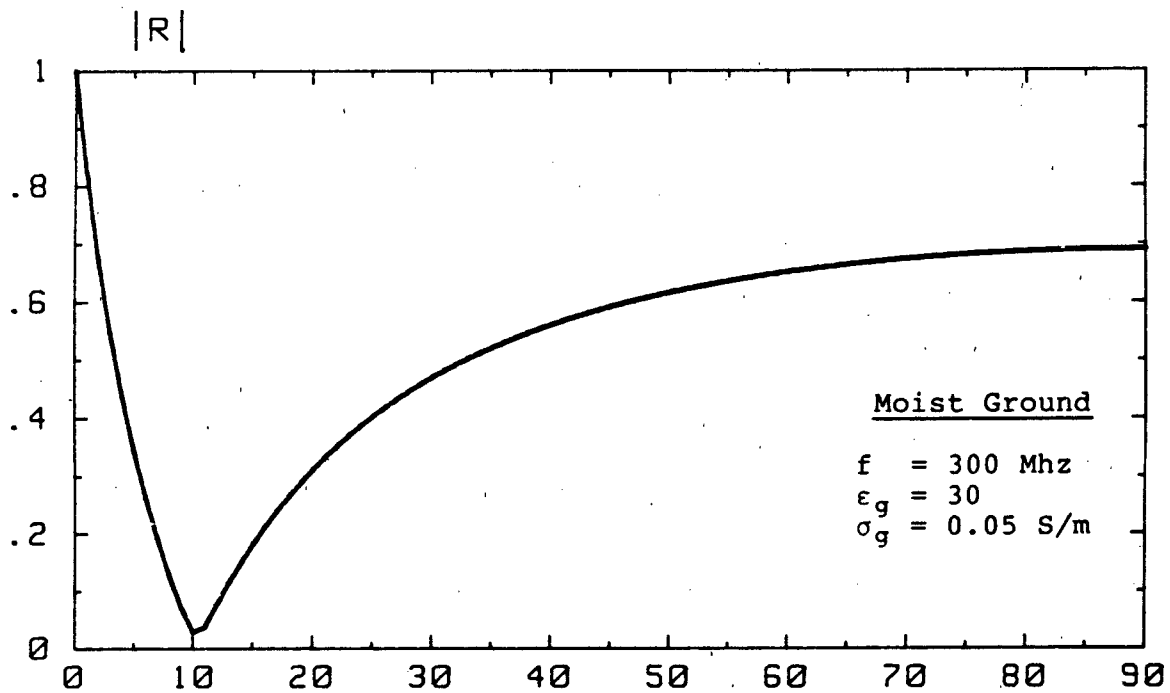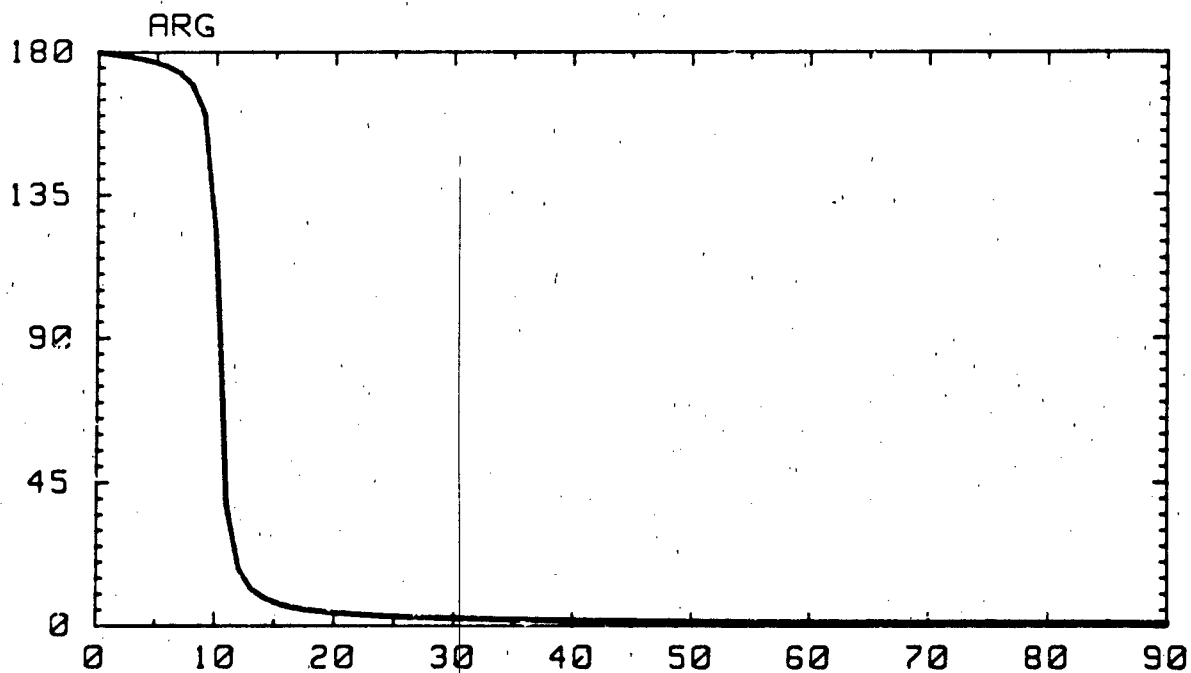
Glancing Angle  (degrees)

Figure 4-4(a):  Reflection Coefficients (Moist Ground)

|R|

f = 300 MHz

$\varepsilon_g$ = 30

$\sigma_g$ = 0.005 S/m

Glancing Angle (degrees)

ARG

Glancing Angle (degrees)
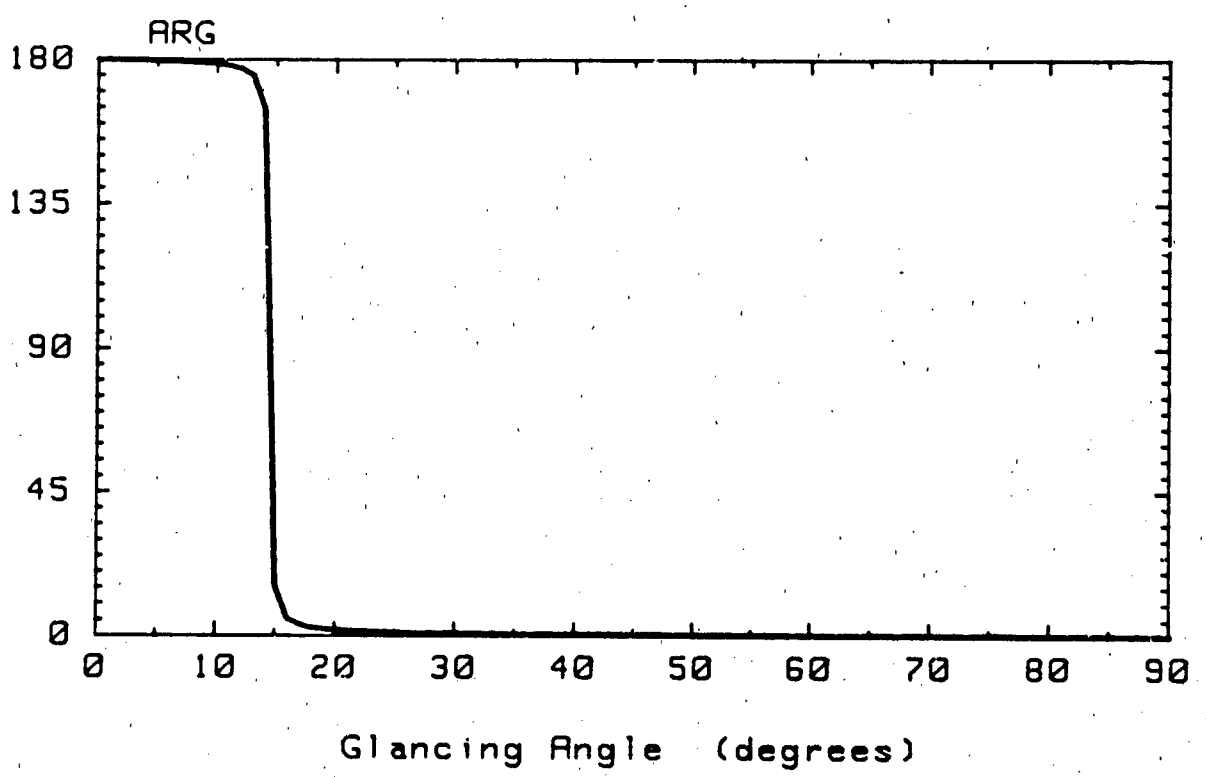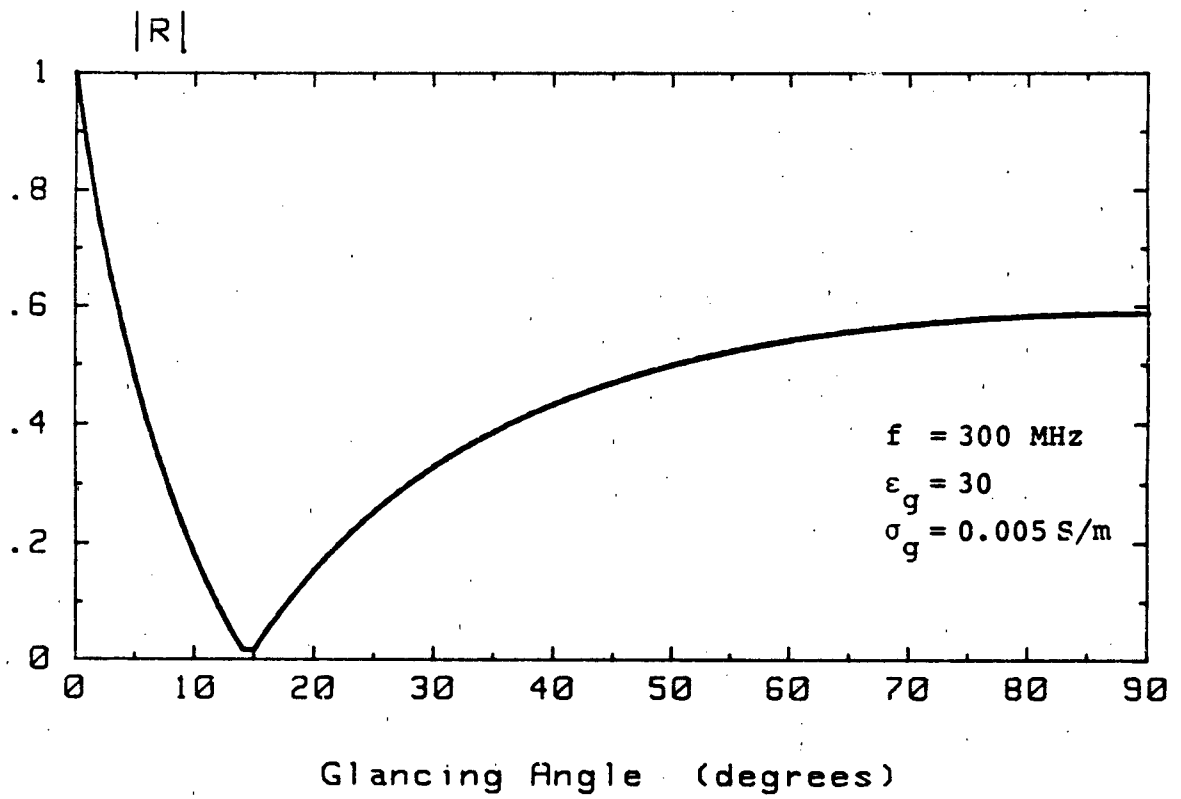
Figure 4-4(b): Reflection Coefficients (Dry Ground)

4-16

of the forest, because $\varepsilon_t$ and $\varepsilon_z$ differ from unity by only a few tenths of one percent, $R_g(\theta)$ is virtually independent of the biophysical forest parameters.

The magnitude $|R|$ and the phase $|\text{Arg}|$ of the Fresnel reflection coefficient for the air-forest interface $R_a(\theta)$ is shown in Figure 4-5(a) for the case of lossless leaves ($\varepsilon_\ell' = 40$, $\varepsilon_\ell'' = 0$) and a frequency of 300 MHz. Note that the corresponding effective dyadic permittivity is purely real ($\varepsilon_.'' = \varepsilon_z'' = 0$). For glancing angles less than the critical glancing angle,

$$\theta_c = \text{Arcsin}(1/\sqrt{\varepsilon_z})  \qquad (4\text{-}3\text{-}3)$$

$|R|$ is unity and the incident radiowave experiences total internal reflection. However, whereas at grazing incidence (glancing angle equal to zero) $R_a(90°) = -1$, at the critical glancing angle $R_a(\theta_c) = +1$. For glancing angles greater than critical, $|R|$ is nearly zero. At the Brewster angle $|R|$ exhibits a barely discernible minimum and the phase $|\text{Arg}|$ changes abruptly by 180 degrees. Analogous results are shown in Figure 4-5(b) for the case of lossy leaves. Note, however, that as a consequence of ohmic losses within the leaves, the incident radiowave no longer experiences total internal reflection for glancing angles less than critical; further, the phase change associated with the Brewster angle is no longer abrupt.

### 4.3.2 Multiply-Reflected Space Waves

The intra-forest multipath associated with multiply-reflected space waves is described by Equation (4-2-37) and illustrated in Figure 4-3(a). It is apparent from Equation (4-2-37) that the relative strength of the intra-forest multipath can be estimated by considering the relative magnitudes of the composite forest reflection coefficients [e.g., $R_a$, $R$, $R_a R_g$, $R_g R_a$, $R_a R_g R_a$, $R_g R_a R_g$ (refer to Figure 4-3(a))] magnitudes of the composite Fresnel reflection coefficients at 300 MHz for a forest of leaves (FV = 0.1%) above a moist earth ($\varepsilon_g' = 30$, $\sigma_g = 0.05$ S/m) have been plotted in Figure 4-6 as a function

|R|

1

.8

.6

.4

.2

0

Lossless Leaves

$f$ = 300 MHz
$\epsilon_t'$ = 1.058678
$\epsilon_t''$ = 0.0
$\epsilon_z'$ = 1.006699
$\epsilon_z''$ = 0.0

0    10    20    30    40    50    60    70    80    90

Glancing Angle (degrees)

ARG

180

135

90

45

0

0    10    20    30    40    50    60    70    80    90

Glancing Angle (degrees)
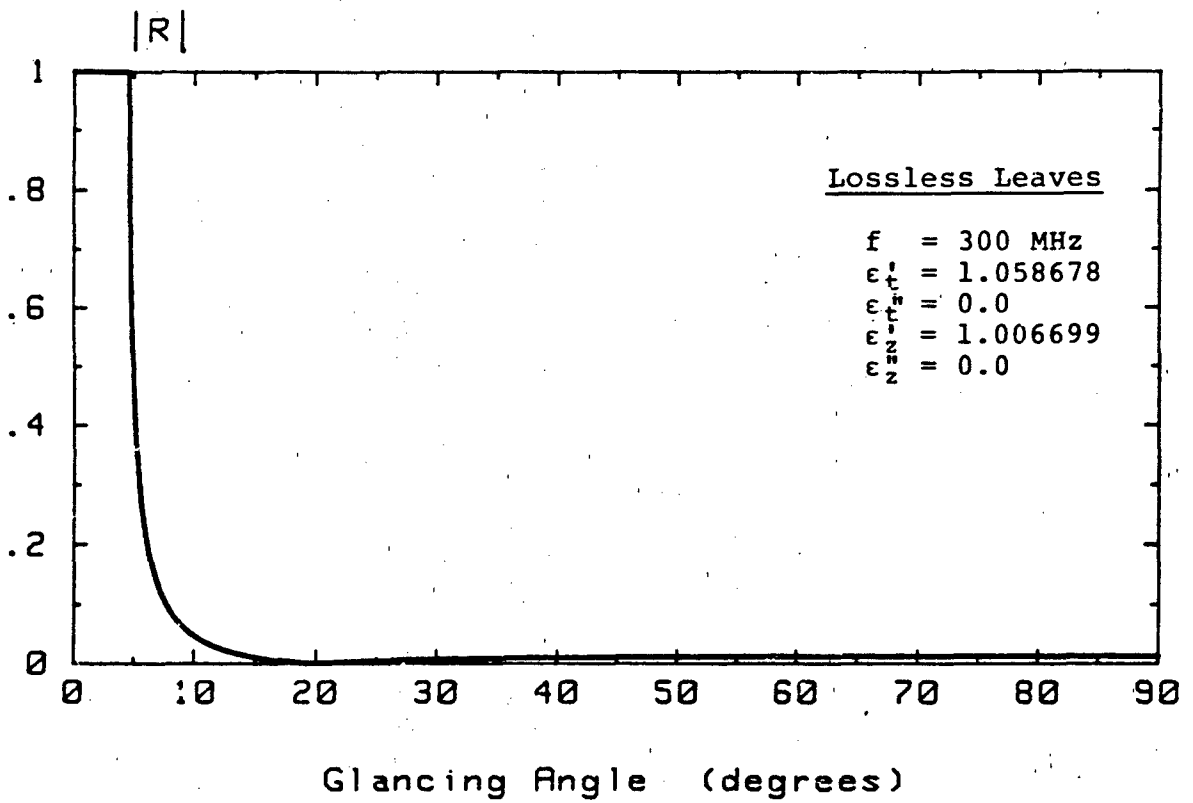
Figure 4-5(a):   Reflection Coefficients (Lossless Leaves)

4-18

|R|

Lossy Leaves

$f = 3\ 0$ MHz
$\epsilon_t' = 1,058678$
$\epsilon_t'' = 0.008416$
$\epsilon_z' = 1.006699$
$\epsilon_z'' = 0.000766$

Glancing Angle (degrees)

ARG

Glancing Angle (degrees)

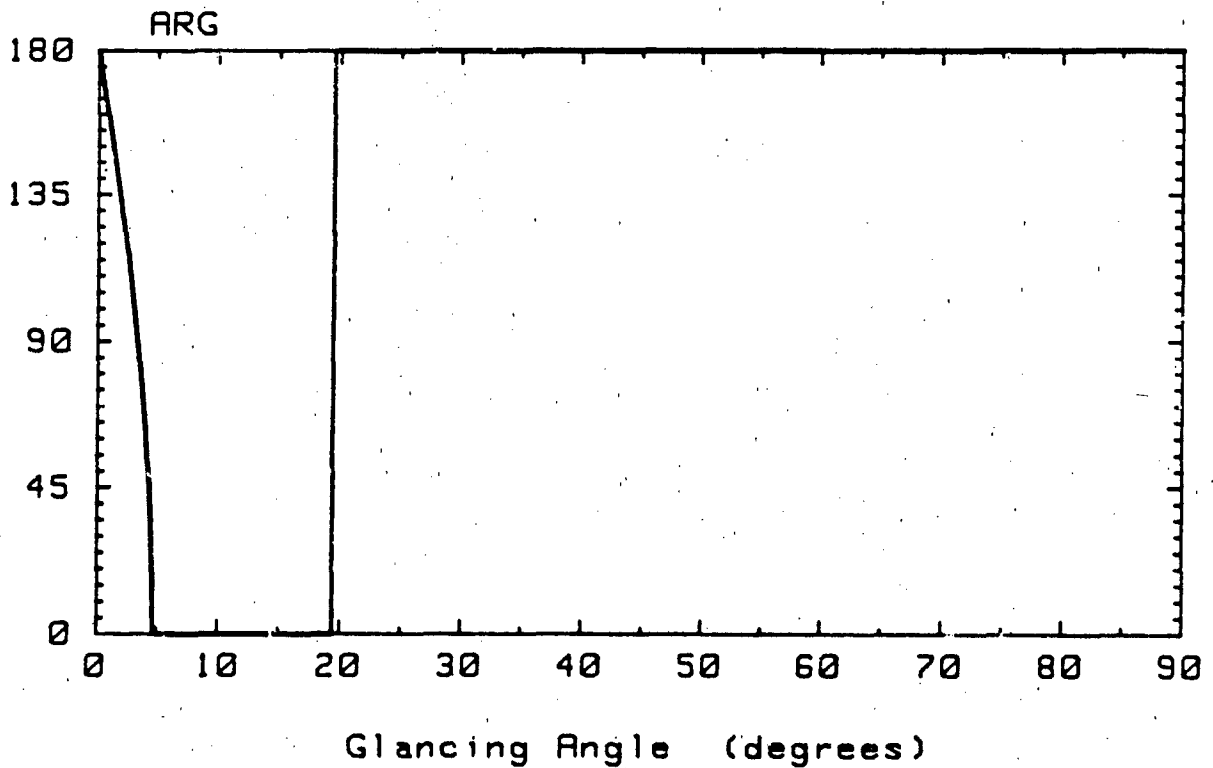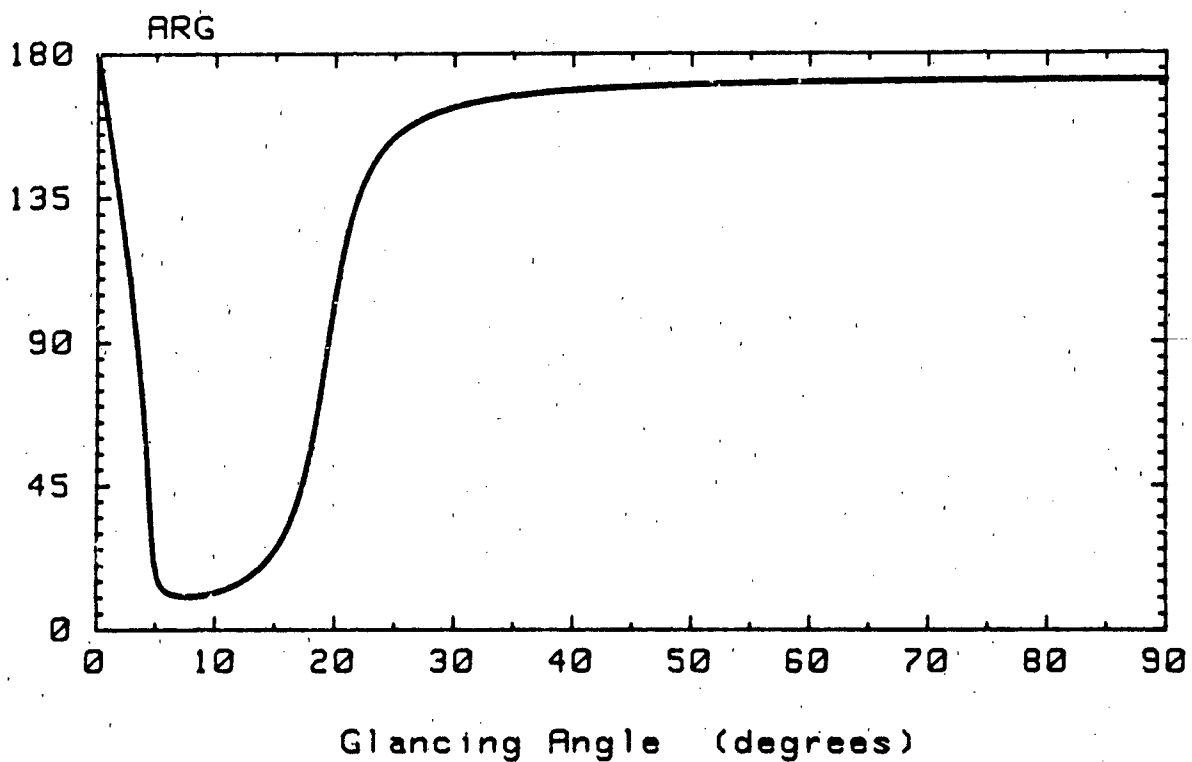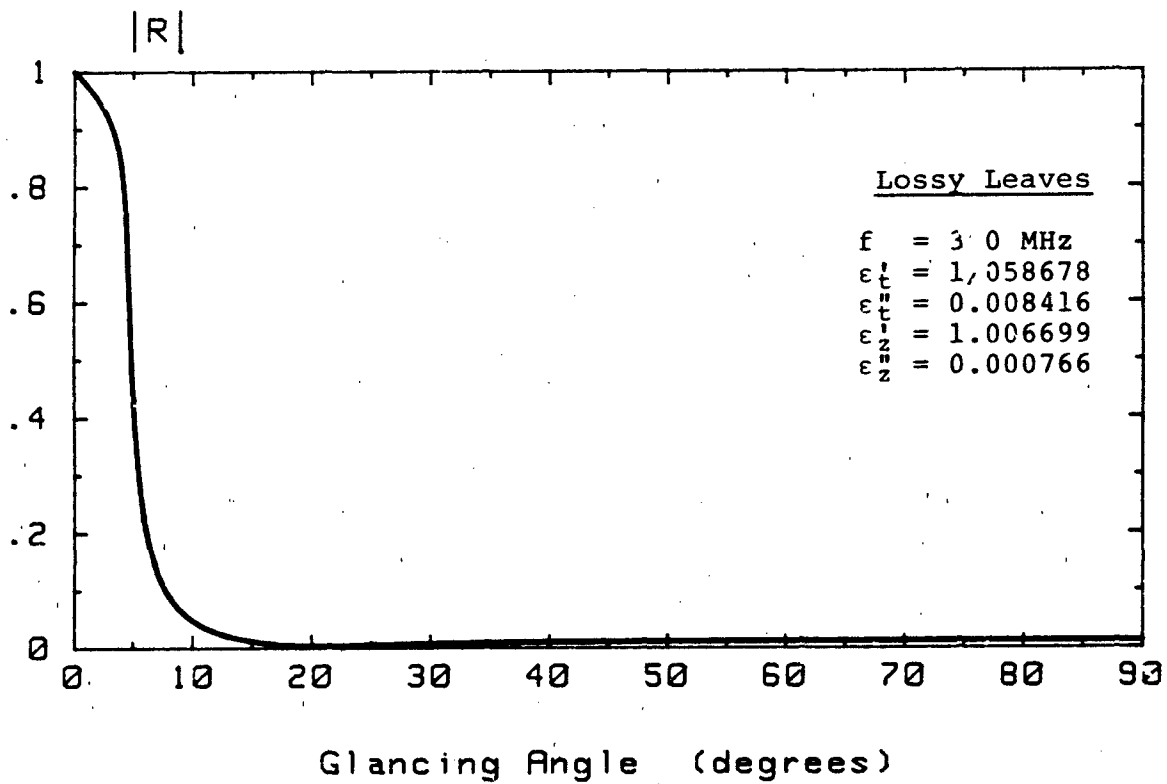Figure 4-5(b): Reflection Coefficients (Lossy Leaves)
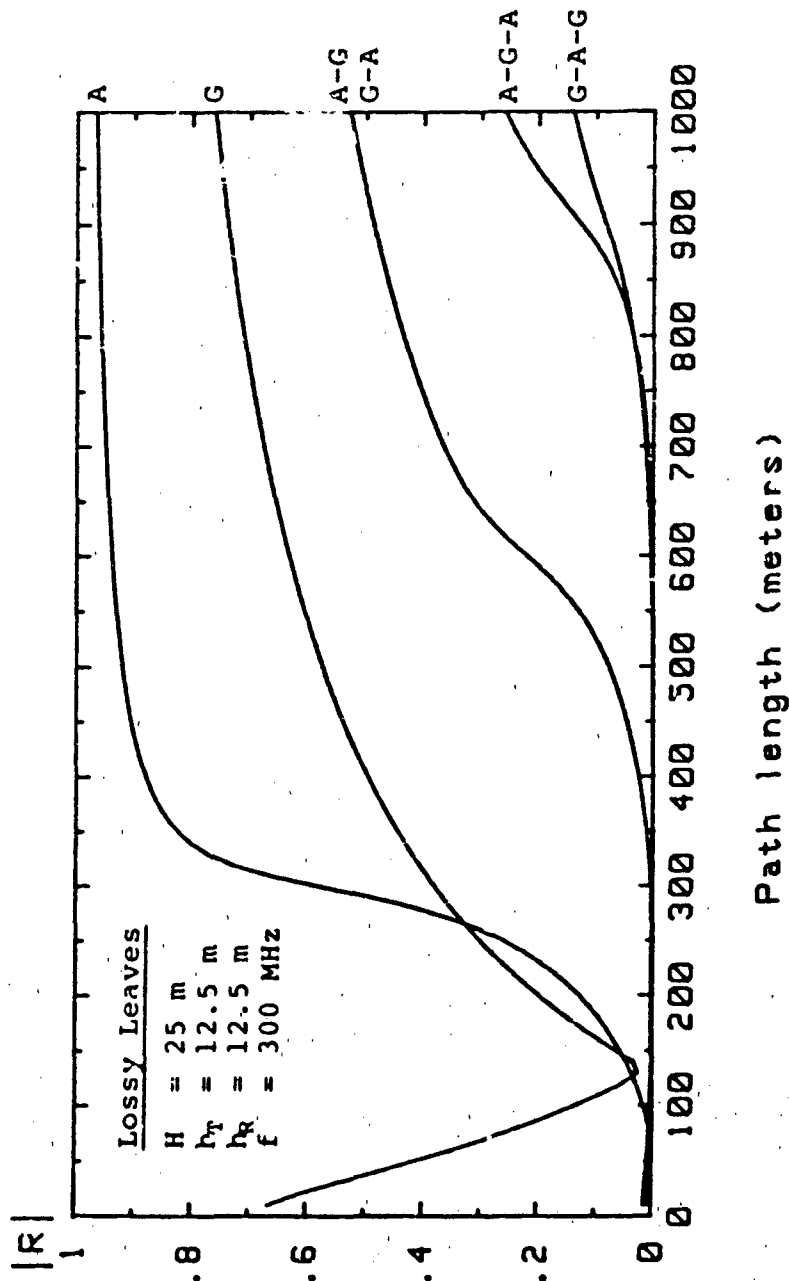
Figure 4-6(a): Reflection Coefficients (Composite)

Path length (meters)

Lossy Leaves
H = 25 m
$h_T$ = 12.5 m
$h_R$ = 12.5 m
f = 300 MHz

|R|

A
G
A-G
G-A
A-G-A
G-A-G
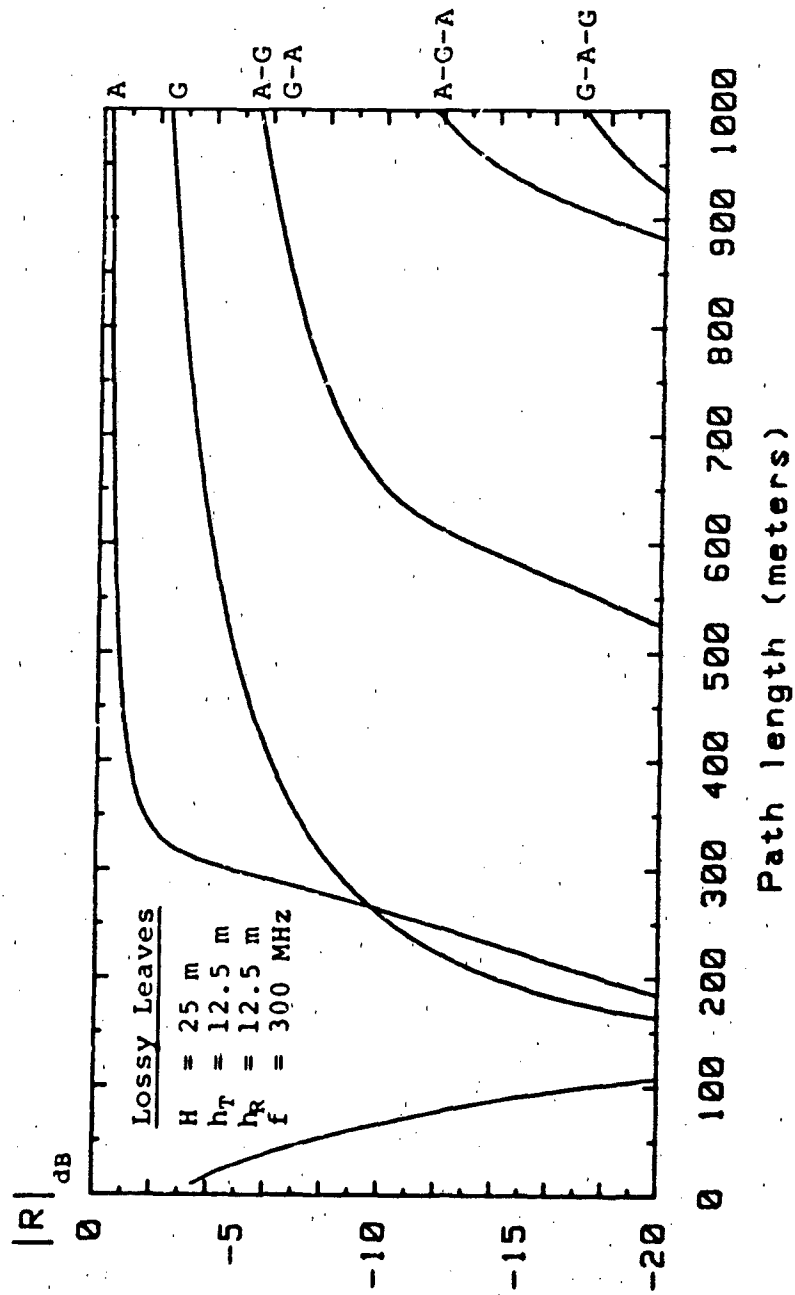
Figure 4-6(b): Reflection Coefficients (Composite) dB

**Lossy Leaves**

$H = 25$ m
$h_T = 12.5$ m
$h_R = 12.5$ m
$f = 300$ MHz

Path length (meters)

$|R|_{dB}$

A
G
A-G
G-A
A-G-A
G-A-G

of path length using the expression

$$\theta = \text{Arctan}\left\{\frac{r}{(n-1)H + \left|\frac{H-z_0}{z_0}\right|_T + \left|\frac{H-z}{z}\right|_R}\right\}^* \qquad (4-3-4)$$

where,   $H$ = height of forest

   $z_0$ = height of transmitter above forest floor

   $z$ = height of receiver above forest floor

   $r$ = distance between transmitter and receiver

   $\theta$ = incidence angle of reflected radiowave

   $n$ = number of reflections experienced by radiowave

to relate the path length to the incidence angle. It is apparent from this figure that for these biophysical forest parameters and a frequency of 300 MHz the ray reflected only once from the air-forest interface [the only ray accounted for in the anisotropic half-space model] is important at all distances in excess of about 300 meters. The ray reflected once from the ground is important not only at distances in excess of 300 meters, but also at very short distances as well. The $R_a R_g$ and $R_g R_a$ contributions become important only at ranges exceeding about 300 meters; and the $R_a R_g R_a$ and $R_g R_a R_g$ contributions can probably be neglected for ranges less than 1000 meters. It should be noted that Figure 4-6 does not account for antenna pattern discrimination, differential geometric spreading losses, or differential absorptive losses.

### 4.3.3   Multiply-Reflected Lateral Waves

The intra-forest multipath associated with multiply-reflected lateral waves is described by Equation (4-2-38) and illustrated in Figure 4-3(b). The correspondence between the multiply-reflected lateral waves of Figure 1-3(b) and the summations of Equations (4-2-38) is summarized in Table 4-1. The

---

*The upper (lower) quantity within $\left|\ \ \right|_{T,R}$ is to be used if the radiowave reflection nearest the transmitter [receiver] is from the air (ground).

## Table 4-1:  Multiply-Reflected Lateral Wave Ray Paths

| $z_{jm}$ | $m = 0$ | $m = 1$ | $m = 2$ | $m = 3$ |
|---|---|---|---|---|
| $z_{1m}$ | None | TakLR | TaBckℓR | TaBcDekLR |
| $z_{2m}$ | TaℓR | TaBcℓR | TaBcDeℓR | TaBcDeFhℓR |
| $z_{3m}$ | None | TabkLR | TAbCdkℓR | TAbCdEfkℓR |
| $z_{4m}$ | TAbℓR | TAbCdℓR | TAbCdEfℓR | TAbCdEfGhℓR |

## Table 4-2:  Transmitter/Receiver Images for Lateral Waves

| $z_{jm}$ | $m = 0$ | $m = 1$ | $m = 2$ | $m = 3$ |
|---|---|---|---|---|
| $z_{1m}$ | N/A | $H-h_T$ <br> $H+h_R$ | $3H-h_T$ <br> $H+h_R$ | $5H-h_T$ <br> $H+h_R$ |
| $z_{2m}$ | $H-h_T$ <br> $H-h_R$ | $3H-h_T$ <br> $H-h_R$ | $5H-h_T$ <br> $H-h_R$ | $7H-h_T$ <br> $H-h_R$ |
| $z_{3m}$ | N/A | $H+h_T$ <br> $H+h_R$ | $3H+h_T$ <br> $H+h_R$ | $5H+h_T$ <br> $H+h_R$ |
| $z_{4m}$ | $H+h_T$ <br> $H-h_R$ | $3H+h_T$ <br> $H-h_R$ | $5H+h_T$ <br> $H-h_R$ | $7H+h_T$ <br> $H-h_R$ |

multipath geometry illustrated in Figure 4-3(b) can be easily constructed by locating the appropriate transmitter/receiver images arising witn successive radiowave reflections from the air and ground interfaces at the critical angle $\theta_c$. The location of these images relative to the air-forest interface can be inferred from the exponents appearing in the summations of Equation (4-2-38); those corresponding to Table 4-1 are shown in Table 4-2.

Equation (4-2-33) can be used in consonance with Equations (4-2-20) through (4-2-27) to show that associated with each (j,m) component lateral wave is a minimum excitation distance

$$r_{min} = |a| z_{jm} / |\sqrt{\varepsilon_z - 1}| \qquad (4-3-5)$$

where $z_{jm}$, the so-called [65] separation distance is given by

$$z_{1m} = 2mH + |z - z_o| \qquad (4-3-6)$$

$$z_{2m} = 2(m+1)H - (z+z_o) \qquad (4-3-7)$$

$$z_{3m} = 2mH + (z+z_o) \qquad (4-3-8)$$

$$z_{4m} = 2(m+1)H - |z-z_o| \qquad (4-3-9)$$

The separation distance $[z_{jm}]$, the minimum excitation distance $[r_{min}]$, and the relative strength of the multiply-reflected lateral waves have been calculated for several 1000-meter, 300-MHz radio links situated within a forest of leaves (FV = 0.01%) and above a moist ground ($\varepsilon_g' = 30$, $\sigma_g = 0.05$ S/m) and presented in Table 4-3. Note that the non-ground-reflected lateral wave [the only lateral wave accounted for in the anisotropic half-space model] is dominant. The phasor sum of all contributing lateral wave components has been calculated and its relative strength denoted in the Table by LDBT. As expected, it differs only slightly from that of the non-ground-reflected lateral wave. When the number of contributing lateral waves is large, the phasor sum is well approximated by

## Table 4-3

### LATERAL WAVE MULTIPATH

PATH: Forest Ht. =    25.m    Ht-xmtr  = 22.5m   Ht-rcvr  = 22.5m
       Critical Angle =  3.83 Deg.    Reflection Coef = .4644

#### Minimum Excitation Distances (m)

| Zm | 0 | 1 | 2 | 3 | 4 |
|---|---|---|---|---|---|
| | 5.00 | 743.79 | 1487.58 | 2231.37 | 2975.15 |
| | 74.38 | 818.17 | 1561.96 | 2305.74 | 3049.53 |
| | .00 | 1413.20 | 2156.99 | 2900.78 | 3644.56 |
| | 743.79 | 1487.58 | 2231.37 | 2975.15 | 3718.94 |

#### Separation Distances (m)

| Zm | 0 | 1 | 2 | 3 | 4 |
|---|---|---|---|---|---|
| | .00 | 50.00 | 100.00 | 150.00 | 200.00 |
| | 5.00 | 55.00 | 105.00 | 155.00 | 205.00 |
| | .00 | 95.00 | 145.00 | 195.00 | 245.00 |
| | 50.00 | 100.00 | 150.00 | 200.00 | 250.00 |

#### Relative Field Strength

| Zm | 0 | 1 | 2 | 3 | 4 |
|---|---|---|---|---|---|
| | ******* | -16.58 | ******* | ******* | ******* |
| | .00 | -11.66 | ******* | ******* | ******* |
| | ******* | ******* | ******* | ******* | ******* |
| | -16.58 | ******* | ******* | ******* | ******* |

LDBT =    -.16338 dB     LDBTT =    -4.32773 dB

$$K(z,z_o,H) = \frac{[1 + R_g(\theta_c)\exp\{j\kappa z_o\}][1 + R_g(\theta_c)\exp\{j\kappa z\}]}{[1 + R_g(\theta_c)\exp\{j\kappa H\}]^2} \qquad (4\text{-}3\text{-}10)$$

where

$$\kappa = 2k_o\sqrt{a}\sqrt{(\varepsilon_z - 1)} \qquad (4\text{-}3\text{-}11)$$

This too has been calculated and is denoted by LDBTT in the Table. It is apparent from this calculation that when only a few lateral wave components contribute significantly, Equation (4-3-10) is inappropriate.

## 4.4  Transmission Loss

The most important parameter characterizing radiowave propagation channels is transmission loss. Loosely defined, transmission loss is the ratio of received power to transmitted power (or its inverse). Basic transmission loss, however, is specifically defined [for unmodulated r-f carriers] as the ratio of the power transmitted to the power received as measured at the terminals of isotropic, lossless, co-polarized antennas. The concept of basic transmission loss may be extended to wideband, modulated r-f carriers by appropriately weighting the basic transmission loss by the transmitted power spectral density.

## 4.4.1  Basic Transmission Loss

For radiowaves propagating through freespace, the basic transmission loss (in decibels) can be calculated from the well-known expression

$$L_{fs} = 32.4 + 20\log_{10}d_{km} + 20\log_{10}f_{MHz} \qquad (4\text{-}4\text{-}1)$$

where $d_{km}$ is the distance between the antennas in kilometers and $f_{MHz}$ is the radiowave frequency in Megahertz. This equation has been used to plot in Figure 4-7 the frequency dependence of basic transmission loss in free space over a 1000-meter path.
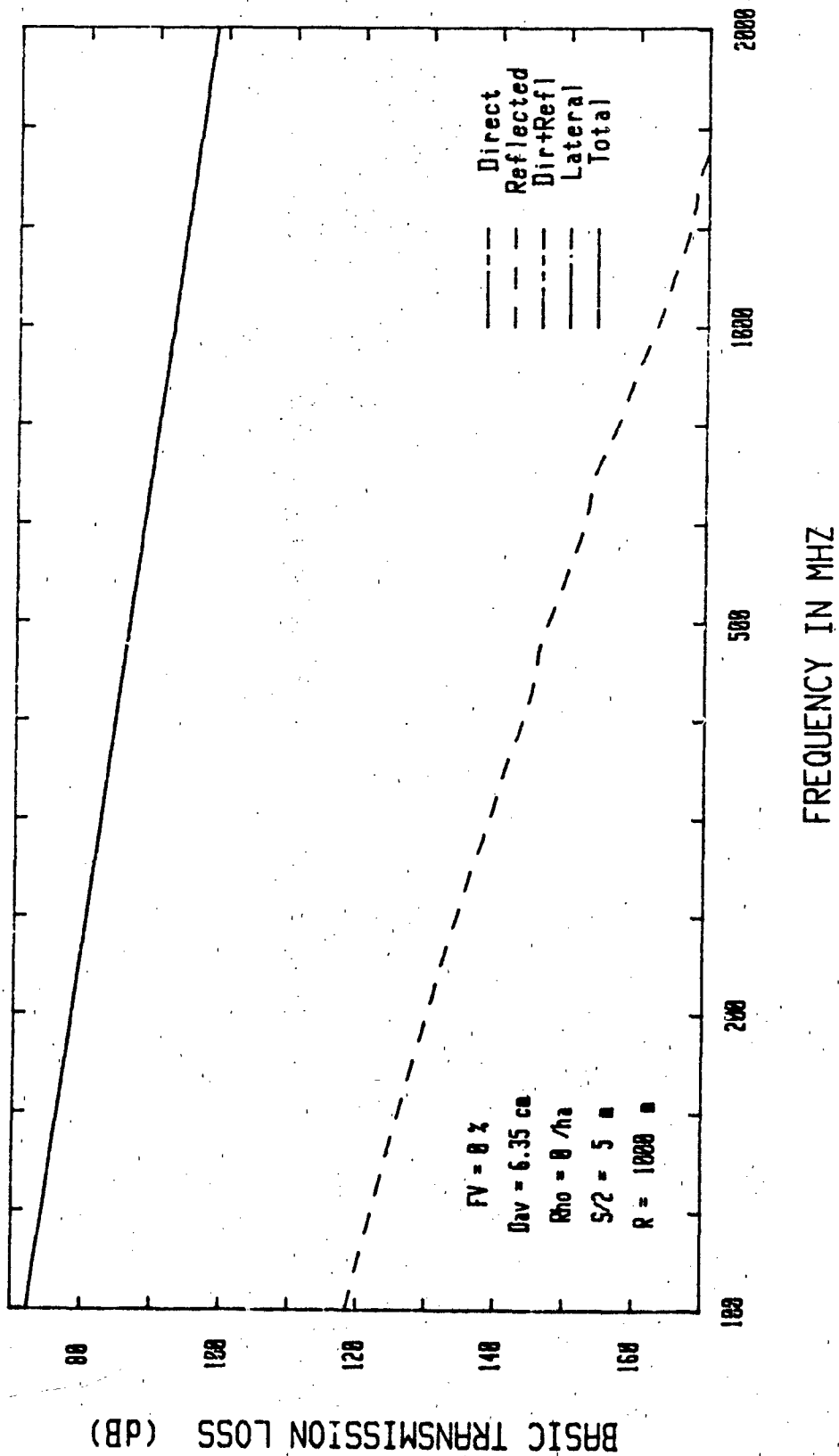
Figure 4-7: Basic Transmission Loss (Free-space)

In calculating the basic transmission loss associated with the stratified forest models described previously, it is important to recognize that postulated for those models was a vertically-polarized electric dipole antenna. Such an antenna is not isotropic. Nevertheless, the basic transmission loss can still be determined by noting that: (1) in free-space, the vertically-polarized electric field can be determined from Equation (4-2-36) by setting $\varepsilon_t = \varepsilon_z = 1$ so that

$$E_{fs} = (\omega\mu_o/4\pi)Id\ell \, \sin^2\theta_{10}\frac{\exp\{-jk_oR_{10}\}}{R_{10}} \qquad (4-4-2)$$

and (2) the power received is directly proportional to the field intensity

$$I(\underline{x}) = \underline{E}(\underline{x})\cdot\underline{E}^*(\underline{x}) \qquad (4-4-3)$$

Thus, for the stratified forest models, the basic transmission loss can be expressed by

$$L_b(d,r,\ell) = L_{fs} + 20\log_{10}|E_{fs}/E_{d,r,\ell}| \qquad (4-4-4)$$

where $E_{d,r,\ell}$ is defined in Equations (4-2-36), (4-2-37), and (4-2-38). Equation (4-4-4) has been used in Section 5.2 to assess the sensitivity of the basic transmission loss to the biophysical forest parameters.

### 4.4.2 Wideband Basic Transmission Loss

Consider a modulated radiowave having a transmitted power spectral density $S(\omega)$. The total power transmitted is then

$$P_T = \int S(\omega)d\omega \qquad (4-4-5)$$

If the basic transmission loss associated with an unmodulated r-f carrier of angular frequency $\omega$ is denoted by $L(\omega)$ then the total power received is

$$P_R = \int S(\omega)L(\omega)d\omega \qquad (4-4-6)$$

The wideband basic transmission loss can then be defined as

$$L_{wb} = \frac{P_R}{P_T} = \frac{\int S(\omega)L(\omega)d\omega}{\int S(\omega)d\omega} \qquad (4\text{-}4\text{-}7)$$

or, expressed* in decibels,

$$L_{dB} = -10\log_{10}L_{wb} \qquad (4\text{-}4\text{-}8)$$

## 4.5 Doppler Frequency Shift

The stratified forest model for the coherent field components of the propagating radiowave has been extended to account for Doppler shift induced by terminal motion. This development is described below. Doppler shift of the coherent component induced by motion of the forest biomass (primarily leaves and branches) is anticipated to be relatively small by comparison.

The effects of terminal motion and the Doppler shift induced thereby can be addressed most simply by first considering only the direct field component

$$E_z(d) = \sqrt{a}\ \left(\frac{\omega\mu_o}{4\pi}\right)\ Id\ell \cdot \sin^2\theta_d\ \frac{\exp\{-jk_o\ \sqrt{\epsilon_z}\ R_d\}}{R_d} \qquad (4\text{-}5\text{-}1)$$

As a consequence of terminal motion, $R_d$ (the distance between the transmitter and receiver) becomes time-variant. If the terminal motion is uniform (no acceleration), $R_d$ may be represented by the first two terms of its Taylor series expansion so that

$$R_d = R_d^{\circ} + R_d' t \qquad (4\text{-}5\text{-}2)$$

Over relatively short time intervals where

$$\delta t << \frac{R_d^{\circ}}{[dR_d/dt]} = \Delta t_{max} \qquad (4\text{-}5\text{-}3)$$

---

* The negative sign has been inserted for consistency with Equation (4-4-4).

Equation (4-5-1) can be well approximated by

$$E_z(d) = \sqrt{a}\ \left(\frac{\omega\mu_o}{4\pi}\right)\ Id\ell\cdot\sin^2\theta_d\cdot\frac{\exp\{\cdot j\kappa_o\sqrt{\varepsilon_z}\ (R_d^o + R_d't)\}}{R_d} \qquad (4\text{-}5\text{-}4)$$

Remembering that the instantaneous frequency of a waveform proportional to $\exp\{\phi(t)\}$ is defined as

$$f = \frac{1}{2\pi}\frac{d\phi''}{dt} \qquad (4\text{-}5\text{-}6)$$

where $\phi''$ represents the imaginary part of $\phi$, and remembering, too, that the factor $\exp\{j2\pi f_o t\}$ is assumed but suppressed in Equations (4-5-1) and (4-5-4), the instantaneous Doppler shift in frequency of the direct field component $E_z(d)$ relative to the carrier frequency $f_o$ is given by

$$\Delta f_d = -f_o Re\{\sqrt{\varepsilon_z}\}R_d'/c \qquad (4\text{-}5\text{-}6)$$

Since

$$R_d = [r^2 + a^2(z - z_o)^2]^{\frac{1}{2}} \qquad (4\text{-}5\text{-}7)$$

then

$$R_d' = \frac{\partial R_d}{\partial r}\cdot\frac{\partial r}{\partial t} + \frac{\partial R_d}{\partial(z - z_o)}\cdot\frac{\partial(z - z_o)}{\partial t} \qquad (4\text{-}5\text{-}8)$$

or

$$R_d' = V_r \sin\theta_d + V_z \cos\theta_d \qquad (4\text{-}5\text{-}9)$$

where,

$V_r$ = radial component of receiving terminal velocity relative to transmitting terminal velocity $[= \partial r/\partial t]$.

$V_z$ = vertical component of receiving terminal velocity relative to transmitting terminal velocity $[= \partial(z - z_o)/\partial t]$.

Note from Equation (4-5-6) and (4-5-9) that the Doppler shift is directly proportional to the carrier frequency $f_o$ and to that component of the differential terminal velocity directed

between the terminals. The negative sign in Equation (4-5-6) signifies that relative terminal motion tending to increase $R_d$ will shift the received frequency downward relative to the carrier.

In a similar manner, the instantaneous Doppler shift of any reflected field component $E_z(r)$ relative to the carrier frequency $f_0$ can be found to be

$$\Delta f_r = -f_0 Re\{\sqrt{\epsilon_z}\}R_r'/c \qquad (4\text{-}5\text{-}10)$$

where

$$R_r' = V_r \sin\theta_r - \hat{V}_z \cos\theta_r \qquad (4\text{-}5\text{-}11)$$

and, in addition to the previously defined variables,

$V_z$ = vertical component of receiving terminal velocity relative to the transmitting terminal image velocity [= $\partial(z+z_0)/\partial t$].

The instantaneous Doppler shift of any lateral wave field component $E_z(\ell)$ relative to the carrier frequency $f_0$ is given by

$$\Delta f_\ell = -(f_0/c)[V_r - Re\{a(\epsilon_z - 1)^{\frac{1}{2}}\}\cdot \hat{V}_z] \qquad (4\text{-}5\text{-}12)$$

The order of magnitude of the Doppler shift may be estimated by considering two vehicles moving apart along the forest floor at speeds of 100 kilometers per hour and utilizing a carrier frequency of 600 megahertz. The Doppler shift of the direct field component will dominate and will be approximately equal to

$$f_d = -(600\text{x}10^6)\ \frac{200\text{x}10^3}{3600}\ \Big/(3\text{x}10^3) \qquad (4\text{-}5\text{-}13)$$

$$= -100\ \text{Hertz}.$$

For a broadband communication system utilizing bandwidths in excess of 100MH$_z$, Doppler shifts of this magnitude can be expected to have negligible effect on performance.

[This page intentionally left blank]

## 5.0  Sensitivity of the Stratified Forest Model

Under this task, the stratified forest model has been used to investigate the sensitivity of the basic transmission loss, the (mean) forest pulse response, and the differential pulse delay to variations in the salient biophysical parameters of the forest [refer to Section 2] and to the frequency, polarization, and path length of the radio link. Three forest types have been considered to illustrate the sensitivity of the stratified forest model: an uneven-aged, trunk-dominated forest characterized by a trunk number density ($\rho_t$) of 1000 trunks per hectare and by an exponential trunk-diameter probability density function* having a mean trunk diameter of 6.35 centimeters (2.5 inches); an all-leaf forest characterized by a fractional volume (FV) of 0.1 percent [5 centimeter leaf radius, 1 millimeter leaf thickness, and 133 leaves per cubic meter]; and a mixed-forest of trunks and leaves derived from the other two. Branches have not yet been incorporated into the stratified forest model.

Although all-leaf forests will be studied systematically for later comparison with uneven-aged, trunk-dominated forests, it seems advisable to start this sensitivity analysis of the stratified forest model with the one all-leaf forest considered previously in Reference [42]. This will permit those previous results to be discussed in a manner not possible at that time and to support an evolutionary development of the formats to be used in the systematic sequel. Figures 6-2 and 6-3 of Reference [42] have been reproduced here in a newer and more complete form as Figures 5-1 and 5-2. As before, the number

---

*Although, as noted in Section 2.2.1, the upper and lower limits on the trunk diameters of real forests must, in practice, be reconciled with the semi-infinite limits available to the exponential probability density function, for present purposes the exponential probability density function was defined only over a 1 to 12 inch diameter range at discrete 1-inch intervals. The area under the density function was, of course, normalized to unity.

density of the leaves has been taken as 133* leaves per cubic meter [corresponding to a fractional volume of 0.1 percent]. The transmitter and receiver antennas have been situated 3.5+ meters below the forest top and the range has been taken as 1000 meters. The forest pulse response shown in Figure 5-2 has been determined for a 5-nanosecond rectangular pulse having an r-f carrier frequency of 600 MHz.

The forest transfer functions shown in Figure 5-1 have been normalized to 0 dB for the direct wave at 600 MHz. The direct wave is reduced by interference with the reflected wave at all frequencies, with nearly complete cancellation occurring near 400 MHz; their resultant is less than the lateral wave at all frequencies. Thus, the forest transfer function of the total wave follows roughly that of the lateral wave with interference lobes arising as a consequence of further interference between the lateral wave and the direct-plus-reflected wave. The forest pulse response of Figure 5-2 shows the same partial cancellation. The lateral wave arrives earlier than the direct wave because it travels faster in free space above the forest than the other waves travel through the forest. The corresponding pulse envelopes are shown in Figure 5-3.

The subsequent presentation of the sensitivity analysis involves two significant changes in format as well as variations in forest type and path geometry. The first is the inclusion of basic transmission loss. This is discussed in Section 4-4 and in Section 5-1 below. The second is the insertion of an ideal (rectangular) bandpass filter centered on the carrier frequency of 600 MHz to improve the simulation of the radio equipment. For an ideal rectangular pulse with its sinc-shaped

---

*All curves presented in Reference [42] citing a leaf number density of 200 leaves per cubic meter were, in fact, based upon a leaf number density of (2/3)(200) = 133 leaves per cubic meter.

+The radio path geometry is slightly different from that actually used in Reference [42]. There, the transmitter and receiver antennas were situated 3 and 4 meters, respectively, below the forest top (not 4 and 6 meters, respectively, as stated); here, both transmitter and receiver antennas are situated 3.5 meters below the forest top.
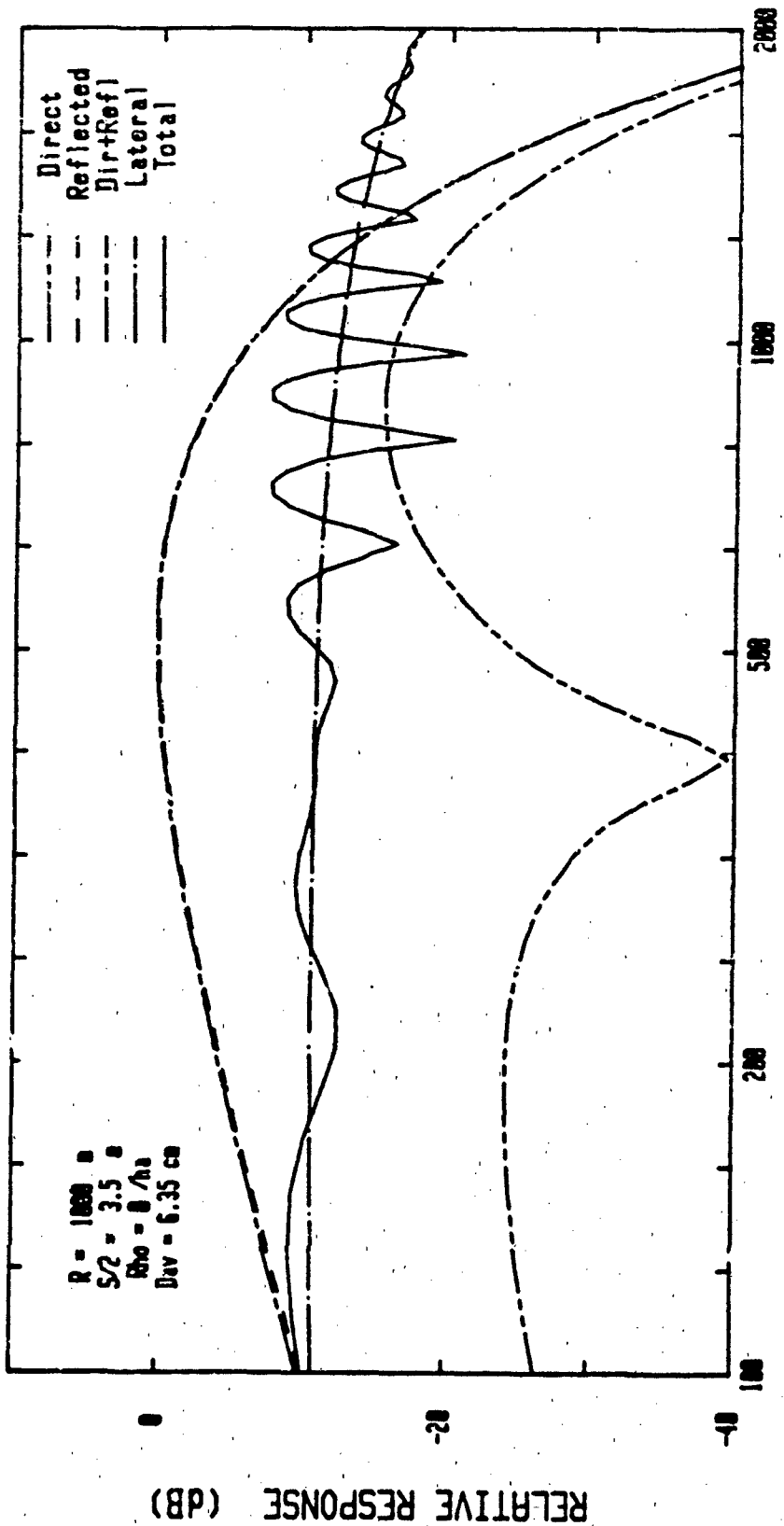
RELATIVE RESPONSE (dB)

FREQUENCY IN MHZ

Direct
Reflected
Dir+Refl
Lateral
Total

R = 1000 m
S/2 = 3.5 m
Rho = 8/h₁
Dav = 6.35 cm

Figure 5-1: Transfer Function for Leaf Forest (R = 1000m, S/2 = 3.5m)

DIRECT +1

0

−1

REFLECTED +1

0

−1

DIR+REFL +.25

0

−.25

LATERAL +.25

0

−.25

TOTAL +.25

0

−.25

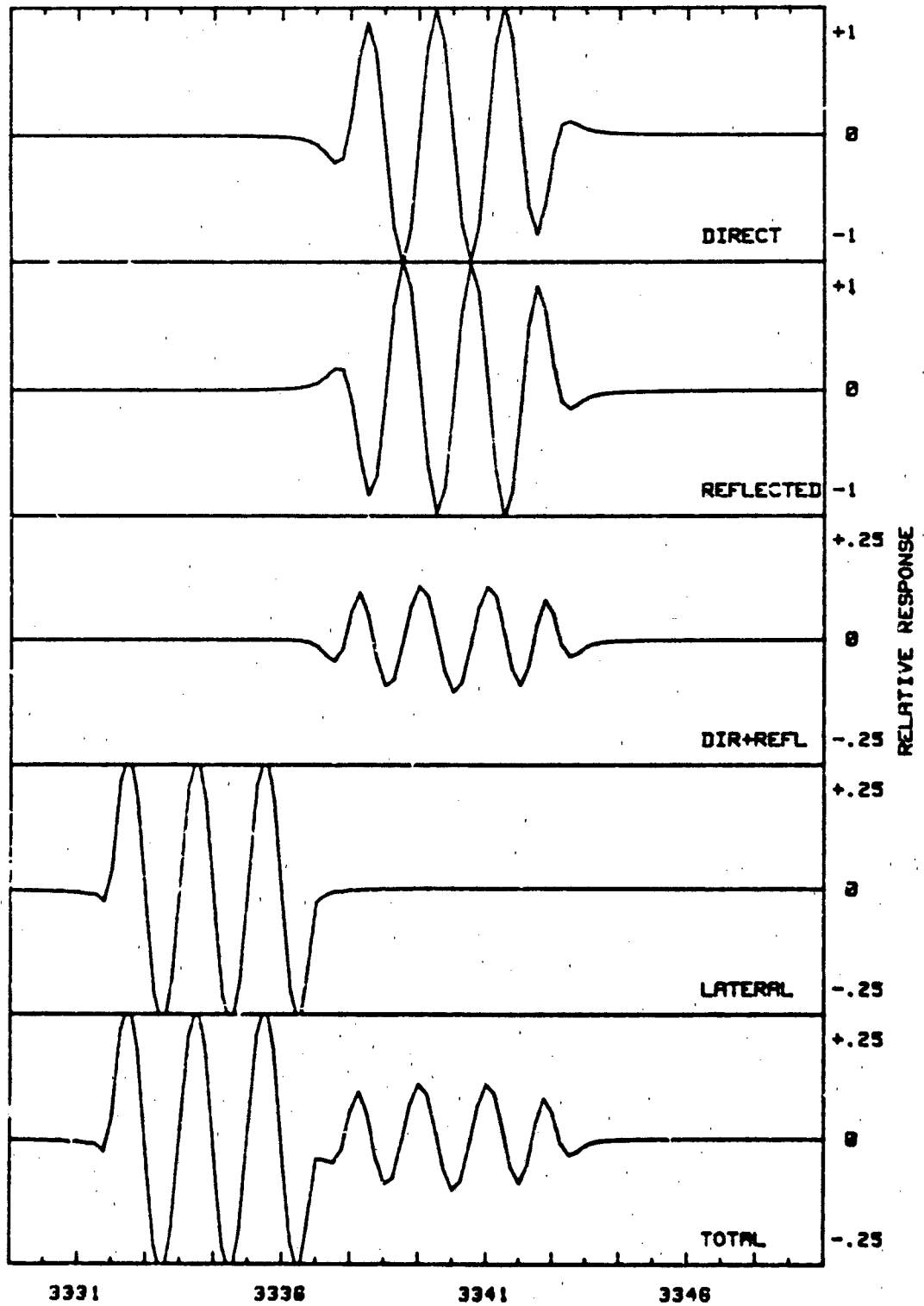RELATIVE RESPONSE

3331    3336    3341    3346

Figure 5-2:   Pulse Response for Leaf Forest
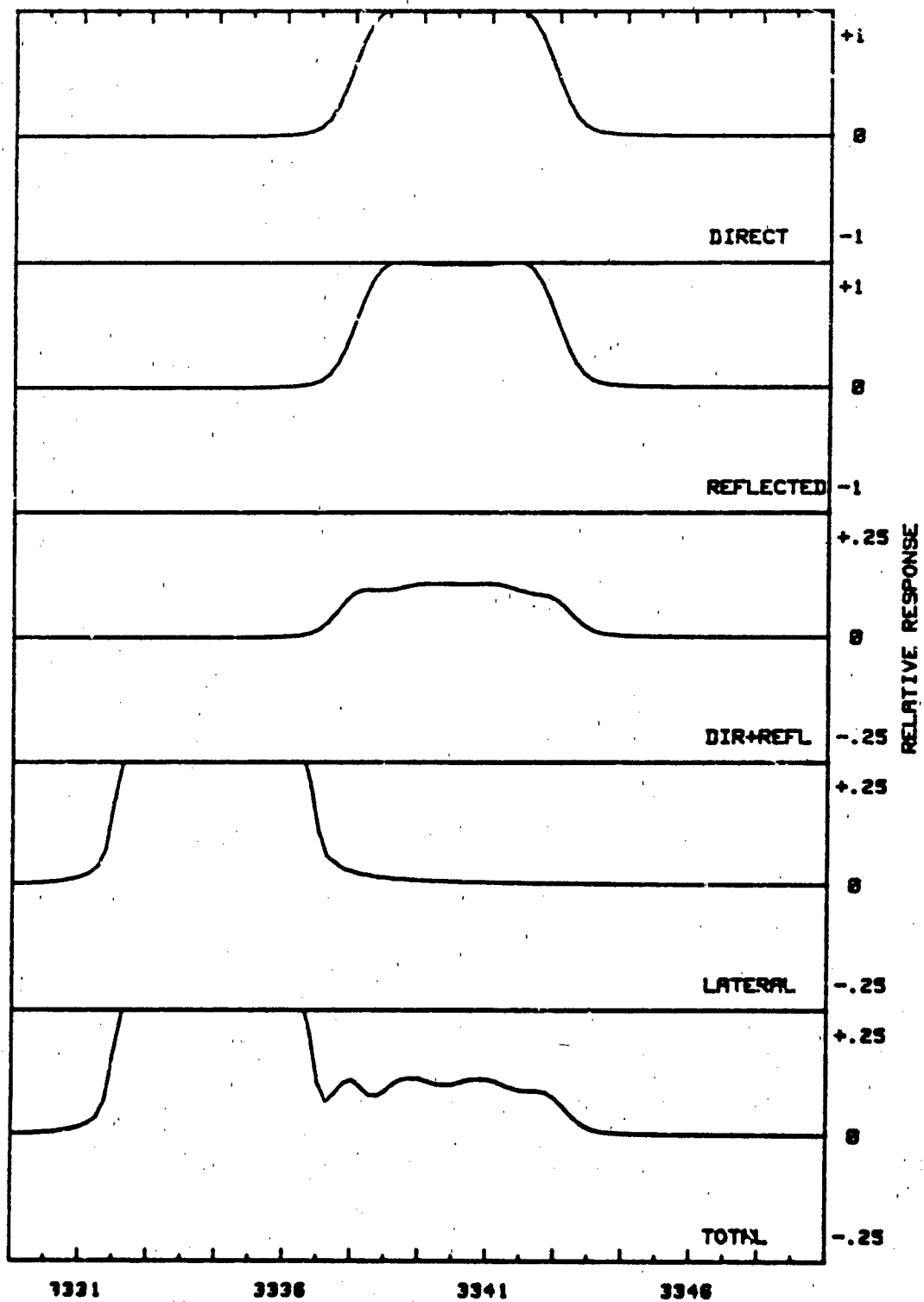(R = 1000m, S/2 = 3.5m)

Figure 5-3:  Pulse Envelope for Leaf Forest
(R = 1000m,  S/2 = 3.5m)

amplitude spectrum, the high- and low-frequency spectral skirts led to intolerable pulse distortion. Therefore, in the sequel only the central lobe of the pulse spectrum is passed by/ideal filter. The corresponding transmitted pulse shape, no longer rectangular, is shown in Figure 5-4.

## 5.1 Basic Transmission Loss

The basic transmission loss experienced within an all-leaf forest characterized by a fractional volume (FV) of 0.1 percent is presented in Figures 5-5 and 5A-1 to 5A-8. The vertically-polarized transmitter and receiver antennas are situated 2.5 meters below the forest top and separated, successively, by 200, 500, and 1000 meters.* The basic transmission losses associated with the direct and reflected waves are virtually indistinguishable and for frequencies less than about 500 MHz increase about 6 dB/octave of frequency. The direct and reflected waves destructively interfere so that their resultant is nearly 20 decibels below either of them at R = 1000 m. Particularly strong destructive interference is apparent near 500 MHz. The basic transmission loss of the total at 1000 m is clearly dominated by that of the lateral wave which decreases about 12 dB/octave of frequency. Note that, in general, a leaf-dominated forest behaves as a low-pass filter for vertically-polarized radiowaves.

The losses for the same ranges with S/2 = 5 m are shown in Figures 5A-4 to 5A-6, and for S/2 = 10 m in Figures 5A-7 to 5A-9. The chief points to notice are the absence of the lateral waves as the angle of incidence exceeds the critical angle (see Section 4.2.6).

The basic transmission loss for the trunk-dominated forest is shown in Figures 5A-10 to 5A-18. As for the leaf-dominated forest, the basic transmission losses associated with the direct and reflected waves are virtually indistinguishable and they destructively interfere so that their resultant lies 10-15 dB below them. The basic transmission loss of the total is clearly dominated by that of the lateral wave (they are indistinguishable) which increases approximately 6 dB/octave of frequency.

_____

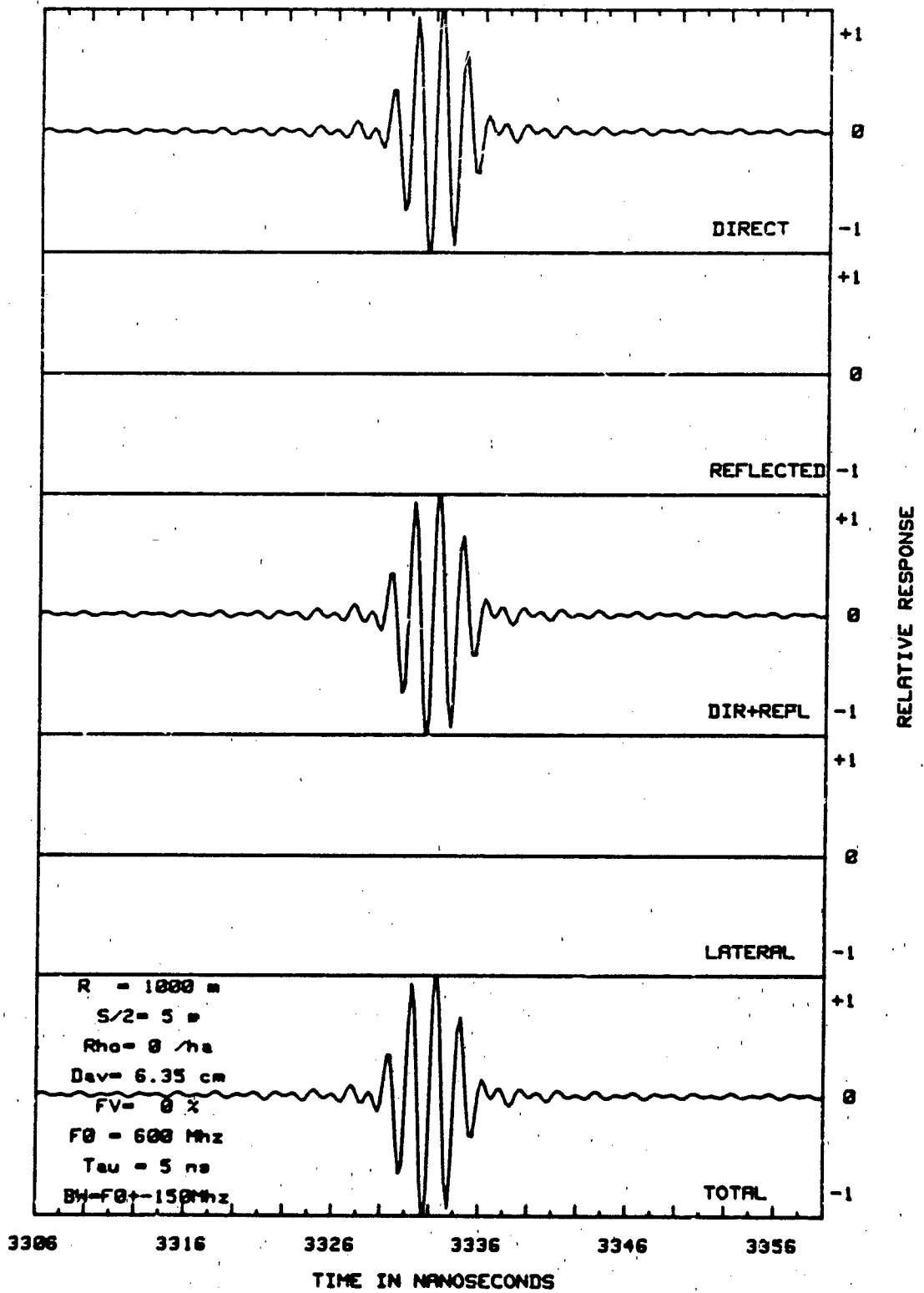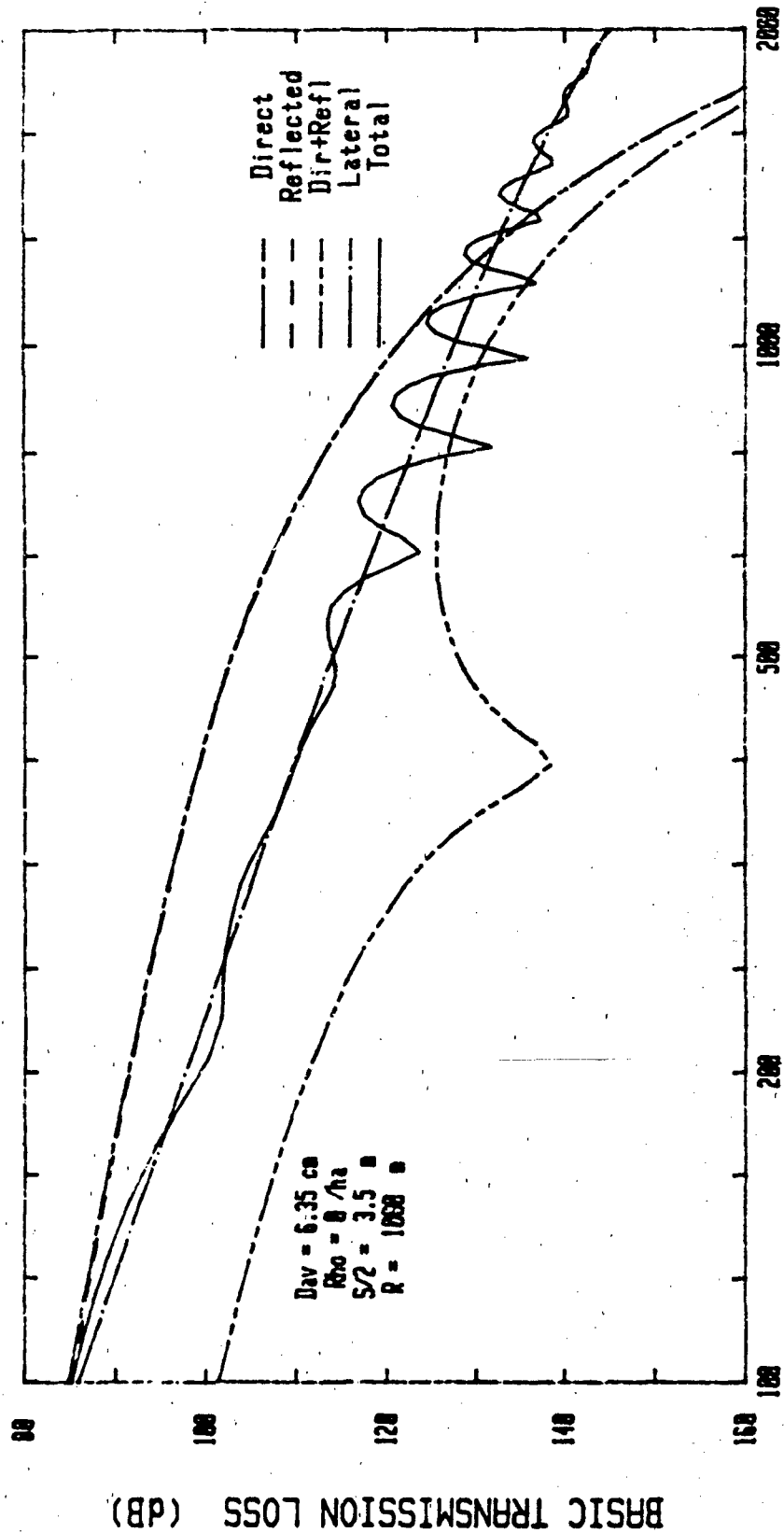* except for Figure 5-5, for which S/2 = 3.5m and R = 1000m as in Figure 5-1.

Figure 5-4:  Filtered Pulse Shape

Figure 5-5:  Basic Transmission Loss (Leaf Forest)
(R = 1000m, S/2 = 3.5m)

## 5.2  Forest Pulse Response

The mean forest pulse response has been determined for a wideband digital radio system having a 600 MHz carrier frequency and a 300 MHz r-f bandwidth as above. The pseudo-noise chips are derived by passing 5-nanosecond rectangular pulses through an ideal bandpass filter. The forest pulse response for the leaf-dominated forest is shown in Figures 5B-1 to 5B-3 for S/2 = 2.5 m, 5B-4 to 5B-6 for S/2 = 5 m and 5B-7 to 5B-9 for S/2 = 10 m. The forest pulse responses associated with radiowave propagation along the direct path are shown uppermost in these figures. The propagation delay along the direct path $\tau_d$, observed to be about 3340 nanoseconds for R = 1000 m, can also be estimated from the approximation

$$\tau_d \approx \frac{R_d \sqrt{\epsilon_z'}}{c} \qquad (5-2-1)$$

where $\epsilon_z'$ is the real part of the longitudinal component of the effective dyadic susceptibility [refer to Figure 3-1(b)]. For this example, $R_d = 1000$ m, $\epsilon_z' = 1.004265$, and c = 3x10⁸ m/sec. The companion pulse response for the reflected pulse also shown in Figure 5B-3 exhibits essentially the same delay. The rather shallow glancing angle at the air-forest interface associated with this particular geometric configuration (about 0.14 degrees) ensures a relatively strong reflected pulse (at 600 MHz the reflection coefficient is 0.9942), although essentially in antiphase with the direct pulse. As shown in the figure, the direct and reflected pulses virtually cancel each other and, as a consequence, the contribution of the lateral wave dominates the resultant. The propagation delay associated with the lateral wave is essentially that of free space.

The forest pulse responses for the trunk-dominated forest are shown in Figures 5B-10 to 5B-18. In Figure 5B-12, the pulse response associated with the direct wave arrives prior to the pulse response associated with the lateral wave. This is a consequence of the fact that the longitudinal component of the effective dyadic susceptibility is negative. Equation (5-2-1) can still

be used to estimate the arrival time of the direct pulse, although for this example, because $\varepsilon'_z = 0.99903$ the velocity of pulse propagation appears to exceed that of light in vacuum. A more exact expression for pulse delay time and the Kramers-König relation can be employed to refute this contention in general; the apparent paradox that Figure 5B-12 supports this contention can be resolved by noting that the strictly band-limited transmitted pulse cannot be localized in time. The small, rapid oscillations may be the so-called Sommerfeld precursor [36]. In any case, the high specific attenuation associated with the propagation of a vertically-polarized wave through a trunk-dominated forest [refer to Figure 3-2(a)] severely attenuates all but the lateral wave which, as is apparent from Figure 5B-12 dominates the resultant pulse response.

## ANNEX 5A: Basic Transmission Loss

|  | S/2 = | 2.5 | 5.0 | 10.0 |
|---|---|---|---|---|
| **Leaf Forest:** | **Range (m)** | **Figure Numbers** | | |
|  | 200 | 5A-1 | 5A-4 | 5A-7 |
|  | 500 | 5A-2 | 5A-5 | 5A-8 |
|  | 1000 | 5A-3 | 5A-6 | 5A-9 |

|  | S/2 = | 2.5 | 5.0 | 10.0 |
|---|---|---|---|---|
| **Inhomogeneous Trunk Forest:** | **Range (m)** | **Figure Numbers** | | |
|  | 200 | 5A-10 | 5A-13 | 5A-16 |
|  | 500 | 5A-11 | 5A-14 | 5A-17 |
|  | 1000 | 5A-12 | 5A-14 | 5A-18 |

## ANNEX 5B: Forest Pulse Response

|  | S/2 = | 2.5 | 5.0 | 10.0 |
|---|---|---|---|---|
| **Leaf Forest:** | **Range (m)** | **Figure Numbers** | | |
|  | 200 | 5B-1 | 5B-4 | 5B-7 |
|  | 500 | 5B-2 | 5B-5 | 5B-8 |
|  | 1000 | 5B-3 | 5B-6 | 5B-9 |

|  | S/2 = | 2.5 | 5.0 | 10.0 |
|---|---|---|---|---|
| **Inhomogeneous Trunk Forest:** | **Range (m)** | **Figure Numbers** | | |
|  | 200 | 5B-10 | 5B-13 | 5B-16 |
|  | 500 | 5B-11 | 5B-14 | 5B-17 |
|  | 1000 | 5B-12 | 5B-15 | 5B-18 |

Figure 5A-1: Basic Transmission Loss (Leaf Forest)

5A-1

FREQUENCY IN MHZ

BASIC TRANSMISSION LOSS (dB)

Figure 5A-2:  Basic Transmission Loss (Leaf Forest)

FV = .1%
Dav = 6.35 cm
Rho = 8 /ha
S/2 = 2.5 m
R = 500 m

Direct
Reflected
Dir+Refl
Lateral
Total

FREQUENCY IN MHZ

BASIC TRANSMISSION LOSS (dB)

Direct
Reflected
Dir+Refl
Lateral
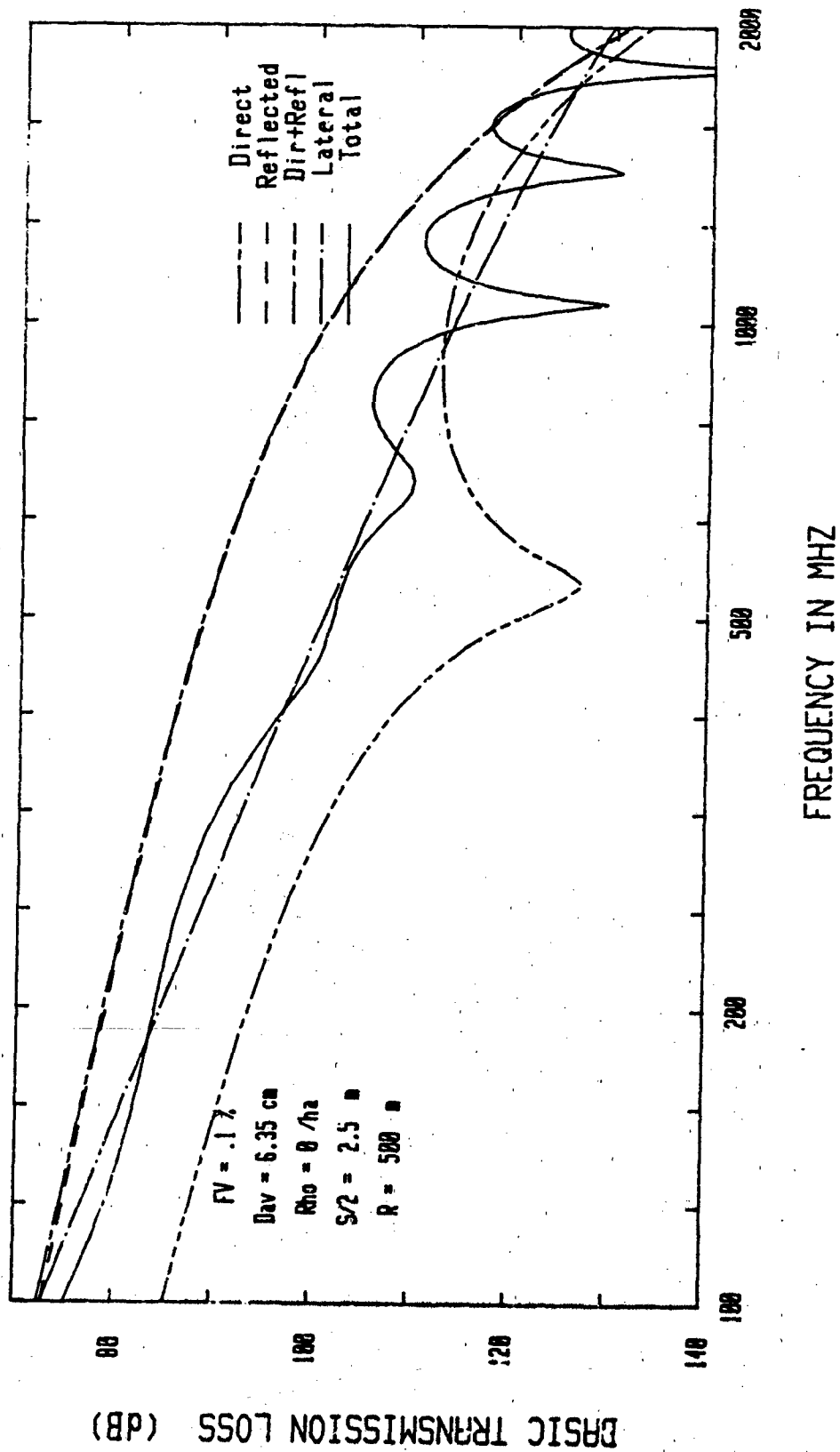Total

FV = .1 %
Dav = 6.35 cm
Rho = 8 /ha
S/2 = 2.5 m
R = 1000 m

Figure 5A-3:  Basic Transmission Loss (Leaf Forest)

Figure 5A-4: Basic Transmission Loss (Leaf Forest)
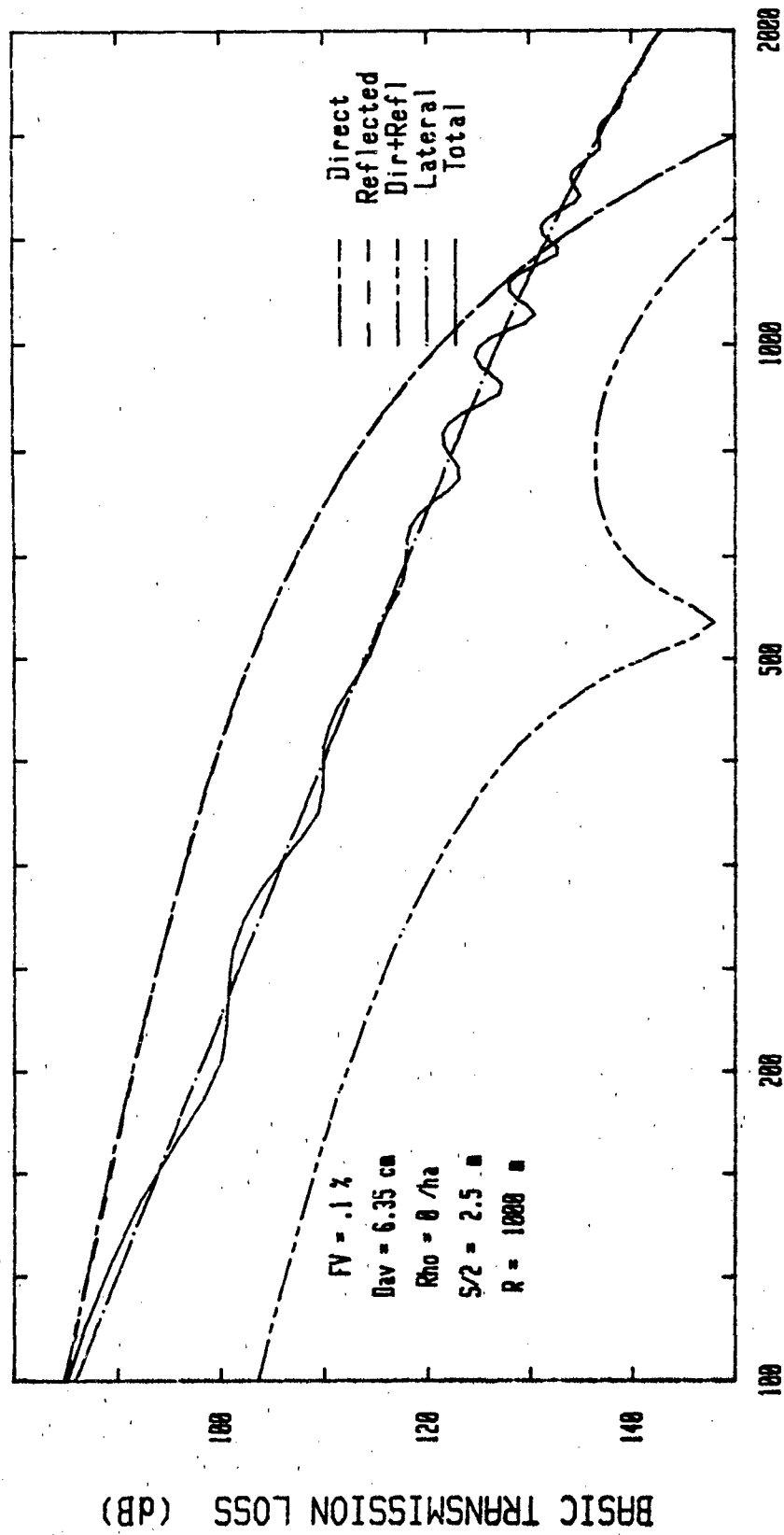
5A-4

Figure 5A-5: Basic Transmission Loss (Leaf Forest)

FREQUENCY IN MHZ

BASIC TRANSMISSION LOSS (dB)

Figure 5A-6: Basic Transmission Loss (Leaf Forest)

FREQUENCY IN MHZ

BASIC TRANSMISSION LOSS (dB)

Figure 5A-7: Basic Transmission Loss (Leaf Forest)
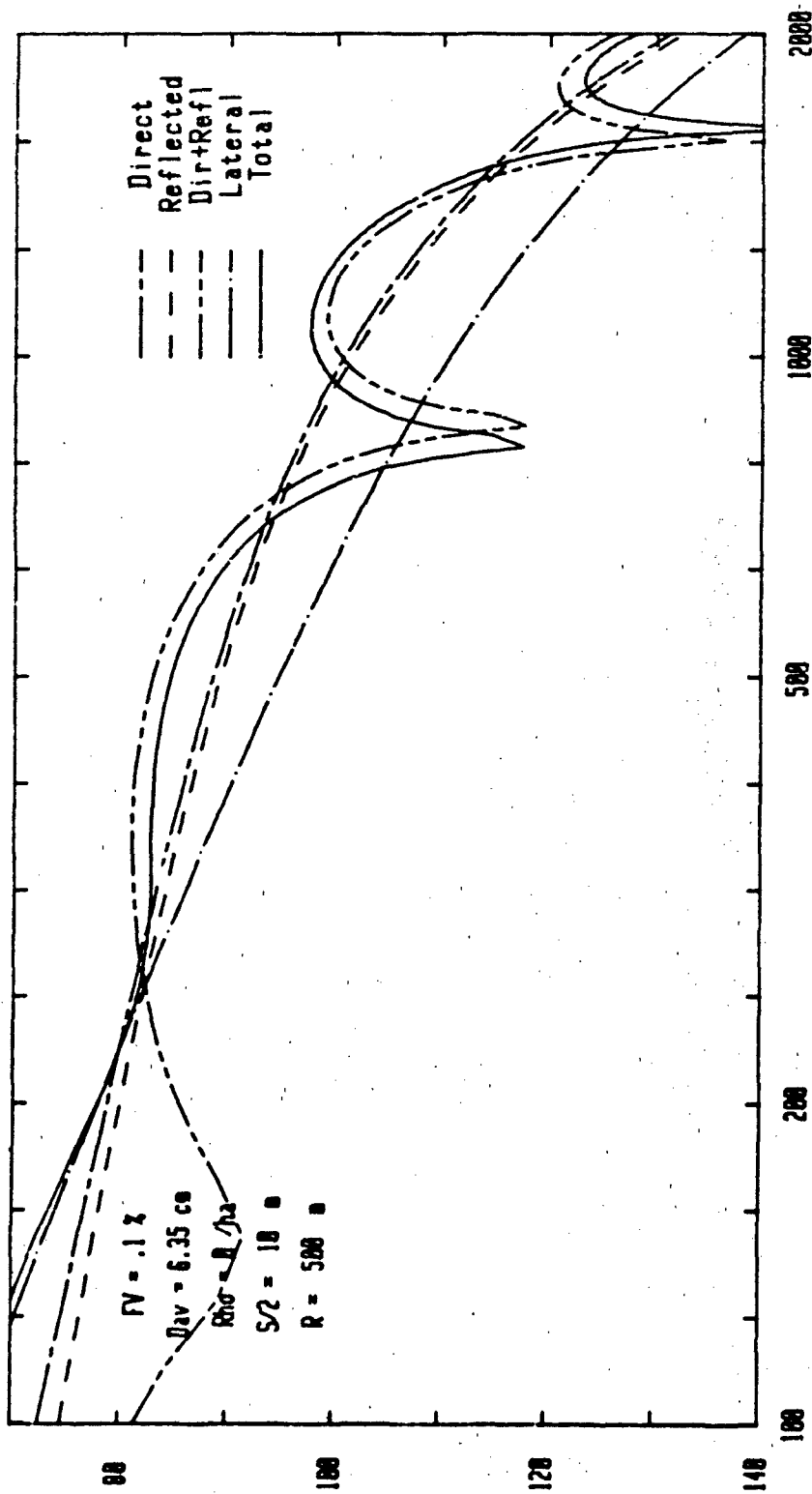
Figure 5A-8: Basic Transmission Loss (Leaf Forest)

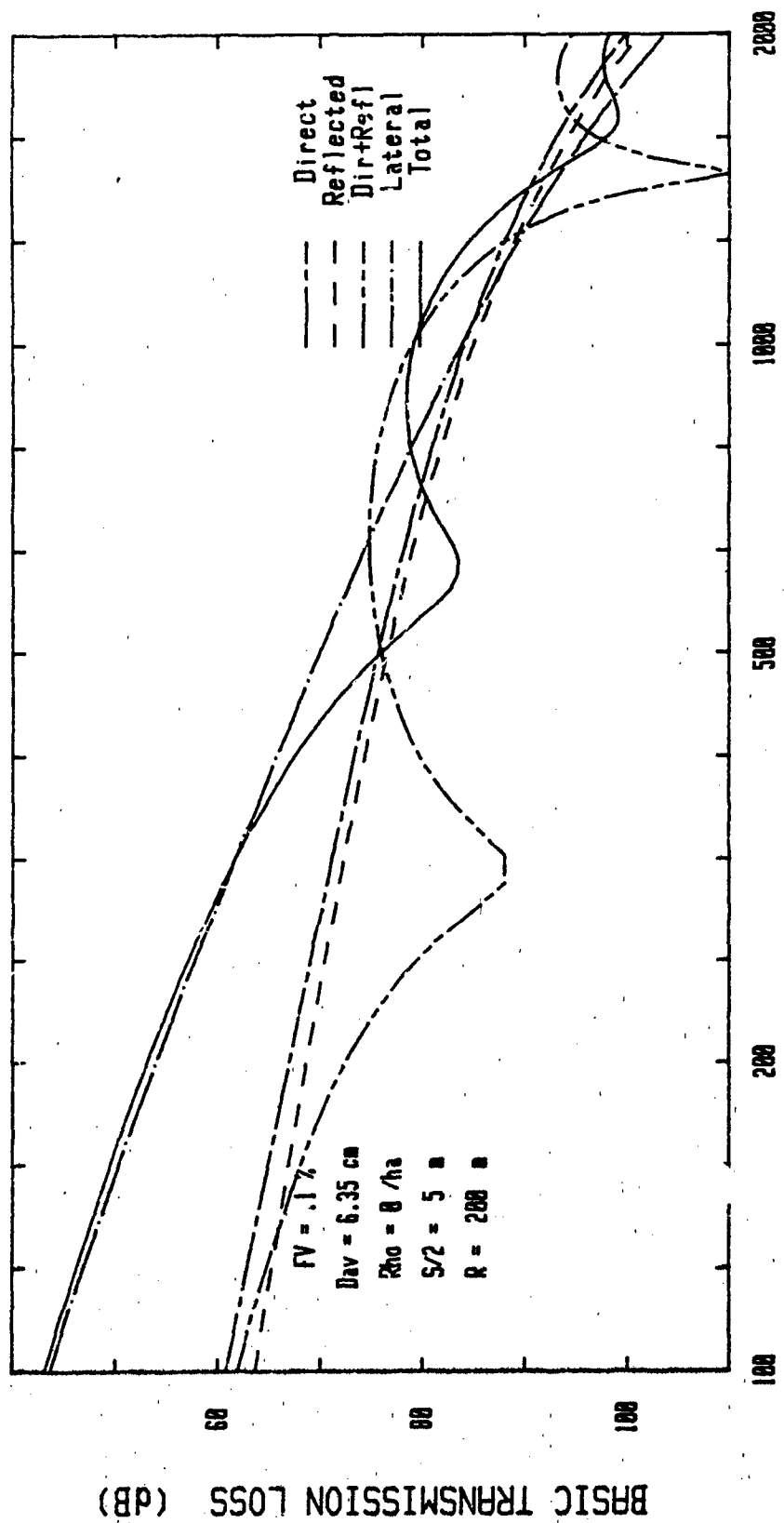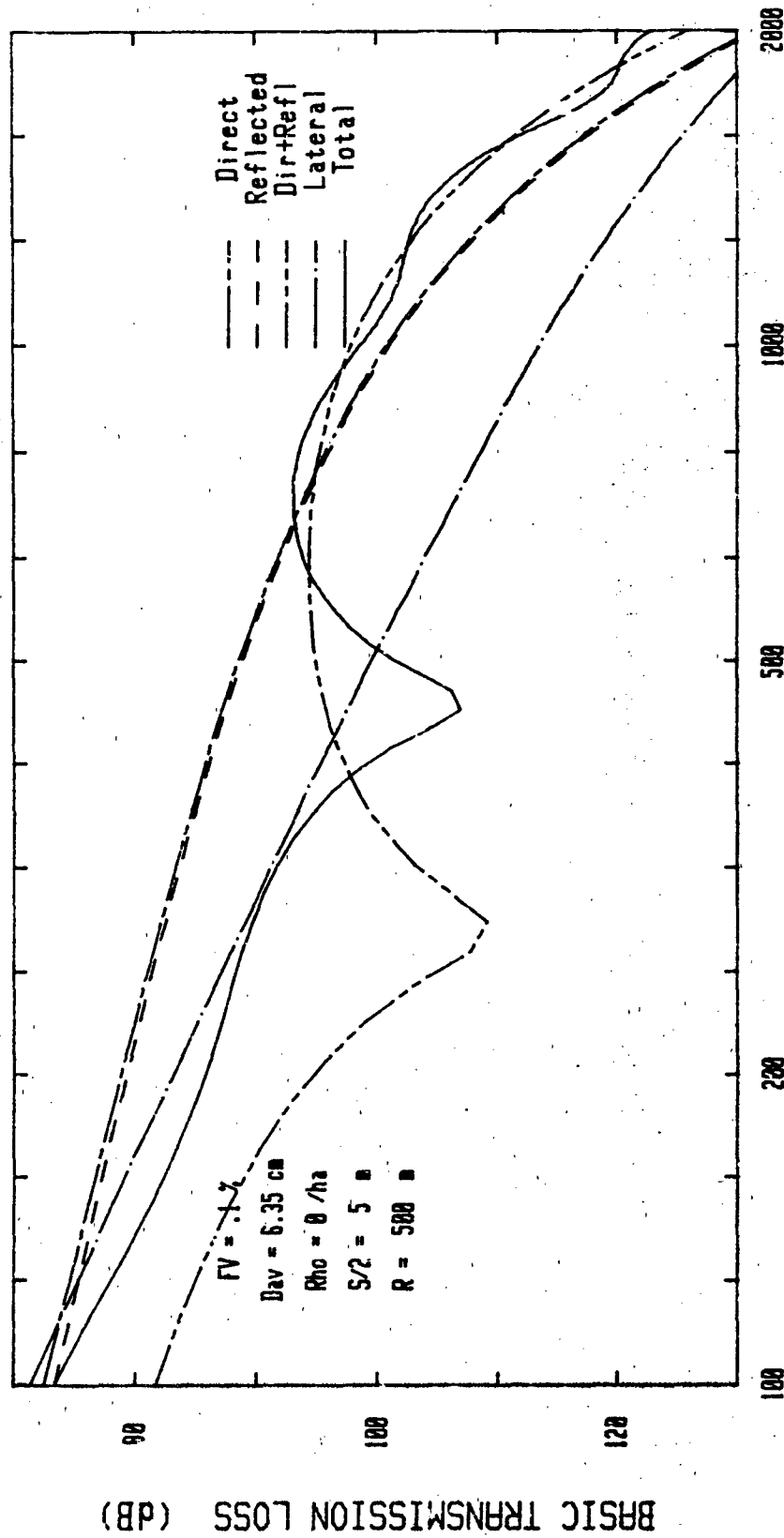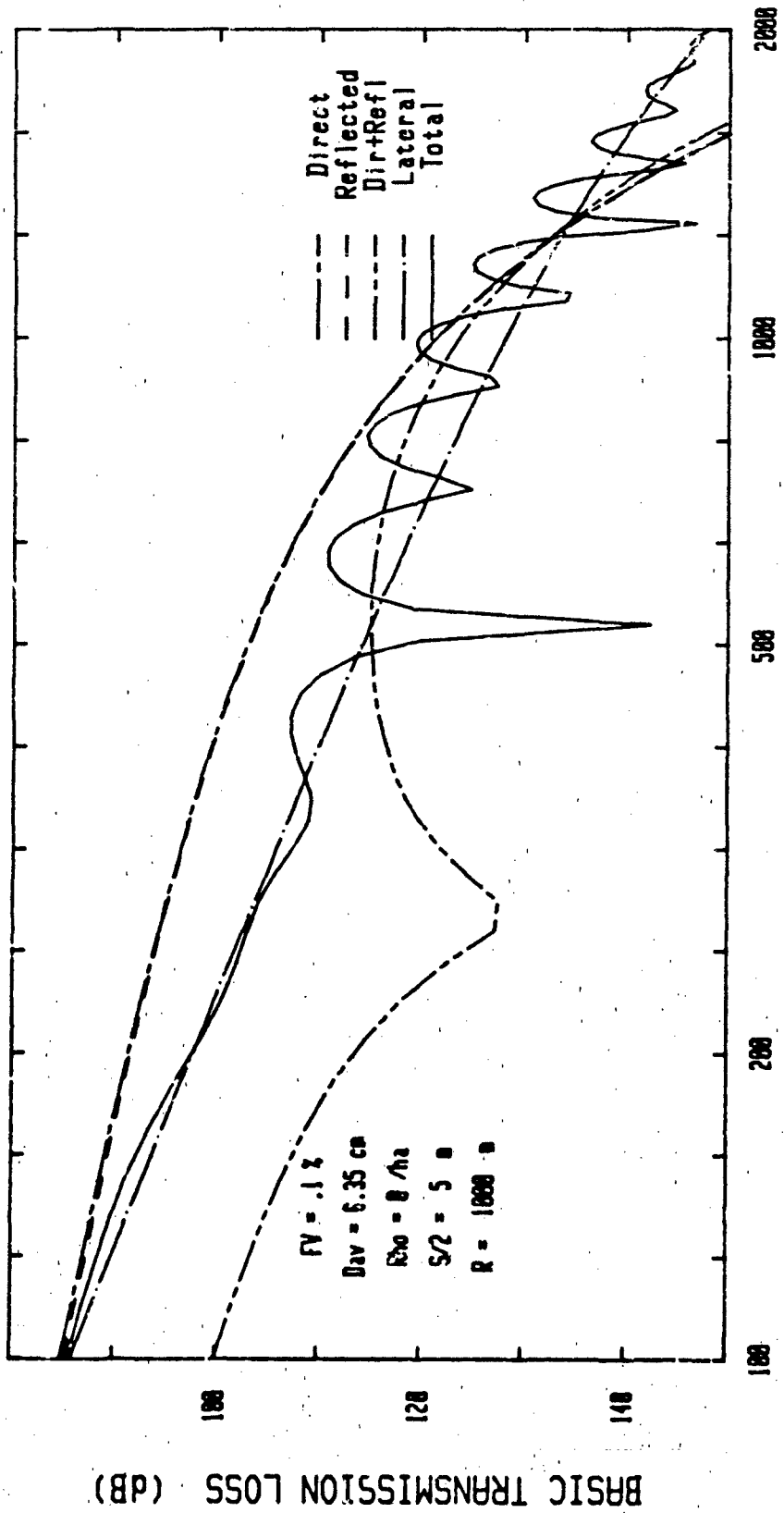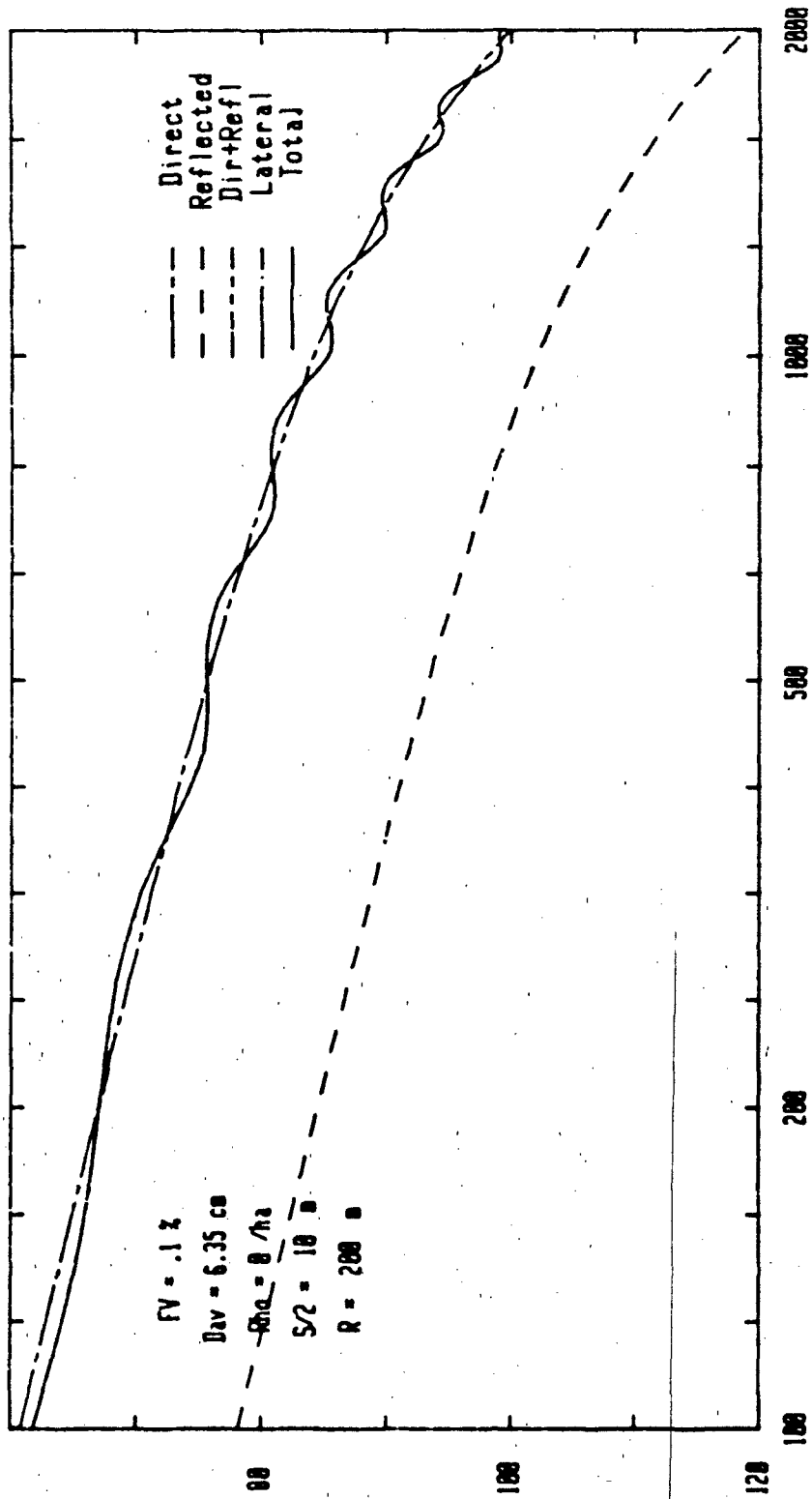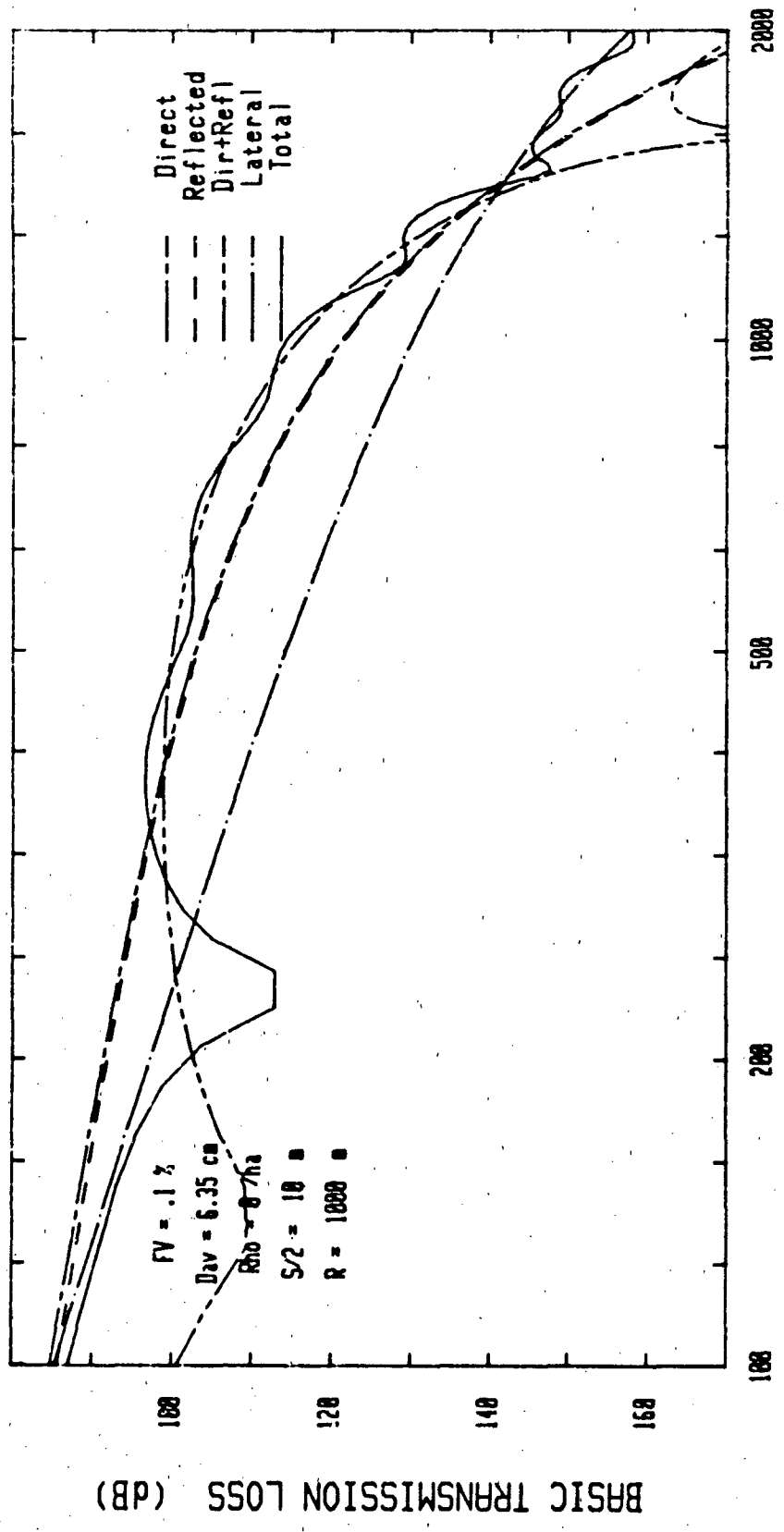Figure 5A-9:  Basic Transmission Loss (Leaf Forest)
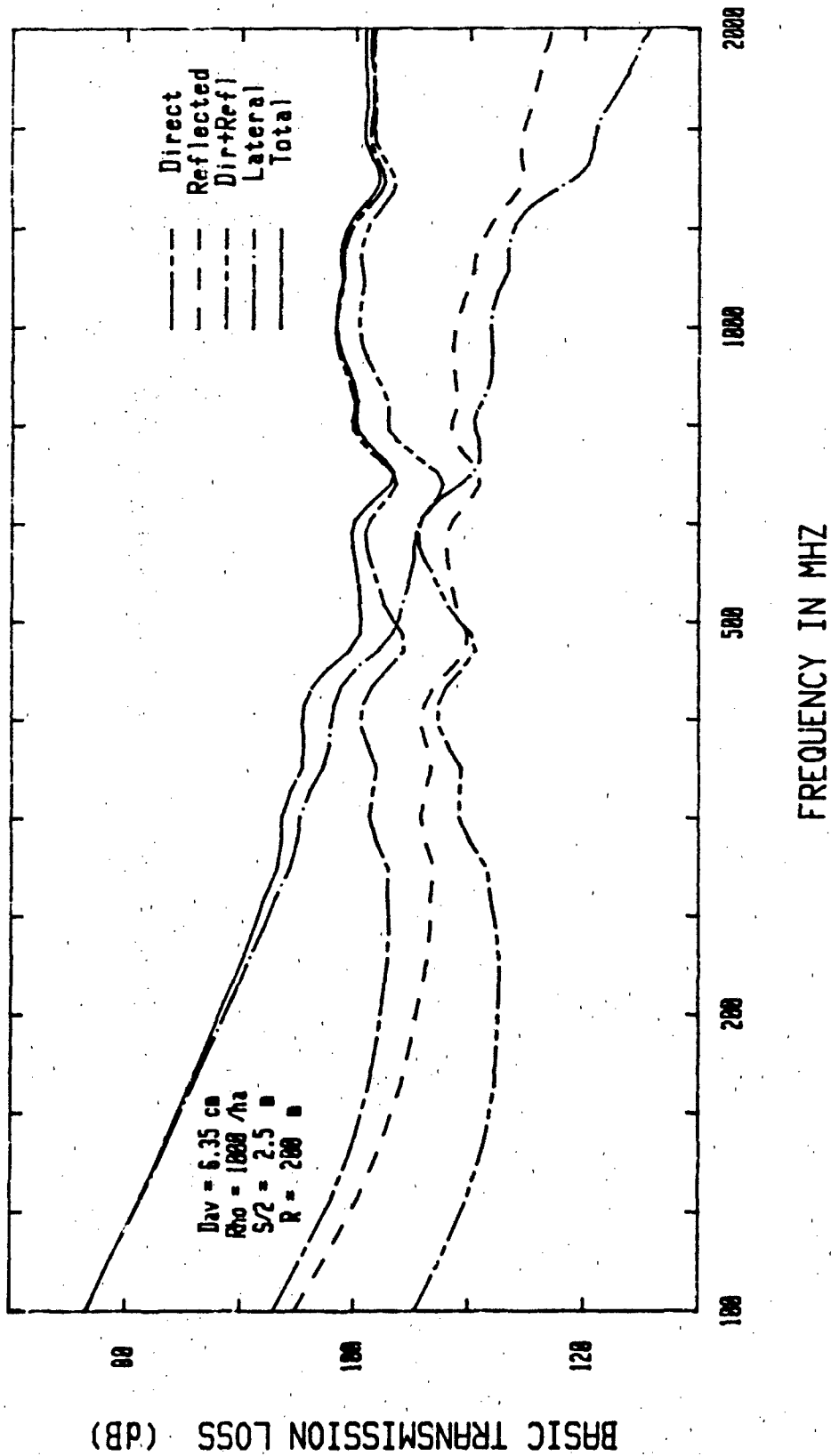
Figure 5A-10:  Basic Transmission Loss (Inhomogeneous Trunk Forest)

FREQUENCY IN MHZ

BASIC TRANSMISSION LOSS (dB)

Legend:
— Direct
— Reflected
— Dir+Refl
— Lateral
— Total

Dav = 6.35 cm
Rho = 1000 /h₄
S/2 = 2.5 m
R = 500 m
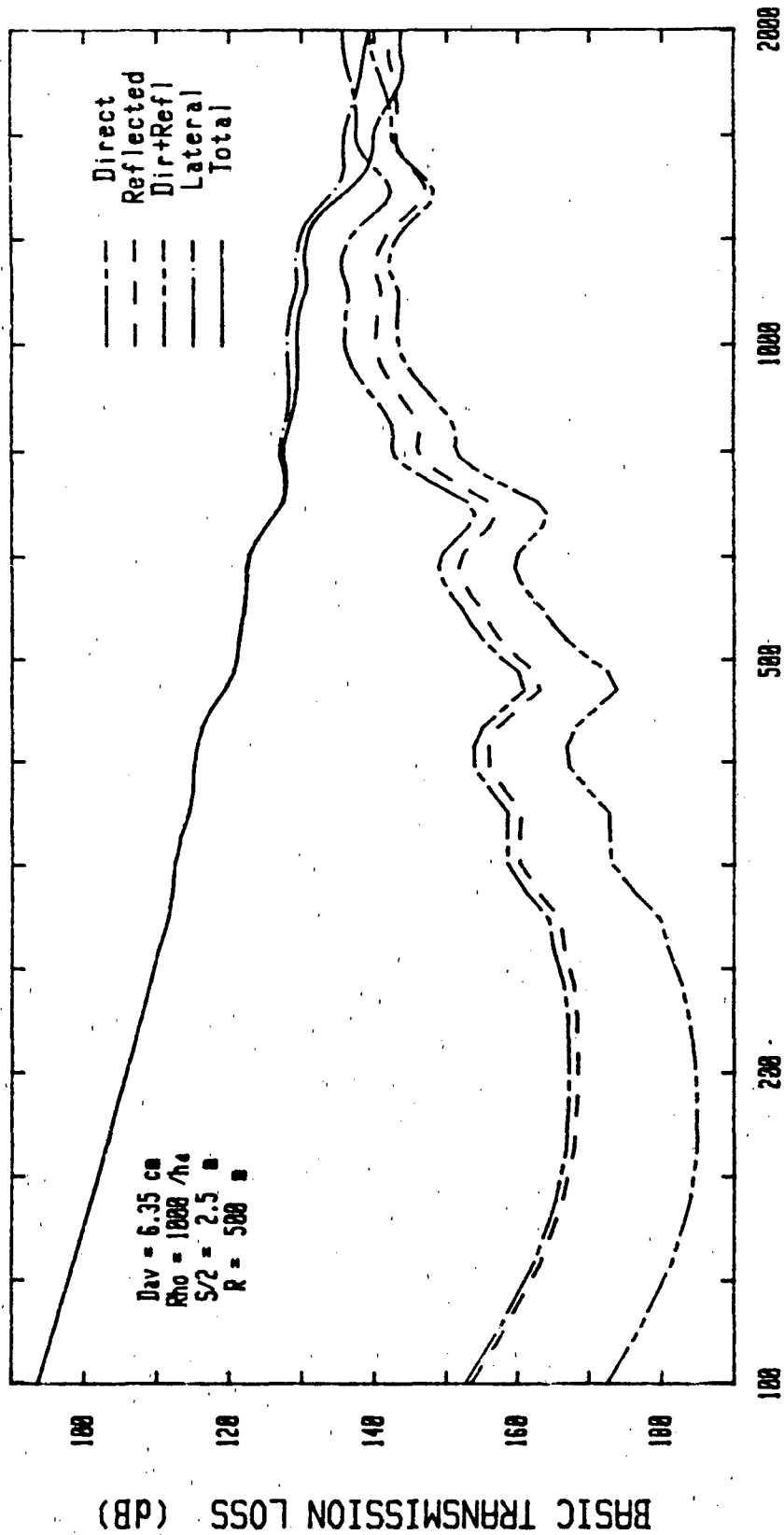
Figure 5A-11: Basic Transmission Loss (Inhomogeneous Trunk Forest)

BASIC TRANSMISSION LOSS (dB)

300 280 260 240 220 200 160 140 120

100    200    500    1000    2000

FREQUENCY IN MHZ

Direct
Reflected
Dir+Refl
Lateral
Total

Dav = 6.35 cm
Rho = 1000 /ha
S/2 = 2.5 m
R = 1000 m
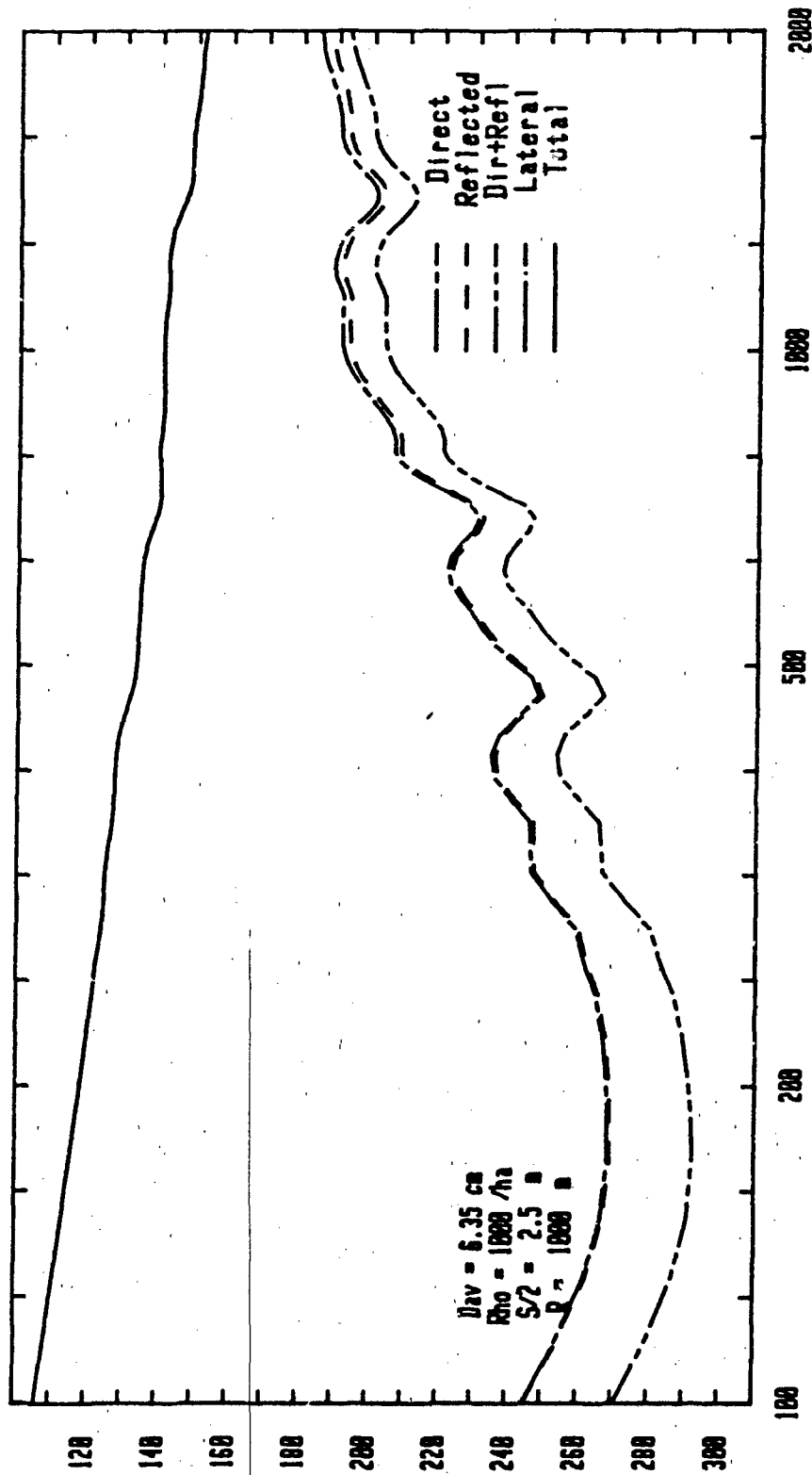
Figure 5A-12:  Basic Transmission Loss (Inhomogeneous Trunk Forest)

FREQUENCY IN MHZ

BASIC TRANSMISSION LOSS (dB)

Dav = 6.35 cm
Rho = 1000 /ha
S/2 = 5 m
R = 200 m

Direct
Reflected
Dir+Refl
Lateral
Total

Figure 5A-13: Basic Transmission Loss (Inhomogeneous Trunk Forest)

FREQUENCY IN MHZ
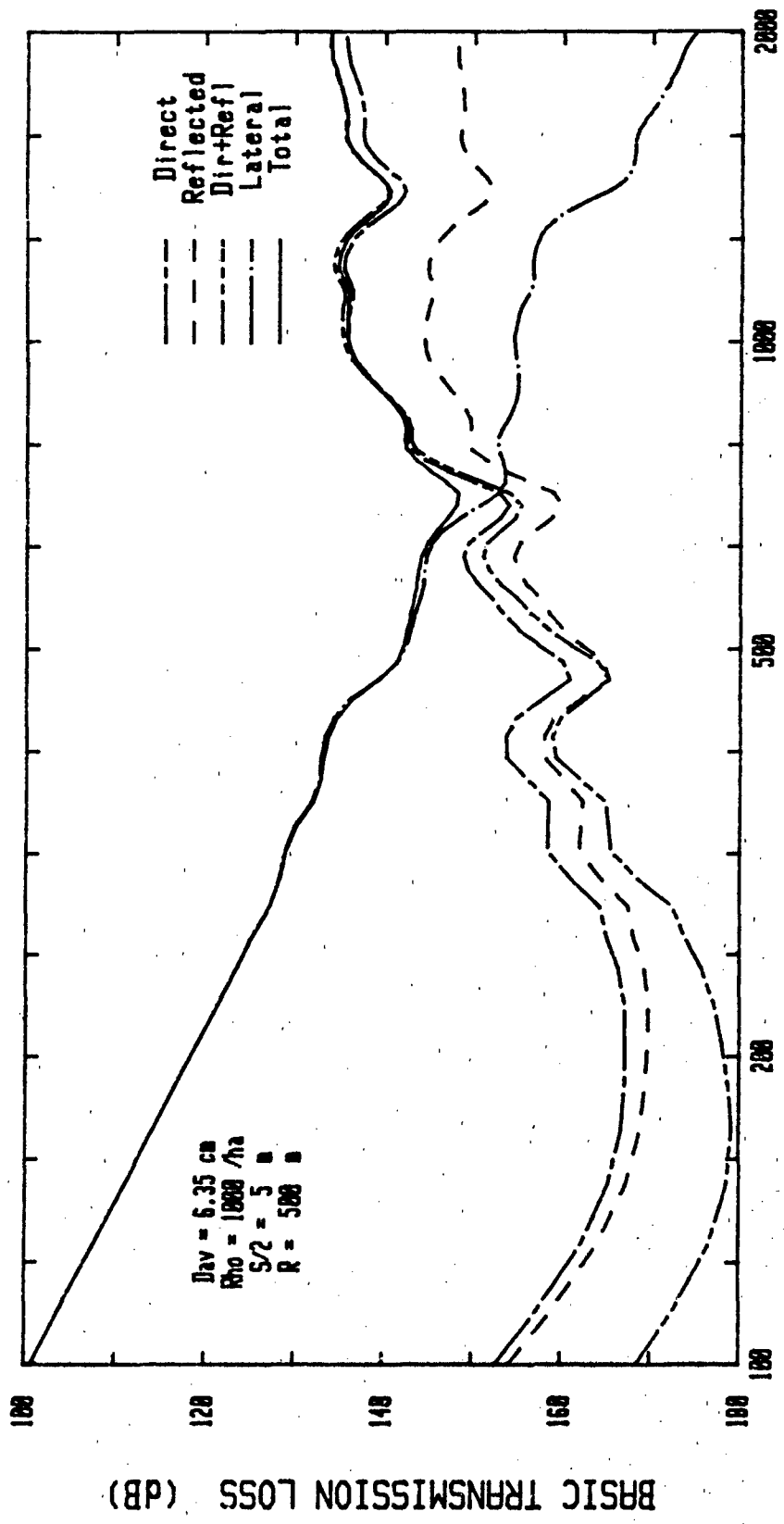
Figure 5A-14: Basic Transmission Loss (Inhomogeneous Trunk Forest)
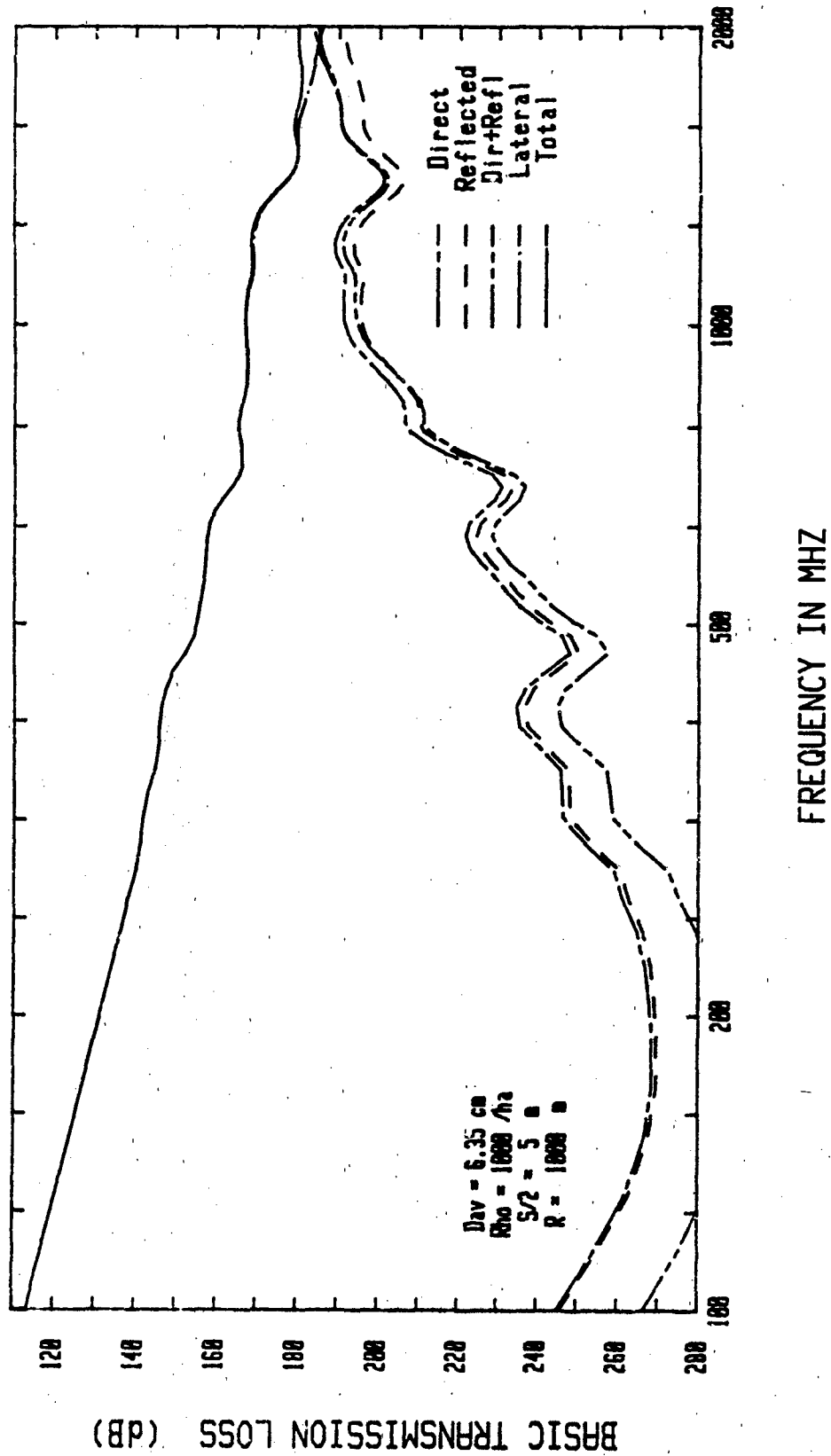
Figure 5A-15: Basic Transmission Loss (Inhomogeneous Trunk Forest)
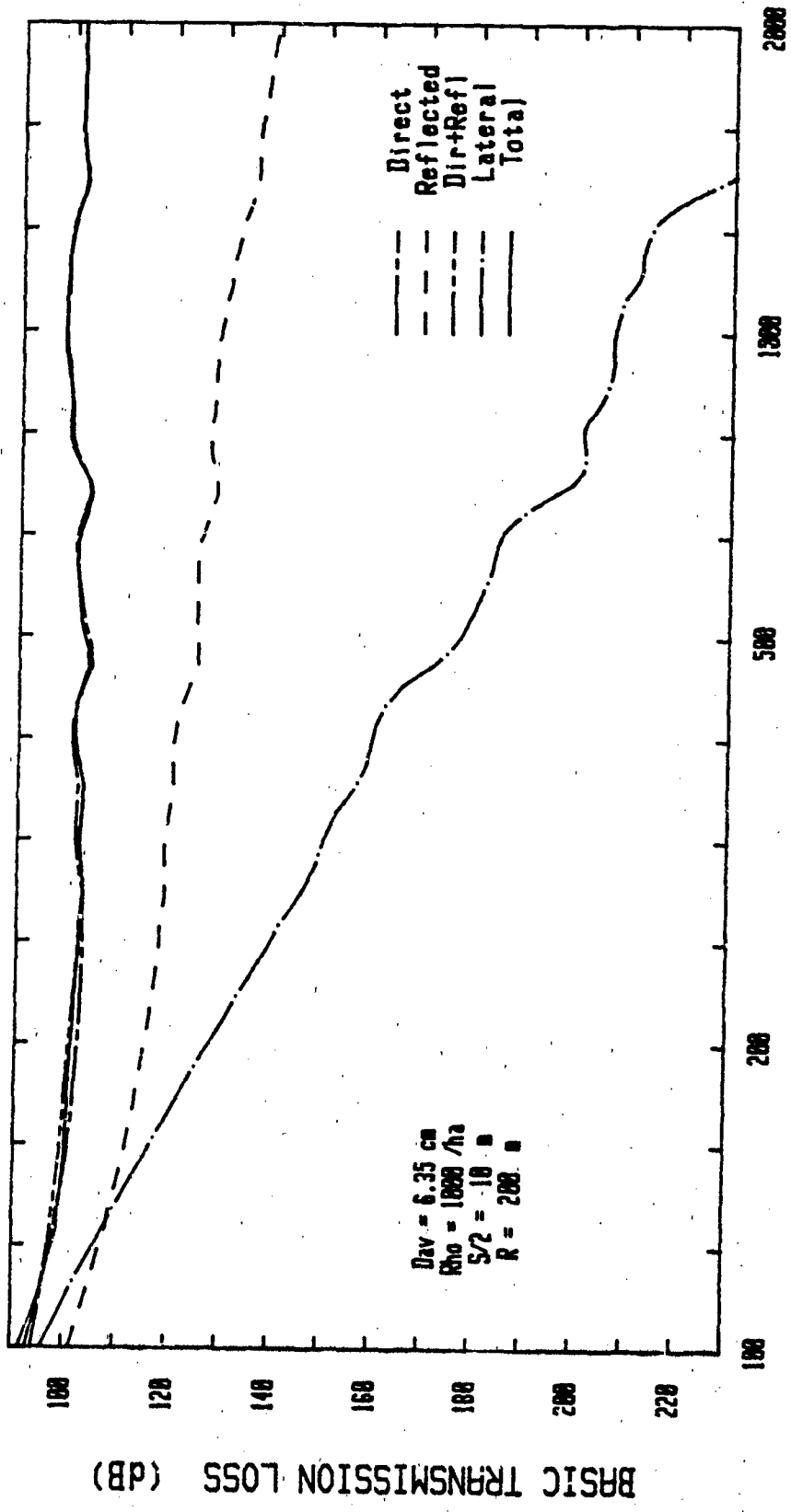
Figure 5A-16:   Basic Transmission Loss (Inhomogeneous Trunk Forest)

BASIC TRANSMISSION LOSS (dB)

FREQUENCY IN MHZ

Direct
Reflected
Dir+Refl
Lateral
Total

Dav = 6.35 cr
Rho = 1000 /he
S/2 = 10 m
R = 500 m
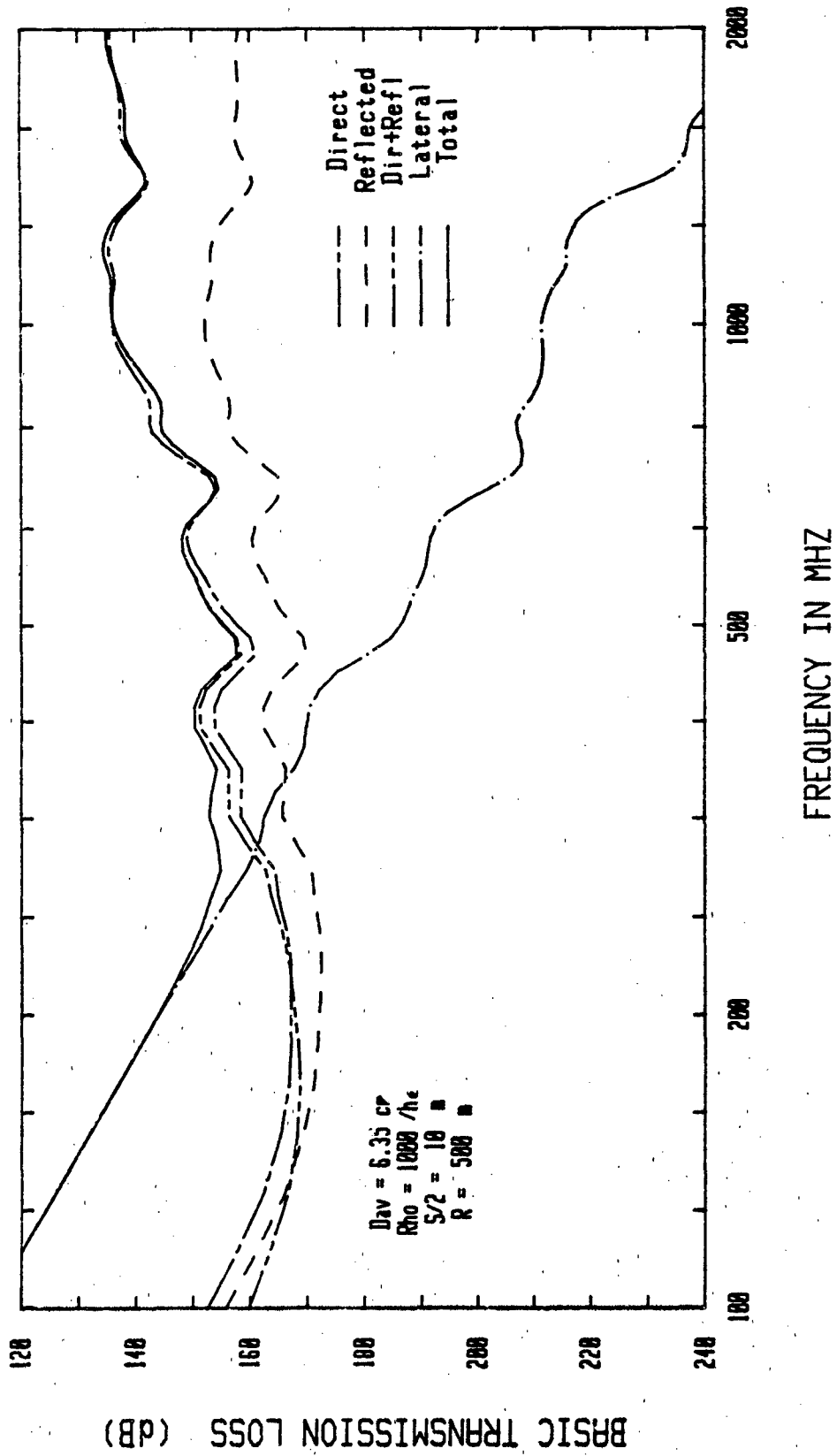
Figure 5A-17: Basic Transmission Loss (Inhomogeneous Trunk Forest)

FREQUENCY IN MHZ

BASIC TRANSMISSION LOSS (dB)

Direct
Reflected
Dir+Refl
Lateral
Total

Dav = 6.35 cm
Rho = 1000 /ha
S/2 = 10 m
R = 1000 m

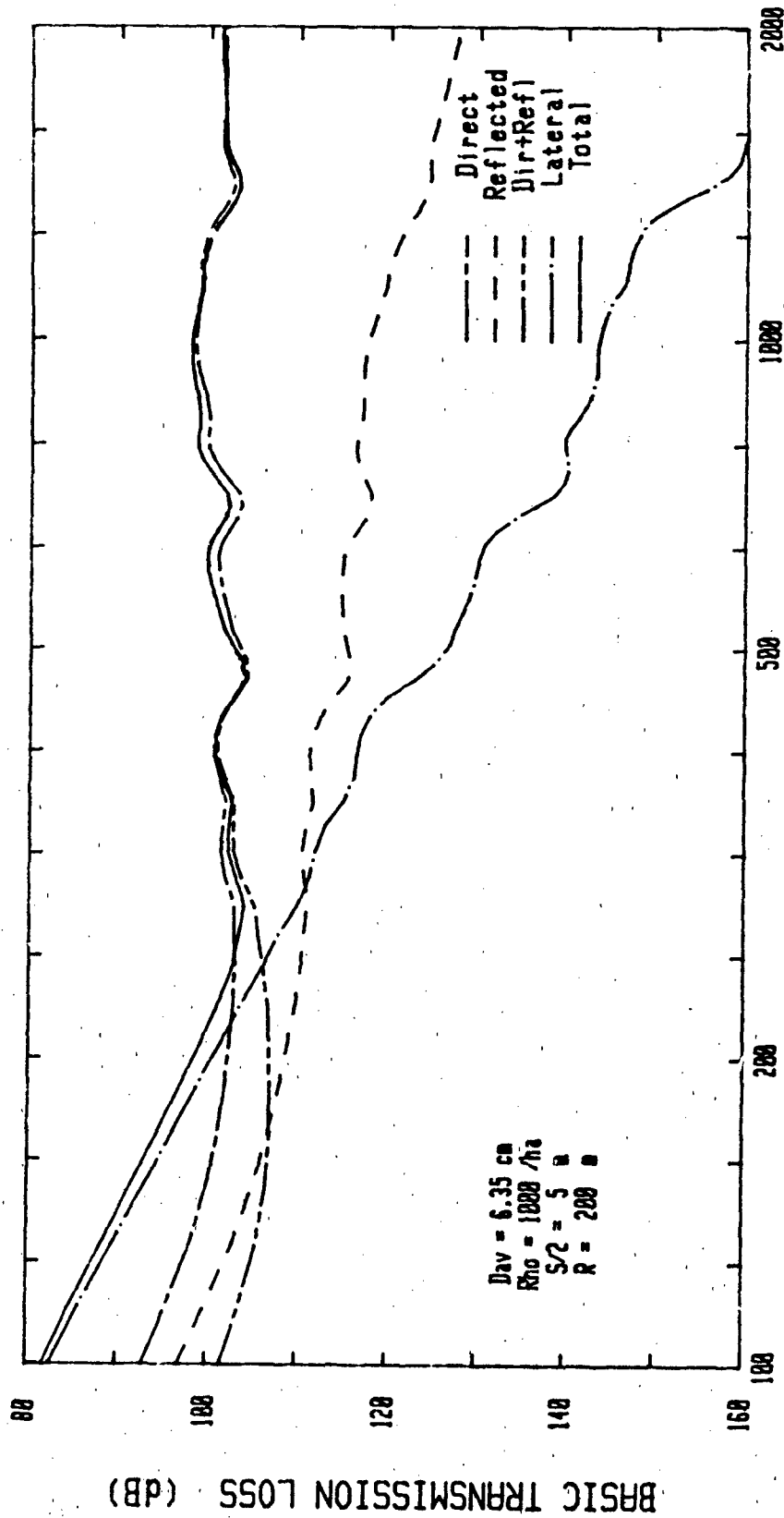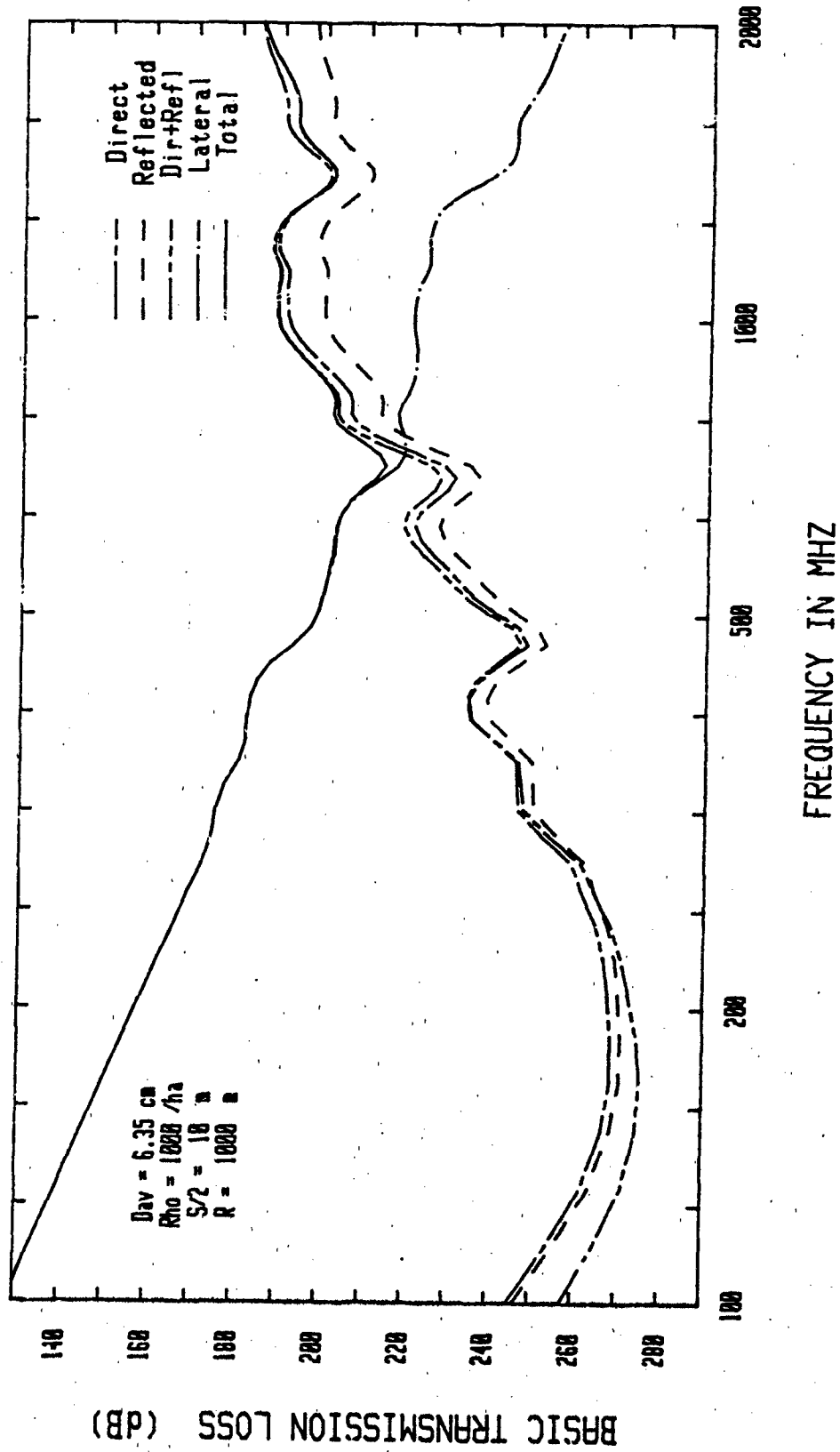Figure 5A-18: Basic Transmission Loss (Inhomogeneous Trunk Forest)

Figure 5B-1:  Pulse Response (Leaf Forest)

The figure contains the following labels and annotations:

Vertical axis label: RELATIVE RESPONSE

Panels (top to bottom) with +1, 0, -1 scale markings:
- DIRECT
- REFLECTED
- DIR+REFL
- LATERAL
- TOTAL

Parameter box:
R   = 200 m
S/2 = 2.5 m
Rho = 0 /ha
Dav = 6.35 cm
Fv  = .1 %
F0  = 600 Mhz
Tau = 5 ns
BW=F0+-150Mhz

Horizontal axis: TIME IN NANOSECONDS
Axis values: 640, 650, 660, 670, 680, 690

5B-1

RELATIVE RESPONSE

| | |
|---|---|
| +1 | |
| 0 | |
| DIRECT | -1 |
| +1 | |
| 0 | |
| REFLECTED | -1 |
| +.1 | |
| 0 | |
| DIR+REFL | -.1 |
| +.2 | |
| 0 | |
| LATERAL | -.2 |

R = 500 m
S/2 = 2.5 m
Rho = 0 /ha
Dav = 6.35 cm
FV = .1 %
F0 = 600 Mhz
Tau = 5 ns
BW=F0+150Mhz

+.2

0

TOTAL

-.2

1653   1663   1673   1683   1693   1703

TIME IN NANOSECONDS

Figure 5B-2:  Pulse Response (Leaf Forest)

5B-2

| | |
|---|---|
| | DIRECT |
| | REFLECTED |
| | DIR+REFL |
| | LATERAL |

R   = 1000 m
S/2= 2.5 m
Rho= 0 /ha
Dav= 6.35 cm
FV=   .1 %
F0 = 600 Mhz
Tau = 5 ns
BW=F0+-150Mhz

TOTAL

RELATIVE RESPONSE

+1   0   -1

3306    3316    3326    3336    3346    3356

TIME IN NANOSECONDS

Figure 5B-3:   Pulse Response (Leaf Forest)

5B-3
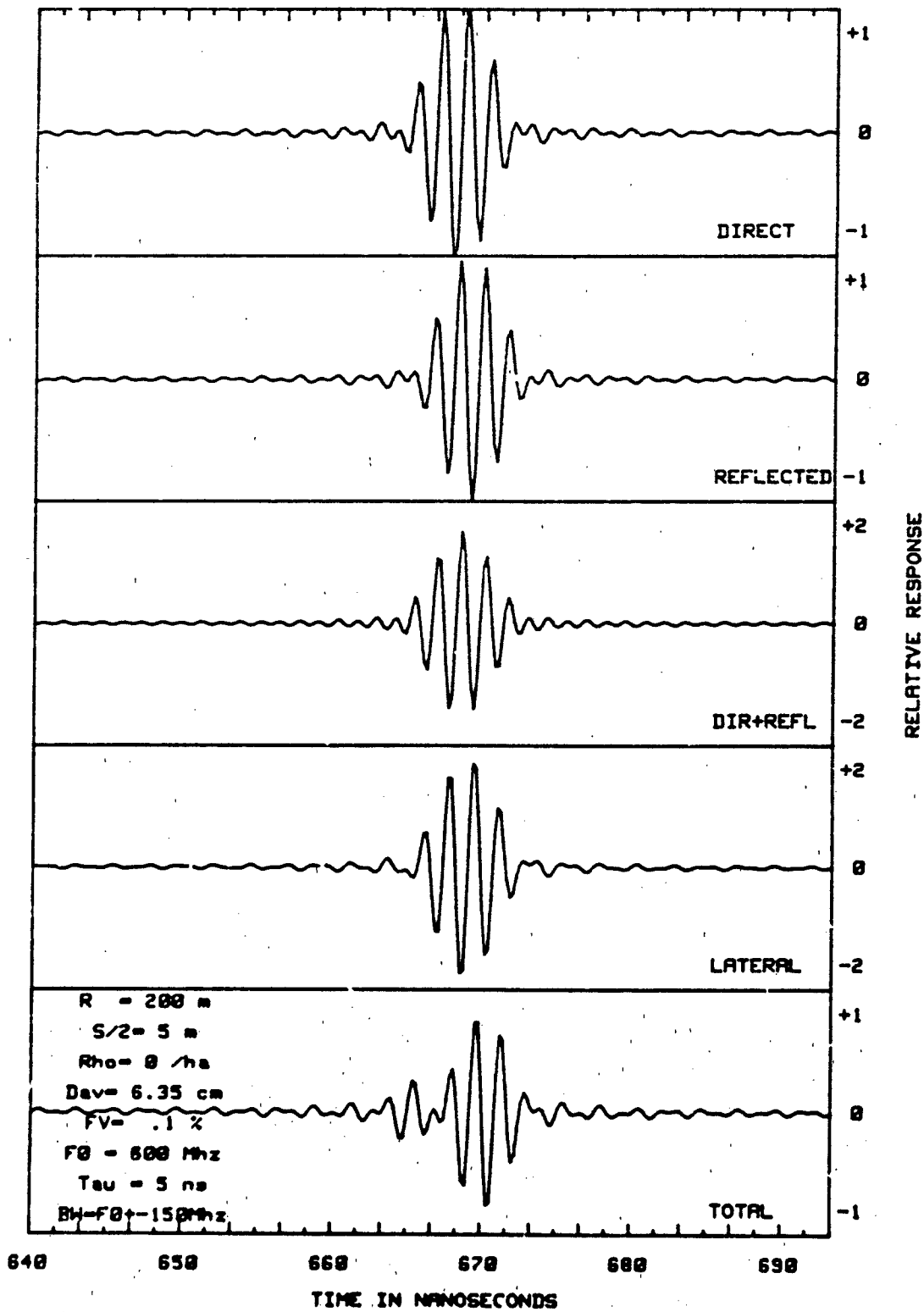
Figure 5B-4: Pulse Response (Leaf Forest)

+1

0

DIRECT      -1

+1

0

REFLECTED   -1

+1

0

DIR+REFL    -1

+1

0

LATERAL     -1

R   = 500 m
S/2= 5 m
Rho= 0 /ha
Dav= 6.35 cm
FV=  .  %
F0 = 600 Mhz
Tau = 5 ns
BW=F0+-150Mhz

+1

0

TOTAL       -1

RELATIVE RESPONSE

1653      1663      1673      1683      1693      1703

TIME IN NANOSECONDS
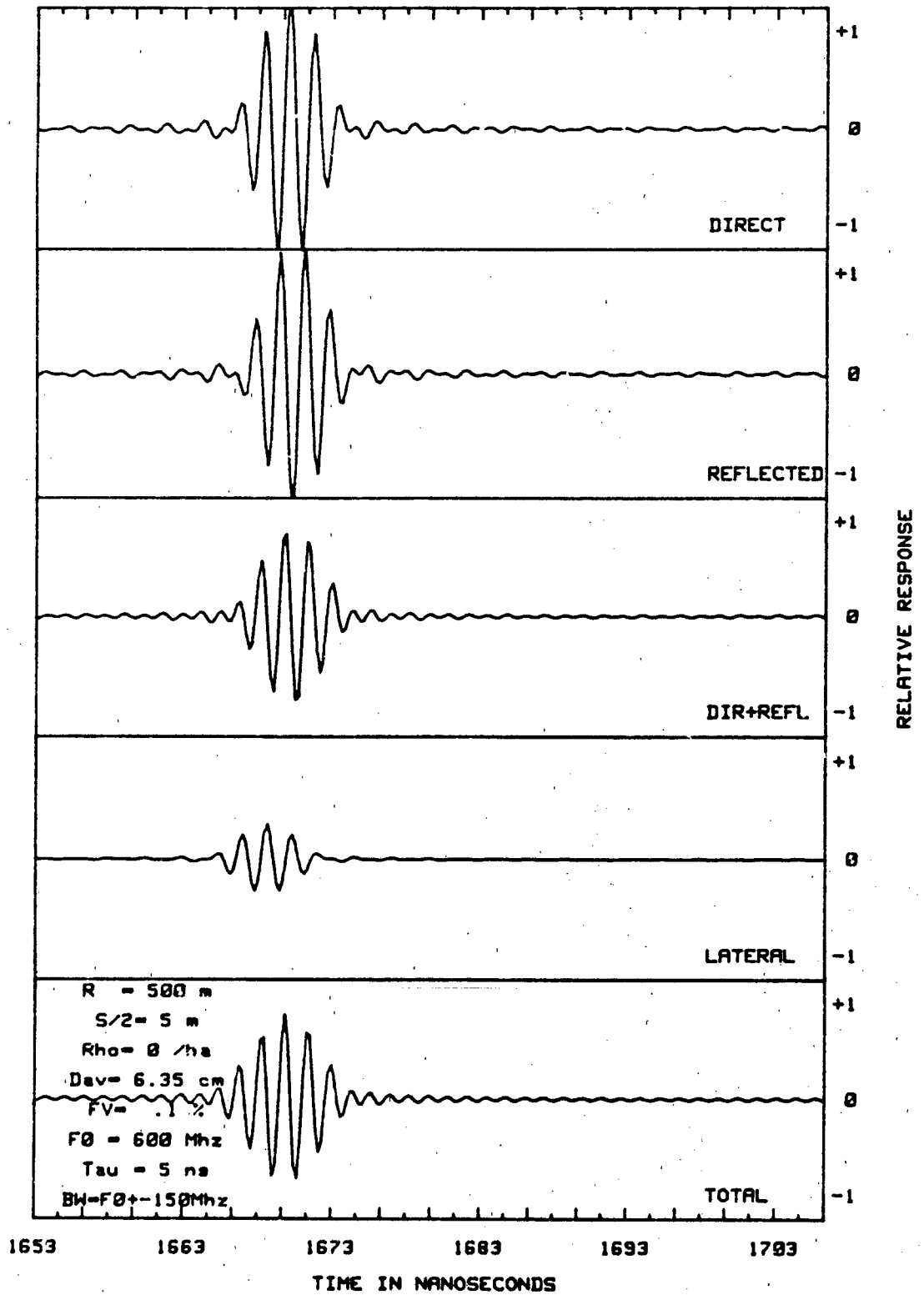
Figure 5B-5:   Pulse Response (Leaf Forest)

5B-5
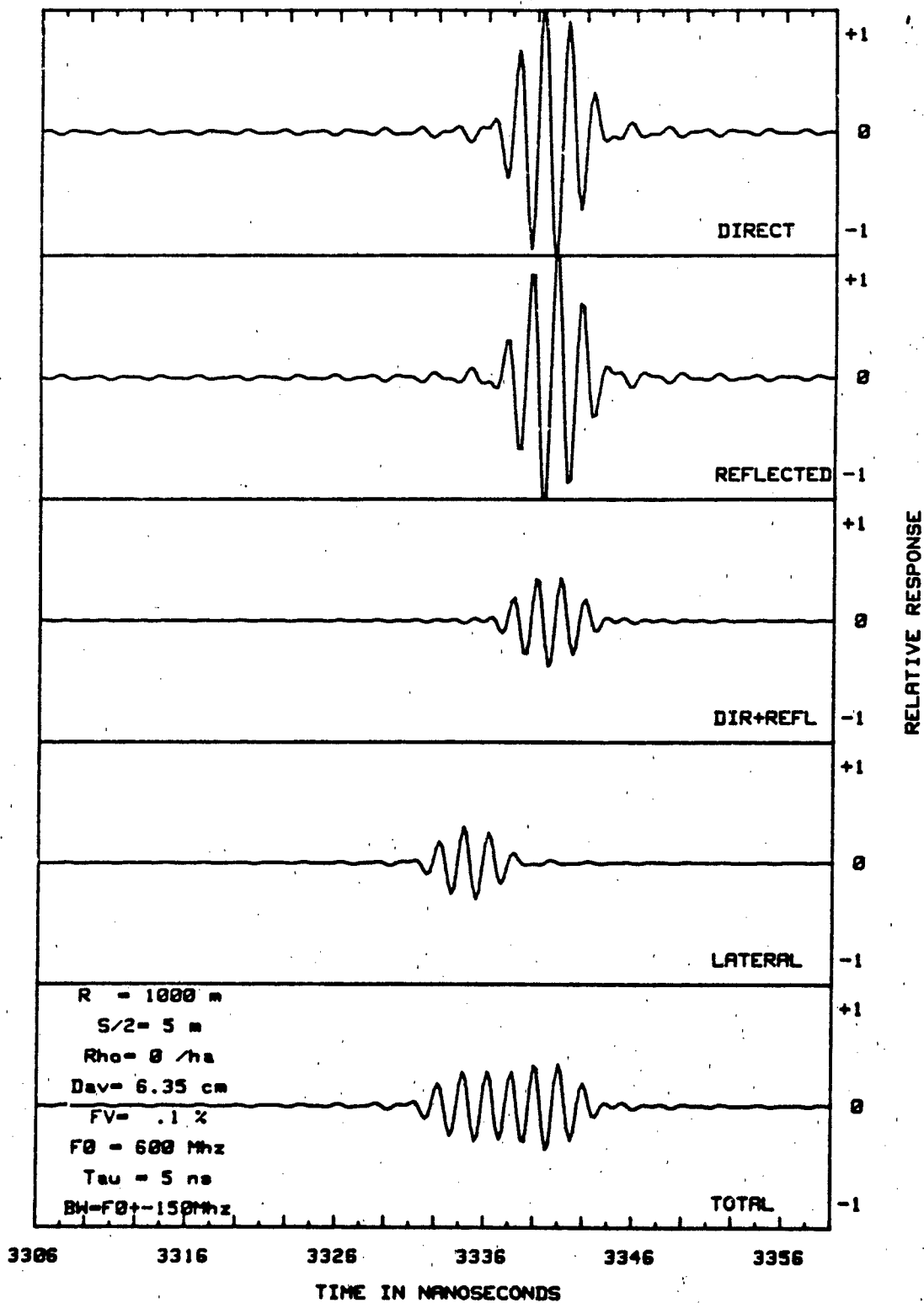
Figure 5B-6: Pulse Response (Leaf Forest)

The figure panels are labeled (top to bottom): DIRECT, REFLECTED, DIR+REFL, LATERAL, TOTAL, each with a vertical scale of +1, 0, -1 on the RELATIVE RESPONSE axis.

Parameters shown in the TOTAL panel:

R = 200 m
S/2 = 10 m
Rho = 0 /ha
Dav = 6.35 cm
FV = .1 %
F0 = 600 Mhz
Tau = 5 ns
BW = F0 +- 150Mhz

TIME IN NANOSECONDS
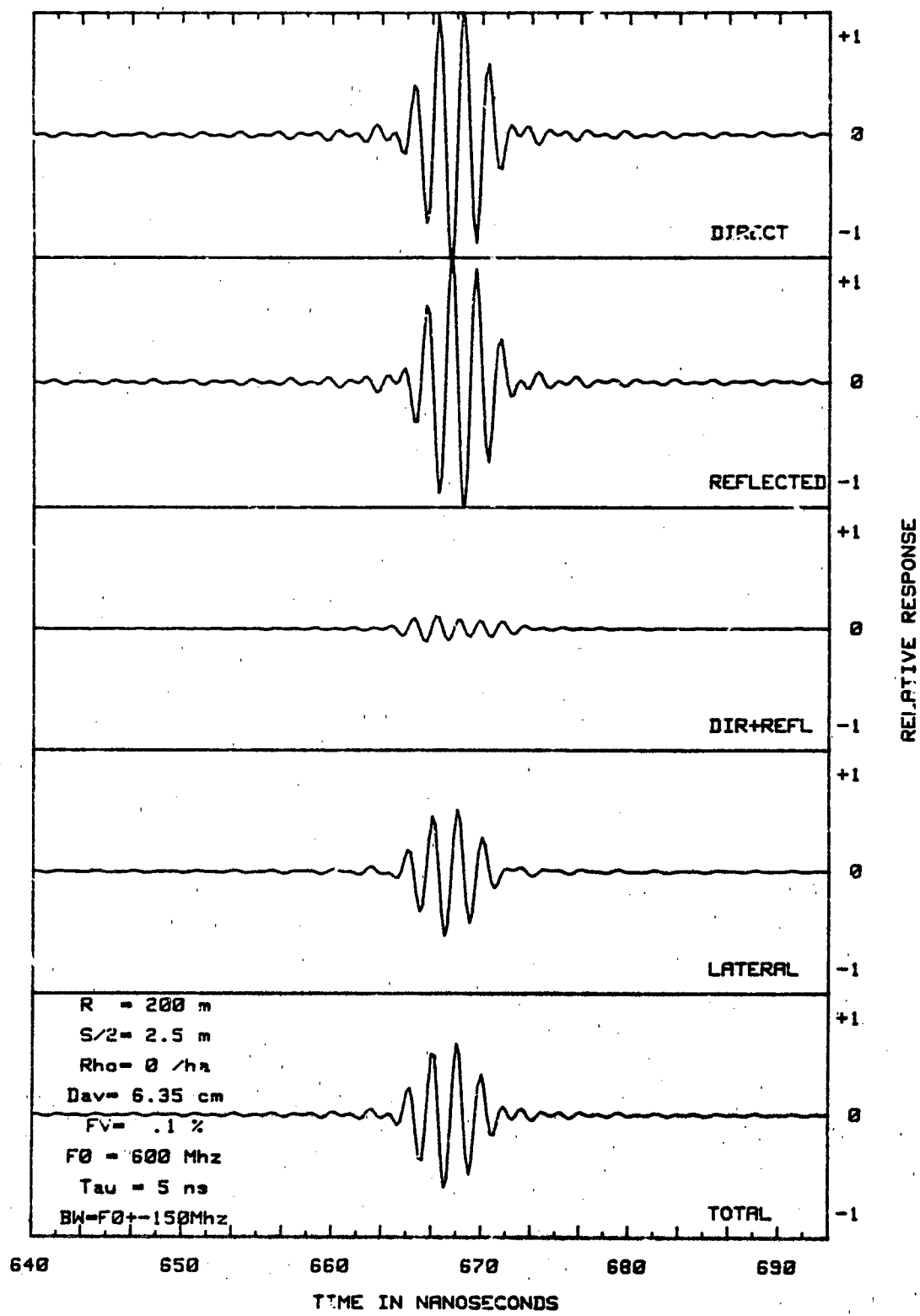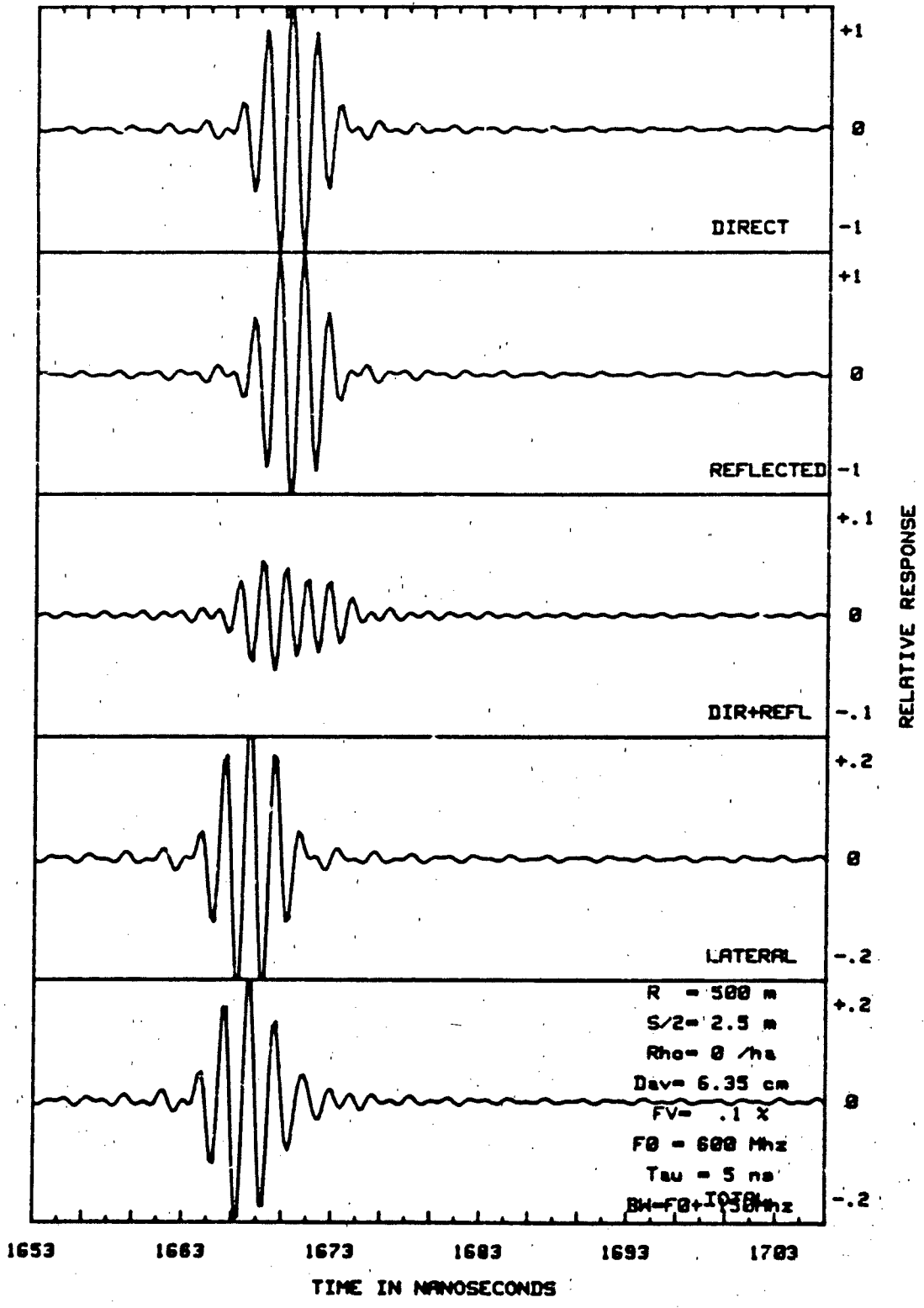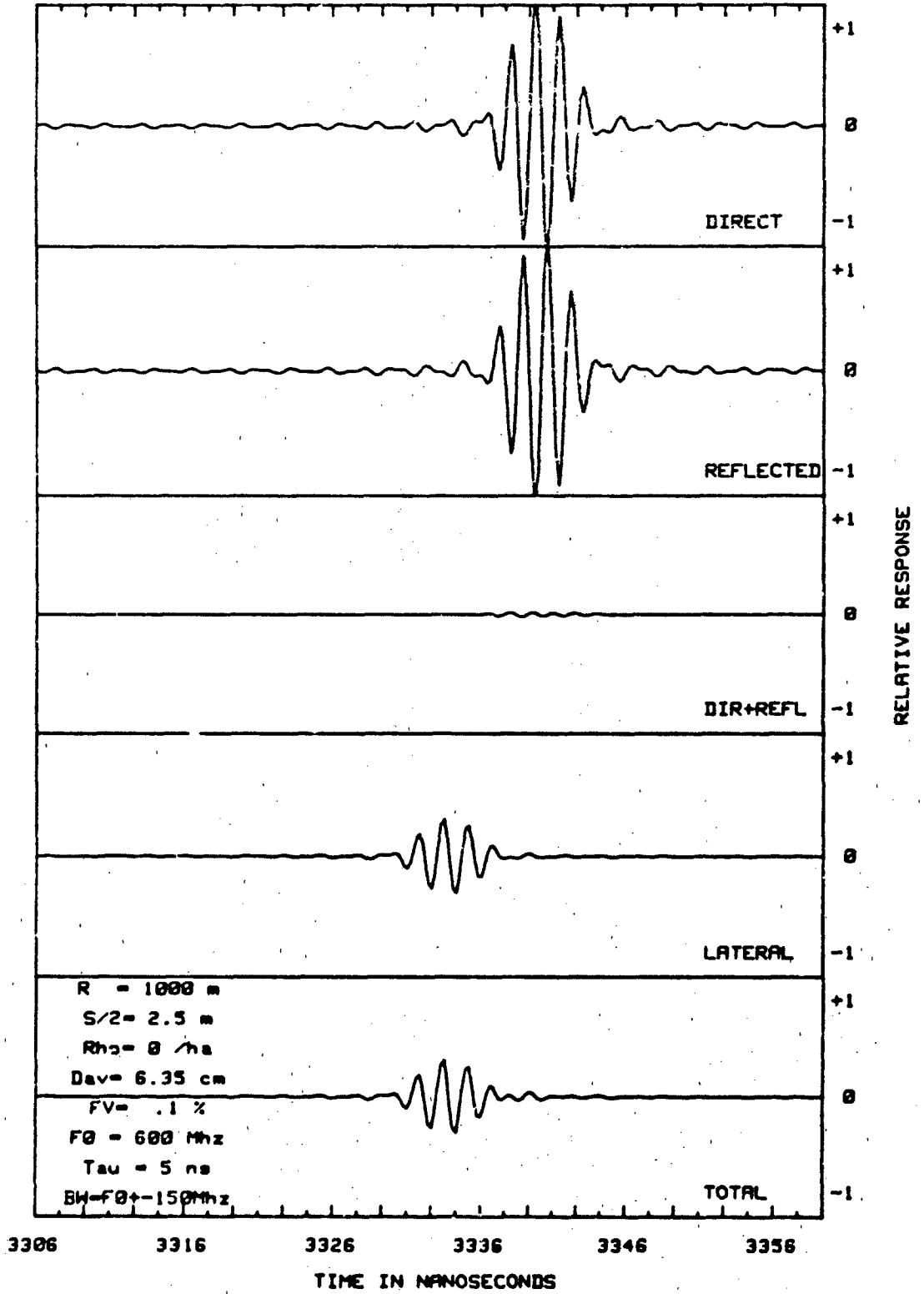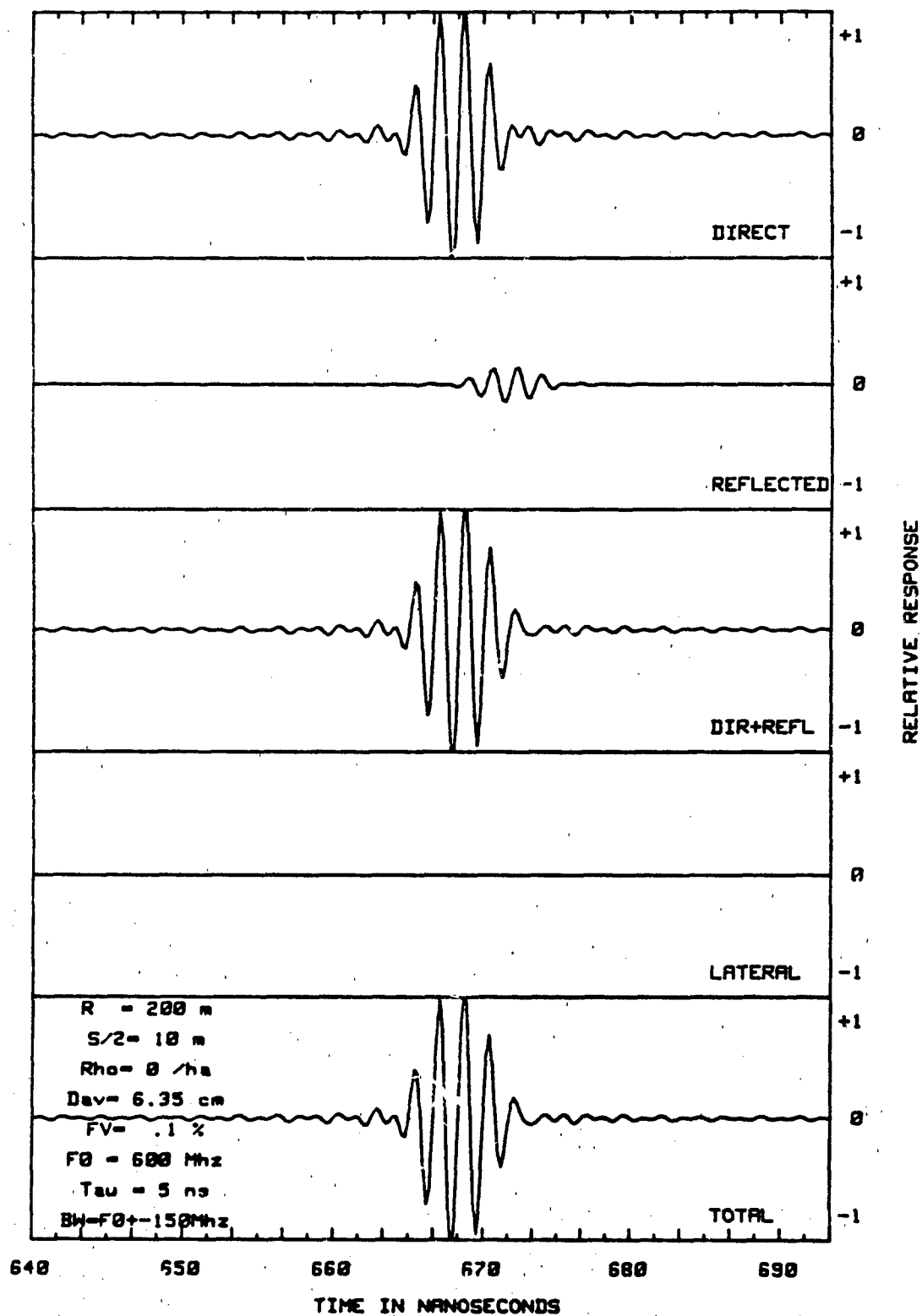
Figure 5B-7:  Pulse Response (Leaf Forest)

5B-7
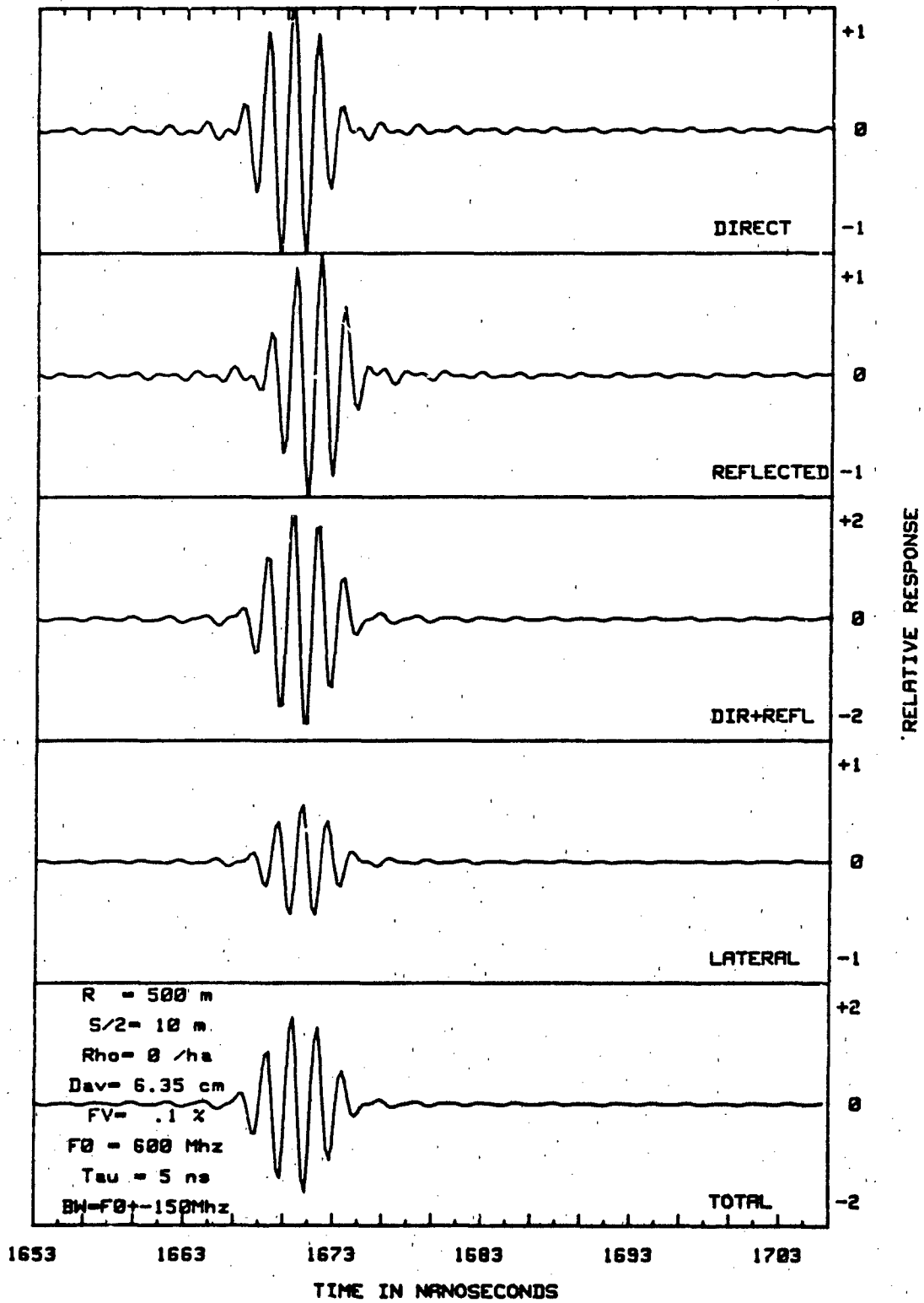
Figure 5B-8: Pulse Response (Leaf Forest)

Figure 5B-9:  Pulse Response (Leaf Forest)

Figure 5B-10:  Pulse Response (Inhomogeneous Trunk Forest)

DIRECT

+1

0

−1

REFLECTED

+1

0

−1

DIR+REFL

+1

0

−1

LATERAL

+25

0

−25

TOTAL

R = 500 m
S/2= 2.5 m
Rho= 1000 /ha
Dav= 6.35 cm
F0 = 600 Mhz
Tau = 5 ns
BW=F0+−150Mhz

+25

0

−25

RELATIVE RESPONSE

1653    1663    1673    1683    1693    1703

TIME IN NANOSECONDS

Figure 5B-11:   Pulse Response (Inhomogeneous Trunk Forest)

5B-11

Figure 5B-12:   Pulse Response (Inhomcgeneous Trunk Forest)

Figure 5B-13:  Pulse Response (Inhomogeneous Trunk Forest)

Figure 5B-14: Pulse Response (Inhomogeneous Trunk Forest)

5B-14

Figure 5B-15: Pulse Response (Inhomogeneous Trunk Forest)
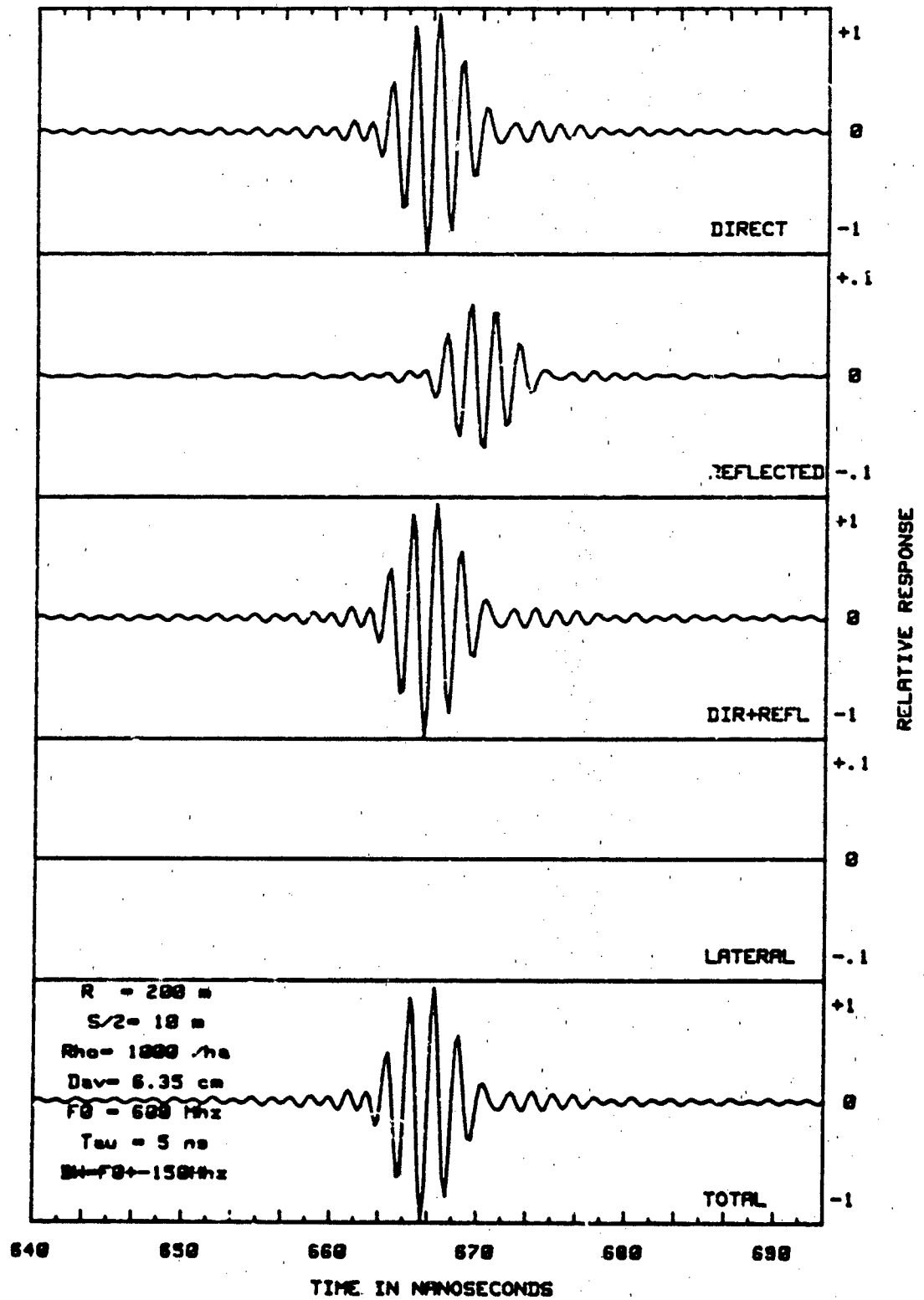
Figure 5B-16:  Pulse Response (Inhomogeneous Trunk Forest)
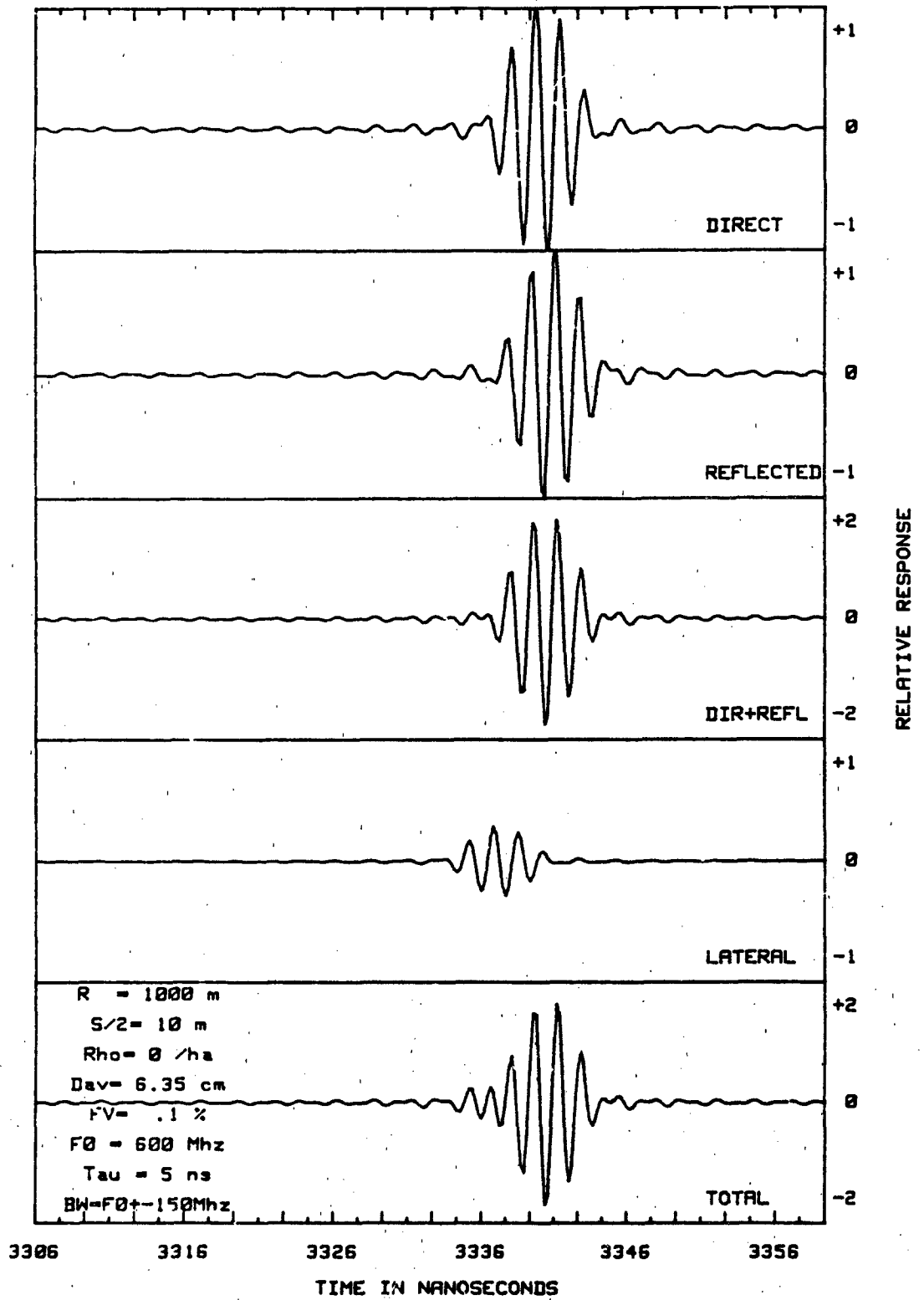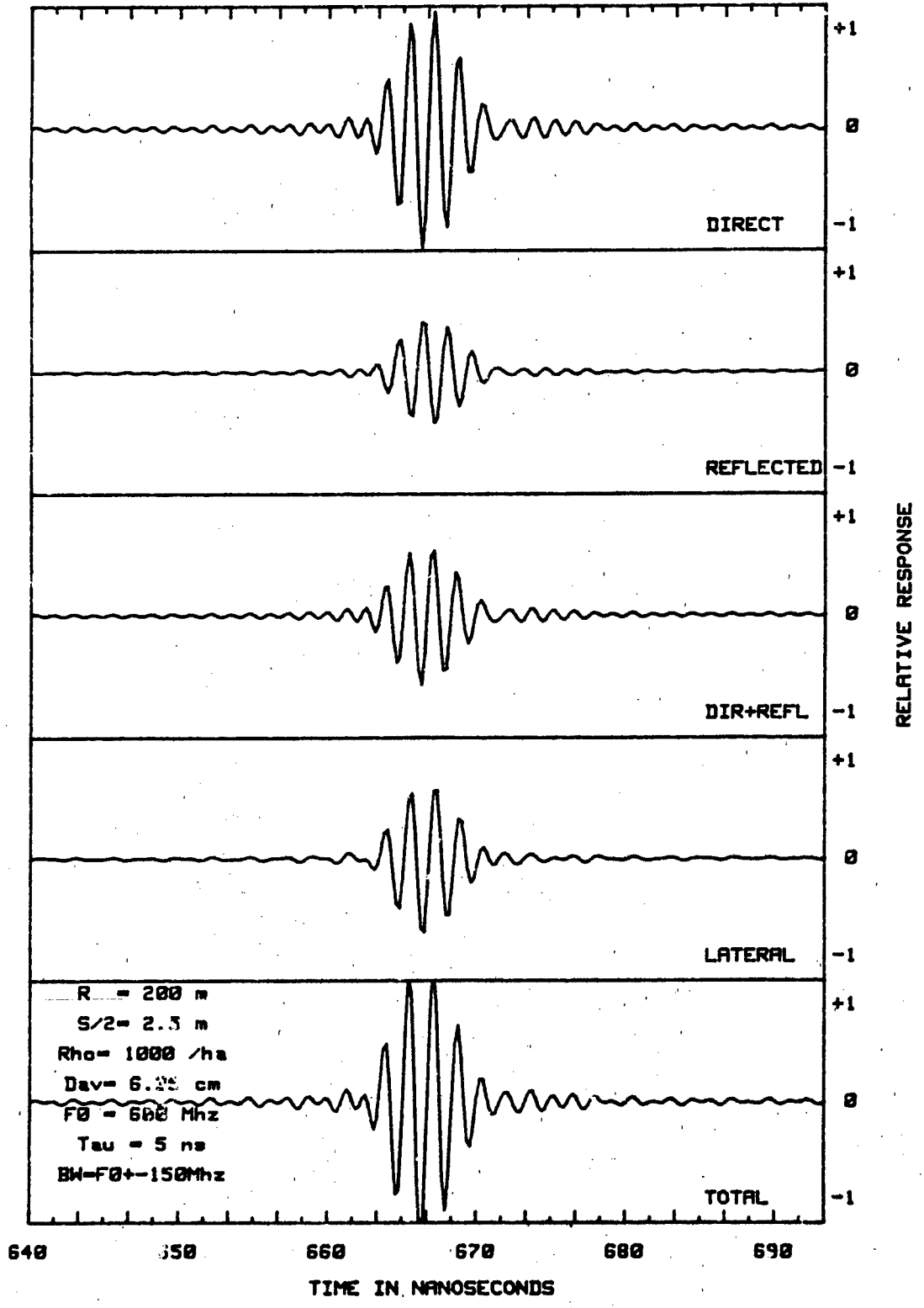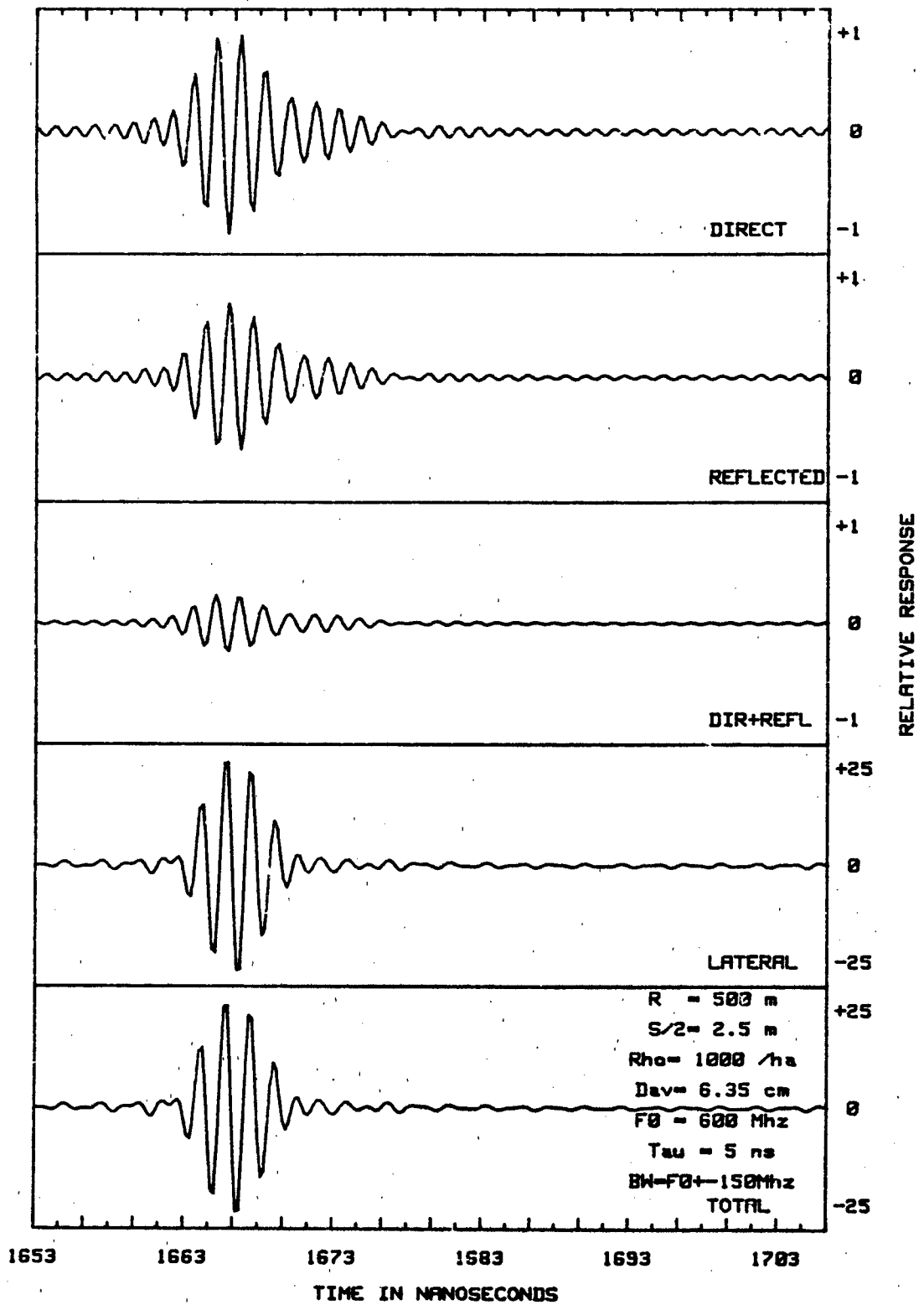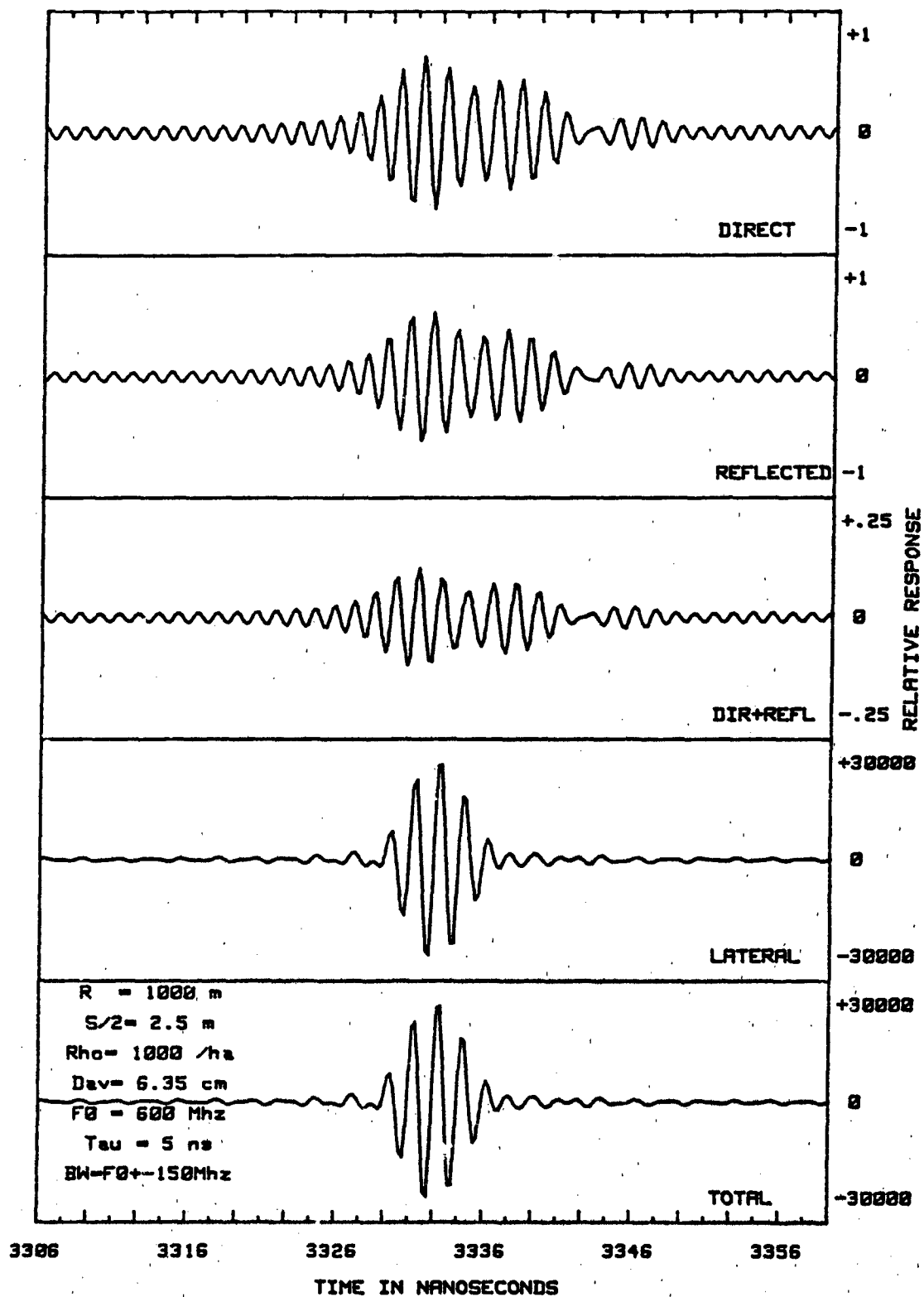
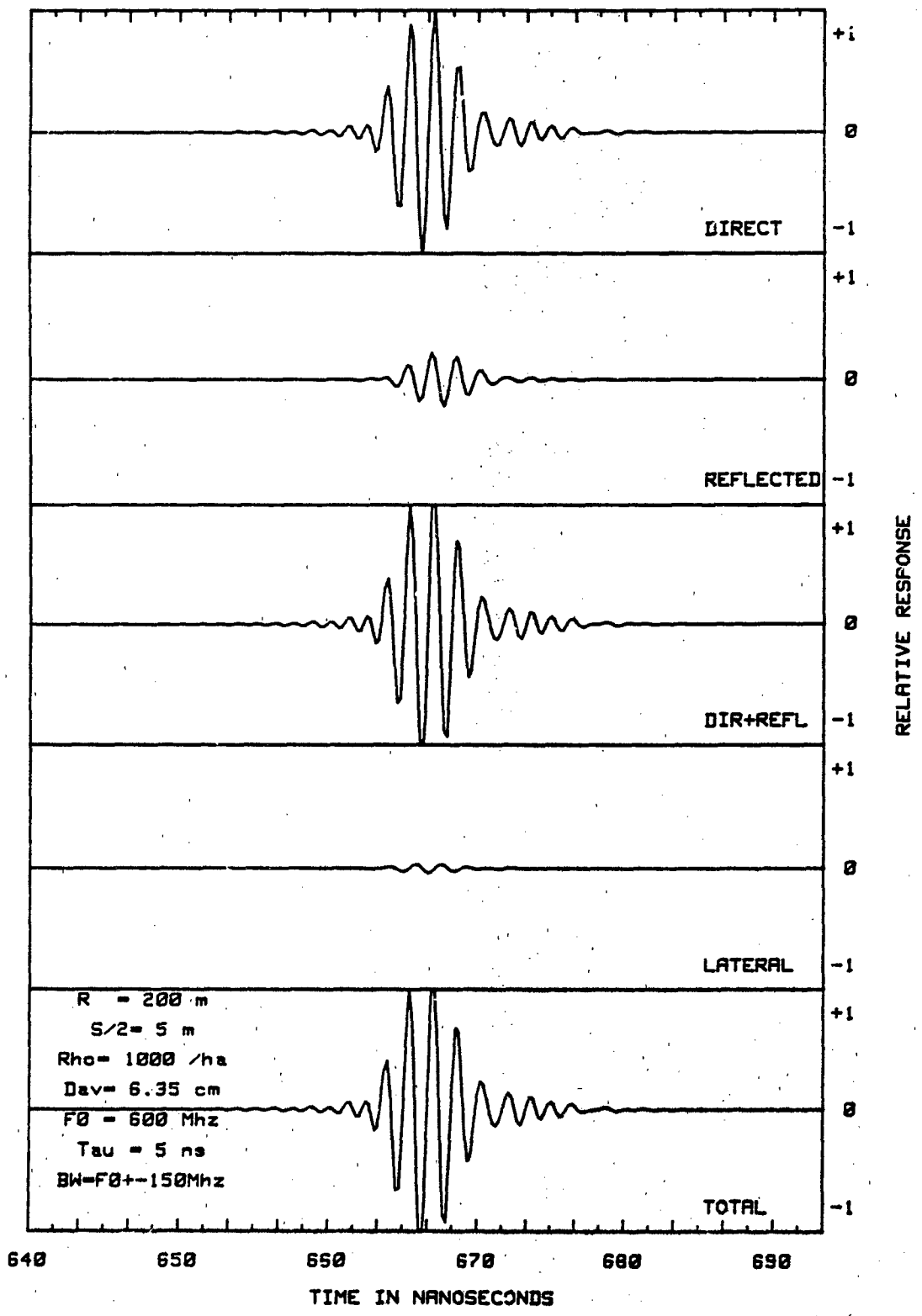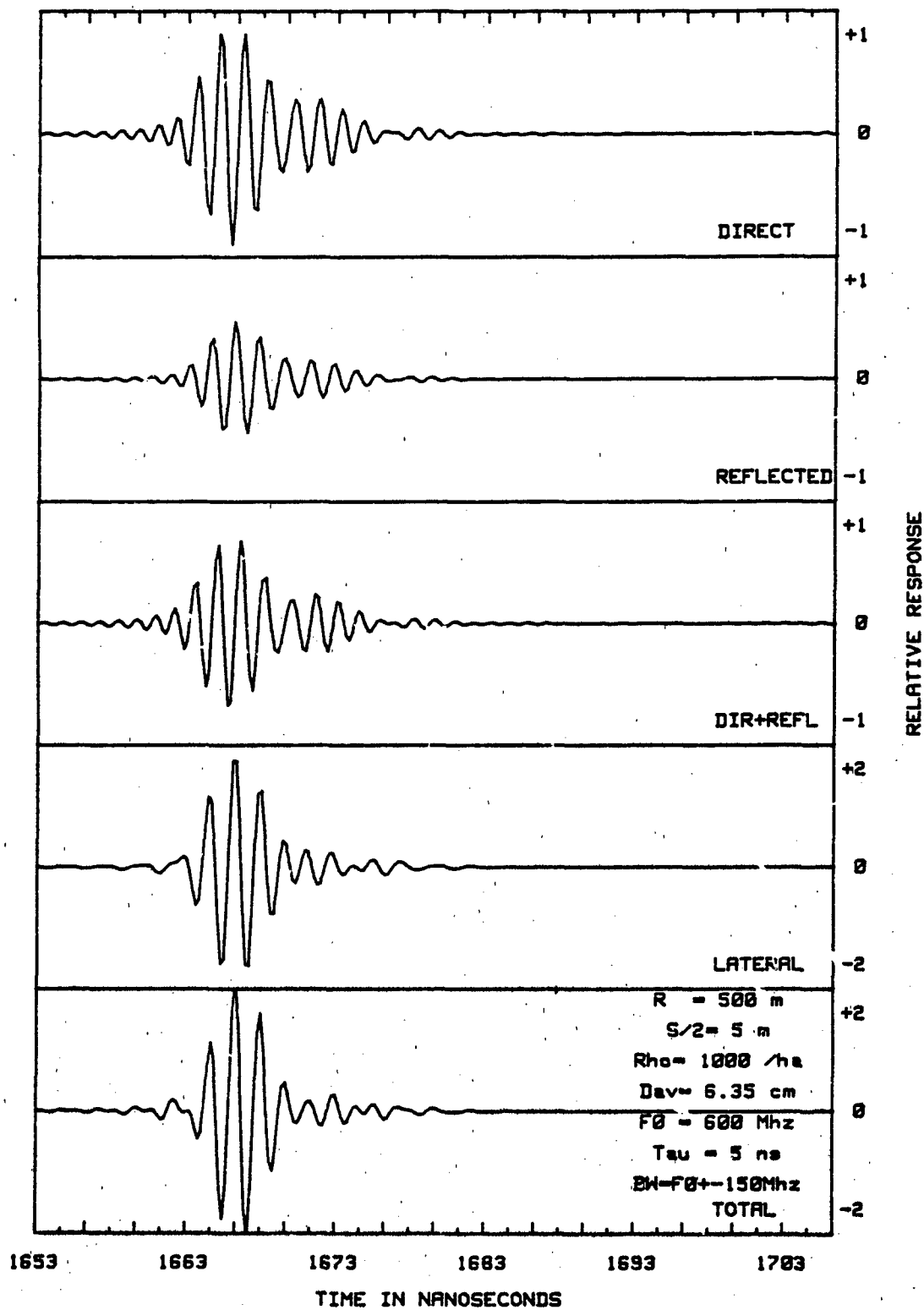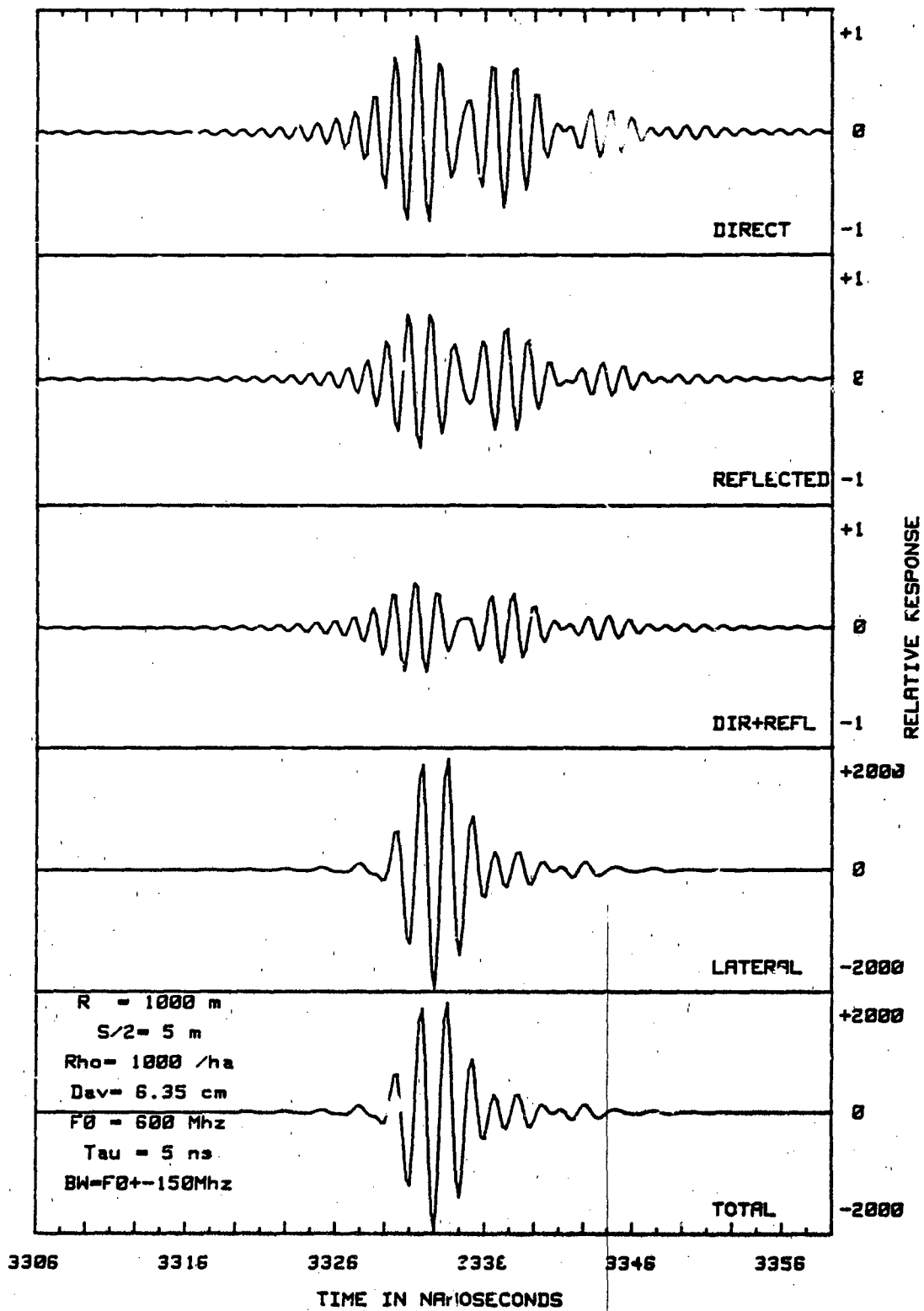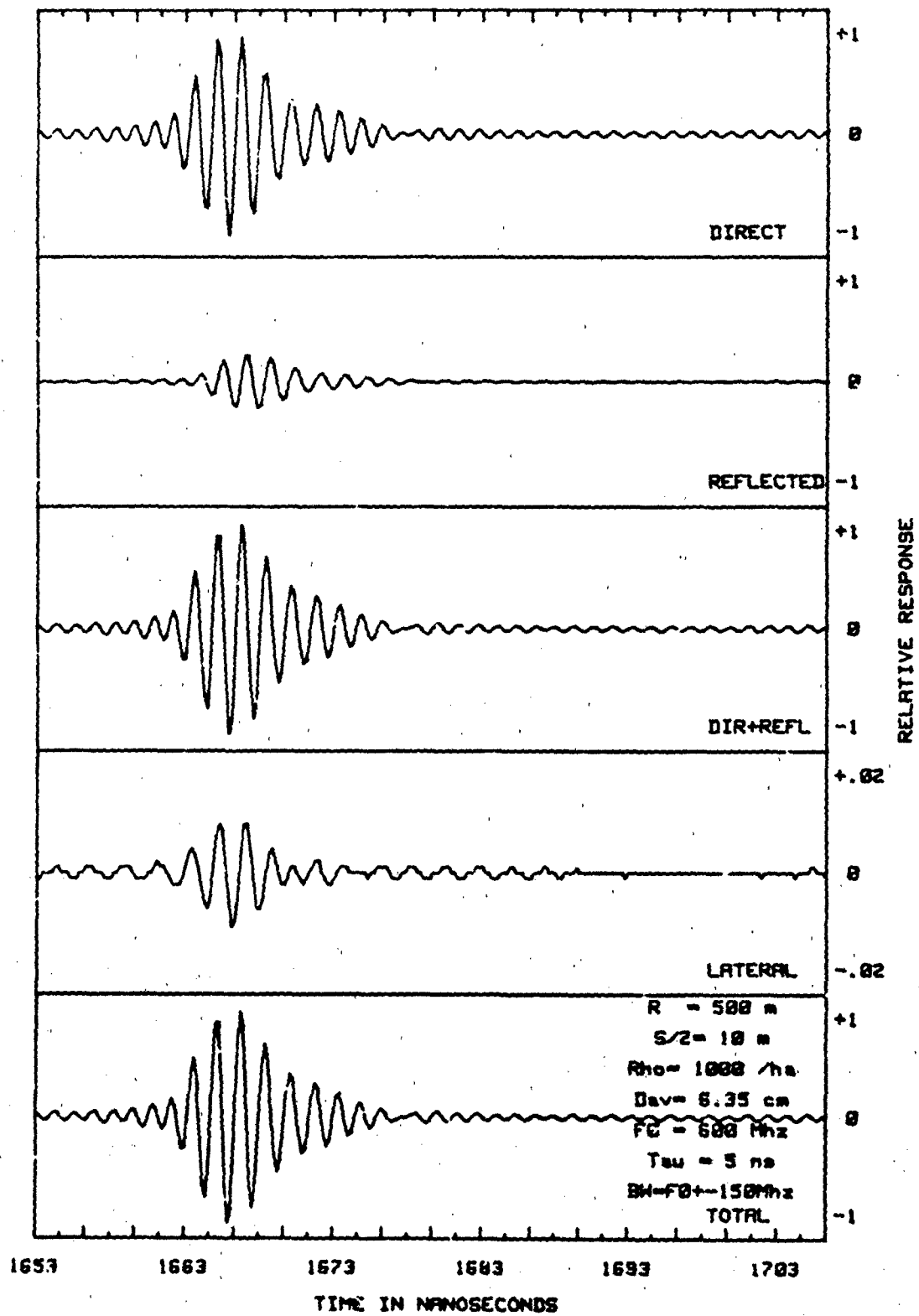Figure 5B-17:   Pulse Response (Inhomogeneous Trunk Forest)

5B-17
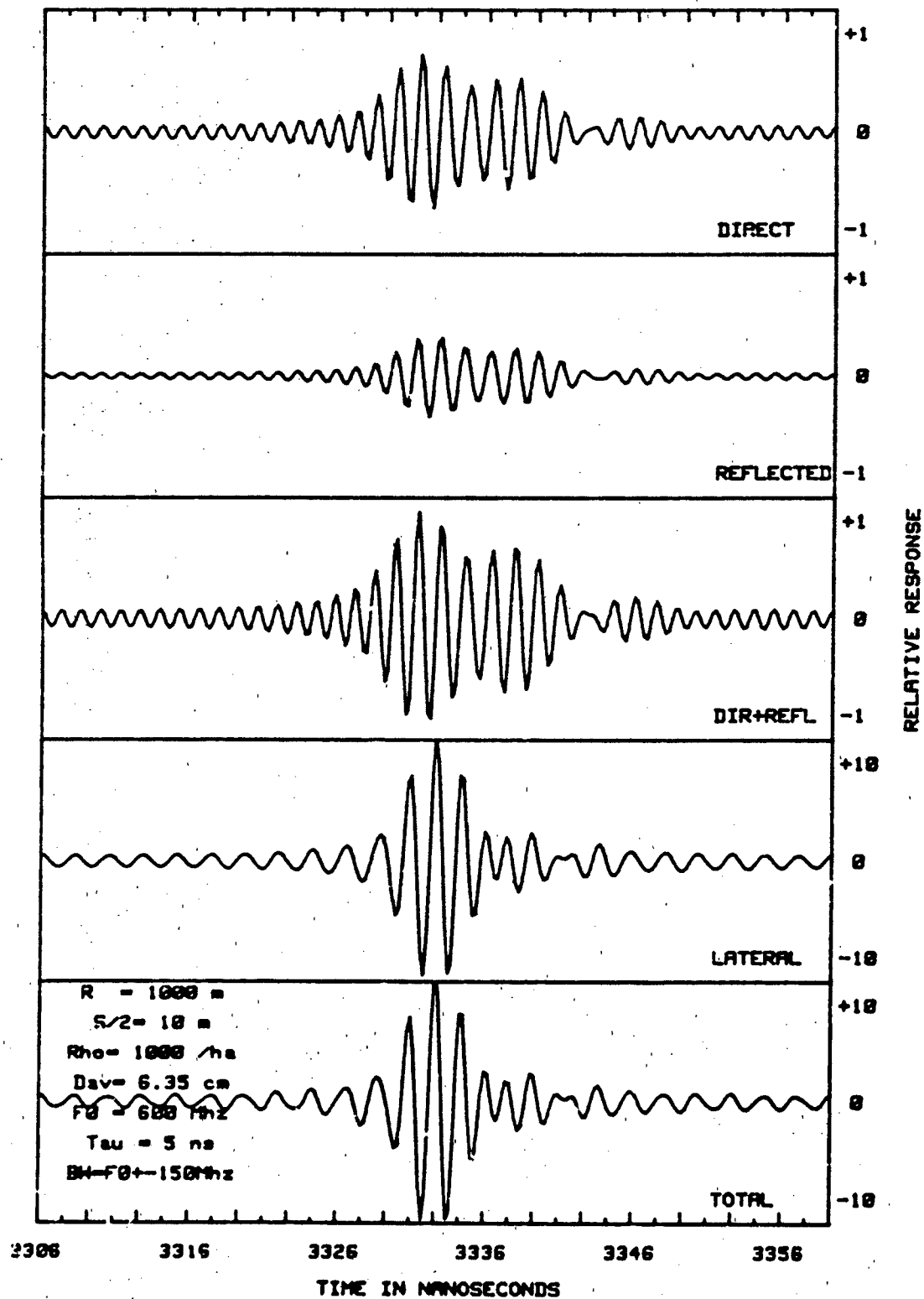
Figure 5B-18:  Pulse Response (Inhomogeneous Trunk Forest)

[This page intentionally left blank]

## 6.0 Incoherent Forest Scattering

The electromagnetic fields of radiowaves propagating through a forest can be decomposed into mean (coherent) and diffuse (incoherent) components. At low frequencies (HF and below) the diffuse component is relatively small and only mean fields need be considered. As the frequency becomes higher, spatial fluctuations in the field become more important, and the diffuse component of the field must be taken into account. In this section, the behavior of the diffuse component at VHF and UHF frequencies is examined for a trunk-dominated forest.

The trunk-dominated forest consists solely of tree trunks which are parallel to each other but randomly placed perpendicular to the forest floor. It is a useful model since trunks are the largest forest component and the first to give rise to substantial random or diffuse component of the fields as the frequency is increased. In addition, if the trunks are assumed to be circular, and propagation is parallel to the forest floor, Maxwell's equations can be replaced by a scalar wave equation; this represents a substantial simplification in the mathematical analysis required.

To characterize propagation in the forest when the diffuse component of the field is significant, the space-frequency correlation function of the field is required. This is the correlation function between the field component at space point $\underline{x}$ and frequency $\omega$ with the conjugate of the field component at space point $\hat{\underline{x}}$ and frequency $\hat{\omega}$. An approximate equation for this correlation function can be obtained for the two-dimensional trunk forest. This equation is the starting point for most of the calculations of this section.

Once the correlation equation has been obtained and the scattering properties of the trunks discussed two problems are addressed. The first is the solution of the correlation equation for trunks thin compared to a wavelength with $\underline{x} = \hat{\underline{x}}$ but $\omega \neq \hat{\omega}$. With this frequency correlation function the coherence bandwidth of the channel can be determined. Following this calculation,

the intensity and space correlation function are evaluated for the general case of a forest of resonant trunks, i.e., trunks that are not necessarily small compared to a wavelength. The intensity calculation represents a generalization of that for thin trunks that appears in [42]. The results of both calculations yield essential physical information on channel behavior which will be discussed subsequently.

## 6.1  Mean and Correlation Equations

In this section, the equation for the mean field and the equation for the space-frequency correlation function are developed. Before this can be done, the two-dimensional forest problem must be formulated. Although some of the material in this section has already appeared in [42], it is repeated here for completeness and convenience.

### 6.1.1  Formulation of Two-Dimensional Trunk Problem

Consider a trunk-dominated forest represented by a collection of parallel circular dielectric cylinders having radius a and complex relative dielectric constant $\varepsilon_\ell$. The collection of trunks is confined to stand within an area S as is shown in Figure 6.1. If only an electric current source having no variation in the direction parallel to the cylinders is considered, the electric field obeys the following scalar wave equation

$$[\nabla_t^2 + k_o^2 \varepsilon(\underline{x}_t, \omega)] E_z(\underline{x}_t, \omega) = j\omega\mu_o J_z(\underline{x}_t, \omega) \qquad (6\text{-}1\text{-}1)$$

Here $E_z(\underline{x}_t, \omega)$ is the only component of the electric field excited; it depends only on the transverse position vector $\underline{x}_t = x\underline{x}^\circ + y\underline{y}^\circ$. In the above formulation, the z coordinate is parallel to the cylinders.

The current source $J_z(\underline{x}_t, \omega)$ can be within the forest region S or outside of it. In some cases the source is allowed to recede to infinity in such a way that it generates plane waves normally incident on the forest. The two-dimensional source distribution is not as realistic as a three-dimensional point
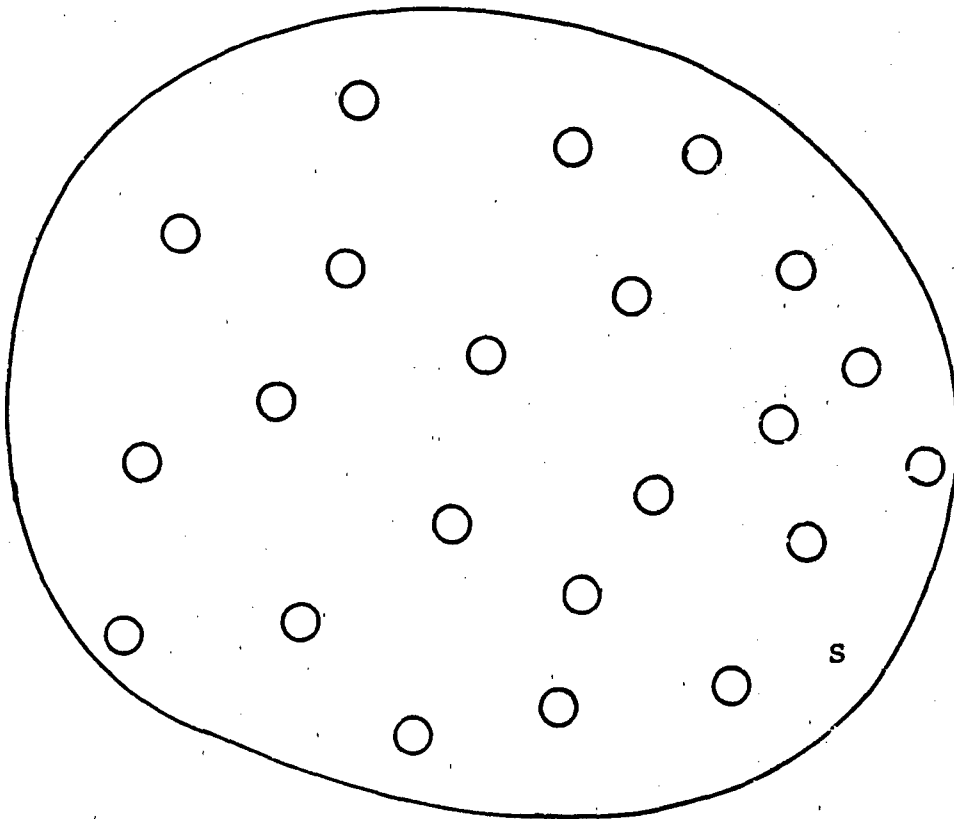
Figure 6-1  Cross-Sectional View of Forest Trunk Model

source, but the scalar formulation of Equation (6-1-1) lead to a much more tractable problem. Since a point source can be represented as a superposition of phased line sources, the results can be generalized to the three-dimensional source case by employing superposition. This, however, will not be done at this time.

The dielectric characteristics of the forest are specified by the relative dielectric permittivity, $\varepsilon(\underline{x}_t, \omega)$. This permittivity can be expressed as a sum of the susceptibilities of the individual scatterers as follows:

$$\varepsilon(\underline{x}_t, \omega) = 1 + \sum_{j=1}^{N} \chi_j(\underline{x}_t, \omega) \qquad (6-1-2)$$

where $\chi_j$ is the susceptibility of the $j^{th}$ scatterer. It is convenient to express the $\chi_j$ as a translation of the susceptibility, $\chi$, of an identical scatterer located at the origin. If $\underline{x}_{t_j}$ is the vector from the origin to the center of the $j^{th}$ scatterer then

$$\chi_j(\underline{x}_t, \omega) = \chi(\underline{x}_t - \underline{x}_{t_j}, \omega) \qquad (6-1-3)$$

where

$$\chi(\underline{x}_t, \omega) = \begin{cases} \chi_\ell(\omega) & , \quad |\underline{x}_t| \leq a \\ \\ 0 & , \quad |\underline{x}_t| > a \end{cases}$$

Here $\chi_\ell(\omega)$ is the susceptibility of the bulk tree trunk material. It is assumed to be isotropic.

Following the methodology of Section 2.1.1, [42], Equation (6-1-1) is expressed in operator notation. If the following quantities are defined:

$$L = -(\nabla_t^2 + k_o^2) \qquad\qquad V_j = k_o^2 \chi_j \qquad (6-1-4)$$

$$\psi = E_z \qquad\qquad g = -j\omega\mu_o J_z \qquad (6-1-5)$$

then Equation (6-1-1) can be written as

$$\left(L - \sum_{j=1}^{N} V_j\right)\psi = g \qquad (6\text{-}1\text{-}6)$$

This notation has been used in Section 2.2.3, [42] to derive the mean equation. It will be used in this report to derive the space-frequency correlation equation (Appendix A). It provides a concise mechanism for writing defining equations for the mean and correlation in the main body of the text.

The formulation of the scattering problem thus far is in terms of the susceptibility of individual scatterers translated from the origin. Past experience has shown that it is more useful to express the characteristics of a scatterer by its response to an incident field. For this purpose, the transition operator T is introduced. If $\psi_i$ is the field incident on a scatterer having susceptibility $X(\underline{x}_t,\omega)$ which is located at the origin, then the induced sources $g_{eq}$ generated within the scatterer are

$$g_{eq} = T\psi_i = \int t(\underline{x},\underline{x}',\omega)\psi_i(\underline{x}',\omega)d\underline{x}' \qquad (6\text{-}1\text{-}7)$$

Here the transition operator has been represented in terms of an integral operator having kernel $t(\underline{x},\underline{x}',\omega)$. From a knowledge of $t(\underline{x},\underline{x}',\omega)$ all properties of the scatterer can be determined.

It has been shown in Section 2.2.2, [42] that the transition operator, $T(\underline{X}_{t_j})$, for scatterers located at $\underline{X}_{t_j}$ can be simply expressed in terms of the transition operator of the scatter located at the origin. This relationship is given by

$$T(\underline{X}_{t_j})\psi = \int t(\underline{x} - \underline{X}_{t_j},\underline{x}' - \underline{X}_{t_j},\omega)\psi(\underline{x}',\omega)d\underline{x}' \qquad (6\text{-}1\text{-}8)$$

Using Equation (6-1-8) the properties of all particles can be expressed solely in terms of $\underline{t}(\underline{x},\underline{x}',\omega)$.

The scatterer can be characterized in an alternative manner by specifying its far-field response to a unit amplitude incident plane wave. If the incident plane wave is given by

$$\psi_i(\underline{x}_t) = \exp\{-jk_o\underline{i}\cdot\underline{x}_t\} \qquad (6\text{-}1\text{-}9)$$

then the scattered field in the radiation zone of the tree trunk has the form

$$\psi_s(\underline{x}_t,\omega) = f(\underline{o},\underline{i}) \frac{\exp\{-jk_ox_t\}}{\sqrt{x_t}} \quad , \quad x_t = |\underline{x}_t| \qquad (6\text{-}1\text{-}10)$$

where $\underline{i}$ and $\underline{o}$ ($= \underline{x}_t/x_t$) are unit vectors in the direction of the incident wave and observation point, respectively. Equation (6-1-10) serves as the defining equation for the scattering amplitude, $f(\underline{o},\underline{i})$. The scattering amplitude is directly related to the Fourier transform of the transition operator. The relationship has been derived in Appendix B of [42] and is given by

$$f(\underline{o},\underline{i}) = \gamma\tilde{t}(k_o\underline{o},k_o\underline{i},\omega) \qquad , \qquad \gamma = \sqrt{\frac{2\pi^3}{k_o}}\, e^{-j\frac{\pi}{4}} \qquad (6\text{-}1\text{-}11)$$

where $\tilde{t}$ is:

$$\tilde{t}(\underline{k}_t,\underline{k}_t',\omega) = (2\pi)^{-2}\int d\underline{x}_t d\underline{x}_t' t(\underline{x}_t,\underline{x}_t',\omega)e^{j(\underline{k}_t\cdot\underline{x}_t - \underline{k}_t'\cdot\underline{x}_t')} \qquad (6\text{-}1\text{-}12)$$

Although the transition kernel $t(\underline{x},\underline{x}',\omega)$ enters into the defining equations for the mean intensity and the correlation function, it is the scattering amplitude that appears in the final results.

Throughout this subsection, the $\omega$ dependence of quantities has been explicitly exhibited. This has been done since the calculation of the space-frequency correlation function to follow requires explicit knowledge of the frequency dependence.

6.1.2  Mean Equation

An approximate equation for the mean field $<\psi>$ was obtained in Section 2.2.3, [42] by employing the Foldy-Lax method [19,35].

The method is valid for collections of two-dimensional discrete scatterers having small fractional area. This criterion is usually satisfied inasmuch as most forests have fractional areas ranging from .05 to .2.

The approximate equation that the mean field satisfies is

$$(\nabla_t^2 + k_o^2)<\psi(\underline{x}_t,\omega)> + \int d\underline{s}_t d\underline{x}_t' \rho(\underline{s}_t) \ t\ (\underline{x}_t - \underline{s}_t, \underline{x}_t' - \underline{s}_t, \omega)<\psi(\underline{x}_t',\omega)>$$

$$= -g(\underline{x}_t,\omega) \qquad\qquad (6-1-13)$$

where the density $\rho(\underline{s}_t)$ is zero for $\underline{s}_t$ outside of S, i.e.,

$$\rho(\underline{s}_t) = \begin{cases} \rho(\underline{s}_t) & , \quad \underline{s}_t \text{ inside S} \\ \\ 0 & , \quad \underline{s}_t \text{ outside S} \end{cases} \qquad (6-1-14)$$

This equation is an integro-differential equation inside the forest but when $\underline{s}_t$ is outside S, the mean equation reduces to the free space scalar wave equation.

The operator notation previously introduced can be used to simplify the appearance of the mean equation. By using the mean operator £ the mean equation becomes

$$£<\psi> = g \qquad\qquad (6-1-15)$$

where

$$£ = L - \int d\underline{s}_t \rho(\underline{s}_t) T(\underline{s}_t) \qquad\qquad (6-1-16)$$

Note that no average bar appears over T as in [42]; because for cylindrical scatterers, $\overline{T} = T$.

The mean operator £ has been introduced since it is important to the formulation of the correlation equation. In this context its inverse will often be required. The inverse of £ is defined in terms of the mean Green's function $G(\underline{x}_t,\underline{x}_t',\omega)$ as

$$\pounds^{-1}\phi = \int d\underline{x}'_t G(\underline{x}_t, \underline{x}'_t, \omega) \phi(\underline{x}'_t, \omega) \qquad (6\text{-}1\text{-}17)$$

where

$$\pounds G = \delta \qquad (6\text{-}1\text{-}18)$$

or more explicitly

$$-(\nabla_t^2 + k_o^2) G(\underline{x}_t, \underline{x}_{t_o}, \omega) - \int d\underline{s}_t\, d\underline{x}'_t\, \rho(\underline{s}_t)\, t(\underline{x}_t - \underline{s}_t, \underline{x}'_t - \underline{s}_t, \omega)\, G(\underline{x}'_t, \underline{x}_{t_o}, \omega)$$

$$= \delta(\underline{x}_t - \underline{x}_{t_o}) \qquad (6\text{-}1\text{-}19)$$

Thus from the solution of Equation (6-1-19) the inverse of $\pounds^{-1}$ can be found from Equation (6-1-17).

In the low-frequency limit, the transition kernel $t(\underline{x}_t, \underline{x}'_t, \omega)$ can be represented as Section 2.2.2, [42]

$$t(\underline{x}_t, \underline{x}'_t, \omega) = k_o^2 \alpha(\omega)\, \delta(\underline{x}_t)\, \delta(\underline{x}'_t) \qquad (6\text{-}1\text{-}20)$$

where $\alpha$ is the two-dimensional polarizability of the cylindrical scatterer. For a circular cylinder of susceptibility $X$ it is given by

$$\alpha(\omega) = -X_\ell(\omega)\, 2\pi a^2 \qquad (6\text{-}1\text{-}21)$$

where $a$ is the radius of the trunk. If the low-frequency form of the transition kernel as it appears in Equation (6-1-20) is used in Equation (6-1-19), the equation for the Green's function simplifies substantially. It is given by

$$\{\nabla_t^2 + k_o^2(1 + \rho(\underline{x}_t)\alpha(\omega))\} G(\underline{x}_t, \underline{x}_{t_o}, \omega) = -\delta(\underline{x}_t - \underline{x}_{t_o}) \qquad (6\text{-}1\text{-}22)$$

This equation will be employed in Section 6.3.

6.1.3  Space-Frequency Correlation Equation

The basic quantity needed to characterize communications channel is the space-frequency correlation function; i.e.,

6-8

$\langle \psi(\underline{x}_t, \omega) \psi^*(\hat{\underline{x}}_t, \hat{\omega}) \rangle$. This represents the correlation between a field component of frequency $\omega$ at position $\underline{x}_t$ and a field component of frequency $\hat{\omega}$ at position $\hat{\underline{x}}_t$. From this function, the frequency correlation and delay spread for the channel can be obtained at a fixed point $\underline{x}_t = \hat{\underline{x}}_t$, and the spatial correlation can be found at a fixed frequency $\omega = \hat{\omega}$.

The correlation of the field can be decomposed into a coherent and incoherent part. Consider the field $\psi(\underline{x}_t, \omega)$ to be represented as a sum of its mean $\langle \psi(\underline{x}_t, \omega) \rangle$ plus its fluctuating component $\tilde{\psi}(\underline{x}_t, \omega)$ so that

$$\psi(\underline{x}_t, \omega) = \langle \psi(\underline{x}_t, \omega) \rangle + \tilde{\psi}(\underline{x}_t, \omega) \qquad (6\text{-}1\text{-}23)$$

where $\langle \psi(\underline{x}_t, \omega) \rangle = 0$ by definition. By using this equation, the correlation can be decomposed as follows

$$\langle \psi(\underline{x}_t, \omega) \psi^*(\hat{\underline{x}}_t, \hat{\omega}) \rangle = \langle \psi(\underline{x}_t, \omega) \rangle \langle \psi^*(\hat{\underline{x}}_t, \hat{\omega}) \rangle$$
$$+ \langle \tilde{\psi}(\underline{x}_t, \omega) \tilde{\psi}^*(\hat{\underline{x}}_t, \hat{\omega}) \rangle \qquad (6\text{-}1\text{-}24)$$

The first term $\langle \psi \rangle \langle \psi^* \rangle$ is the mean intensity. It represents the complete correlation function when there are no fluctuations. The second term $\langle \tilde{\psi} \tilde{\psi}^* \rangle$ represents the effects of fluctuations. Thus, the representation afforded by Equation (6-1-23) permits the channel to be divided into two parallel components each with its own distinctive channel characterization. This is shown pictorially in Figure 6.2.

The equation that the space-frequency correlation function satisfies has been derived in Appendix A. The methodology is the same as the derivation appearing in Appendix C of [42] where the space correlation equation is derived. The inclusion of two different frequencies only changes the equation slightly. The equation is then given by

$$\mathcal{L}\mathcal{L}^* \langle \psi \psi^* \rangle - \int d\underline{s}_t \rho(\underline{s}_t) T(\underline{s}_t) T^*(\underline{s}_t) \langle \psi \psi^* \rangle = gg^* \qquad (6\text{-}1\text{-}25)$$
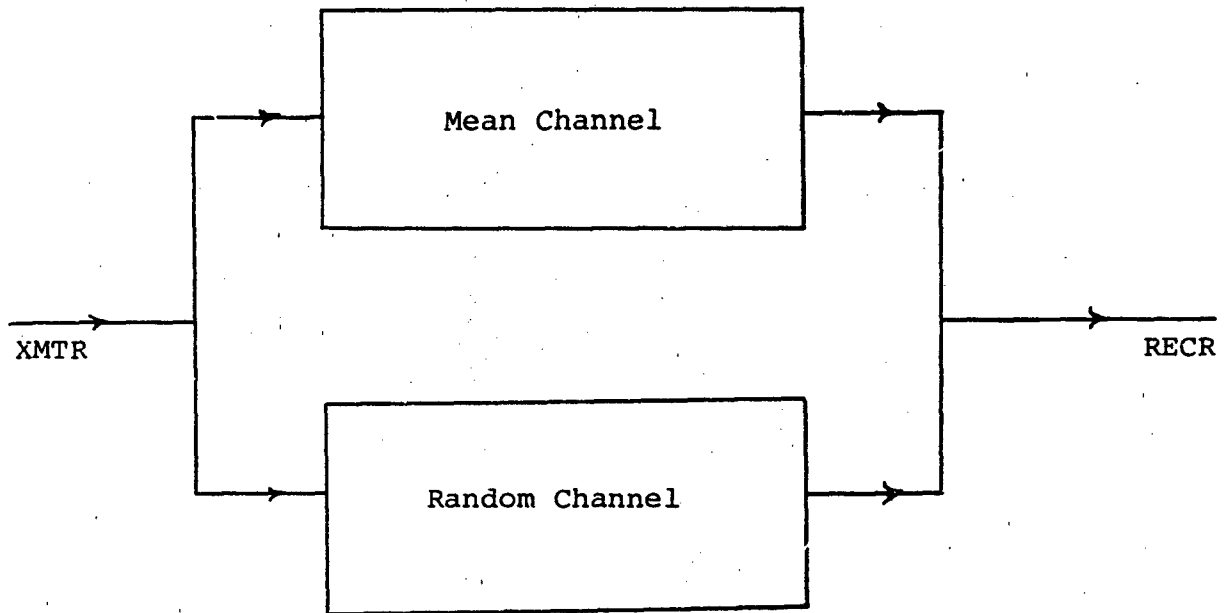
Figure 6-2   Channel Decomposition into Mean and
Random Components

where the notational device has been used that unstarred quantities are functions of $\underline{x}_t$ and $\omega$ while starred or conjugated quantities are functions of $\hat{\underline{x}}_t$ and $\hat{\omega}$. The integral term is the scattering or diffusion term and when small

$$\pounds\pounds^* \langle \psi\psi^* \rangle \approx gg^* \qquad (6\text{-}1\text{-}26)$$

or

$$\langle \psi\psi^* \rangle = \pounds^{-1}\pounds^{*-1}gg^* \qquad (6\text{-}1\text{-}27)$$

$$= \pounds^{-1}g\pounds^{*-1}g^* \qquad (6\text{-}1\text{-}28)$$

$$= \langle\psi\rangle\langle\psi^*\rangle \qquad (6\text{-}1\text{-}29)$$

Thus when the scattering term is small, the random component of the channel can be neglected.

In the following subsections, the space-frequency correlation equation is presented for the two special cases mentioned earlier. First in Subsection 6.3, the frequency correlation function ($\underline{x}_t = \hat{\underline{x}}_t$) is given for an infinite forest having a line source excitation. The low-frequency approximation will be used to make the equation tractable. In Subsection 6.4 the spatial correlation function ($\omega = \hat{\omega}$) is given for a half-space forest with a normally incident plane wave. The low-frequency approximation is not employed here, so the results are valid for all frequencies of interest.

## 6.2 Single-Scatterer Characteristics

The properties of the scatterer ensembles to be treated in the next two subsections will be closely related to the characteristics of the individual scattering elements. In this subsection, the differential scattering cross-section and total cross-section of an isolated tree trunk (circular cylinder) are plotted for typical tree trunk diameters. The curves obtained are used in latter subsections to help interpret multiple scattering results.

Consider a circular lossy dielectric cylinder of radius a whose axis coincides with the z-axis. The cylinder has the complex permittivity $X_\ell = X'_\ell - jX''_\ell$. The fundamental quantity characterizing the scattering properties of the cylinder is the scattering amplitude as defined in Equation (6-1-10). The scattering amplitude $f(\underline{o}, \underline{i})$ measures the response of the scatterer in the direction $\underline{o}$ to a plane-wave incident upon the scatterer in the direction $\underline{i}$. These unit vectors are shown in Figure 6.3 along with the angle of incidence $\phi_i$ and the scattering angle $\phi_s$.

The dyadic scattering amplitude for a cylinder has been computed in Section 3.1, [42]. The scalar scattering amplitude can be obtained from it by using the $\underline{h}°\underline{h}°$ component of the dyadic at $\theta_i = \pi/2$. The result is

$$f(\underline{o}, \underline{i}) = f_{hh}(\underline{o}, \underline{i})\Big|_{\theta_i = \pi/2} =$$

$$\sqrt{\frac{\pi}{2k_o}}\, e^{j\pi/4} \sum_{n=-\infty}^{+\infty} (-1)^n c_n^{hh}\, e^{jn(\phi_i - \phi_s)} \qquad (6-2-1)$$

The expressions for the $c_n^{hh}$ are given in Section 3.1, [42] and will not be repeated here. The $c_n^{hh}$ are functions of the cylinder radius, the frequency, and the complex permittivity $X_\ell$.

The scattering characteristics of the cylinder are described by the differential scattering cross-section $\sigma_d$, the scattering cross-section $\sigma_s$, the total cross-section $\sigma_t$, and the scattering albedo W. These are addressed separately in the subsections which follow.

### 6.2.1 Scattering Formulas

### 6.2.1.1 Differential Scattering Cross-Section

The differential scattering cross-section is defined as

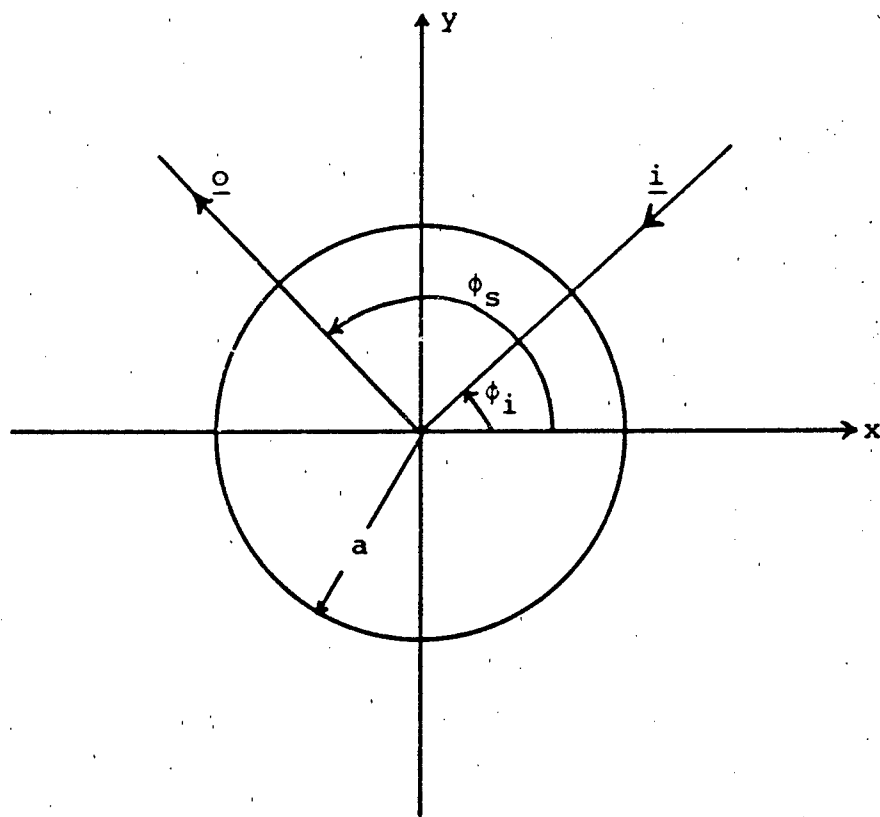$$\sigma_d(\underline{o}, \underline{i}) = |f(\underline{o}, \underline{i})|^2 \qquad (6-2-2)$$

Figure 6-3  Cylinder Scatterer Geometry

Using Equation (6-2-1) in the above equation gives

$$\sigma_d(\underline{o}, \underline{i}) = \sigma_d(\phi')$$

$$= \frac{2}{\pi k_o} \sum_{n=-\infty}^{+\infty} \sum_{m=-\infty}^{+\infty} (-1)^{n+m} C_n^{hh} C_n^{hh^*} e^{j(n-m)\phi'} \qquad (6-2-3$$

where $\phi' = \phi_i - \phi_s$. Thus $\sigma_d$ can be computed from a knowledg of the $C_n^{hh}$ and it is only a function of the difference betwee the incidence angle $\phi_i$ and the scattering angle $\phi_s$. The differ ential scattering cross-section also has the following tw properties:

$$\sigma_d(\phi') = \sigma_d(\phi' + 2\pi) \qquad (6-2-4$$

$$\sigma_d(\phi') = \sigma_d(-\phi') \qquad (6-2-5$$

Thus it is seen that $\sigma_d(\phi')$ is an even periodic function o $\phi'$.

A quantity closely related to $\sigma_d$ is the bistatic scatterin cross-section, $\sigma_{bi}$, which is given by

$$\sigma_{bi}(\underline{o}, \underline{i}) = 4\pi \sigma_d(\underline{o}, \underline{i}) \qquad (6-2-6$$

It is often used in radar applications. The differential scat tering cross-section gives the gain pattern or angular distri bution of scattered power of the scatterer. It is usually function of incident angle but since the cylinder is rotationall invariant, $\sigma_d$ depends only on the difference between $\phi_s$ an $\phi_i$.

## 6.2.1.2  Scattering Cross-Section

The next quantity of interest is the total power scat tered at all angles surrounding the cylinder. The cross-sectio of a particle which would produce this amount of scatterin is called the scattering cross-section $\sigma_s$ and is given by

$$\sigma_s = \int_0^{2\pi} \sigma_d(\underline{o},\underline{i}) \, d\phi_s = \int_0^{2\pi} \sigma_d(\phi') \, d\phi' \qquad (6\text{-}2\text{-}7)$$

If Equation (6-2-3) is used in the above equation; the result is

$$\sigma_s = \frac{4}{k_o} \sum_{n=-\infty}^{+\infty} |c_n^{hh}|^2 \qquad (6\text{-}2\text{-}8)$$

### 6.2.1.3  Total Cross-Section

The total cross-section, $\sigma_t$, is the sum of the scattering cross-section $\sigma_s$ and the absorption cross-section $\sigma_a$. It measures the amount of power the scatterer extracts from the incident wave in scattering and absorption. Since $\sigma_a$ is not directly related to the scattering amplitude, the calculation of $\sigma_t$ in terms of the $c_n^{hh}$ can most easily be done by using the optical theorem. According to Appendix F of [42], the optical theorem for two-dimensional media states

$$\sigma_t = -\frac{2\sqrt{2\pi}}{\sqrt{k_o}} \, \text{Re}\left[ f(\underline{i},\underline{i}) e^{-j\pi/4} \right] \qquad (6\text{-}2\text{-}9)$$

Now using Equation (6-2-1) in the above equation yields

$$\sigma_t = -\frac{4}{k_o} \sum_{n=-\infty}^{+\infty} \text{Re}\left[ c_n^{hh} \right] \qquad (6\text{-}2\text{-}10)$$

### 6.2.1.4  Albedo

The final quantity of interest is the albedo W which is the ratio of $\sigma_s$ to $\sigma_t$, i.e.

$$W = \sigma_s / \sigma_t \qquad (6\text{-}2\text{-}11)$$

The albedo always lies between zero and unity and measures the ratio of power scattered to power absorbed. Scatterers having albedos close to zero are very absorptive while scatterers with albedos close to one scatter much more power than they absorb.

6-15

## 6.2.2  Single-Scatterer Properties

The parameters that affect the cross-sections are the trunk radius, $a$, the frequency, $f$, and the complex susceptibility, $\chi_\ell$. The scattering cross-sections will be computed for trunk radii of 1, 5 and 10 centimeters since these represent typical trunk radii found in forests. The frequency range will be chosen from 200 MHz to 2000 MHz and three models for the susceptibility will be used. These three models have been called CyberCom Model I, II and III. They have been defined and discussed in Appendix A, [42]. All three models have a constant real susceptibility independent of frequency. The imaginary part of the susceptibility $\chi_\ell''$ differs in the models. For Model I, $\chi_\ell''$ is constant; for Model II, the conductivity of the medium is constant, while for Model III relaxation losses have been added to Model II. The variation of $\chi_\ell''$ for each model is shown in Figure 6.4. Model III most closely depicts the actual trunk medium. The other models are used to show the sensitivity of the results to variations in the trunk susceptibility.

## 6.2.2.1  Differential Scattering Cross-Section

The first curves to be discussed are the plots of $\sigma_d$ versus $\phi'$ shown in Figures 6.5, 6.6 and 6.7. Each figure presents $\sigma_d$ curves (scattering patterns) at frequencies of 200, 300, and 600 MHz at a fixed tree radius. The curves have been normalized but the same normalization constant is used for all plots having the same tree radius, i.e., curves on the same figure have the same normalization. CyberCom Model III has been used in the computations. Scattering patterns have not been plotted for CyberCom Model I and II.

An examination of the curves shows that at low frequencies, i.e. 200 and 300 MHz, the trunks of radii 1 and 5 cm are almost perfect isotropic radiators. As expected, as the frequency increases for a fixed trunk radius, the scattering pattern becomes more directed toward the forward direction. This trend becomes more pronounced as the trunk radius is increased.
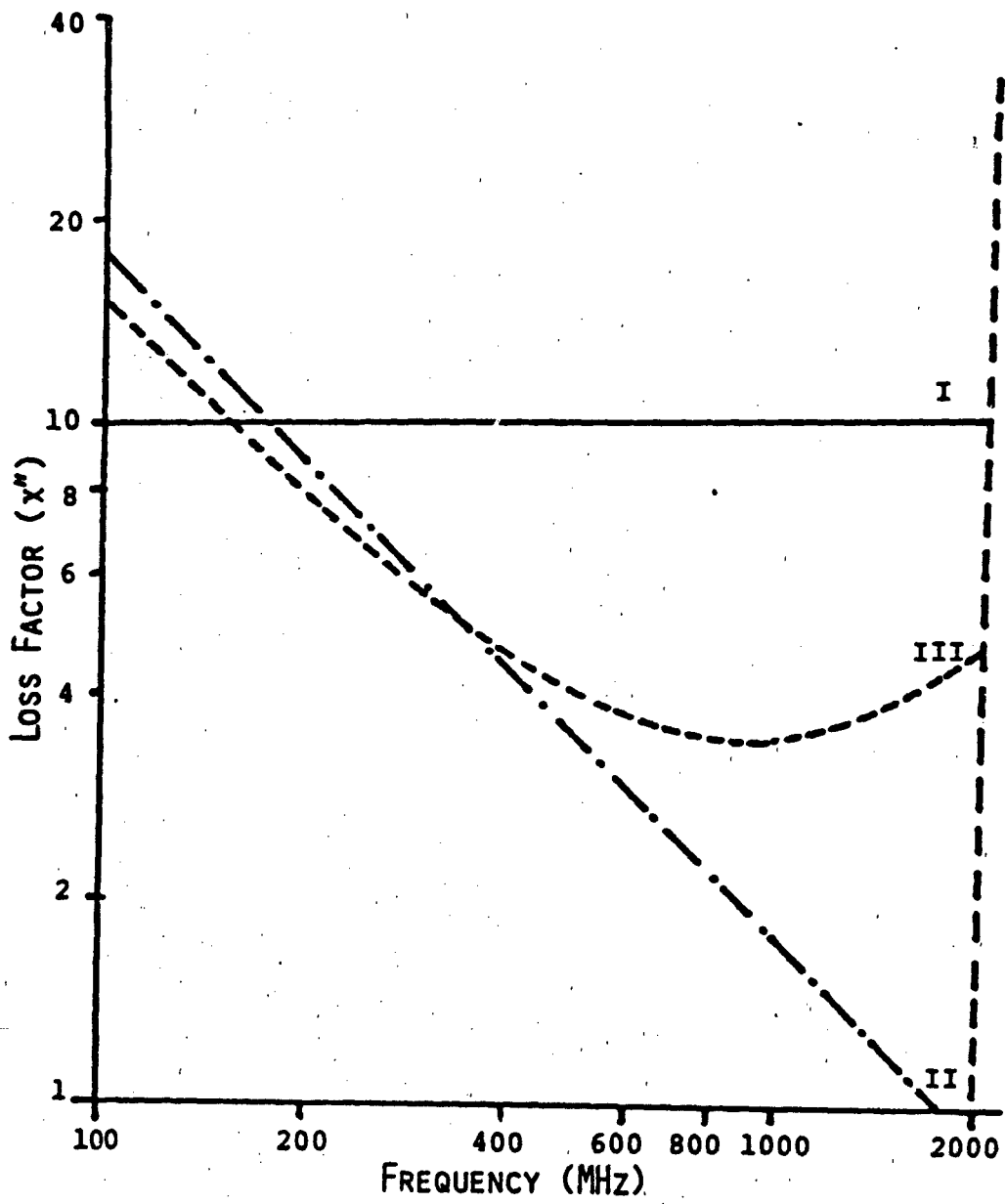
Figure 6-4: Loss Factor of Trunk Material

Radius = 1.0 cm
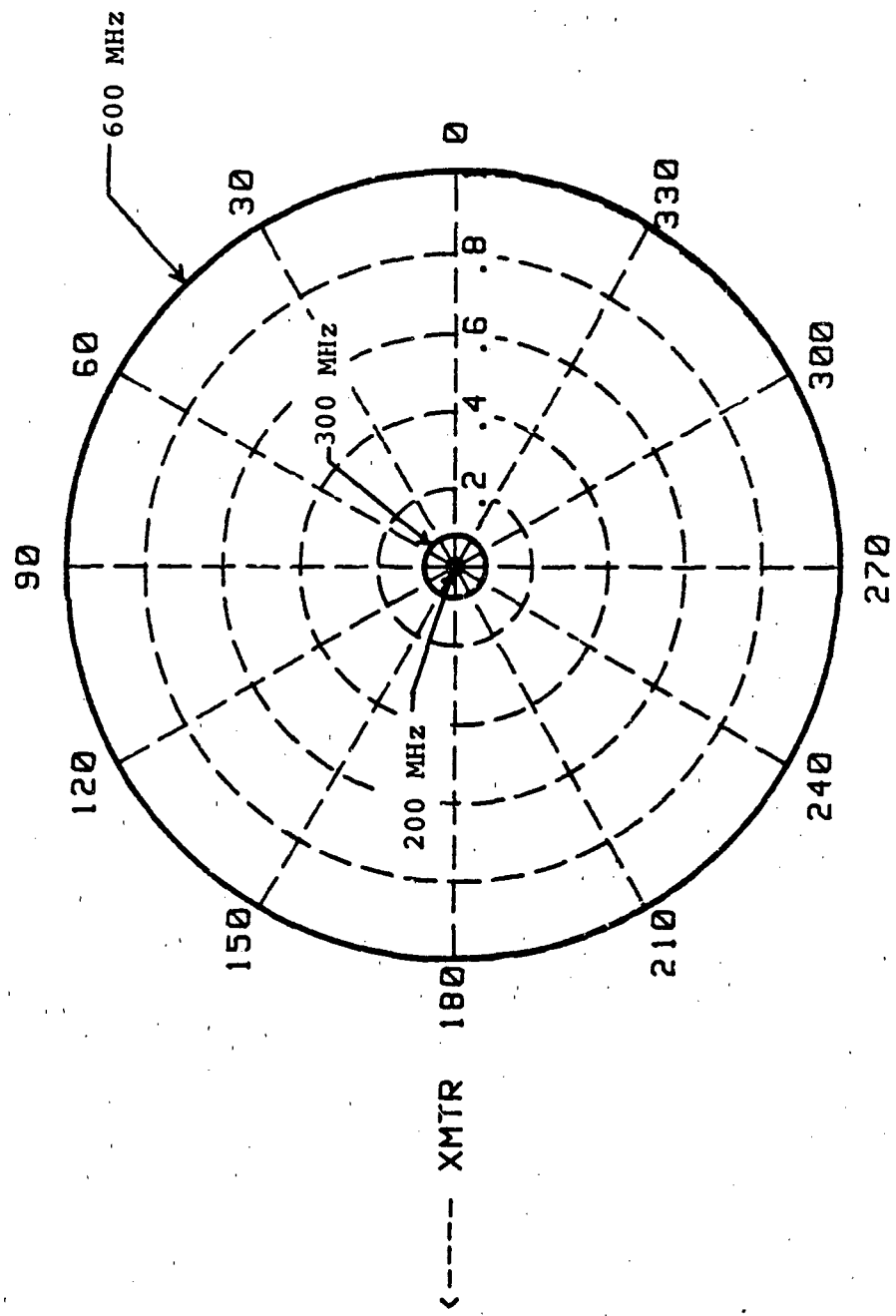
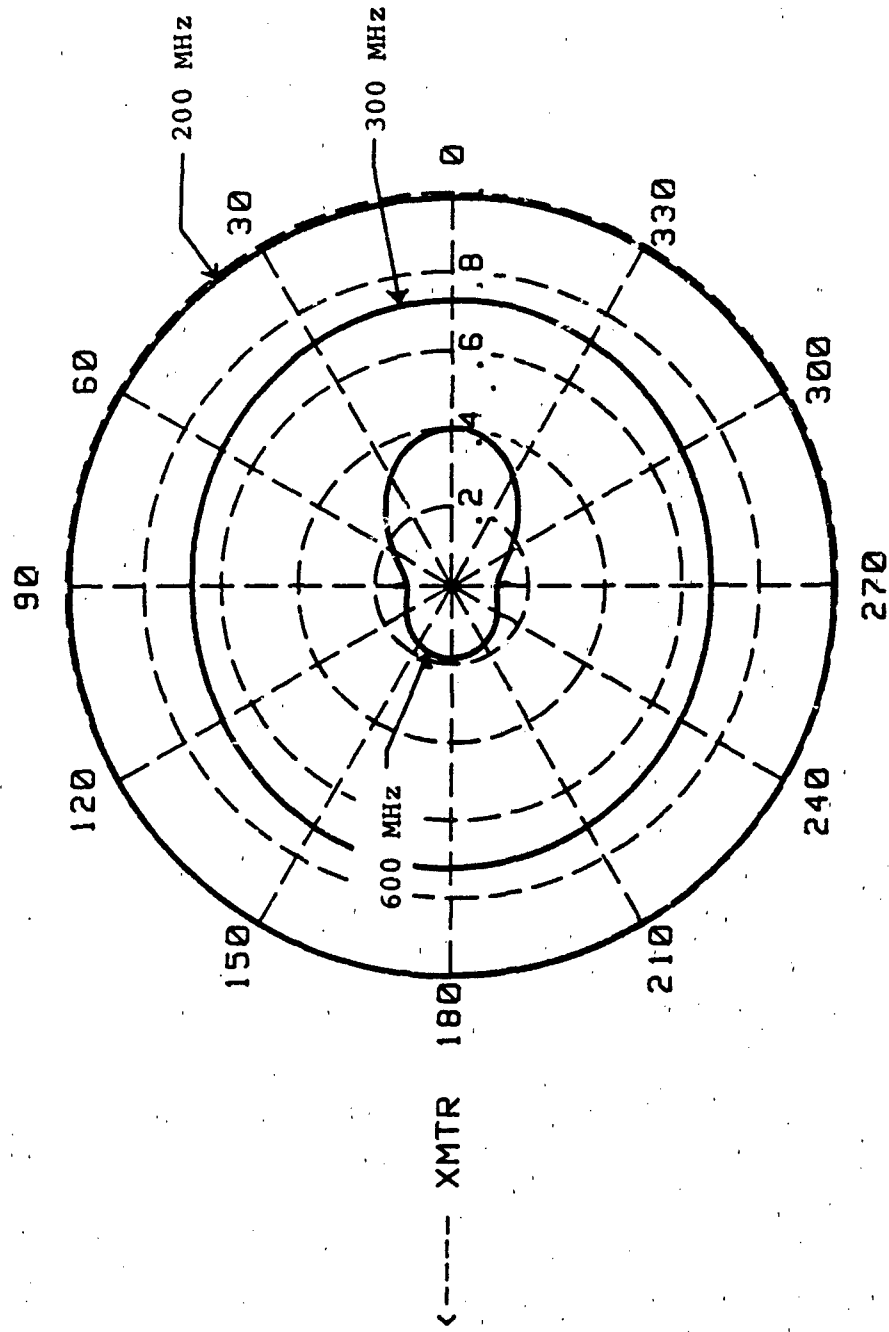Figure 6-5   Plane-Wave Scattering Pattern From a Single Trunk

6-18

Radius = 5.0 cm



Figure 6-6  Plane-Wave Scattering Pattern From a Single Trunk
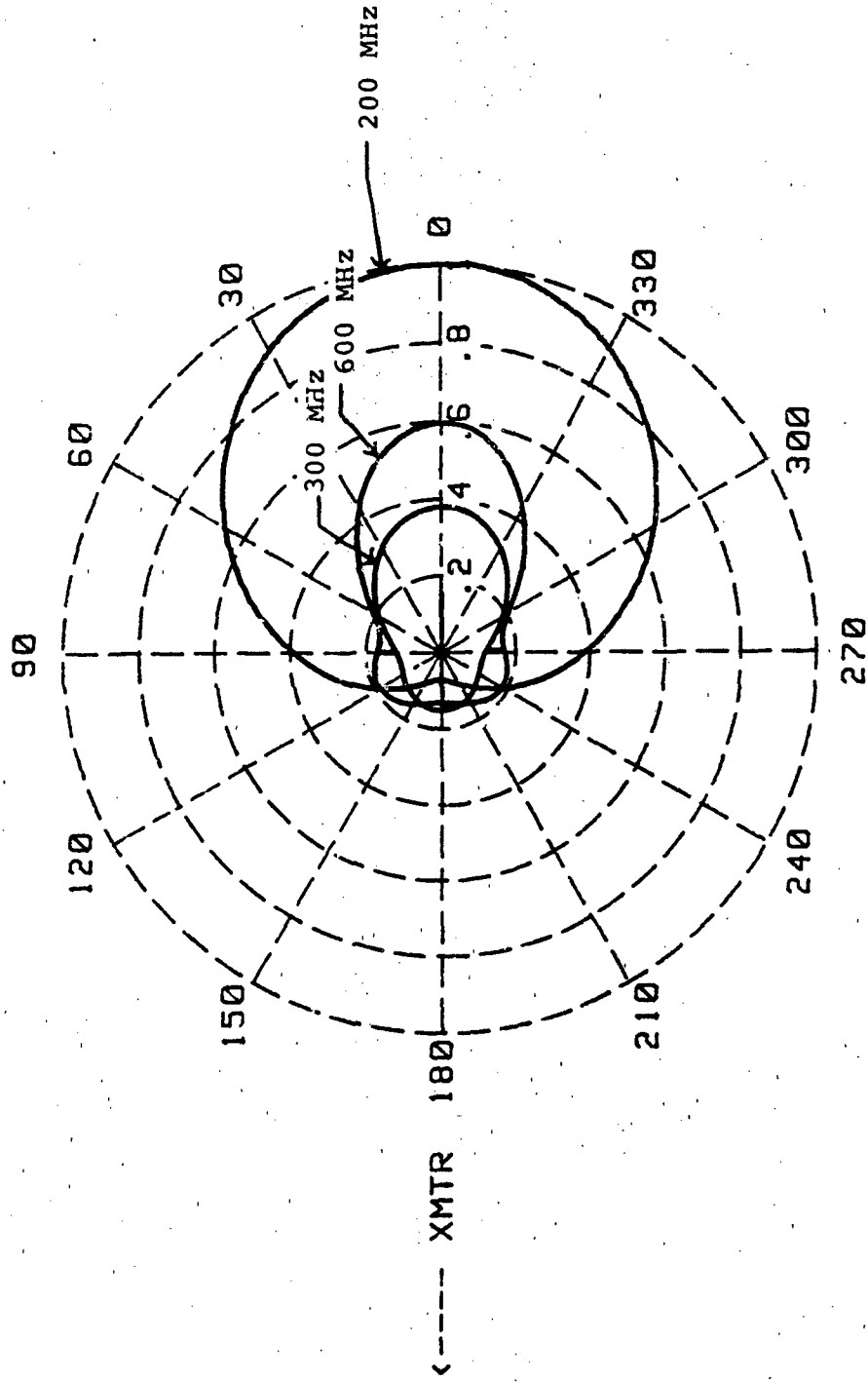
6-19

Radius = 10.0 cm



Figure 6-7  Plane-Wave Scattering Pattern From a Single Trunk

## 6.2.2.2 Albedo and Total Cross-Section

In Figures 6.8 through 6.13 the albedos and the total cross-sections are plotted as functions of frequency for CyberCom Models I, II and III. This is done for trunk radii of 1, 5 and 10 centimeters. The albedo curves indicate the importance of scattering compared to absorption while the $\sigma_t$ curves are directly related to the mean wave since the mean wave decays at a rate $\exp[-\rho\sigma_t z]$. Values for $\sigma_s$ have not been plotted since they can be computed by inspection from the albedo and $\sigma_t$ curves by using Equation (6-2-11).

An examination of the albedo graphs shows similar curves for all permittivity models and that as the trunk radius becomes larger, the curves oscillate more rapidly with smaller amplitudes. This is because large trunks reach resonance at lower frequencies. It is interesting to compare the $\sigma_t$ curves for 1 and 5 centimeters. The one centimeter curves increase with increasing frequency up to 600 MHz. This indicates the attenuation of the mean wave is becoming greater with increasing frequency. For the 5 centimeter trunks, however, the $\sigma_t$ curves are decreasing with increasing frequency and thus the mean wave propagates farther as the frequency increases.

It is also interesting to compare Models I, II and III to see the effects of loss on the albedo curves. Examining Figure 6.10, it is seen at the high frequency part of the band (1 GHz < f < 2 GHz) that the more lossy the trunk medium, the smaller are the oscillations or resonances that occur. It should be pointed out however, that these oscillations will be averaged out when a distribution of trunk sizes is used to represent a realistic forest.

The curves of the albedo for trunk radii of 5 and 10 centimeters are very high, indicating that the scattered component of field will be important. Only for trunk radii of 1 centimeter and for frequencies of less than 400 MHz does the albedo drop to lower values. Thus even though the mean wave may have decreasing attenuation for increasing frequencies in large tree

Figure 6-8:   Albedo Versus Frequency for a Trunk Radius of 1cm



Figure 6-9:   Total Cross-Section Versus Frequency
for a Trunk Radius of 1cm
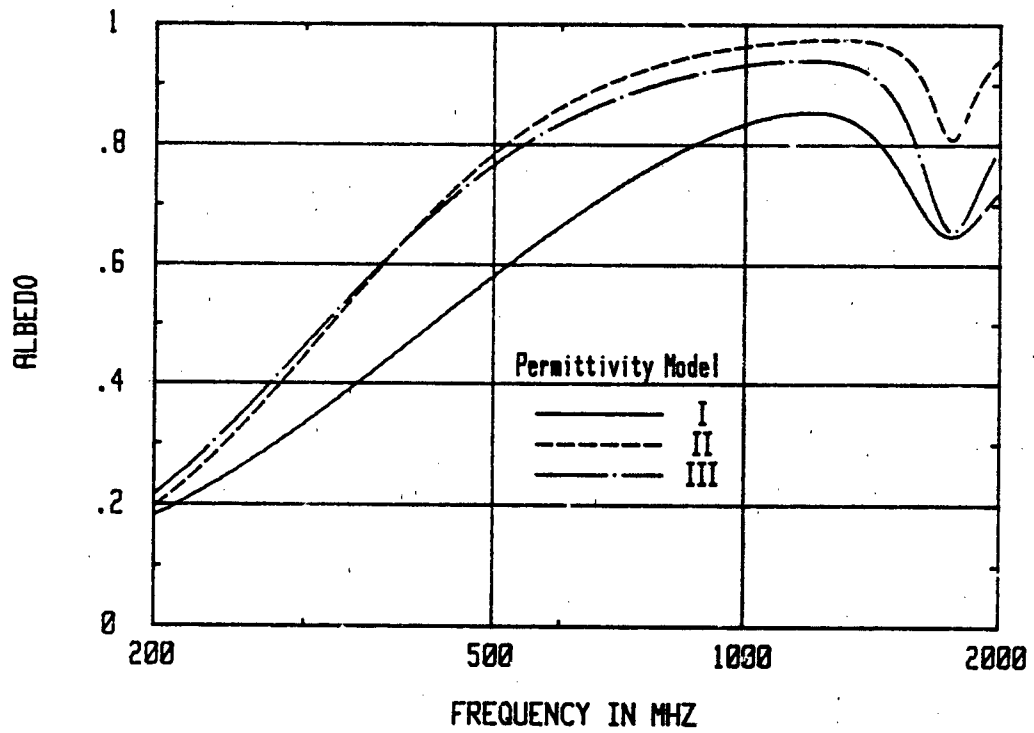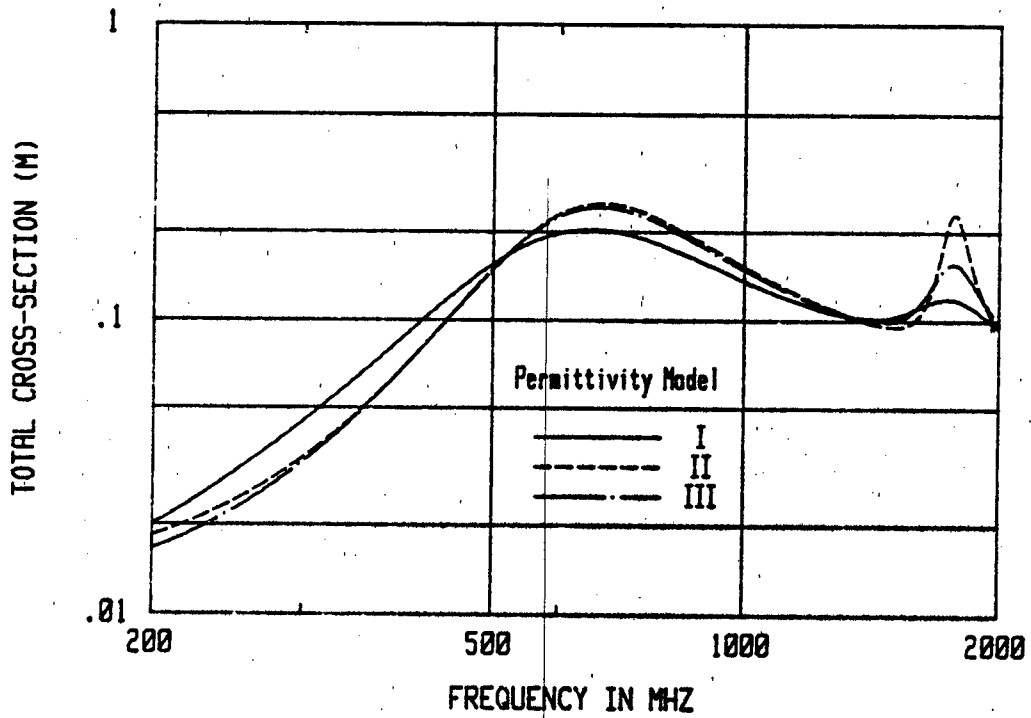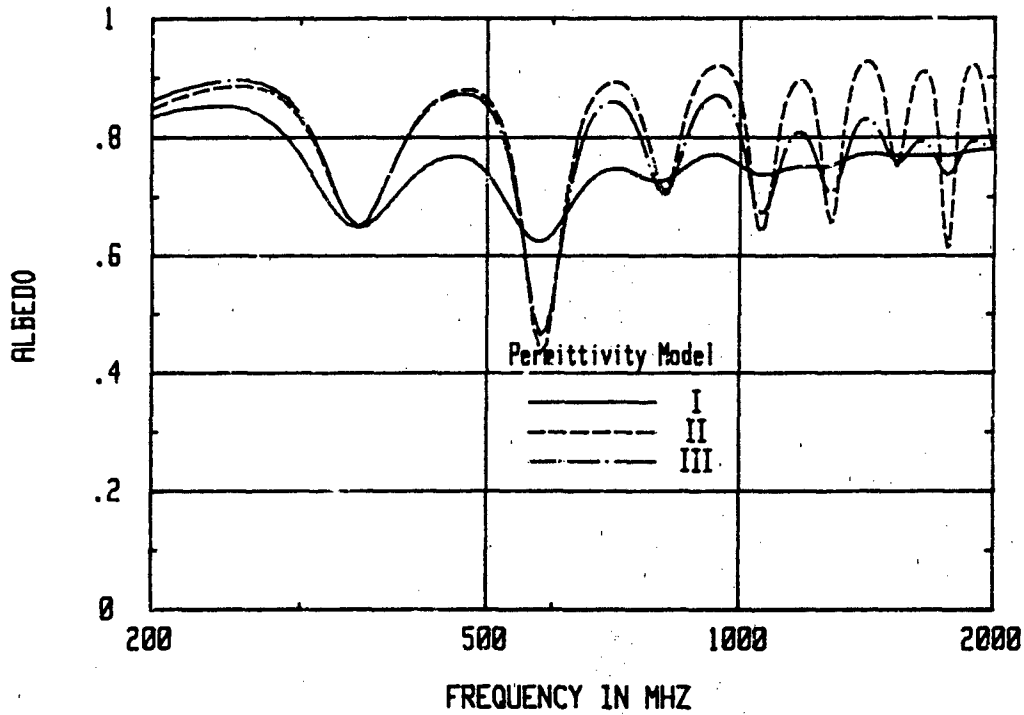
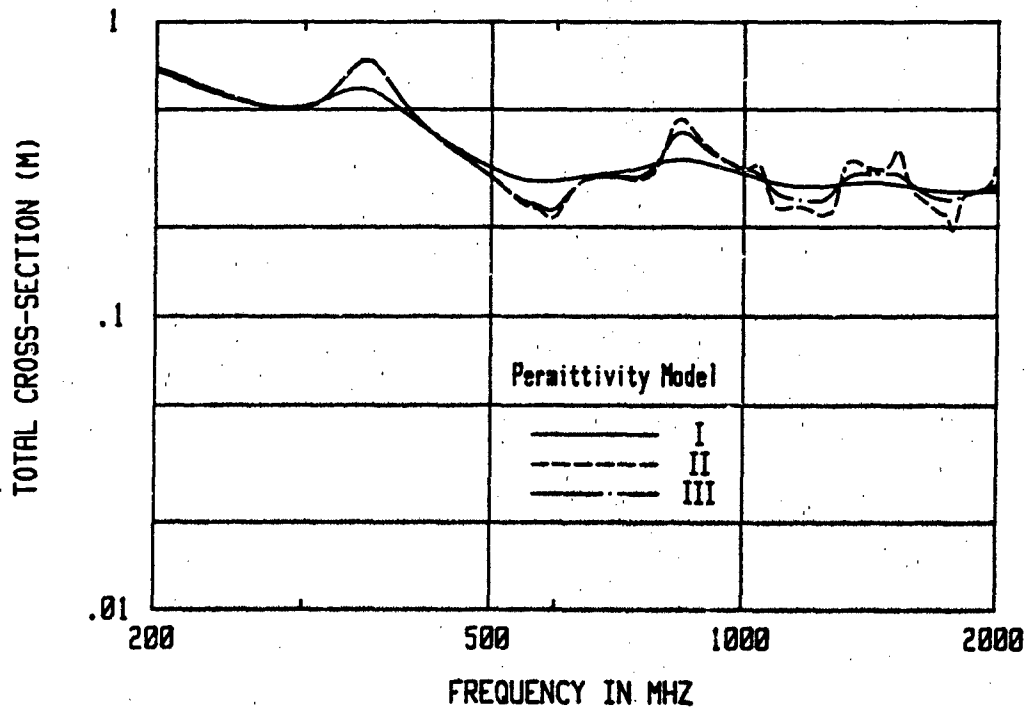Figure 6-10:   Albedo Versus Frequency for a Trunk Radius of 5cm



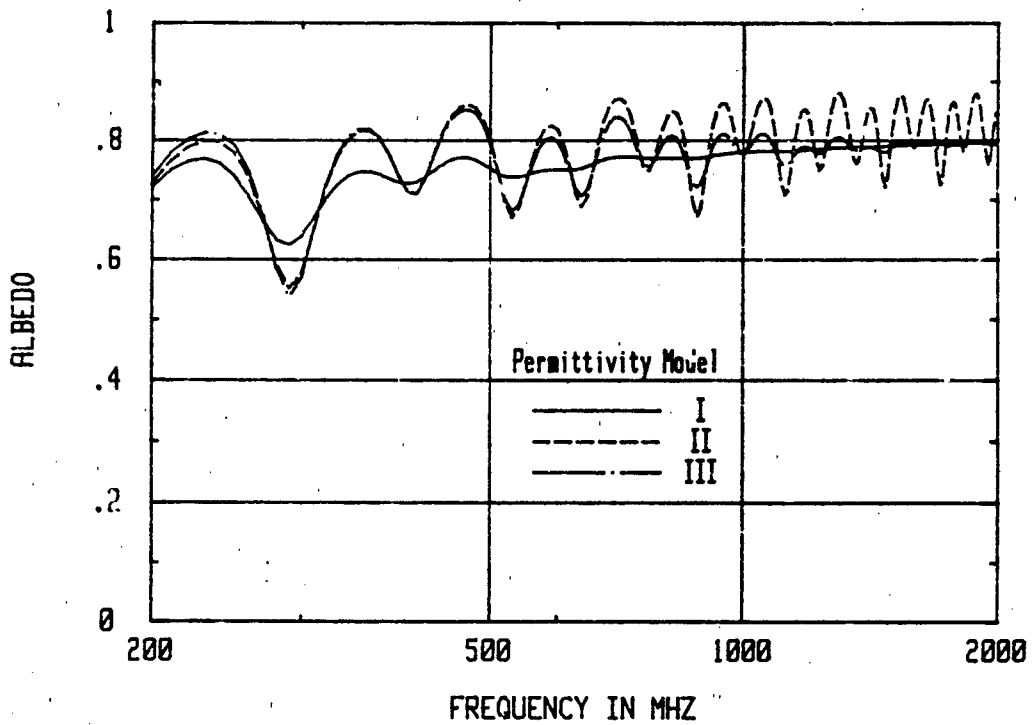Figure 6-11:   Total Cross-Section Versus Frequency
for a Trunk Radius of 5cm

6-23

Figure 6-12: Albedo Versus Frequency for a Trunk Radius of 10cm
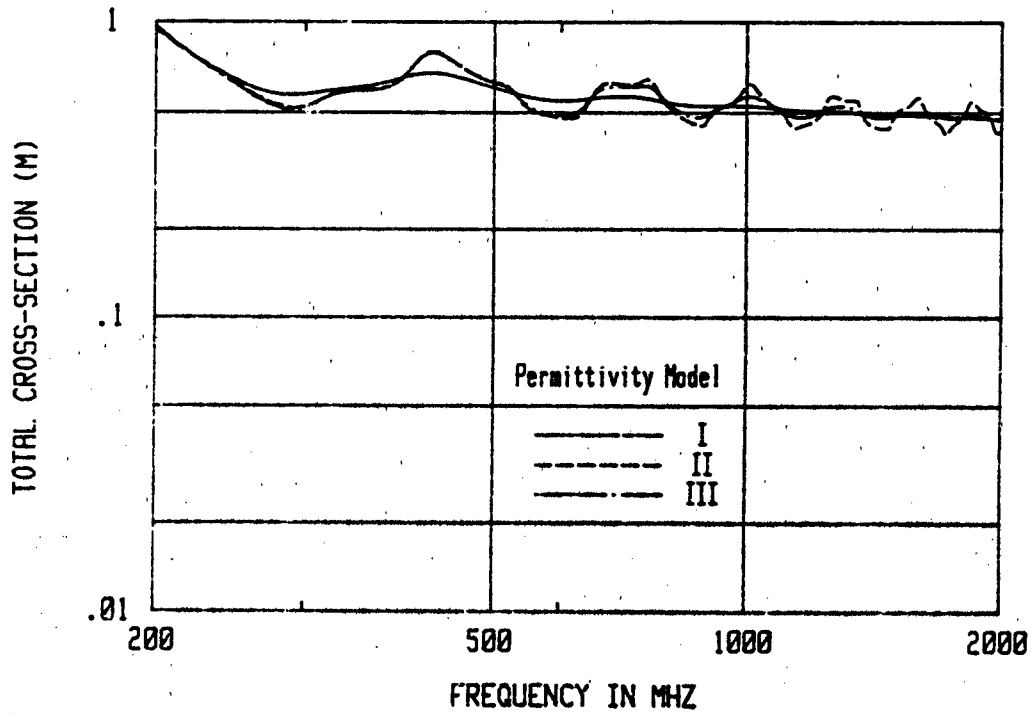


Figure 6-13; Total Cross-Section for a Trunk Radius of 10cm

radii, the scattered component may be much larger than the mean, making the behavior of the mean unimportant.

## 6.3   Frequency Correlation Function for a Thin-Trunk Forest

Propagation of wideband signals through a forested environment requires a knowledge of the frequency correlation function of the medium. With the channel characterized in this manner, the deleterious effects of multiple scattering between forest components can be properly assessed. The frequency correlation function can be found by solving the correlation Equation (6-1-25) with $\underline{x}_t = \hat{\underline{x}}_t$. The equation is difficult to solve unless special assumptions are made. In the present case, trunks whose radii are small compared to a wavelength will be assumed.

In the past, several investigators have found approximate expressions for the frequency correlation function. This calculation has been made for channels having fluctuating media such as those channels involving ionospheric [41,53,77,78] or tropospheric [34,35,69] turbulence, as well as channels involving hydrometeors [35]. In all of these applications, the forward scattering assumption has been made because wavelengths of interest were large compared to medium correlation lengths or particle sizes. In the present case of forest propagation, the forward scattering assumption is not valid over the frequency band of interest for most scatterers. Thus, the correlation equation must be solved directly.

In this subsection, an infinite forest is considered having constant density $\rho$. The waves in the forest are excited by an infinite line source located at the origin; thus $J_z(\underline{x}_t) = \delta(\underline{x}_t)$. The space-frequency correlation equation, (6-1-25) with $\underline{x}_t = \hat{\underline{x}}_t$ will be solved for trunks with diameters small compared to a wavelength. Using this low-frequency assumption, the correlation equation can be substantially simplified. To see this, multiply Equation (6-1-25) from the left by $\pounds^{-1}\pounds^{*-1}$ and use Equation (6-1-20). The resulting equation for the frequency correlation function is:

$$\Gamma(\underline{x}_t, \omega_1, \omega_2) = \Gamma_o(\underline{x}_t, \omega_1, \omega_2)$$

$$- \beta_{12} \int d\underline{s}_t \, G(\underline{x}_t - \underline{s}_t, \omega_1) G^*(\underline{x}_t - \underline{s}_t, \omega_2) \Gamma(\underline{s}_t, \omega_1, \omega_2) \qquad (6\text{-}3\text{-}1)$$

where $\Gamma(\underline{x}_t, \omega_1, \omega_2) = \langle \psi(\underline{x}_t, \omega_1) \psi^*(\underline{x}_t, \omega_2) \rangle$ is the frequency correlation function; $\Gamma_o(\underline{x}_t, \omega_1, \omega_2) = \langle \psi(\underline{x}_t, \omega_1) \rangle \langle \psi^*(\underline{x}_t, \omega_2) \rangle$ is the coherent portion of the correlation function,

$$\beta_{12} = \rho k_1^2 k_2^2 \alpha_1 \alpha_2^* \quad , \qquad (6\text{-}3\text{-}2)$$

$$k_i = \omega_i / c_o \quad , \qquad \alpha_i = \alpha(\omega_i) \qquad i = 1, 2 \qquad (6\text{-}3\text{-}3)$$

and $c_o = (\mu_o \epsilon_o)^{-\frac{1}{2}}$ is the free-space velocity of light.

The Green's function $G(\underline{x}_t, \omega)$ appearing in Equation (6-3-1) satisfies Equation (6-1-9) with the low—frequency assumption and $\underline{x}_{t_o} = 0$. The equation is

$$[\nabla_t^2 + k^2(1 + \rho\alpha)] G(\underline{x}_t, \omega) = \delta(\underline{x}_t) \qquad (6\text{-}3\text{-}4)$$

The solution to this two-dimensional mean Green's function equation is given by

$$G(\underline{x}_t, \omega) = \frac{j}{4} H_o^{(2)}(\kappa x_t) \quad , \qquad x_t = |\underline{x}_t| \qquad (6\text{-}3\text{-}5)$$

where

$$\kappa = k\sqrt{1 + \rho\alpha} \quad , \qquad k = \omega / c_o \qquad (6\text{-}3\text{-}6)$$

and $H^{(2)}(r)$ is the Hankel function of zero order and second kind. The mean wave $\langle \psi(\underline{x}_t, \omega) \rangle$ can easily be found by multiplying Equation (6-3-4) by $j\omega\mu_o$. Referring to Equation (6-1-13) it is seen that

$$\langle \psi(\underline{x}_t, \omega) \rangle = G(\underline{x}_t, \omega) / j\omega\mu_o . \qquad (6\text{-}3\text{-}7)$$

The frequency correlation equation, (6-3-1) can be recast by employing the Fourier transform since the integral term is

a convolution of $GG^*$ and $\Gamma$. Rather than proceeding this way, the Green's functions and $\Gamma_0$ will be replaced by their far-field approximations. This simplifies the calculation substantially and only restricts the observation point to be in the far-field of the source. Tree trunks that are in the near field of each other are not correctly accounted for. This does not represent a large error, however, since the fractional area occupied by tree trunks is small.

Now using the asymptotic approximation for the Hankel function in Equation (6-3-5), the Green's function becomes

$$G(x_t, \ ) \sim \frac{j}{2\sqrt{2\pi k x_t}}\, e^{-j\left(kx_t - k\rho\frac{\alpha}{2} - \frac{\pi}{4}\right)} \qquad (6\text{-}3\text{-}8)$$

where

$$\kappa \approx k(1 + \rho\,\alpha/2) \qquad (6\text{-}3\text{-}9)$$

has been used. The latter is a good approximation for $\kappa$ since $\rho\alpha \ll 1$ for sparse forests.

If this far-field approximation is used in the frequency correlation equation, for the Green's function and for $\Gamma_0$, the result is the following approximate correlation equation:

$$\Gamma(\underline{x}_t, \omega_1, \omega_2) = K_0(\underline{x}_t, \omega_1, \omega_2)$$
$$- \beta_{12} \int d\underline{s}_t K(\underline{x}_t - \underline{s}_t, \omega_1, \omega_2)\, \Gamma(\underline{x}_t, \omega_1, \omega_2) \qquad (6\text{-}3\text{-}10)$$

where

$$K(\underline{x}_t, \omega_1, \omega_2) = \frac{c}{x_t}\, e^{-j\gamma x_t} \qquad (6\text{-}3\text{-}11)$$

with

$$\gamma = \Delta k - \rho(k_1\alpha_1 - k_2\alpha_2^*)/2 \quad , \quad \Delta k = k_1 - k_2 \qquad (6\text{-}3\text{-}12)$$

$$c = [(8\pi)^2 k_1 k_2]^{-\frac{1}{2}} \qquad (6\text{-}3\text{-}13)$$

and

$$K_o(\underline{x}_t, \omega_1, \omega_2) = K(\underline{x}_t, \omega_1, \omega_2) / (\omega \mu_o)^2 \qquad (6\text{-}3\text{-}14$$

This approximate frequency correlation equation is easier t transform since the Fourier transform of $K(\underline{x}_t, \omega_1, \omega_2)$ can b calculated explicitly.

Taking the Fourier transform

$$\tilde{\Gamma}(\underline{k}_t, \omega_1, \omega_2) = \frac{1}{(2\pi)^2} \int d\underline{x}_t \, \Gamma(\underline{x}_t, \omega_1, \omega_2) e^{j\underline{k}_t \cdot \underline{x}_t} \qquad (6\text{-}3\text{-}15$$

of the correlation Equation (6-3-10) and solving for $\tilde{\Gamma}(\underline{k}_t, \omega_1, \omega_2$ yields

$$\tilde{\Gamma}(\underline{k}_t, \omega_1, \omega_2) = \frac{\tilde{K}_o(\underline{k}_t, \omega_1, \omega_2)}{1 - \tilde{\beta}_{12}\tilde{K}(\underline{k}_t, \omega_1, \omega_2)} \qquad , \qquad \tilde{\beta}_{12} = (2\pi)^2 \beta_{12} \qquad (6\text{-}3\text{-}16$$

where

$$\tilde{K}(\underline{k}_t, \omega_1, \omega_2) = \frac{c}{2\pi\sqrt{k_t^2 + \hat{\gamma}^2}} \qquad , \qquad k_t = |\underline{k}_t| \qquad (6\text{-}3\text{-}17$$

$$\tilde{K}_o(\underline{k}_t, \omega_1, \omega_2) = \tilde{K}(\underline{k}_t, \omega_1, \omega_2) / \omega^2 \mu_o^2 \qquad (6\text{-}3\text{-}18$$

and

$$\hat{\gamma} = j\gamma \qquad (6\text{-}3\text{-}19$$

The solution for the frequency correlation function is no obtained by transforming Equation (6-3-16). This calculatio yields

$$\Gamma(x_t, \omega_1, \omega_2) = c \int_0^\infty \frac{dk_t k_t J_o(k_t x_t)}{\sqrt{k_t^2 + \hat{\gamma}^2} - b} \qquad (6\text{-}3\text{-}20$$

where

$$b = \frac{\tilde{\beta}_{12} c}{2\pi} = \rho(k_1 k_2)^{3/2} \, \alpha_1 \alpha_2^* / 4 \qquad (6\text{-}3\text{-}21$$

In obtaining Equation (6-3-20) the integration over the angular variable $\phi$ has been performed giving the Bessel function $J_0(k_t x_t)$. The calculations of this subsection are similar to those appearing in Chapter 7, [42]; in fact, this calculation reduces to that one for $\omega_1 = \omega_2 = \omega$.

The integral representation for $\Gamma(x_t, \omega_1, \omega_2)$ is very slowly convergent and thus difficult to numerically evaluate. Following a parallel development to that performed in Appendix G, [42], an alternate representation for $\Gamma(x_t, \omega_1, \omega_2)$ can be obtained. It is

$$\Gamma(x_t, \omega_1, \omega_2) = -j\pi c b H_0^{(2)}(-j\sqrt{\hat{\gamma}^2 - b^2}\, x_t)$$

$$- jc \int_0^\infty dp\, p^2\, \frac{H_0^{(2)}(-j\sqrt{p^2 + \hat{\gamma}^2}\, x_t)}{p^2 + b^2} \qquad (6-3-22)$$

Before proceeding to evaluate numerically the above expression it is useful to represent the correlation function as a sum of a coherent part $\Gamma_0$ and an incoherent part $\Gamma_I$, i.e.

$$\Gamma(x_t, \omega_1, \omega_2) = \Gamma_0(x_t, \omega_1, \omega_2) + \Gamma_I(x_t, \omega_1, \omega_2) \qquad (6-3-23)$$

It is the incoherent portion of the correlation function $\Gamma_I$ that should tend to zero as $|\omega_1 - \omega_2|$ becomes large.

The incoherent correlation $\Gamma_I$ can be obtained by subtracting $\Gamma_0$ from $\Gamma$. An expression for $\Gamma_0$ can be obtained from Equation (6-3-22) by setting $\beta_{12} = 0$, which implies that $b = 0$. The result is

$$\Gamma_0(x_t, \omega_1, \omega_2) = -jc \int_0^\infty dp\, H_0^{(2)}(-j\sqrt{p^2 + \hat{\gamma}^2}\, x_t) \qquad (6-3-24)$$

Now subtracting $\Gamma_0$ from $\Gamma$ as given in Equation (6-3-22) yields the desired expression for $\Gamma_I$

$$\Gamma_I(x_t, \omega_1, \omega_2) = -j\pi cb H_o^{(2)}(-j\sqrt{\hat{\gamma}^2 - b^2}\, x_t)$$

$$- jc\int_0^\infty dp\, p^2\, \frac{H_o^{(2)}(-j\sqrt{p^2 + \hat{\gamma}^2}\, x_t)}{p^2 + b^2} \qquad (6\text{-}3\text{-}25$$

A normalized form of $\Gamma_I$ has been plotted in Figures 6.1 and 6.15 for center frequencies of 200 and 300 MHz respectively. For each frequency a plot is shown for distances of 200 and 500 meters. Only frequencies close to the lower edge of the band of interest and trunks of small radius are considered because of the Rayleigh assumption implicit in the derivation of Equation (6-3-1). The normalized correlation function $\overline{\Gamma}_I$ represents $\Gamma_I$ divided by its value at $\omega_1 = \omega_2$, i.e.

$$\overline{\Gamma}_I(x_t, \omega_1, \omega_2) = \Gamma_I(x_t, \omega_1, \omega_2)/\Gamma_I(x_t, \omega_1, \omega_1) \qquad (6\text{-}3\text{-}26$$

This has been plotted versus the frequency difference $\omega_1 - \omega_2$. Both the real and imaginary parts of $\overline{\Gamma}_I$ have been plotted in each case. The upper and lower envelopes represent graphs of the magnitude of $\overline{\Gamma}_I$ and its negative respectively. The curves are plotted until the value of $|\overline{\Gamma}_I|$ reaches 0.1 and then they are terminated. The correlation bandwidth $B_C$ measures the frequency difference, $\omega_1 - \omega_2$ for which $\overline{\Gamma}_I$ is negligible. It will be assumed that $B_C$ is the value at which $|\overline{\Gamma}_I|$ is equal to 0.1.

The curves will now be discussed wholly in terms of the correlation bandwidth, $B_C$. Examining Figure 6.14 for 200 MHz, it is seen that the correlation bandwidth decreases from 6 MHz to 4 MHz as the distance increases from 200 to 500 meters. Increasing the frequency by 50% to 300 MHz lowers the correlation bandwidth to 2 MHz at 200 meters and 1 MHz at 500 meters. The trends appear to be that the correlation bandwidth decreases with increasing distance and increasing frequency. It should be recalled, however, that this is just a low-frequency result, and the trends should not be interpreted too broadly.

Frequency = 200. MHz
Rho = 1000./ha
Rad. = .01 m

Distance = 200. m
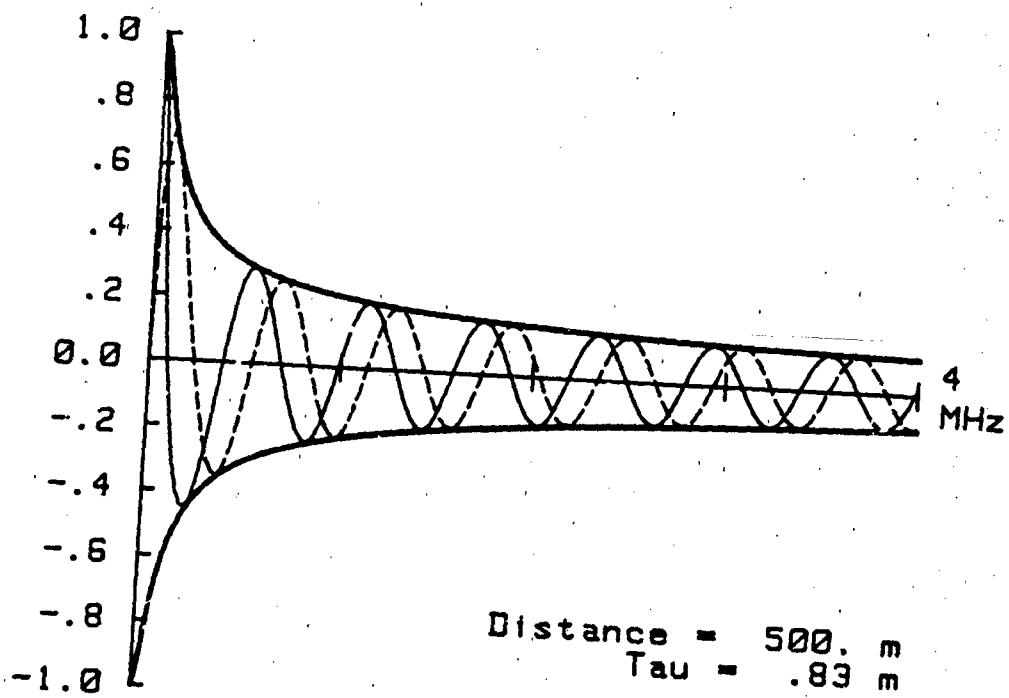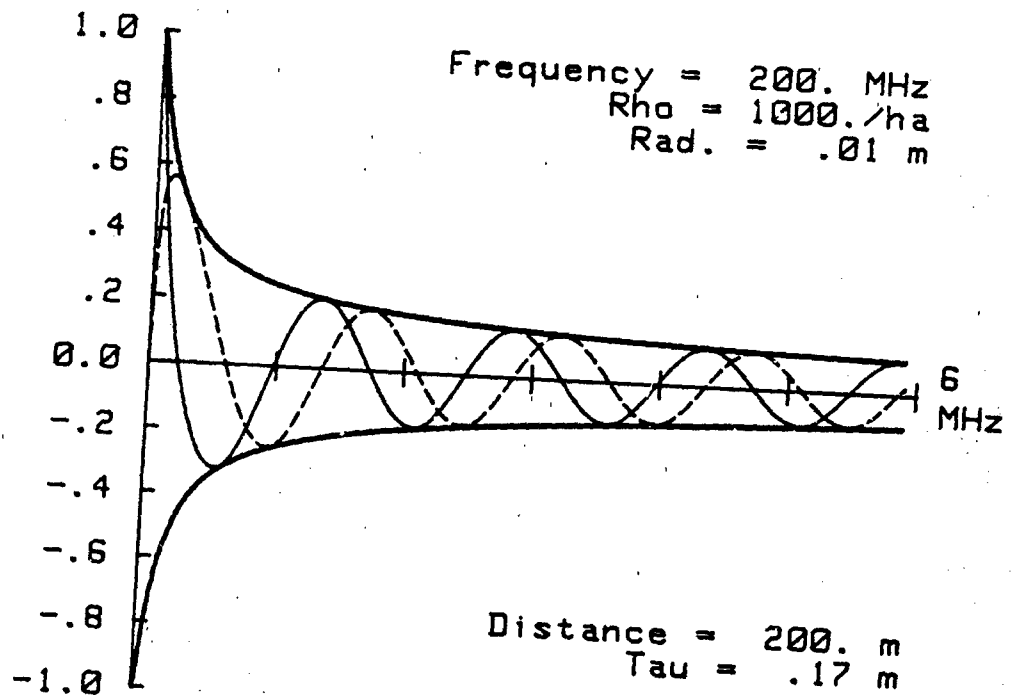Tau = .17 m

Distance = 500. m
Tau = .83 m

Figure 6-14:  Normalized Frequency Correlation Functions
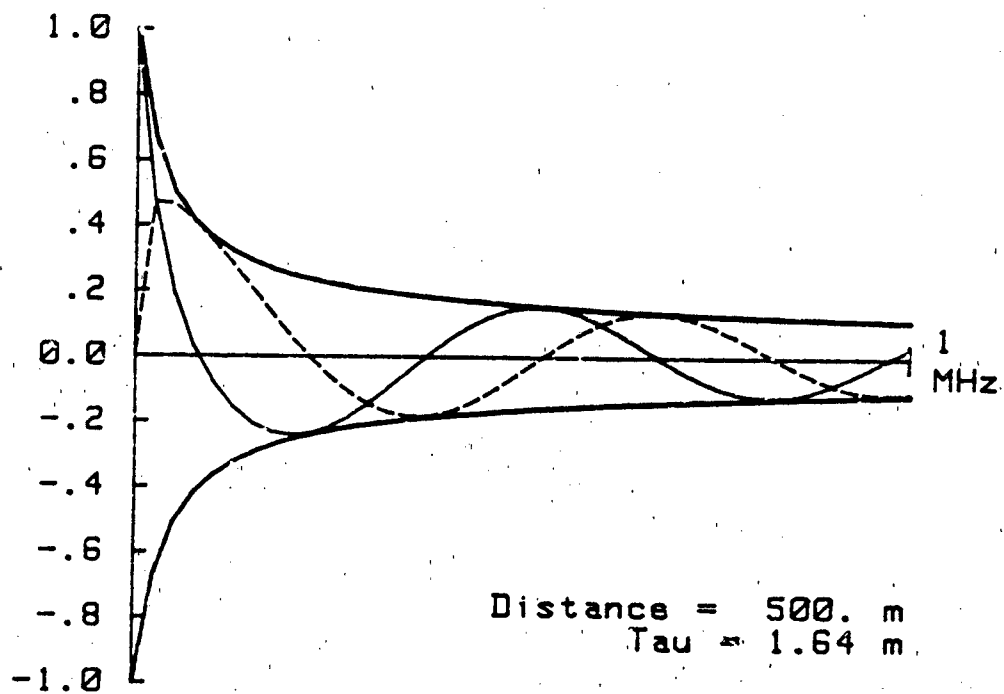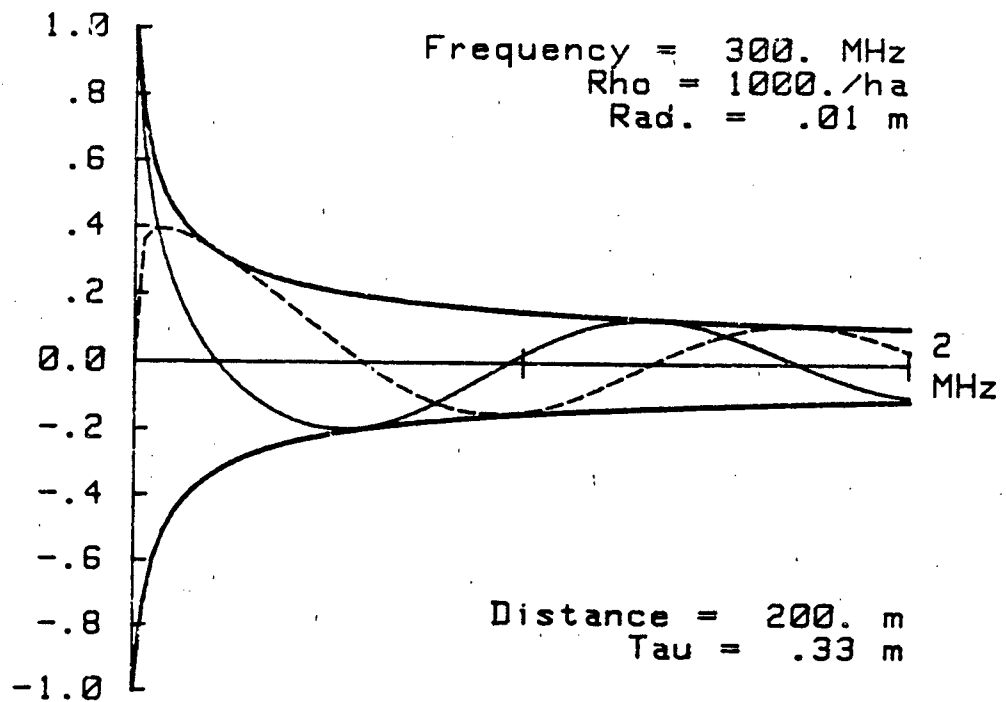Versus Difference Frequency

Figure 6-15: Normalized Frequency Correlation Functions Versus Difference Frequency

## 6.4 Intensity Fluctuations and Space Correlation Function for a Forest of Resonant Tree Trunks

Propagation through a random medium of discrete scatterers such as a forest is characterized by a two-component channel model. This model is illustrated in Figure 6.2 and consists of mean and random or fluctuating components. In this subsection, the properties of these components will be studied in a trunk-dominated forest of resonant trees. Emphasis will be placed on obtaining the two-point correlation function $\langle \psi(\underline{x}) \psi^*(\hat{\underline{x}}) \rangle$ at one frequency $\omega$. Two properties of major interest are: the relationship of coherent to incoherent intensity fluctuations as a function of distance and frequency; and the behavior of the space correlation function, $\langle \psi(\underline{x}) \psi(\hat{\underline{x}}) \rangle$, as the distance between $\underline{x}$ and $\hat{\underline{x}}$ increases.

The work of this subsection in part represents a continuation of the material in Chapter 7, [42]. There the relationship between the coherent and incoherent intensity has been examined for an infinite forest of thin tree trunks. The thin tree trunk assumption, although valid for only the lower portion of the frequency band of interest, allowed the correlation Equation (6-1-25) with $\underline{x} = \hat{\underline{x}}$ and $\omega = \hat{\omega}$ to be solved exactly. The results showed that for frequencies as low as 300 MHz intensity fluctuations are quite important and that they increase with distance. These findings will now be extended to the case of resonant trunks.

For the resonant trunk case, solution of the correlation equation by a transform technique does not seem possible, instead, a two-variable perturbation procedure is used to derive a generalized transport equation from the correlation equation. The fractional area is the small perturbation parameter used in the above analysis. The derivation of the transport equation from the correlation equation is presented in Appendix C. The analysis of the transport equation will be given in this subsection. Transport theory has been applied extensively to

discrete scatter problems [25,34,54,58], however, CyberCom has found no application to tree trunk-dominated forests.

## 6.4.1 Problem Formulation

Consider a trunk-dominated forest that occupies the half space, $z > 0$, as is shown in Figure 6.16. The forest is composed of parallel circular dielectric cylinders having radius a. They are distributed with constant density $\rho$. A plane wave of unit intensity is normally incident on the half space and the space correlation function $\langle \psi(\underline{x}) \psi(\hat{\underline{x}}) \rangle$ is evaluated at $\underline{x}$ and $\hat{\underline{x}}$ as shown in Figure 6-16. To allow for certain simplifications due to symmetry, the two points will be assumed to be in the same transverse plane, i.e., their z coordinates will be the same. This restriction will limit the investigation to transverse correlations, however, this is the case of most practical interest for diversity antenna siting.

Because of the assumed location of the observation points $\underline{x}$ and $\hat{\underline{x}}$ and the uniformity of the problem in the transverse direction, the correlation function $\Gamma(\underline{x},\hat{\underline{x}}) = \langle \psi(\underline{x}) \psi^*(\hat{\underline{x}}) \rangle$ only depends on the difference of the transverse coordinates $x-\hat{x}$ and the normal distance into the half space z, thus

$$\Gamma = \Gamma(z,r_x) \quad , \quad r_x = x - \hat{x} \qquad (6-4-1)$$

This correlation function can be written in terms of a generalized specific intensity function, $J(z,r_x,\phi)$, as follows:

$$\Gamma(z,r_x) = \int_0^{2\pi} d\phi \, J(z,r_x,\phi) e^{ik_0 r_x \sin\phi} \qquad (6-4-2)$$

When $r_x = 0$ the generalized specific intensity reduces to the specific intensity $I(z,\phi)$, i.e.

$$J(z,0,\phi) = I(z,\phi) \qquad (6-4-3)$$

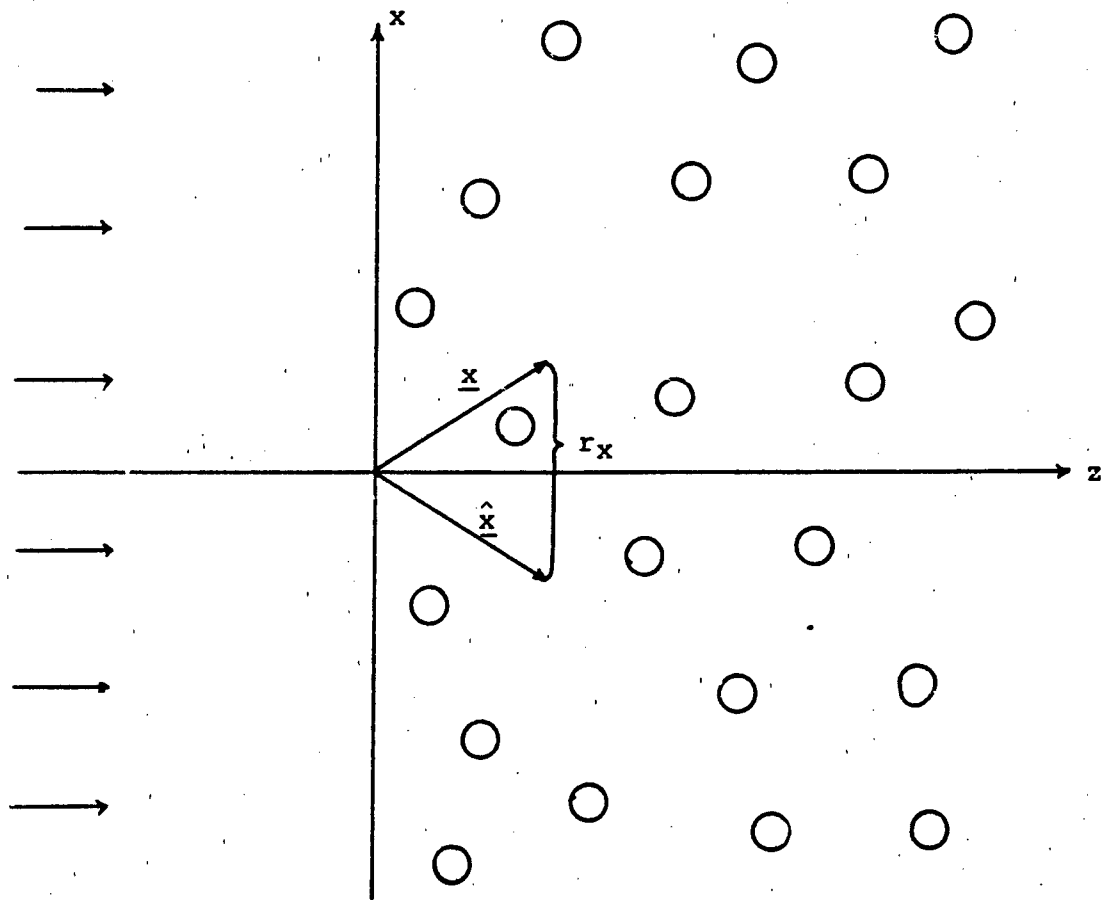From Appendix C, it is seen that $J(z,r_x, )$ satisfies the following transport equation:

Figure 6-16: Plane Wave Normally Incident
on a Trunk-Dominated Forest

$$\cos \phi \ \frac{dJ(z,r_x,\phi)}{dz} + \rho\sigma_t J(z,r_x,\phi)$$

$$(6\text{-}4\text{-}4)$$

$$= \rho A(r_x \sin\phi) \int_0^{2\pi} d\phi' \sigma_{bi}(\phi,\phi') I(z,\phi')$$

$$\phi \in [0, 2\pi]$$

where

$$A(\zeta) = \exp\{i2\pi^2 \rho f(\underline{o},\underline{o}) \zeta/\gamma k_o\} \qquad (6\text{-}4\text{-}5)$$

Here $A(\zeta)$ is the slowly varying part of the mean Green's function discussed in Appendix B. The forward scattering amplitude $f(\underline{o},\underline{o})$ appears in Equation (6-4-5). It is in the direction $\underline{o}$, a unit vector making an angle $\phi$ with the z-axis as in Figure 6-17.

The solution of Equation (6-4-4) for the generalized specific intensity when used in Equation (6-4-2) will give the desired space correlation function. This equation will be solved in two stages. First, $r_x$ will be set equal to zero and the equation will be solved for the specific intensity $I(z,\phi)$; second, the solution for $J(z,r_x,\phi)$ will be found in terms of $I(z,\phi)$. It should be pointed out that the transport equation for $J(z,r_x,\phi)$ is the standard radiative transfer equation that has been considered by many other research workers when $r_x$ is set equal to zero.

### 6.4.2 Intensity Fluctuations

In this subsection, the transport equation for the specific intensity will be solved numerically and the results discussed. The transport equation for the specific intensity is given by

$$\cos \phi \frac{dI(z,\phi)}{dz} + \rho\sigma_t I(z,\phi) = \rho \int_0^{2\pi} \sigma_{bi}(\phi - \phi') I(z,\phi') d\phi' \qquad (6\text{-}4\text{-}6)$$

where the rotational symmetry of the cylindrical scatterers has been utilized by replacing $\sigma_{bi}(\phi,\phi')$ by $\sigma_{bi}(\phi-\phi')$ (see Equation (6-2-3). To solve the transport equation, the boundary conditions at $z = 0$ and $z = \infty$ will be needed. These boundary conditions are:
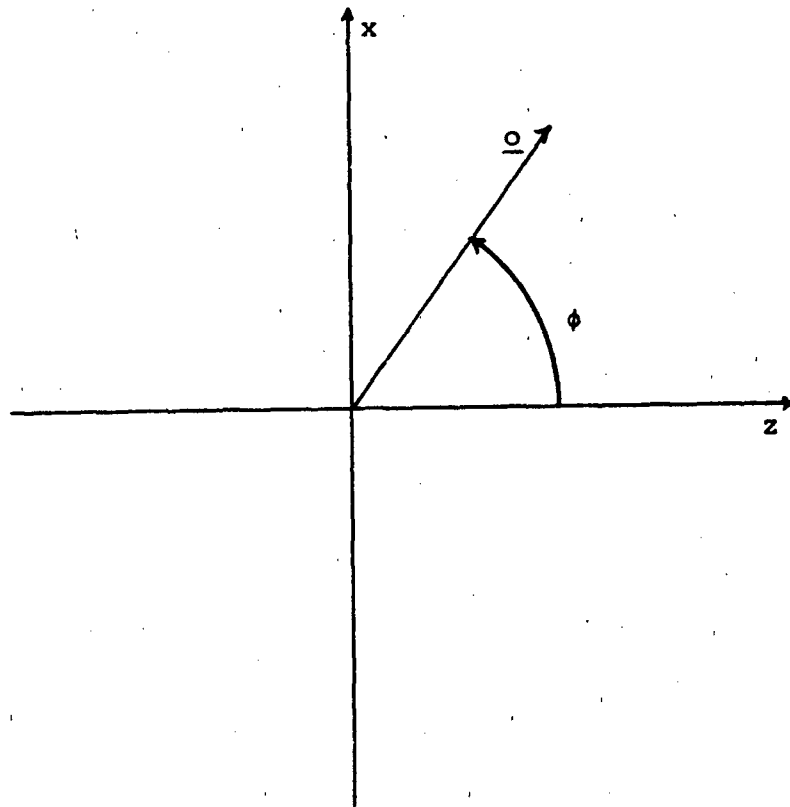
Figure 6-17:   Relationship Between $\underline{o}$ and $\phi$

$$I(0,\phi) = \delta(\phi) \quad , \qquad \phi \in \phi^+ \qquad\qquad (6\text{-}4\text{-}7)$$

$$I(\infty,\phi) = 0 \quad , \qquad \phi \in [0, 2\pi] \qquad\qquad (6\text{-}4\text{-}8)$$

where $\phi^+$ is the set of angles $\phi$ corresponding to propagation in the forward direction. The first boundary condition as given by Equation (6-4-7) states that the incident energy on the half space is in the $\phi = 0$ direction only. The second condition says that all energy will be absorbed as z approaches infinity.

The specific intensity is now decomposed into two parts called the reduced specific intensity $I_r(z,\phi)$, and the diffuse specific intensity $I_d(z,\phi)$. Thus

$$I(z,\phi) = I_r(z,\phi) + I_d(z,\phi) \qquad\qquad (6\text{-}4\text{-}9)$$

where $I_r$ is the solution of the transport equation without the scattering term. It satisfies the equation

$$\cos\phi \, \frac{dI_r(z,\phi)}{dz} + \rho\sigma_t I_r(z,\phi) = 0 \qquad\qquad (6\text{-}4\text{-}10)$$

with boundary conditions as given in Equations (6-4-7) and (6-4-8). The equation for the diffuse intensity is obtained by subtracting Equation (6-4-10) from Equation (6-4-6). The result is

$$\cos\phi \, \frac{dI_d(z,\phi)}{dz} + \rho\sigma_t I_d(z,\phi) = \rho\int_0^{2\pi} \sigma_{bi}(\phi - \phi') I_d(z,\phi')d\phi'$$

$$+ \rho\int_0^{2\pi} \sigma_{bi}(\phi - \phi') I_r(z,\phi')d\phi' \qquad (6\text{-}4\text{-}11)$$

with boundary conditions

$$I_d(0,\phi) = 0 \quad , \qquad \phi \in \phi^+ \qquad\qquad (6\text{-}4\text{-}12)$$

$$I_d(\infty,\phi) = 0 \quad , \qquad \phi \in [0, 2\pi] \qquad\qquad (6\text{-}4\text{-}13)$$

It should be pointed out that the reduced and diffuse specific intensities are exactly the same as the mean or coherent and the incoherent specific intensities respectively. These quantities when substituted in Equation (6-4-2) yield the coherent and incoherent intensities.

The solution of the reduced equation is obtained by inspection. It is

$$I_r(z,\phi) = \delta(\phi) e^{-\tau} \quad , \quad \tau = \rho \sigma_t z \qquad (6\text{-}4\text{-}14)$$

where $\tau$ is the optical depth. Next, the reduced intensity is substituted into the right-hand side of the diffuse Equation (6-4-11). Before solving this equation, the symmetry of $I(z,\phi)$ about $\phi = \pi$, i.e.,

$$I(z,\phi) = I(z, 2\pi - \phi) \qquad \phi \in [0,\pi] \qquad (6\text{-}4\text{-}15)$$

is used to reduce Equation (6-4-11) from the angular range $\phi \in [0, 2\pi]$ to the angular range $\phi \in [0,\pi]$. The diffuse equation becomes

$$\mu \frac{dI_d(\tau,\mu)}{d\tau} + I_d(\tau,\mu) = \int_{-1}^{+1} \frac{p(\mu,\mu')}{\sqrt{1-\mu'^2}} I_d(\tau,\mu') d\mu' \qquad (6\text{-}4\text{-}16)$$

$$+ \frac{\sigma_{bi}(\mu)}{\sigma_t} e^{-\tau} \quad , \quad \mu \in [-1,1]$$

and

$$I_d(0,\mu) = 0 \quad , \quad \mu \in [0,1] \qquad (6\text{-}4\text{-}17)$$

$$I_d(\infty,\mu) = 0 \quad , \quad \mu \in [-1,+1] \qquad (6\text{-}4\text{-}18)$$

The above equation has been written in terms of the dependent variable $\mu$ ($\mu = \cos\phi$) and $\tau$ instead of $\phi$ and $z$. The phase function $p(\mu,\mu')$ is given by

$$p(\mu,\mu') = \frac{\sigma_{bi}(\phi + \phi') + \sigma_{bi}(\phi - \phi')}{\sigma_t} \qquad (6\text{-}4\text{-}19)$$

The integro-differential equation for $I_d(\tau,\mu)$ cannot be solved analytically unless $\sigma_{bi}$ is independent of angle (isotropic

scatterer) [20] which is not the present case as evidenced by the radiation patterns shown in Figures 6.5 thru 6.7. Numerical methods must be used to obtain quantitative results. The method of discrete ordinates [20] will be employed. The integral term is represented by a discrete sum using the Chebyshev-Gauss quadrature formula

$$\int_{-1}^{+1} \frac{f(\mu)}{\sqrt{1-\mu^2}} \, d\mu = \frac{\pi}{2N} \sum_{\substack{n=-N \\ j \neq 0}}^{N} f(\mu_j) \qquad (6\text{-}4\text{-}20)$$

where the $\mu_j$'s correspond to discrete angles $\phi_j$ ($\phi_j = \cos^{-1}\mu_j$) which are defined by

$$\mu_j = \begin{cases} \sin(2j-1)\pi/4N & j=1,\dots,N \\ \mu_{-j} & j=-1,\dots,-N \end{cases} \qquad (6\text{-}4\text{-}21)$$

Using the quadrature formula in the transport equation, (6-4-16) to approximate the integral, and evaluating the equation at $\mu = \mu_j$, $j = \pm 1,\dots,\pm N$, results in a system of 2N ordinary differential equations with constant coefficients. These equations are:

$$\frac{dI_d(\tau,\mu_i)}{d\tau} + \frac{1}{\mu_i} I_d(\tau,\mu_i) = \frac{\pi}{2N} \sum_{\substack{j=-N \\ j \neq 0}}^{N} \frac{p(\mu_i,\mu_j)}{\mu_i} I_d(\tau,\mu_j)$$

$$\pm \frac{\sigma_{bi}(\mu_i)}{\sigma_t} e^{-\tau} \ , \quad i=\pm 1,\dots,\pm N \quad (6\text{-}4\text{-}22)$$

with boundary conditions

$$I_d(0,\mu_i) = 0 \qquad\qquad i=1,\dots,N \qquad (6\text{-}4\text{-}23)$$

$$I_d(\infty,\mu_i) = 0 \quad , \quad i=\pm 1,\dots,\pm N \qquad (6\text{-}4\text{-}24)$$

The equations can be solved for the $I_d(\tau,\mu_i)$, $i = \pm 1,\dots,\pm N$, by standard numerical techniques. The larger the value of N chosen, the closer the computed values come to the actual solution

of Equation (6-4-22), and the more points are available to approximate $I_d(\tau,\mu)$ over the complete angular range.

The calculation of $I_d(\tau,\mu)$ has been carried out for N = 20. All calculations in this subsection have been done using CyberCom Model III for the trunk permittivity, a tree radius of 5 centimeters and a density of 1000 trees per hectare. Curves of the normalized diffuse specific intensity, $I_d$, versus the azimuthal scattering angle, $\phi$, have been plotted for frequencies of 200, 300, and 600 MHz and optical depths of 0.5, 1 and 5. This is a total of nine graphs which have been included in the Annex with figure numbers 6A-1 through 6A-9. In addition, three curves have been plotted at a constant distance of 200 meters for frequencies of 200, 300, and 600 MHz. These are included in the Annex with figure numbers 6A-10 through 6A-12. The curves have been presented in a polar format. A spline routine has been used to connect the discrete output results of the computation by a smooth curve.

An examination of the complete set of curves shows several trends. The first trend is an increase in the amount of forward scattering as the optical depth increases for fixed frequency. This effect is illustrated in Figures 6-18 and 6-19. The first figure is for an optical depth of 0.5 and it shows a relatively large amount of backscatter. The second figure is for an optical depth of 5 and it shows that the radiation is almost all in the forward direction.

This effect has been observed by Whitman et al. [75] in their examination of millimeter wave scattering from a half space of three-dimensional scalar isotropic spheres. To aid in making a comparison with their work, Figures 6A-1, 6A-2 and 6A-3 have been redrawn in rectangular format and presented in Figure 6-20. A comparison of this figure with several of Schwering et al. [58] shows quite good qualitative agreement.

The second trend can be observed by examining Figures 6A-10 through 6A-12. There, for a constant distance of 200 meters, the amount of forward scattering increases as the frequency increases. This increase in forward scattering can be explained

6-41

Freq. = 600. MHz
Rho = 1000/ha
Rad. = 5.0 cm

Range = 21.4 m
Opt. Dist. = .5



Figure 6-18:  Normalized Specific Intensity Versus Azimuthal Scatter Angles

Freq. = 600. MHz
Rho = 1000/ha
Rad. = 5.0 cm

Range = 214.0 m
Opt. Dist. = 5.0

<---- XMTR

Figure 6-19:   Normalized Specific Intensity Versus Azimuthal Scatter Angles

Freq. = 200. MHz
Rho = 1000/ha
Rad. = 5.0 cm

Range = 7.2 m
Opt. Dist. = .5



Figure 6-20(a): Normalized Specific Intensity Versus Azimuthal Scattering Angle

Freq. = 200. MHz
Rho = 1000/ha
Rad. = 5.0 cm

Range = 14.3 m
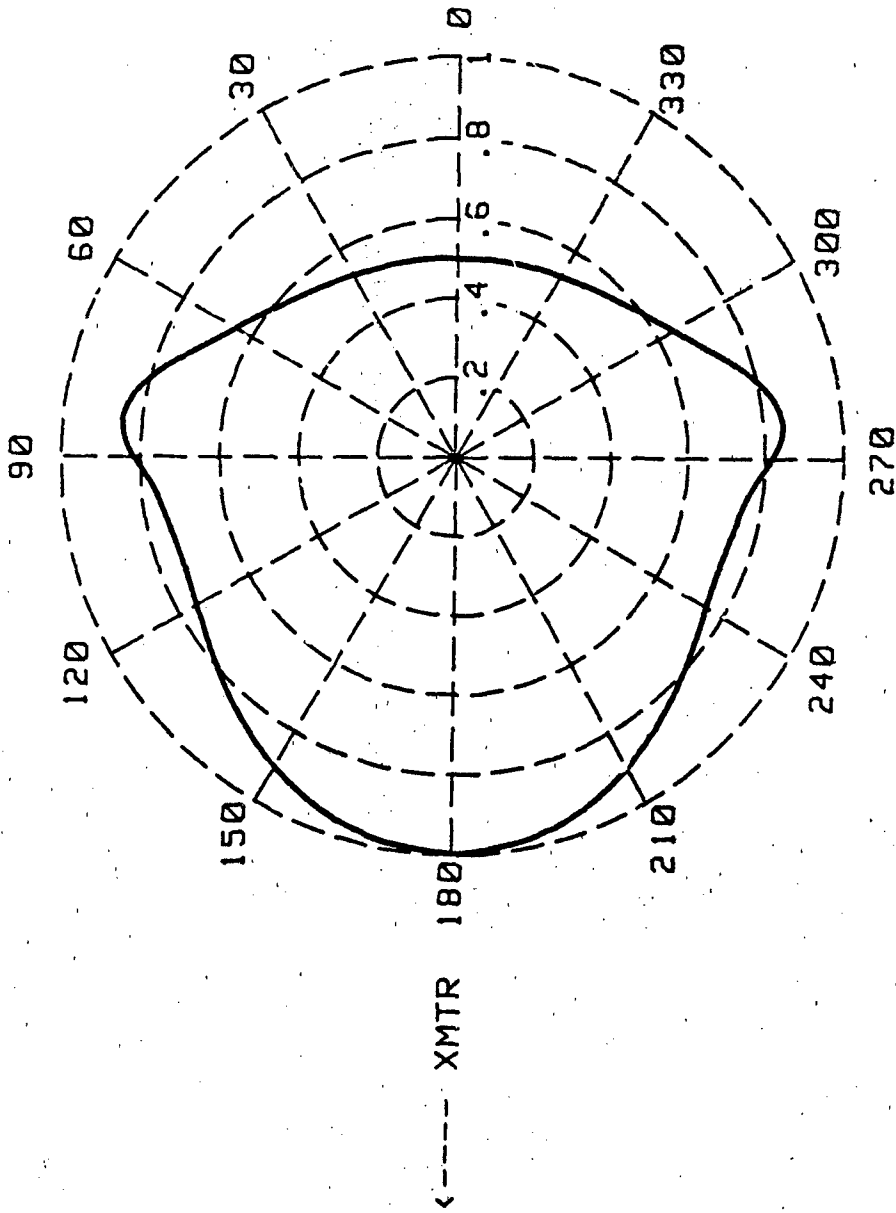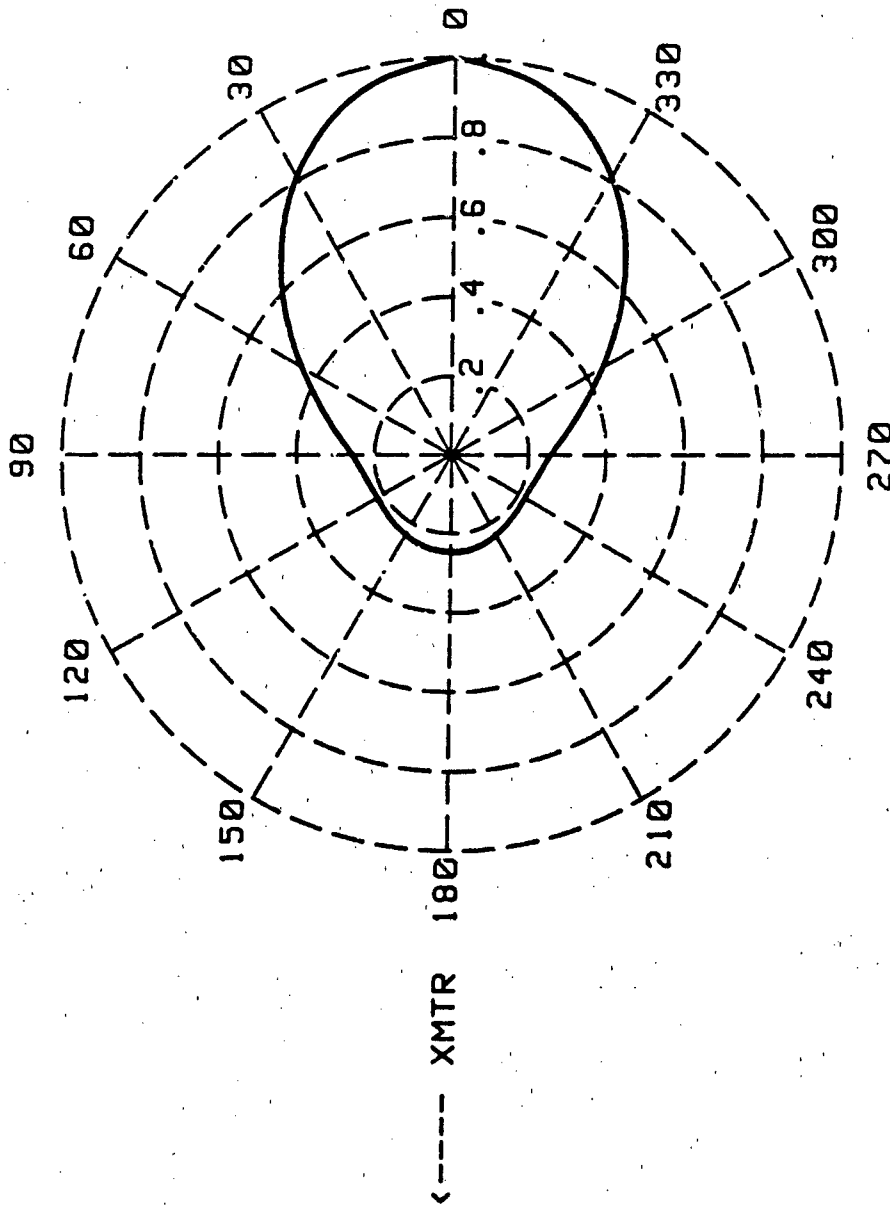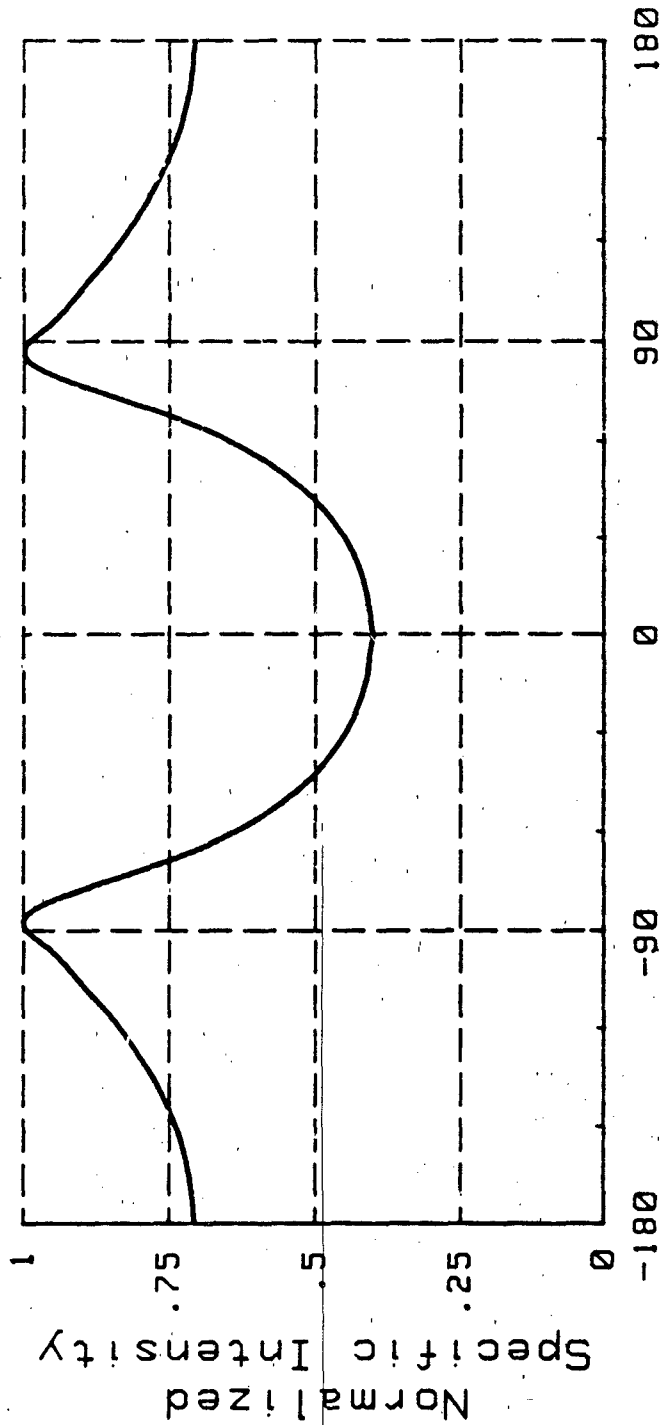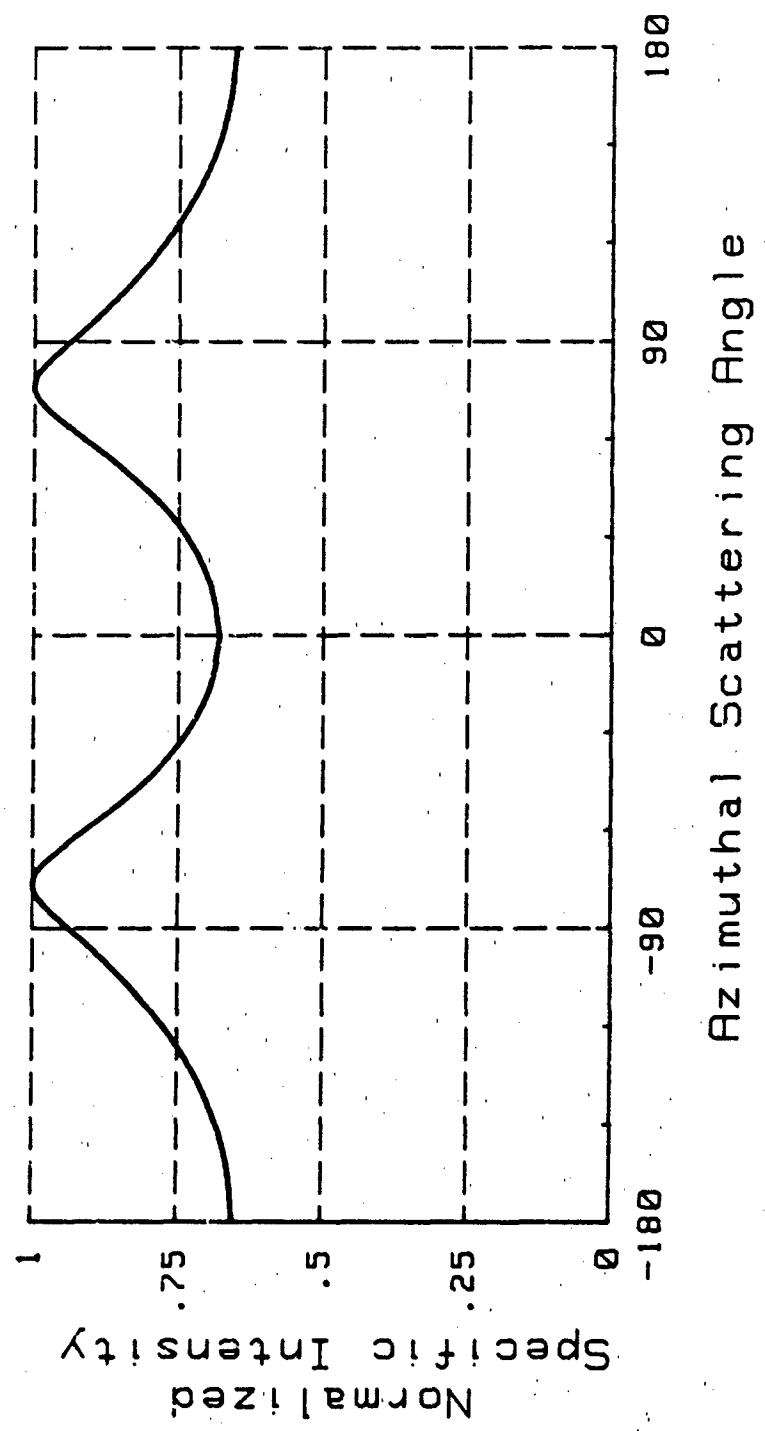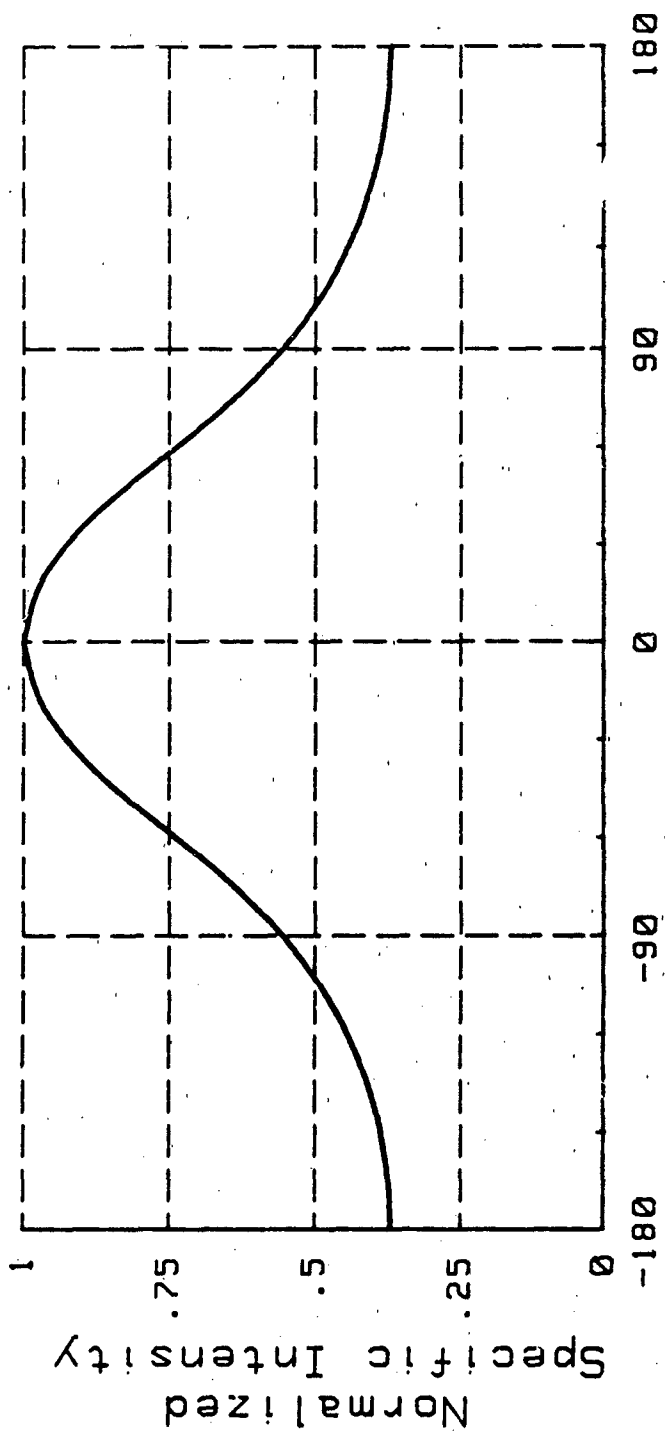Opt. Dist. = 1.0



Figure 6-20(b):  Normalized Specific Intensity Versus Azimuthal Scattering Angle

Freq.  =  200. MHz
Rho   = 1000/ha
Rad.  =  5.0 cm

Range  =  71.6 m
Opt. Dist.  =  5.0

Azimuthal Scattering Angle

Normalized Specific Intensity

Figure 6-20(c):  Normalized Specific Intensity Versus Azimuthal Scattering Angle

6-44c

by examining the radiation pattern of the scatterer (Figure 6.6). There it is observed that the radiation pattern becomes more forward-directed as frequency increases.

The specific intensity at a point represents the amount of energy passing through that point at a specific angle. When this specific intensity is summed over all angles, the total intensity at a point is obtained. To see this, rewrite Equation (6-4-2) for $r_x = 0$. The result is

$$< |\psi(x)|^2 > = I(z) = \int_0^{2\pi} d\phi\, I(z,\phi) \qquad (6\text{-}4\text{-}25)$$

where the correlation function $\Gamma(z,0)$ has been set equal to $I(z)$, i.e., $\Gamma(z,0) = I(z)$.

The intensity can be broken up into a mean or coherent component $I_o(z)$ and a random or incoherent component $I_I(z)$. These components correspond to angular integrals over the reduced and diffuse specific intensities respectively. From Equations (6-4-25) and (6-4-9), it is found that

$$I_o(z) = \int_0^{2\pi} d\phi\, I_r(z,\phi) \qquad (6\text{-}4\text{-}26)$$

and

$$I_I(z) = \int_0^{2\pi} d\phi\, I_d(z,\phi) \qquad (6\text{-}4\text{-}27)$$

The coherent intensity can be obtained directly by using result (6-4-14) in (6-4-26); thus

$$I_o(z) = e^{-\tau} \quad , \quad \tau = \rho\sigma_t z \qquad (6\text{-}4\text{-}28)$$

The angular symmetry of the diffuse specific intensity about $\phi = \pi$ can be used to reduce the integral given in Equation (6-4-27) to the interval $[0,\pi]$; then, a transform to $\mu = \cos\phi$, results in the following expression for $I_I(z)$:

$$I_I(z) = 2 \int_{-1}^{+1} \frac{I_d(\tau,\mu)}{\sqrt{1 - \mu^2}} \, d\mu \qquad (6\text{-}4\text{-}29)$$

Now employing the Chebyshev-Gauss quadrature formula given in Equation (6-4-20), an approximate expression for the incoherent intensity is found in terms of the numerical results previously obtained. The incoherent intensity is expressed as

$$I_I(z) = \frac{\pi}{N} \sum_{\substack{j=-N \\ j\neq 0}}^{N} I_d(\tau,\mu_j) \qquad (6\text{-}4\text{-}30)$$

The results of the computer calculations will be plotted in three formats. These formats are: normalized intensity versus distance; incoherent-to-coherent intensity ratio versus distance; and finally, normalized coherent and normalized incoherent versus distance. The intensity has been normalized to the value of the incident intensity. Curves will be drawn for frequencies of 200, 300, and 600 MHz and radii of 1, 5, and 10 centimeters. All curves have been included in the Annex under figure numbers 6A-13 through 6A-21. Sample curves have been placed in the text bearing figure numbers 6.21 and 6.22 for illustrative purposes.

An examination of the normalized coherent intensity as shown in Figures 6A-15, 6A-18 and 6A-21 shows that all curves decrease with increasing distances. The rate of decrease is directly related to $\sigma_t$ since the normalized coherent intensity varies as $\exp(-\rho\sigma_t z)$. This can be verified by referring to the total scattering cross-section curves shown in Figures 6.9, 6.11 and 6.13. (Note tick marks have been included at 300 and 600 MHz.) It can be seen that both the coherent intensity values and the $\sigma_t$ values increase with frequency for a trunk radius of 1 centimeter, while they both decrease with frequency for trunk radii of 5 and 10 centimeters.

In Figures 6A-14, 6A-17 and 6A-20 the ratios of the incoherent to coherent intensities have been plotted. The basic trend
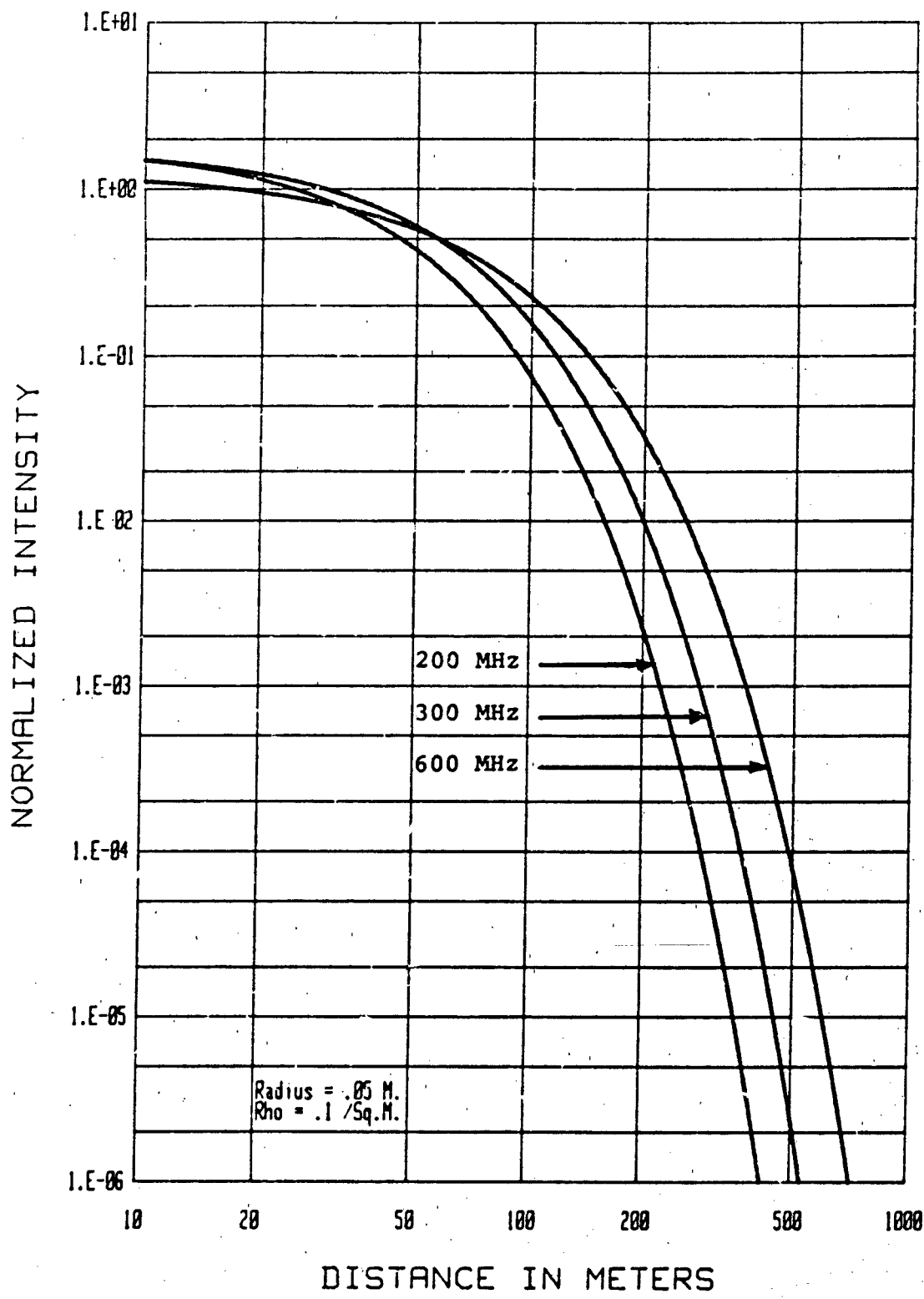
Figure 6-21:  Total Normalized Intensity Versus Distance
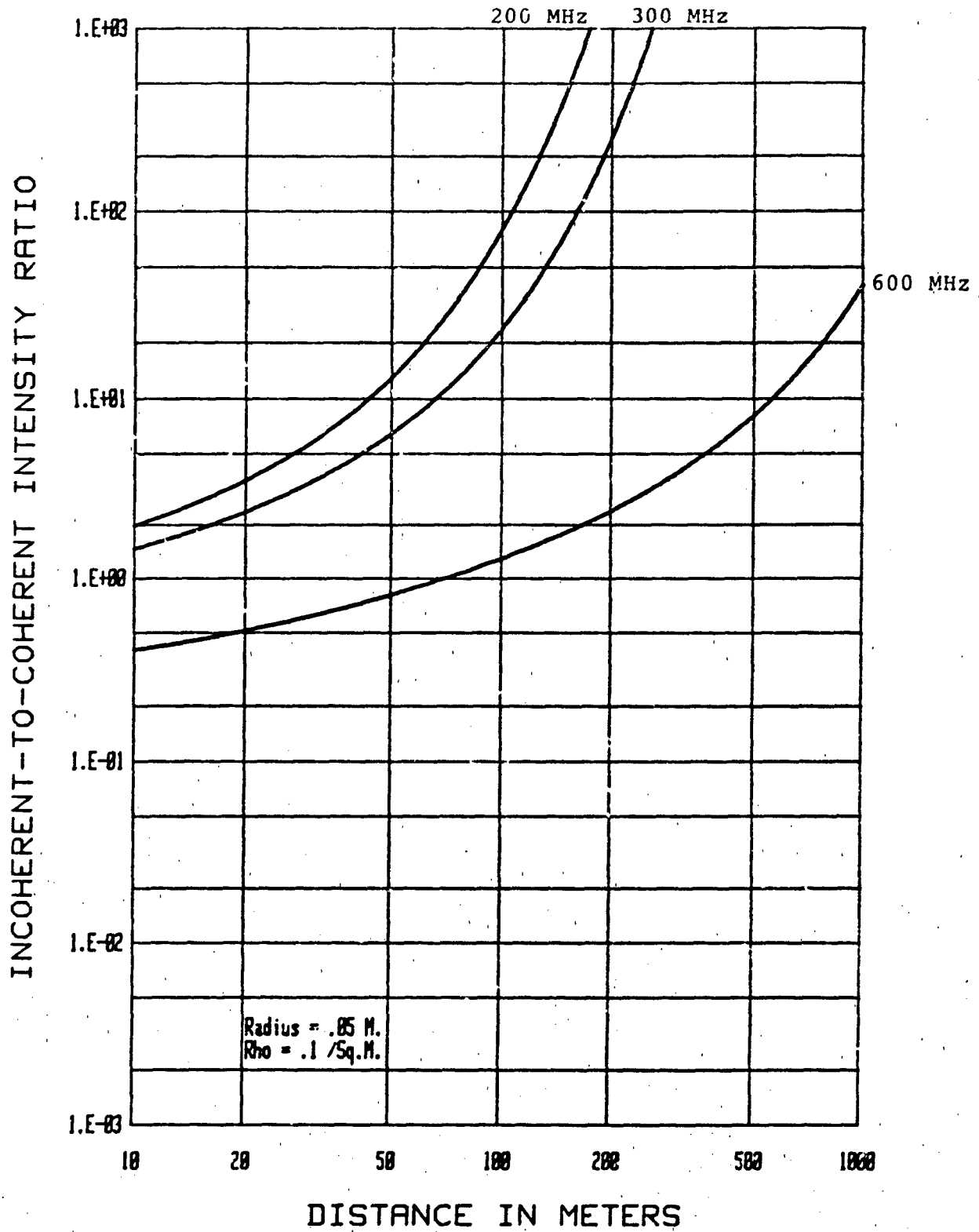
Figure 6-22:   Incoherent-to-Coherent Intensity Ratio Versus Distance

these curves show is that the incoherent wave becomes increasingly important as frequency and distance increase. Since the amount of scattering directly affects the importance of the diffuse term, it is interesting to compare the albedo curves presented in Figures 6.8, 6.10 and 6.12, to the curves for the intensity ratio under consideration. The comparison shows that in almost all cases an increase or decrease of albedo corresponds to an increase or decrease in the incoherent -to- coherent intensity ratio. This is not the case for curves having a trunk radius of 10 centimeters where the 200 and 600 MHz curves are interchanged. It should be noted, however, that the albedo values and the curves are close to each other in this case.

### 6.4.3  Space Correlation Function

The space correlation function $\Gamma(z, r_x)$ can be found by solving the generalized transport Equation (6-4-4) for $J(z, r_x, \phi)$ and then using this quantity in Equation (6-4-2) for $\Gamma(z, r_x)$. Because of the transverse placement of the observation points $\underline{x}$ and $\underline{\hat{x}}$, the generalized specific intensity $J(z, r_x, \phi)$ can be found directly in terms of $I(z, \phi)$. It can be verified by direct substitution that

$$J(z, r_x, \phi) = A(r_x \sin\theta) I(z, \phi) \qquad (6\text{-}4\text{-}31)$$

and thus $J$ can be obtained by using the intensity values already computed.

Substituting Equation (6-4-31) into the expression for the intensity gives

$$\Gamma(z, r_x) = \int_0^{2\pi} d\phi A(r_x \sin\theta) I(z, \phi) e^{ik_0 r_x \sin\phi} \qquad (6\text{-}4\text{-}32)$$

$$= \int_0^{2\pi} d\phi I(z, \phi) e^{i\kappa r_x \sin\phi} \qquad (6\text{-}4\text{-}33)$$

where

$$\kappa = k_0 + \delta\kappa \qquad (6\text{-}4\text{-}34)$$

$$\delta\kappa = \delta\kappa' - j\delta\kappa'' = 2\pi^2\rho f(\underline{o},\underline{o})/\gamma k_o \tag{6-4-35}$$

Here $\kappa$ is the mean wave propagation constant given in Equation (4-2-30) of [42] with $\theta_i = 0$.

Before proceeding further, the correlation function is broken up into coherent and incoherent components as follows:

$$\Gamma(z,r_x) = \Gamma_o(z,r_x) + \Gamma_I(z,r_x) \tag{6-4-36}$$

where

$$\Gamma_o(z,r_x) = e^{-\rho\sigma_t z} \tag{6-4-37}$$

and

$$\Gamma_I(z,r_x) = \int_0^{2\pi} d\phi I_d(z,\phi) e^{i\kappa r_x \sin\phi} \tag{6-4-38}$$

Here $\Gamma_o(z,r_x)$ is the coherent portion of the correlation function. It should be noted that it does not depend on $r_x$; thus the mean fields at $\underline{x}$ and $\underline{\hat{x}}$ remain completely correlated for all values of $r_x$. This is not surprising since the mean field is a deterministic quantity.

The incoherent portion of the correlation function is $\Gamma_I(z,r_x)$. Using the symmetry of $I_d(z,\phi)$ about $\phi = \pi$, Equation (6-4-38) can be rewritten as

$$\Gamma_I(z,r_x) = 2\int_0^{\pi} d\phi I_d(z,\phi) \cos[(k_o + \delta\kappa')r_x \sin\phi] e^{-\delta\kappa'' r_x \sin\phi}$$

$$\tag{6-4-39}$$

It can be seen from Equation (6-4-39) that the correlation function, $\Gamma_I$, is real. This is not a general property of $\Gamma_I$ but results from the transverse location of the observation points $\underline{x}$ and $\underline{\hat{x}}$.

The numerical analysis of the integral for $\Gamma_I$ must be treated with care. The function $I_d(z,\phi)$ and $\exp(-\delta\kappa'' r_x \sin\phi)$ are slowly

varying functions of angle, while the cosine function becomes a rapidly varying function of angle as $k_0 r_x$ becomes large.

To see the behavior for large $k_0 r_x$, the integral can be asymptotically evaluated by the method of stationary phase. The stationary point occurs at $\phi = \pi/2$ and the resulting asymptotic evaluation yields

$$\Gamma_I(z, r_x) \sim 2 \sqrt{\frac{2\pi}{k_0 r_x}} \; I_d(z, \pi/2) e^{-\delta \kappa'' |r_x|}$$

$$\cos[(k_0 + \delta \kappa'') r_x + \pi/2] \qquad \qquad (6\text{-}4\text{-}40)$$

This approximate expression shows that for large $k_0 r_x$ the correlation function falls off at the decay rate of the mean wave. The validity of the above asymptotic expansion requires the $I_d(z, \phi)$ be a slowly varying function of $\phi$. As $z$ becomes large, $I_d(z, \phi)$ varies more rapidly with $\phi$. Thus as $z$ becomes large, the correctness of the above result falls into question.

The correlation function has been plotted for frequency values of 200, 300 and 600 MHz in Figures 6.23, 6.24 and 6.25 for distances of 100 and 500 meters. A spline curve fit to $I_d(z, \phi)$ has been used to numerically evaluate the $\phi$ integral. The computed correlation function in the figures is shown by the thin solid line. The thick solid line is the envelope, and the dashed line is the asymptotic expression given in Equation (6-4-40).

An examination of the correlation curve shows that for 200 and 300 MHz the correlation function does not change substantially as the distance varies from 100 to 500 meters. It should also be noted that at these frequencies, the asymptotic expansion is quite close to the computed curve for most of the plotted range. Referring to the approximate correlation function given in Equation (6-4-40), it is seen that the correlation distance does not depend on $r_x$. This explains the invariance of the correlation length with distance observed in Figures 6.23 and 6.24.
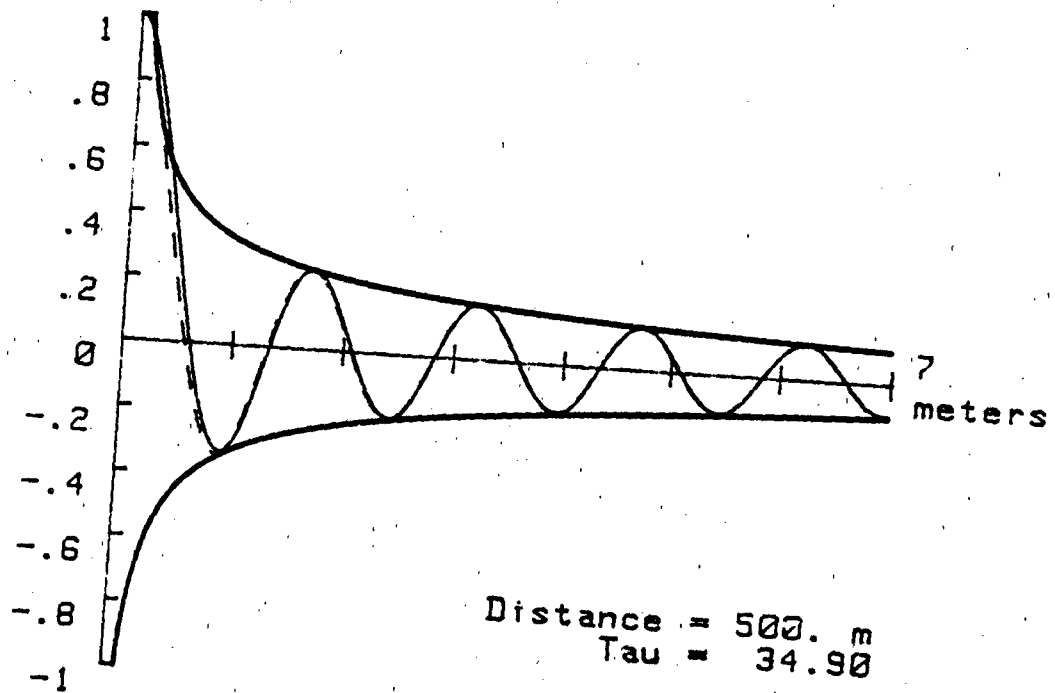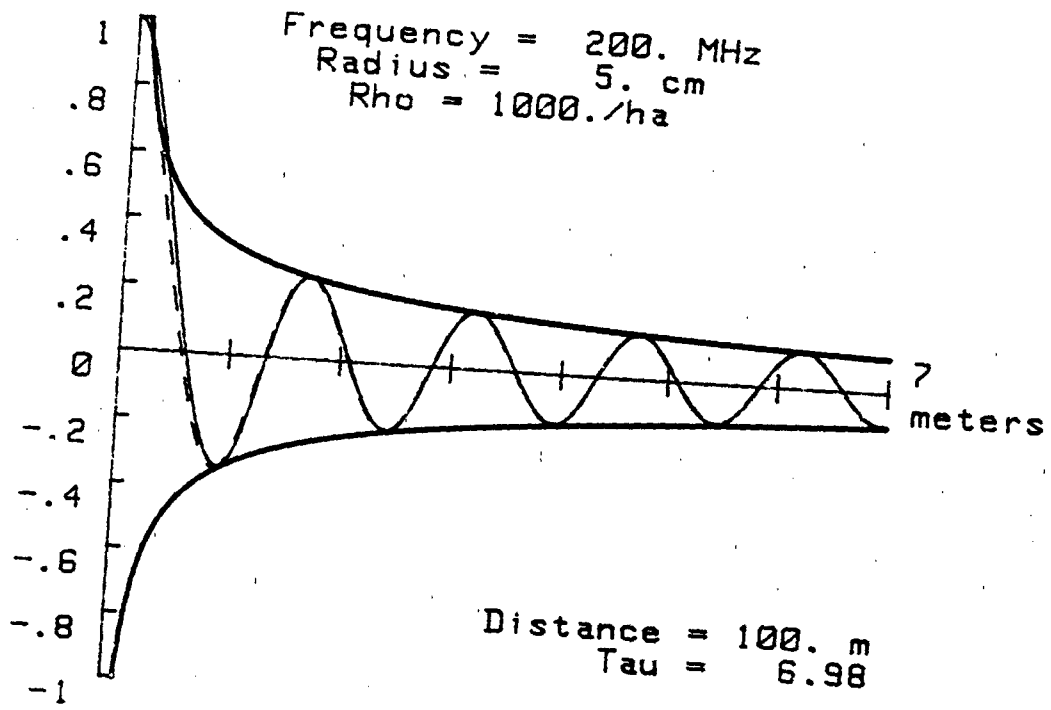
Figure 6-23: Space Correlation Function Versus Transverse Separatio

6-52
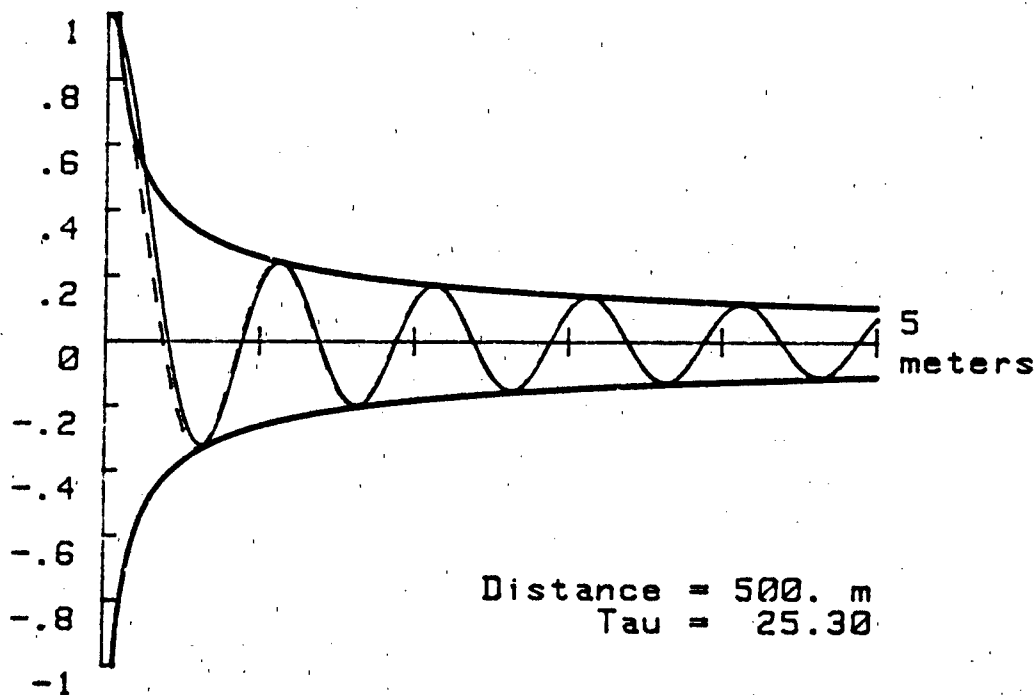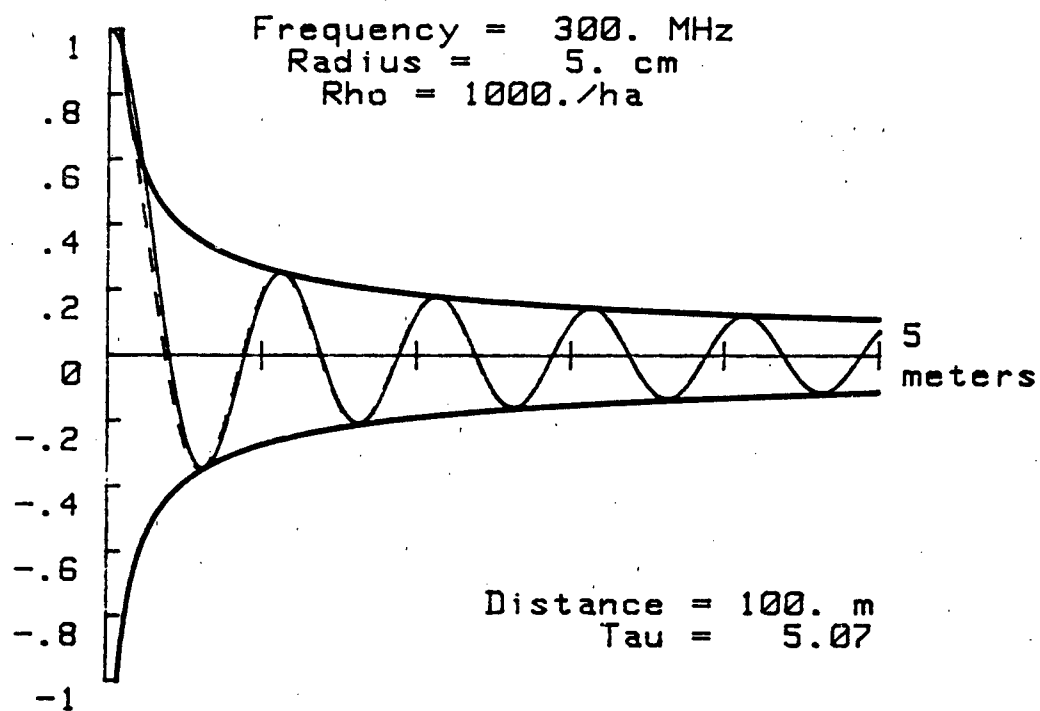
Figure 6-24: Space Correlation Function Versus Transverse Separation
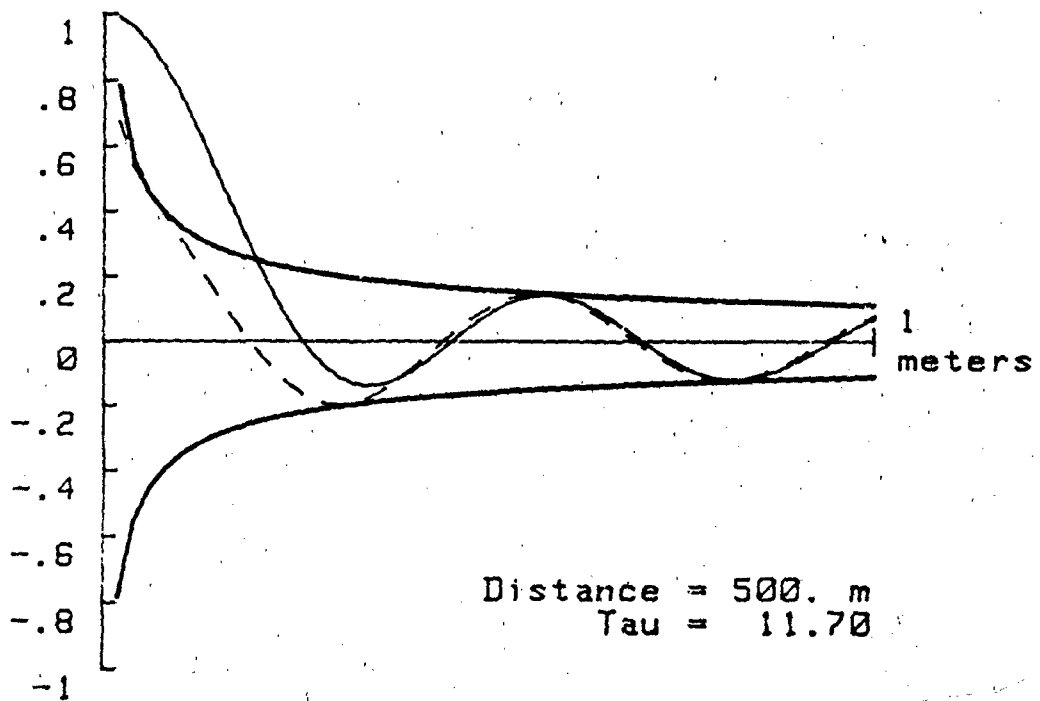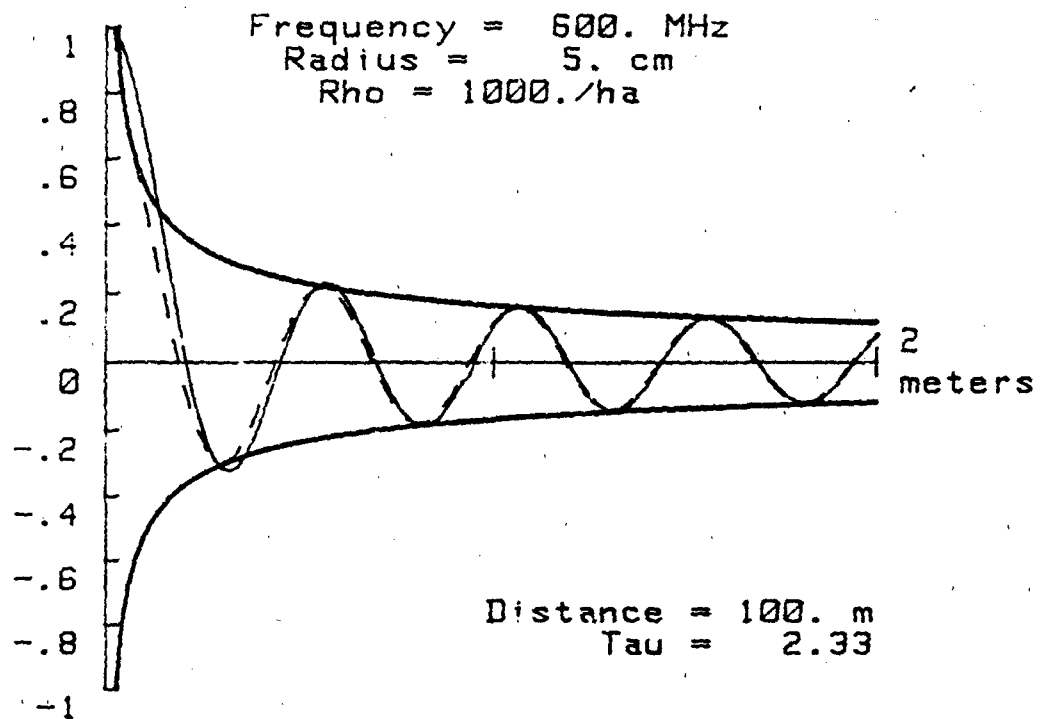
Figure 6-25:   Space Correlation Function Versus Transverse Separation

The situation is different in Figure 6.25 at 600 MHz. Here the $I_d(z,\phi)$ becomes more rapidly varying for large z and the asymptotic expansion is not valid for a large portion of the z = 500 meter curve. Thus it is seen for this case that the space correlation function appears to decrease with distance.

As a final observation, it should be noted that the space correlation length decreases with increasing frequency. This is the expected result.

ANNEX 6A

## Normalized Specific Intensity versus Scattering Angle

| a = 0.5 m | Optical Distance | | (Tau) | Range    (m) |
|-----------|------|------|------|------|
| Frequency | 0.5 | 1.0 | 5.0 | 200 |
| 200 | 6A-1 | 6A-2 | 6A-3 | 6A-10 |
| 30C | 6A-4 | 6A-5 | 6A-6 | 6A-11 |
| 600 | 6A-7 | 6A-8 | 6A-9 | 6A-12 |

## Normalized Intensities versus Distance

| Intensities | Trunk Radius    (m) | | |
|-------------|------|------|------|
| | 0.01 | 0.05 | 0.10 |
| Total | 6A-13 | 6A-16 | 6A-19 |
| Incoherent/Coherent | 6A-14 | 6A-17 | 6A-20 |
| Coherent & Incoherent | 6A-15 | 6A-18 | 6A-21 |

Freq. = 200. MHz
Rho = 1000/ha
Rad. = 5.0 cm

Range = 7.2 m
Opt. Dist. = .5

Figure 6A-1: Normalized Specific Intensity Versus Azimuthal Scatter Angles
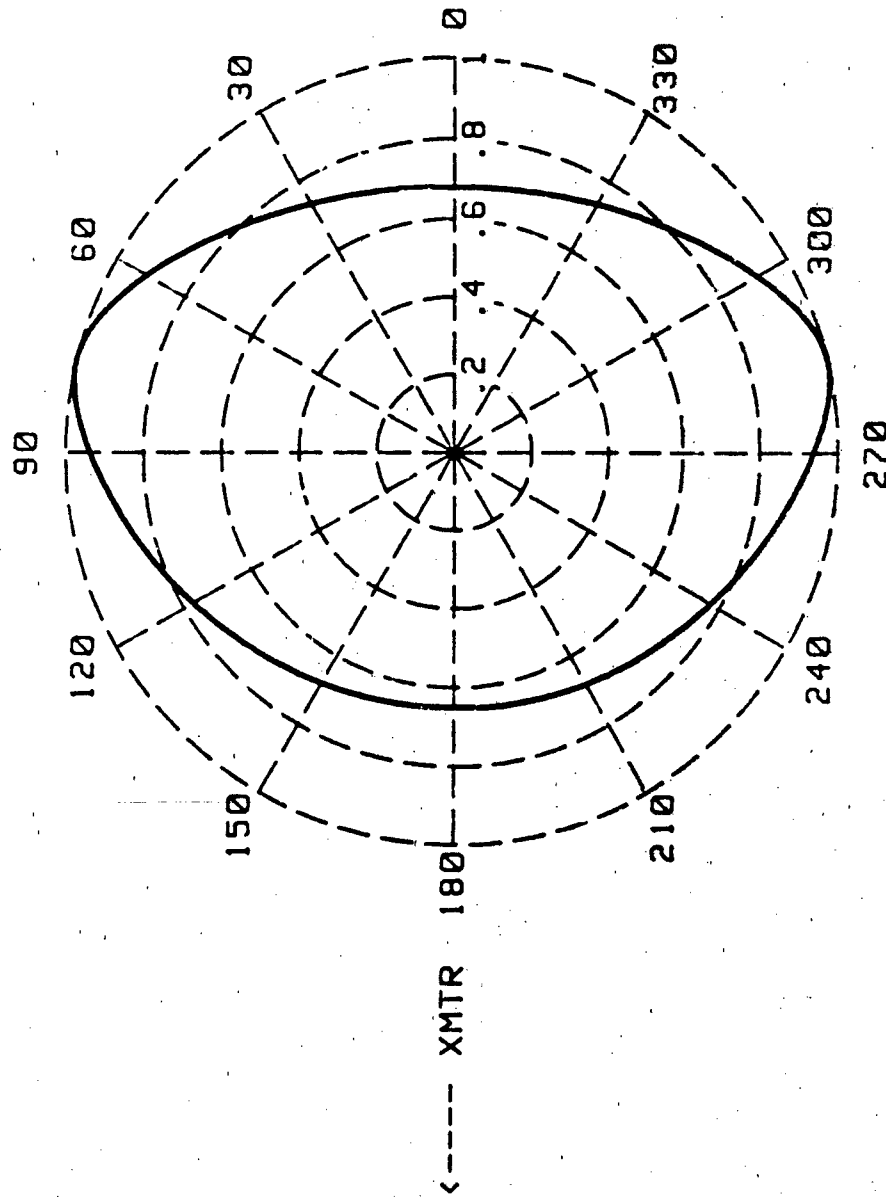
Figure 6A-2: Normalized Specific Intensity Versus Azimuthal Scatter Angles

Freq.  =  200. MHz
Rho  =  1000/ha
Rad.  =  5.0 cm

Range  =  14.3 m
Opt. Dist.  =  1.0

<----- XMTR

Freq. = 200. MHz
Rho = 1000/ha
Rad. = 5.0 cm

Range = 71.6 m
Opt. Dist. = 5.0
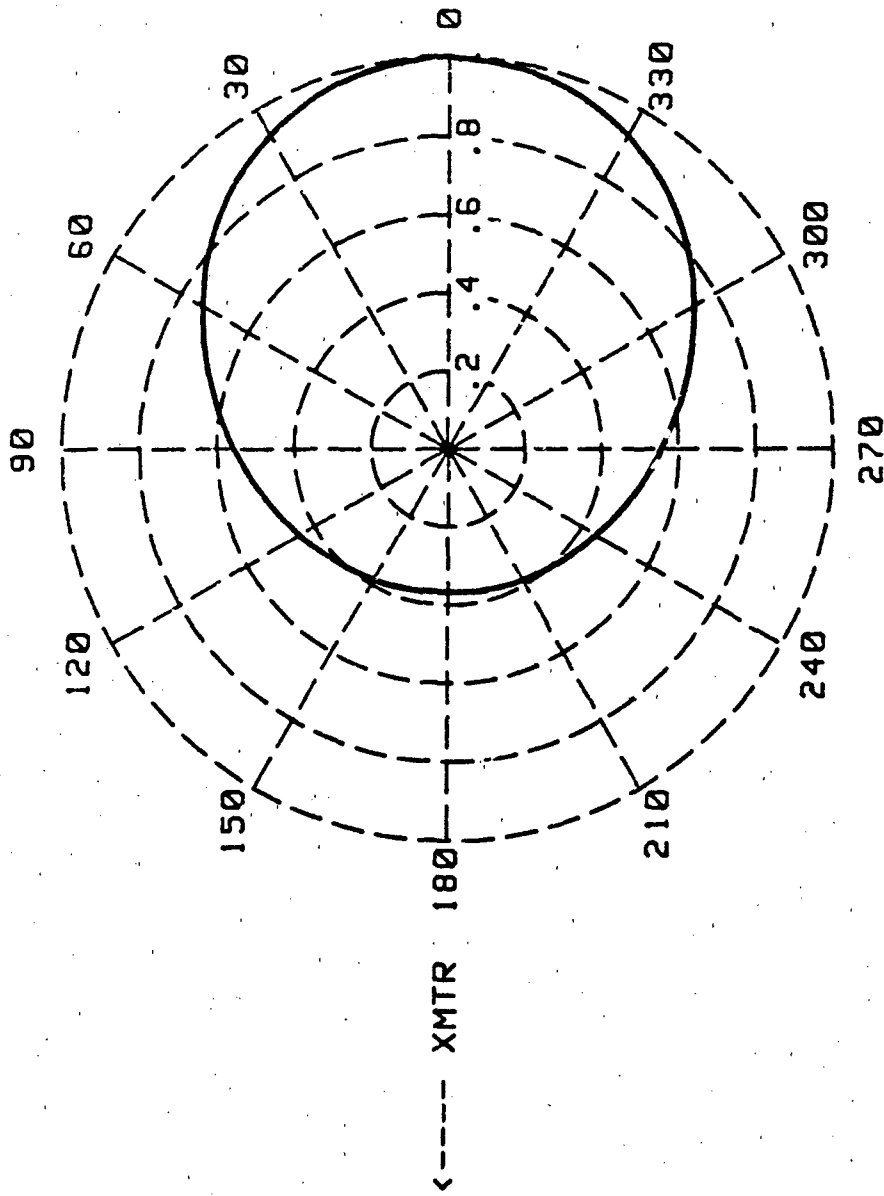


Figure 6A-3: Normalized Specific Intensity Versus Azimuthal Scatter Angles

Freq. = 300 MHz
Rho = 1000/ha
Rad. = 5.0 cm

Range = 9.9 m
Opt. Dist. = .5
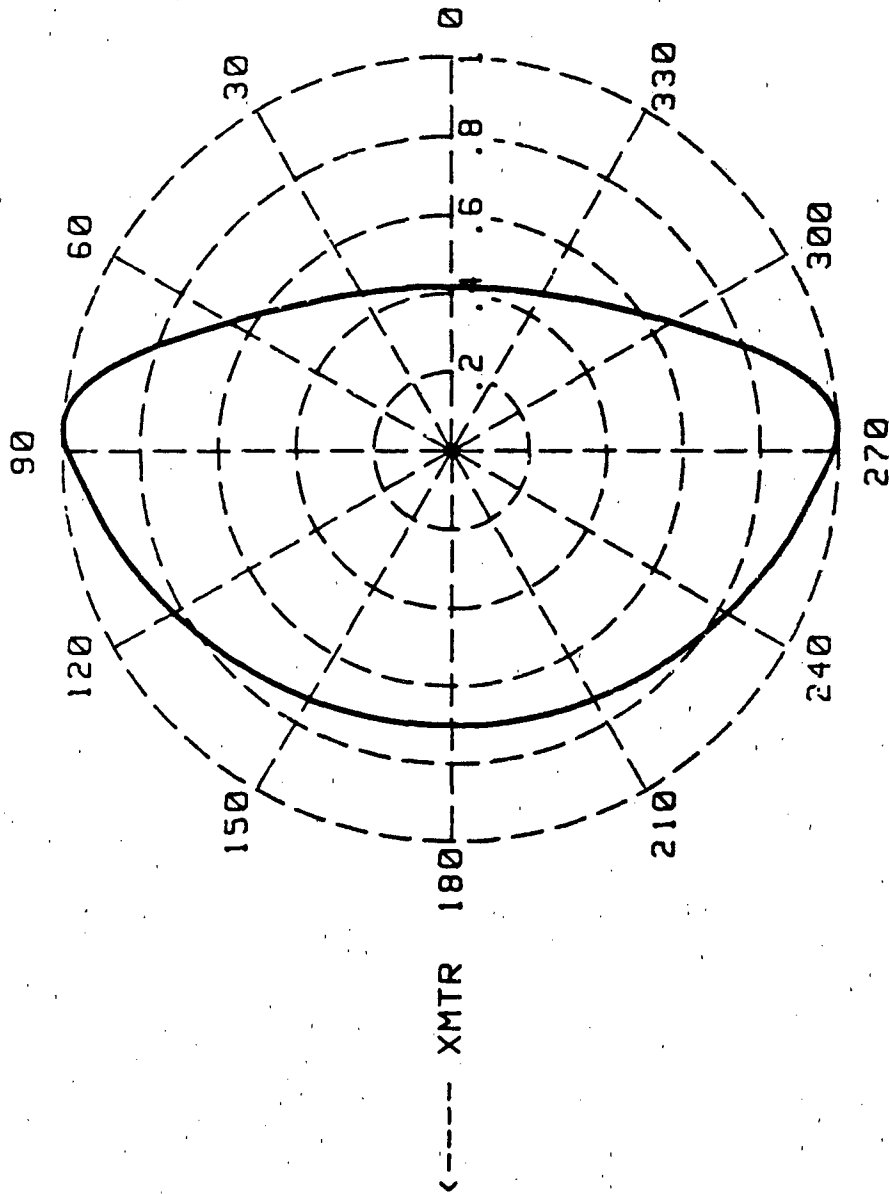
Figure 6A-4: Normalized Specific Intensity Versus Azimuthal Scatter Angles

Freq. = 300 MHz
Rho = 1000/ha
Rad. = 5.0 cm

Range = 19.7 m
Opt. Dist. = 1.0
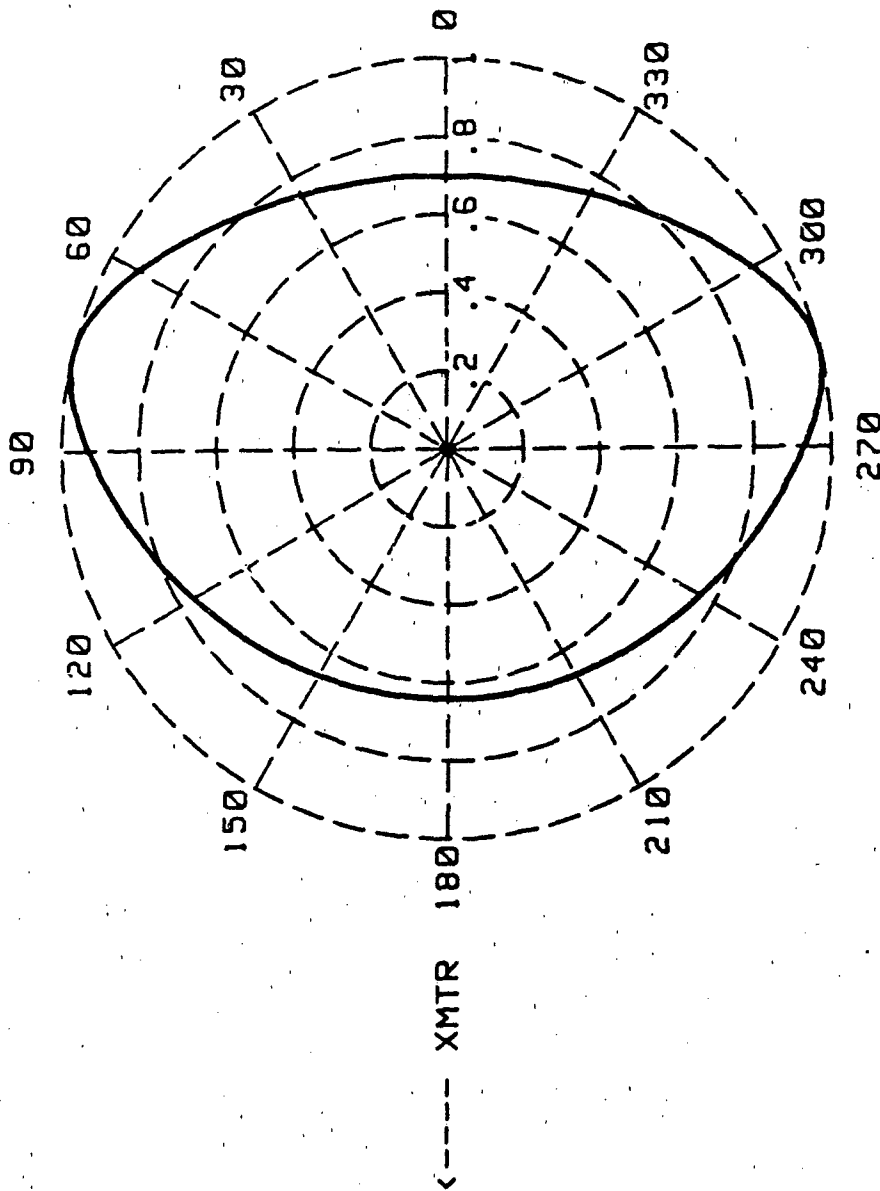


Figure 6A-5: Normalized Specific Intensity Versus Azimuthal Scatter Angles

Range = 98.6 m
Opt. Dist. = 5.0

Freq. = 300 MHz
Rho = 1000/ha
Rad. = 5.0 cm

0
30
330
60
300
90
270
120
240
150
210
180

.2
.4
.6
.8

XMTR
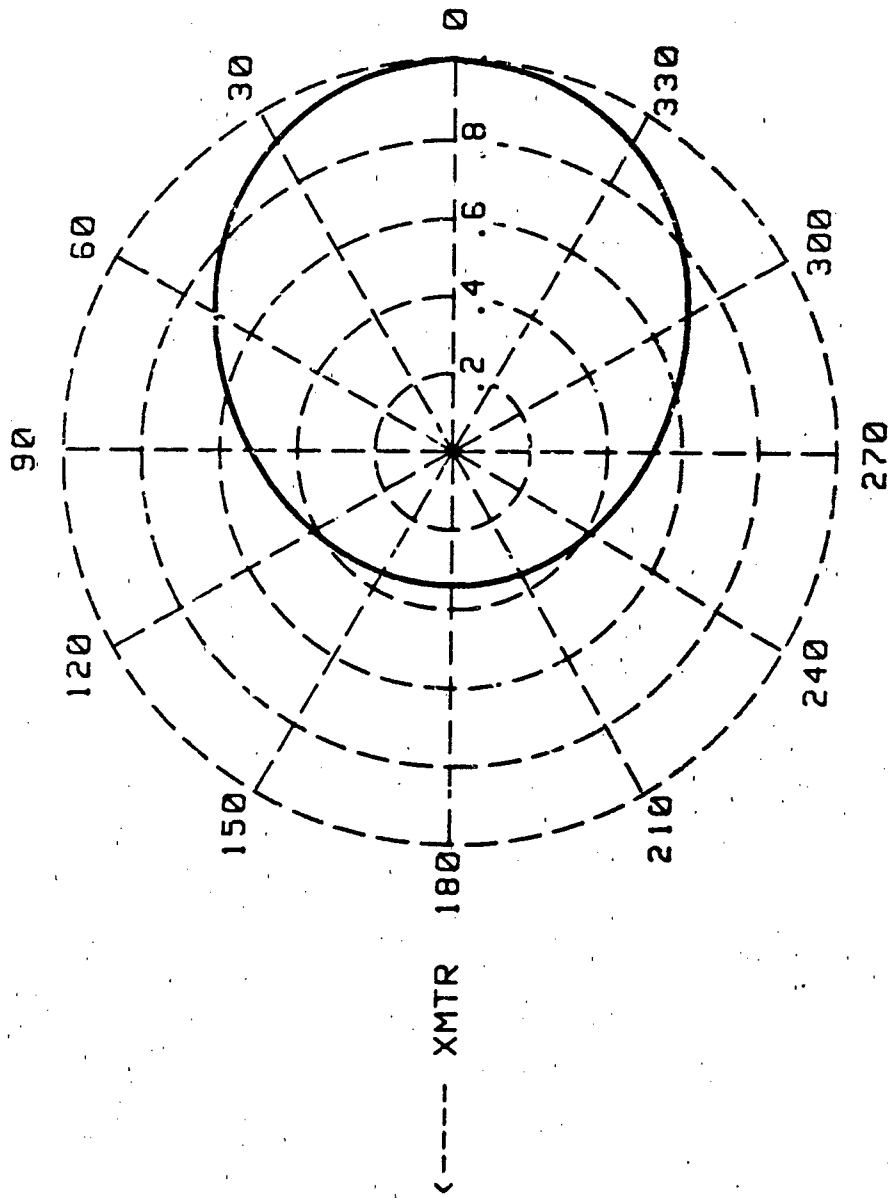
Figure 6A-6: Normalized Specific Intensity Versus Azimuthal Scatter Angles

Freq.  =  600. MHz
Rho  =  1000/ha
Rad.  =  5.0 cm

Range  =  21.4 m
Opt. Dist.  =  .5
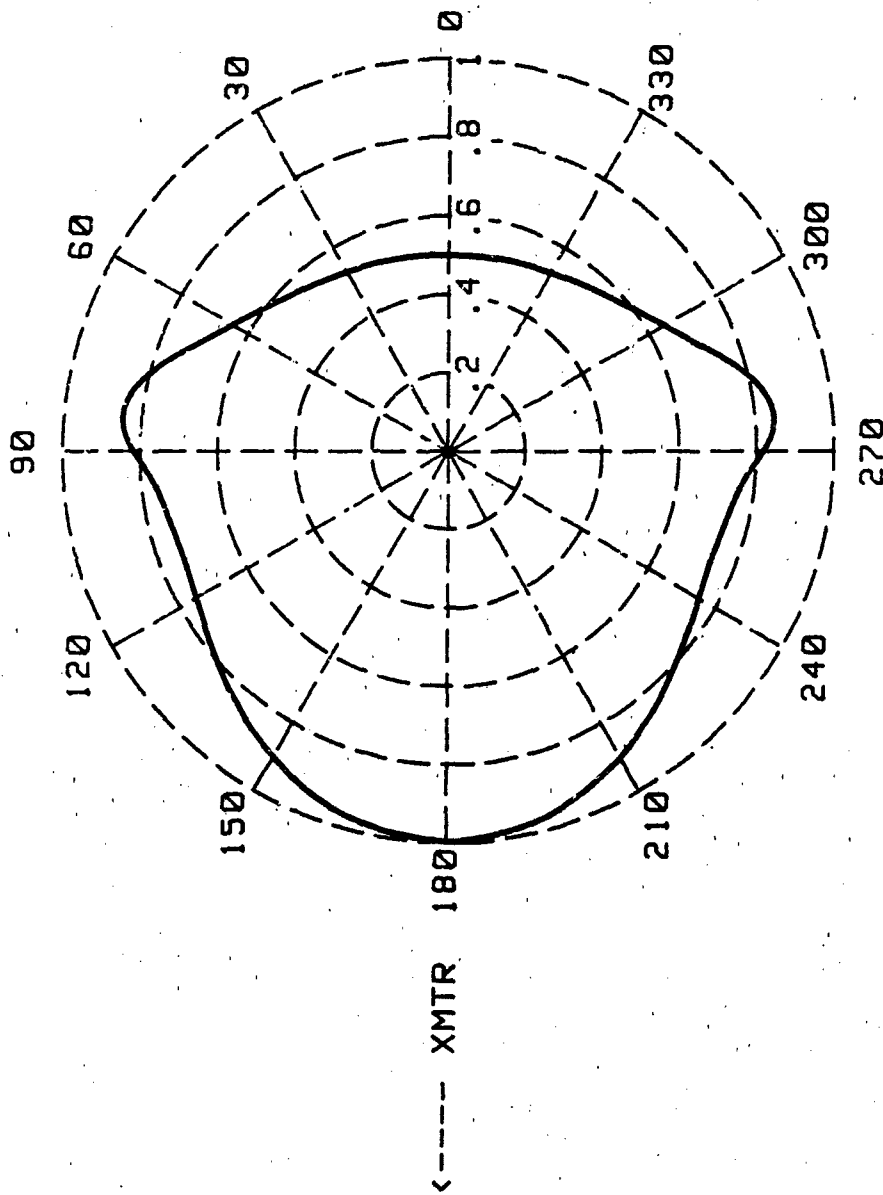
Figure 6A-7:  Normalized Specific Intensity Versus Azimuthal Scatter Angles
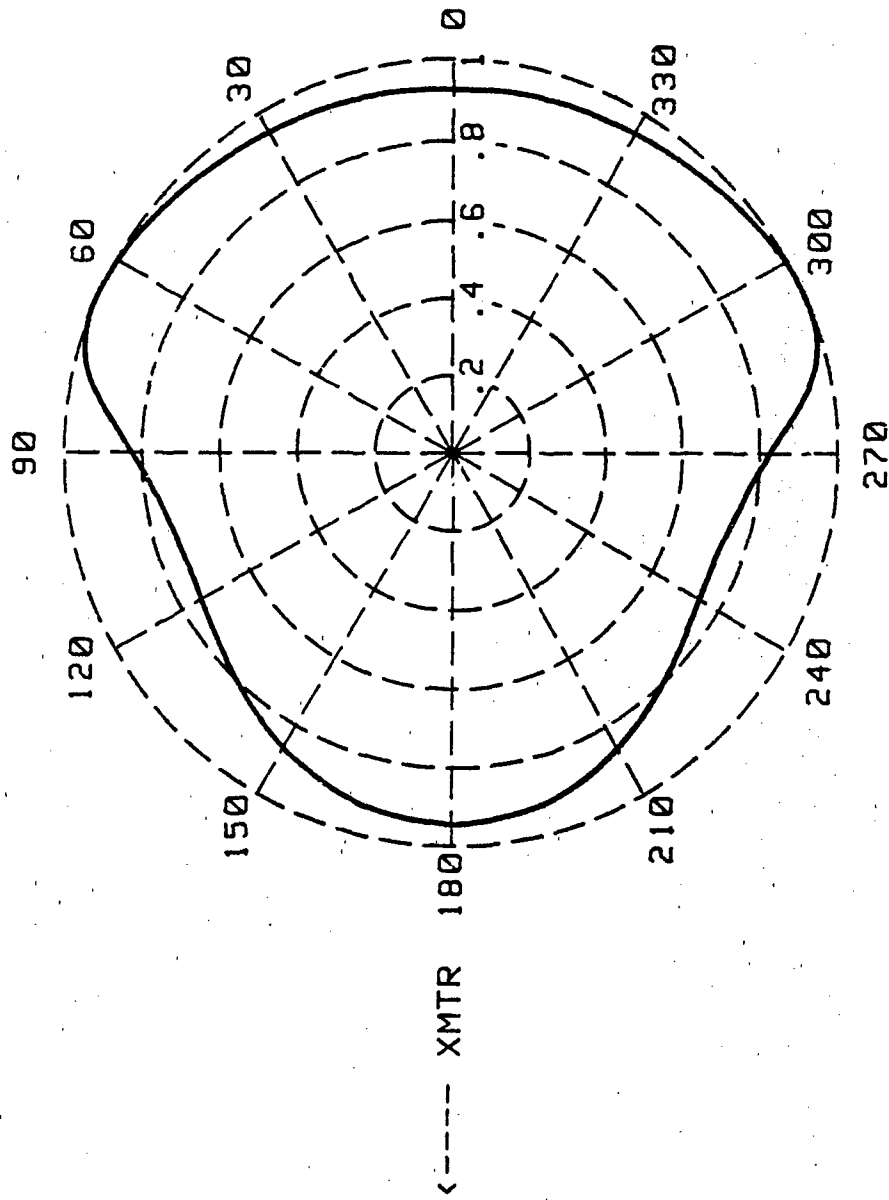
Figure 6A-8: Normalized Specific Intensity Versus Azimuthal Scatter Angles

Range = 42.9 m
Opt. Dist. = 1.0

Freq. = 600. MHz
Rho = 1000/ha
Rad. = 5.0 cm

<------ XMTR

Range = 214.0 m
Opt. Dist. = 5.0

Freq. = 600. MHz
Rho = 1000/ha
Rad. = 5.0 cm

XMTR 180
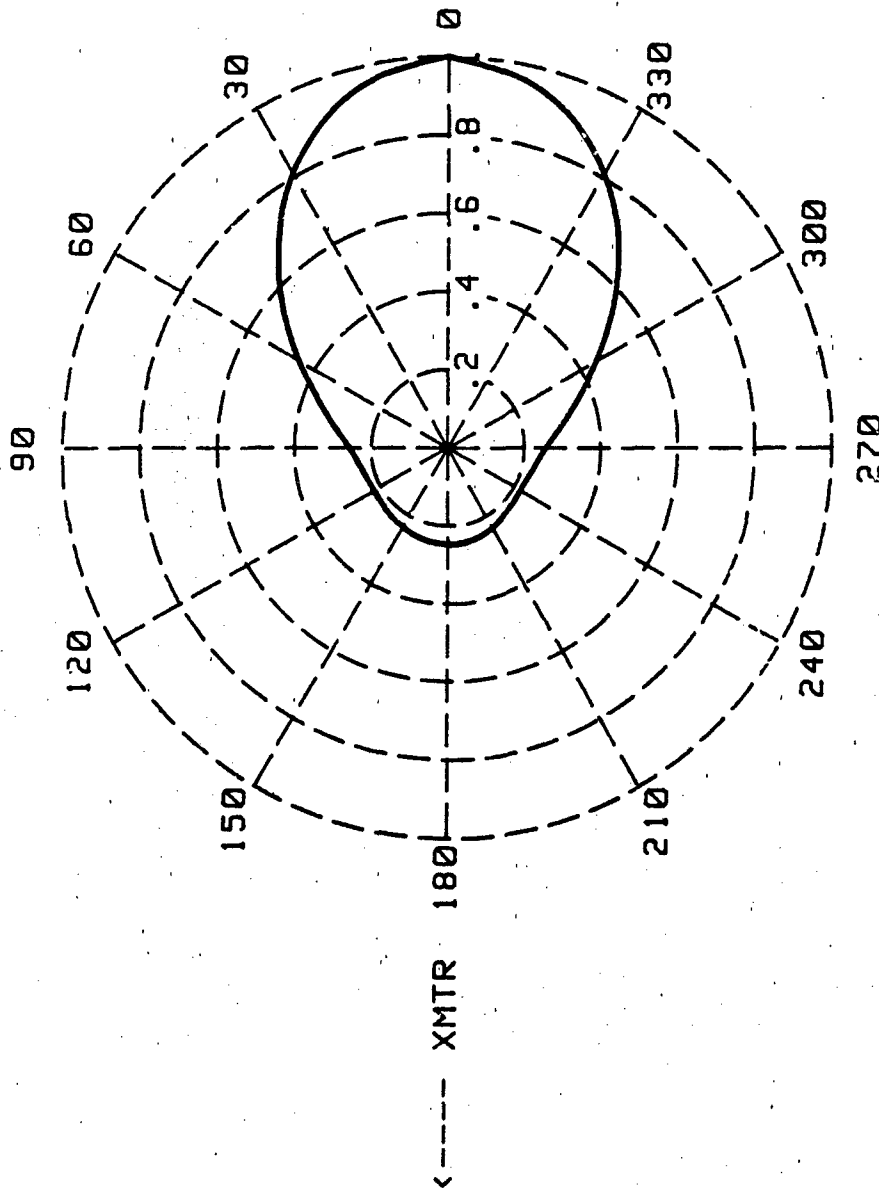
Figure 6A-9: Normalized Specific Intensity Versus Azimuthal Scatter Angles

Freq. = 200 MHz
Rho = 1000/ha
Rad. = 5.0 cm

Range = 200.0 m
Opt. Dist. = 14.0



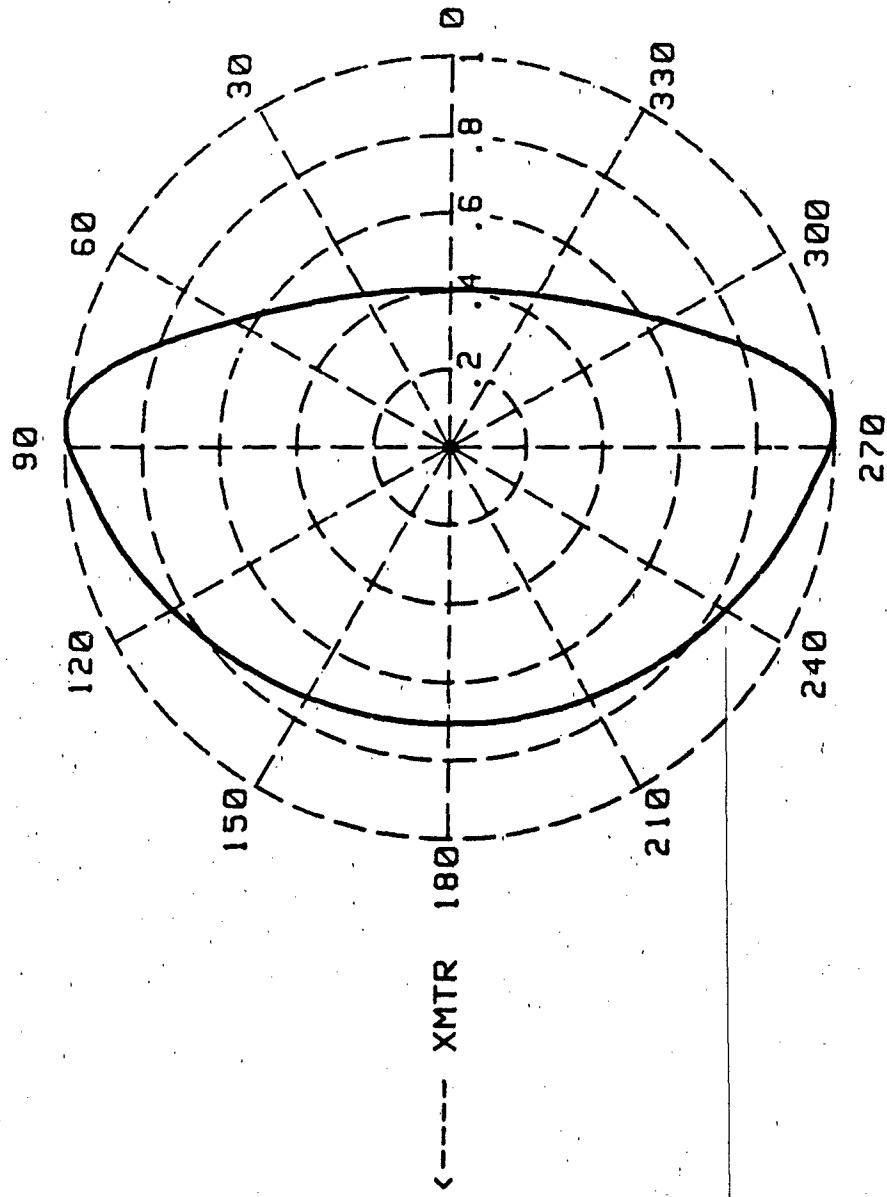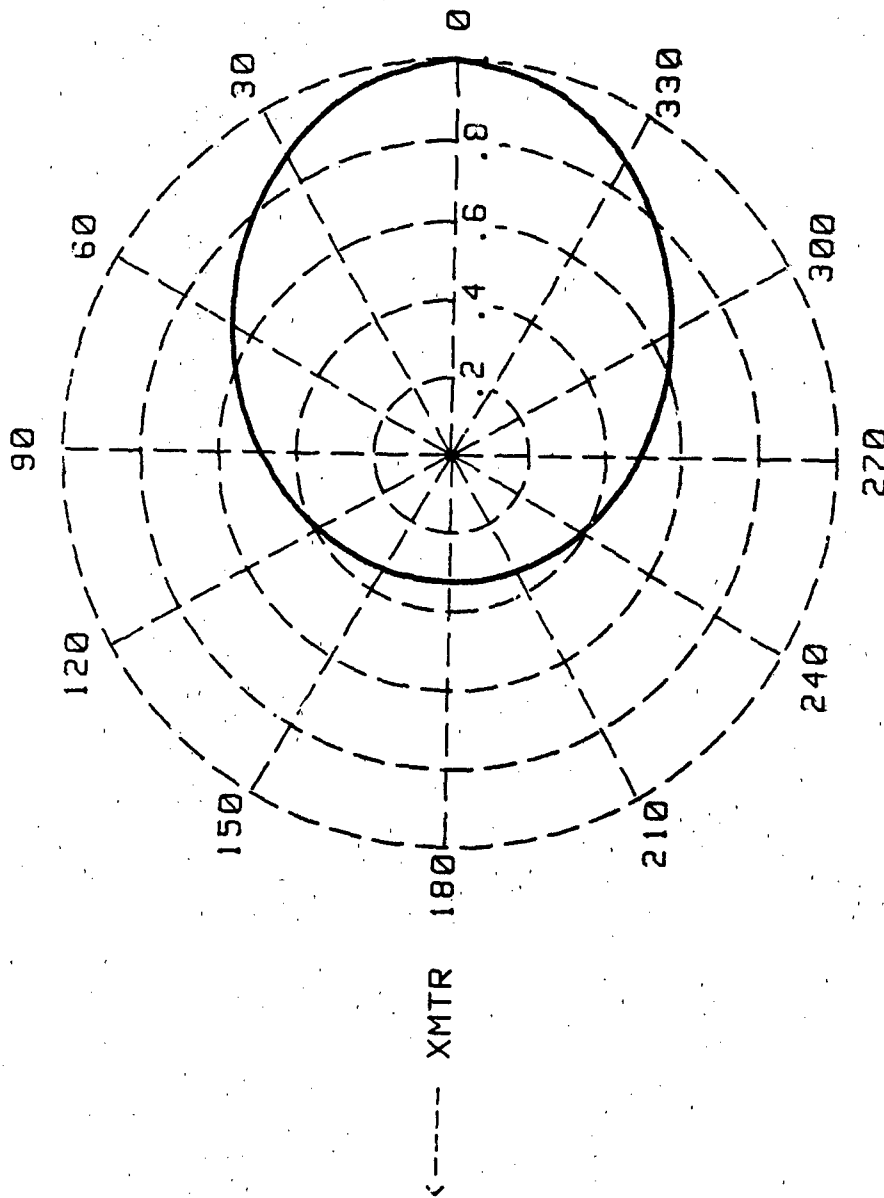Figure 6A-10: Normalized Specific Intensity Versus Azimuthal Scatter Angles
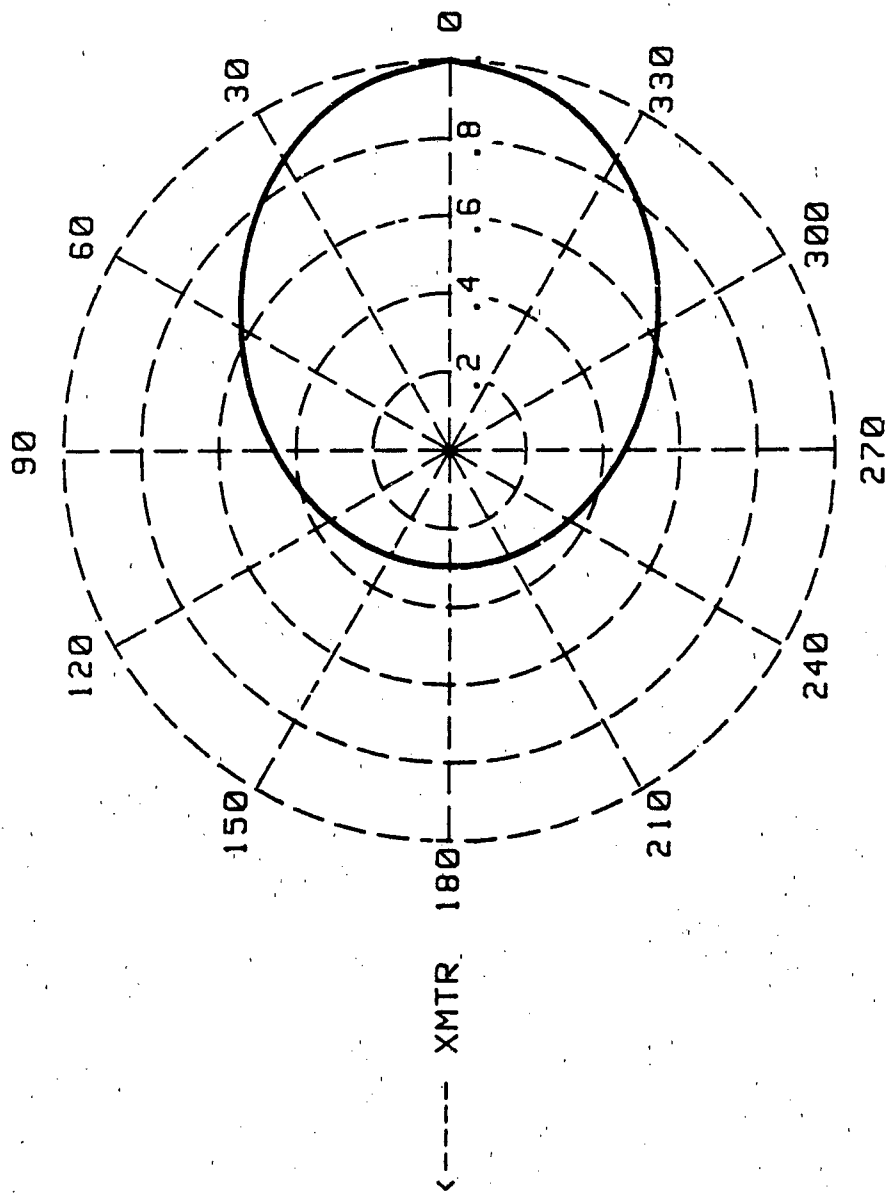
Figure 6A-11:   Normalized Specific Intensity Versus Azimuthal Scatter Angles

Freq. = 300 MHz
Rho  = 1000/ha
Rad. = 5.0 cm

Range = 200.0 m
Opt. Dist. = 10.0

Range = 200.0 m
Opt. Dist. = 4.6

Freq. = 600 MHz
Rho = 1000/ha
Rad. = 5.0 cm
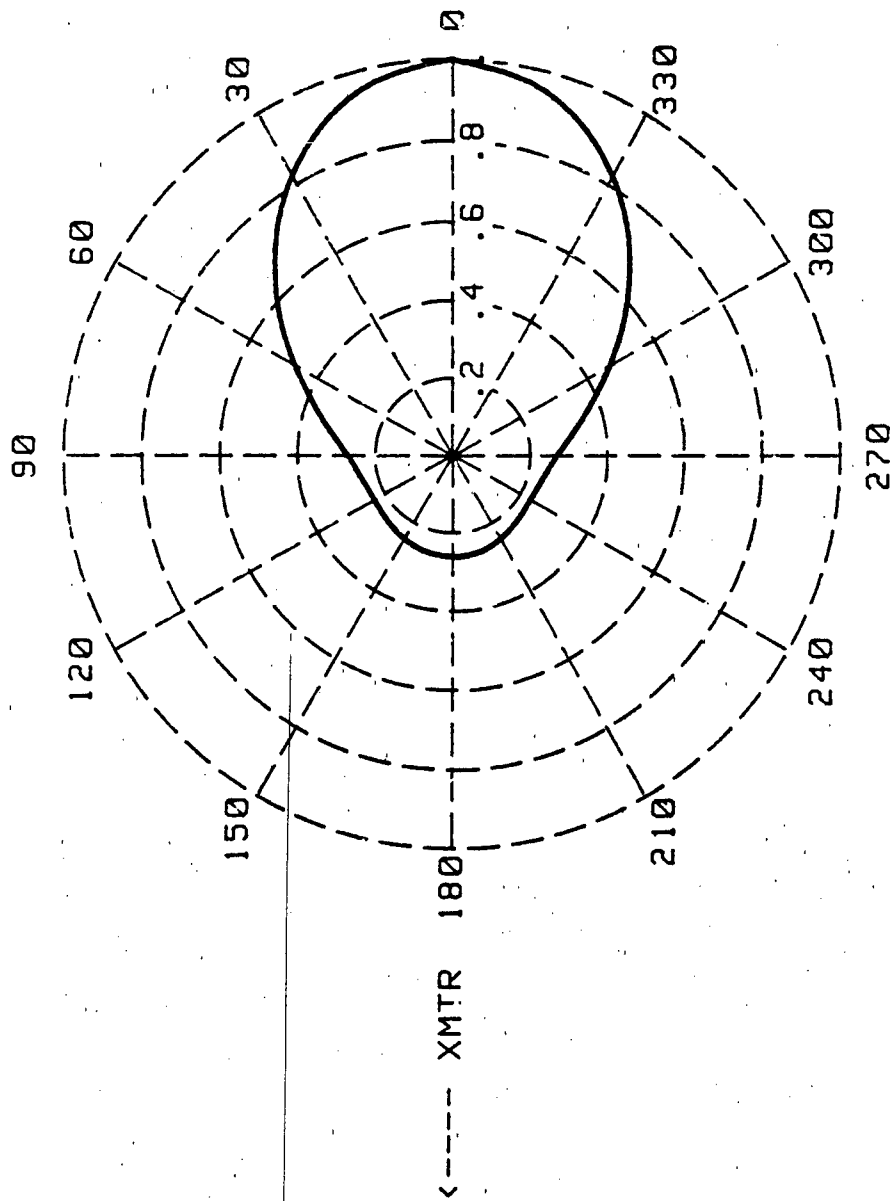


Figure 6A-12:  Normalized Specific Intensity Versus Azimuthal Scatter Angles
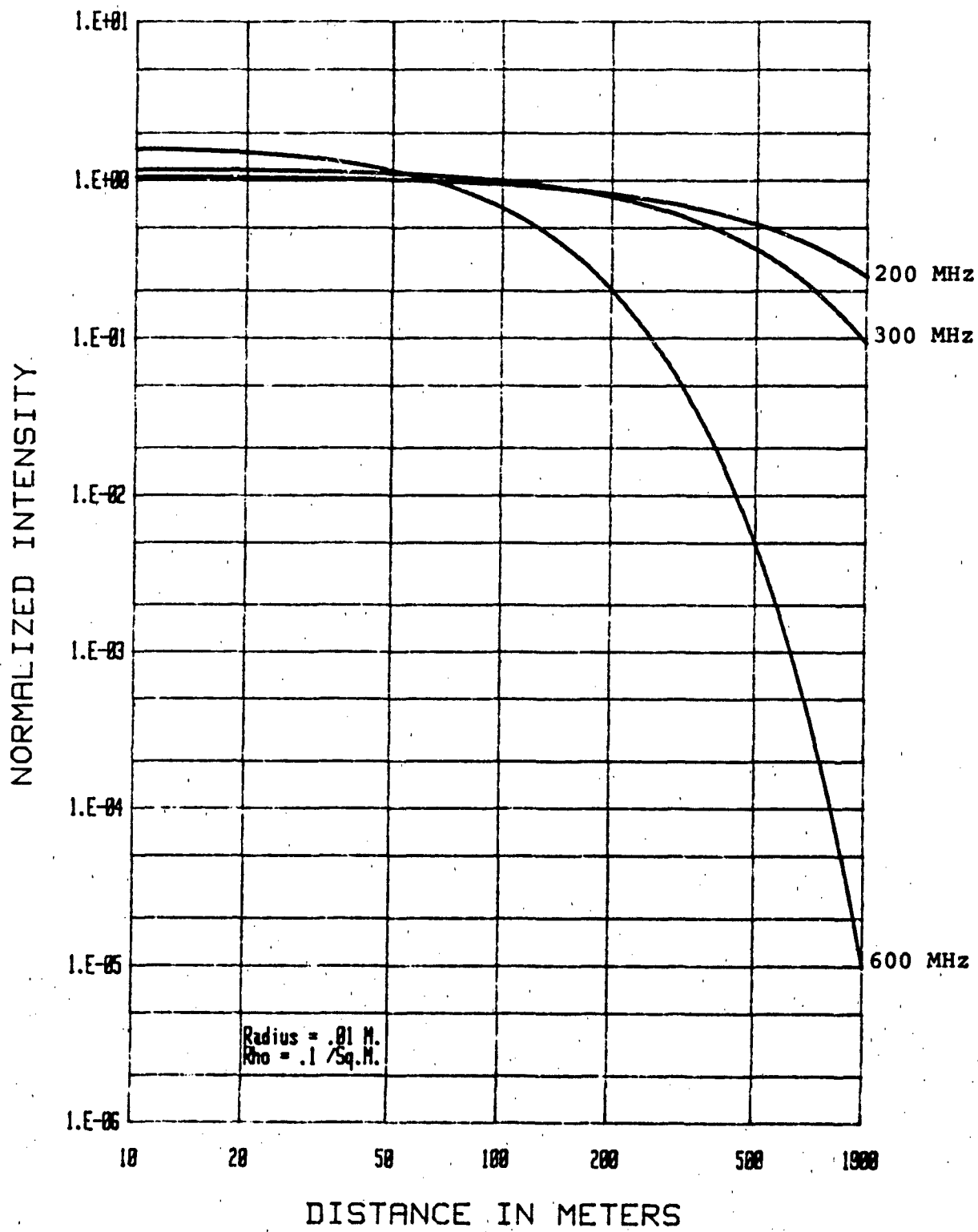
Figure 6A-13:  Total Normalized Intensity Versus Distance
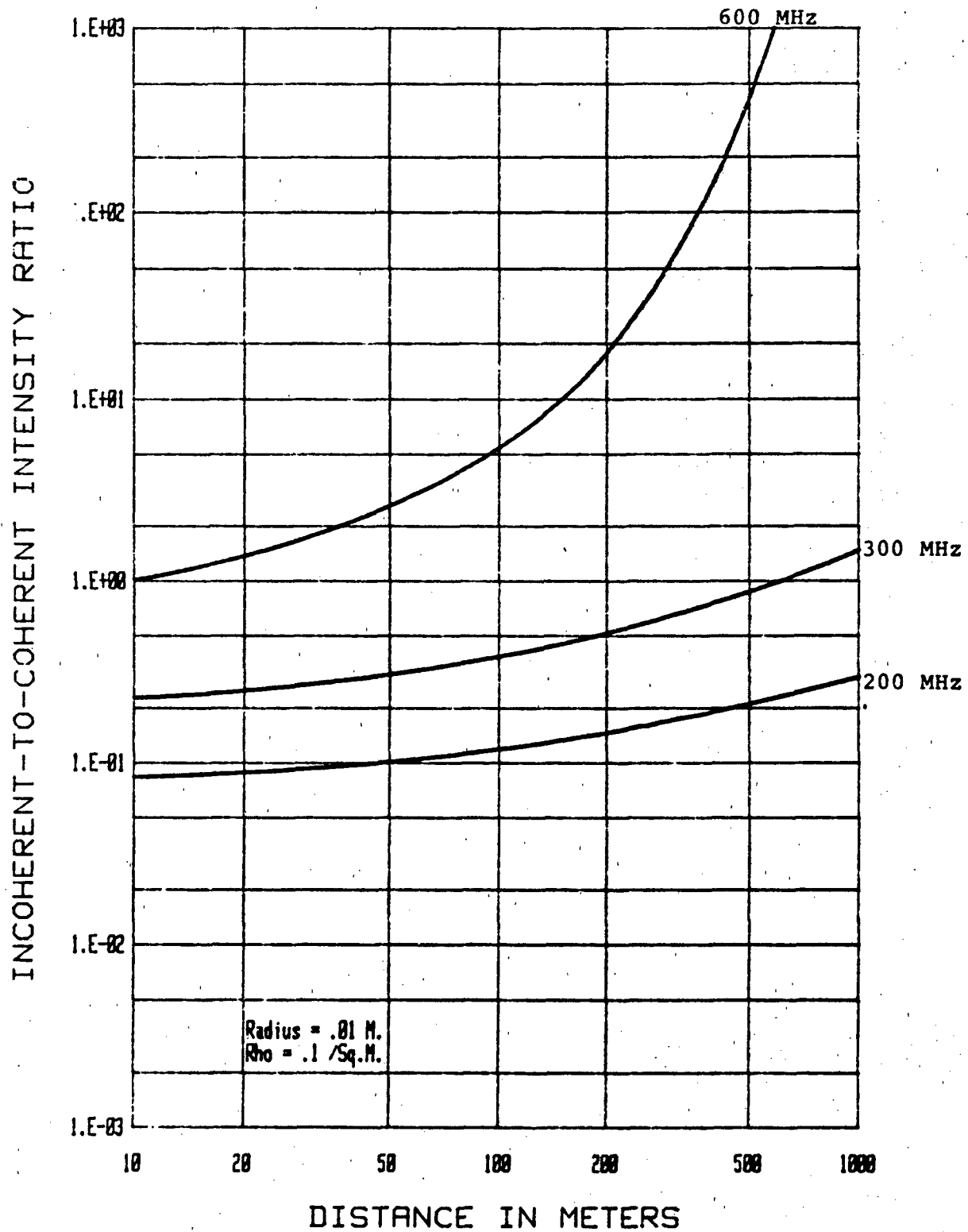
Figure 6A-14: Incoherent-to-Coherent Intensity Ratio Versus Distance
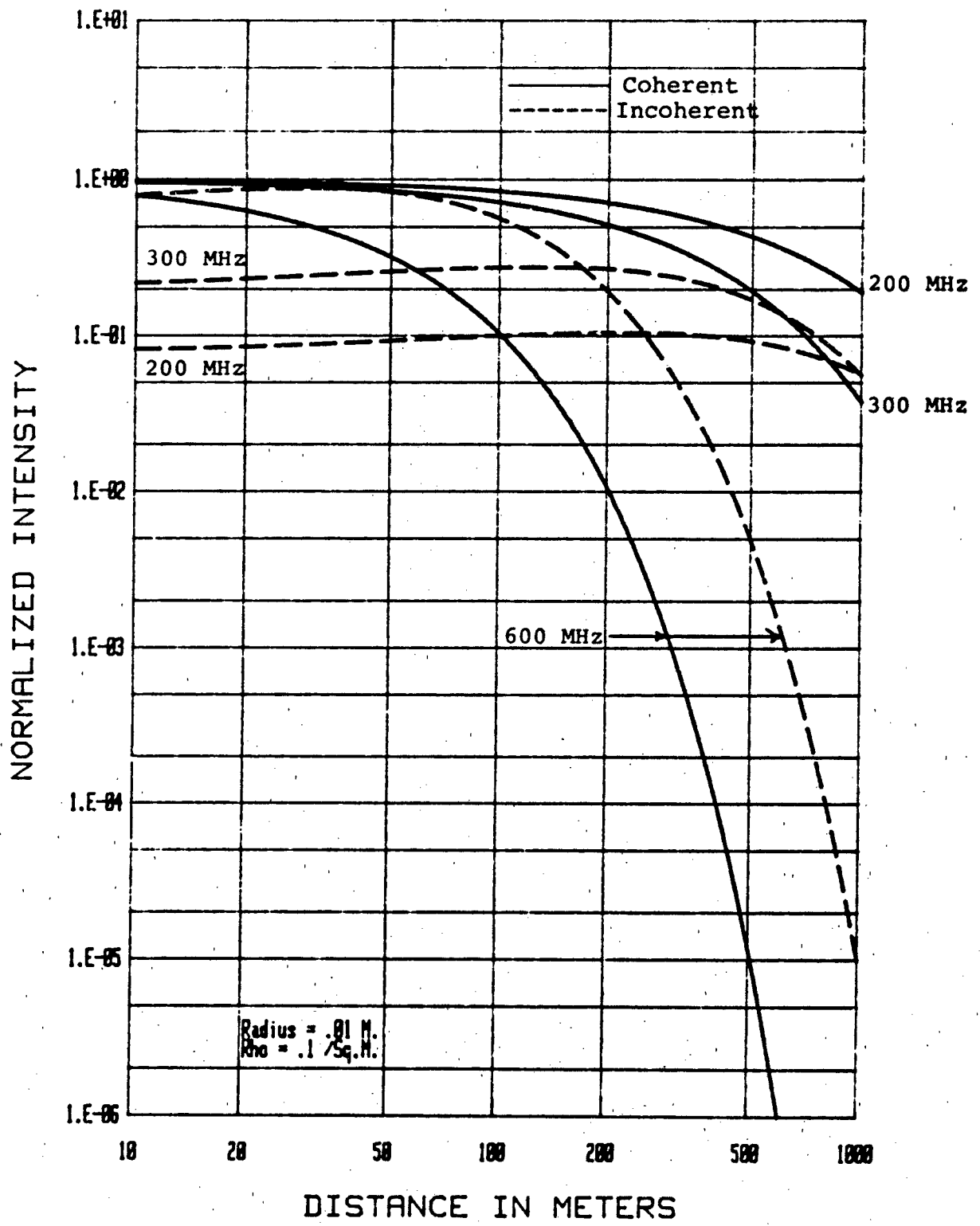
Figure 6A-15:   Normalized Intensities Versus Distance
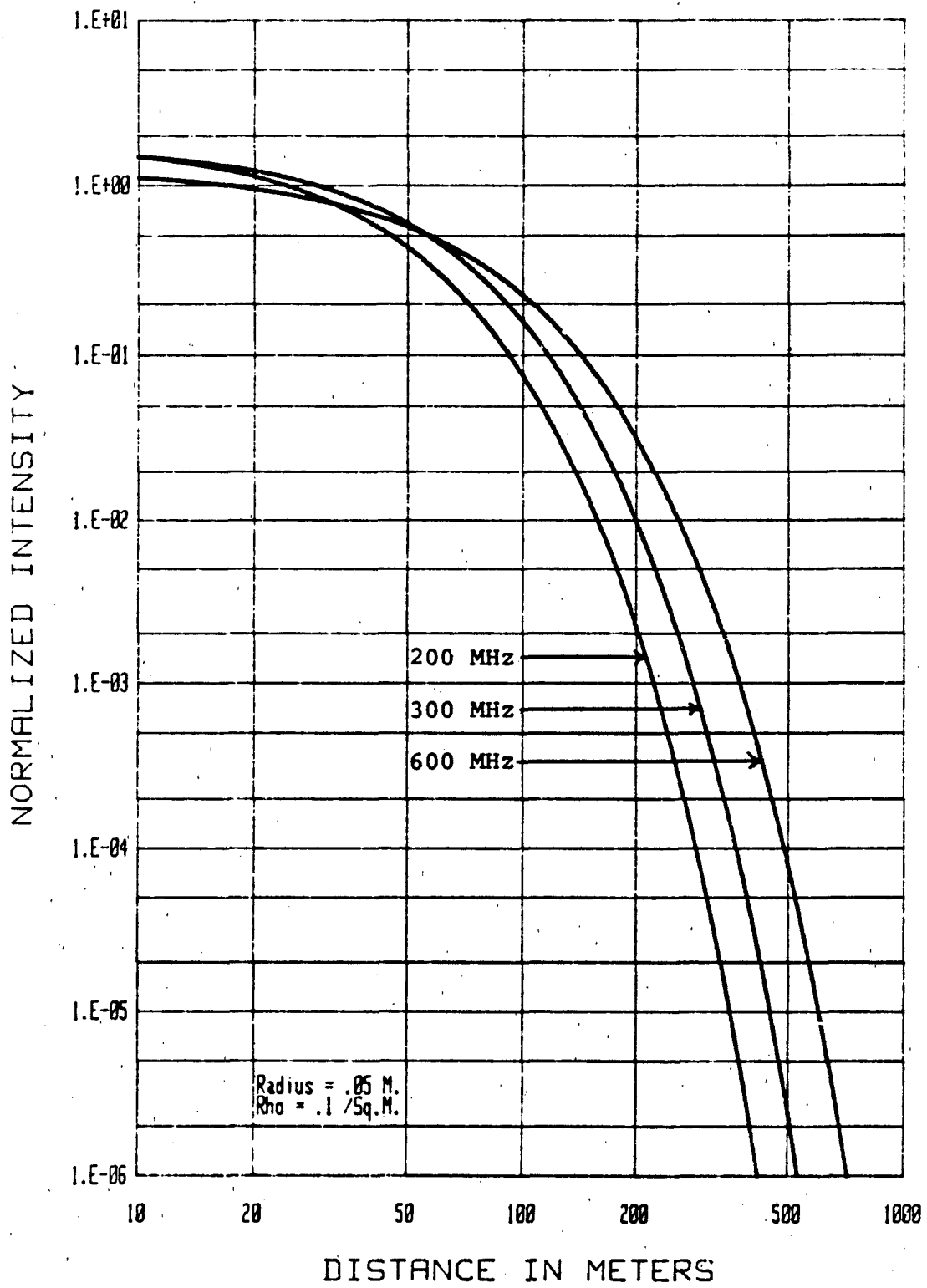
Figure 6A-16: Total Normalized Intensity Versus Distance

The chart shows NORMALIZED INTENSITY (vertical axis, from 1.E-06 to 1.E+01) versus DISTANCE IN METERS (horizontal axis, from 10 to 1000), with curves labeled 200 MHz, 300 MHz, and 600 MHz.

Radius = .05 M.
Rho = .1 /Sq.M.

6A-16
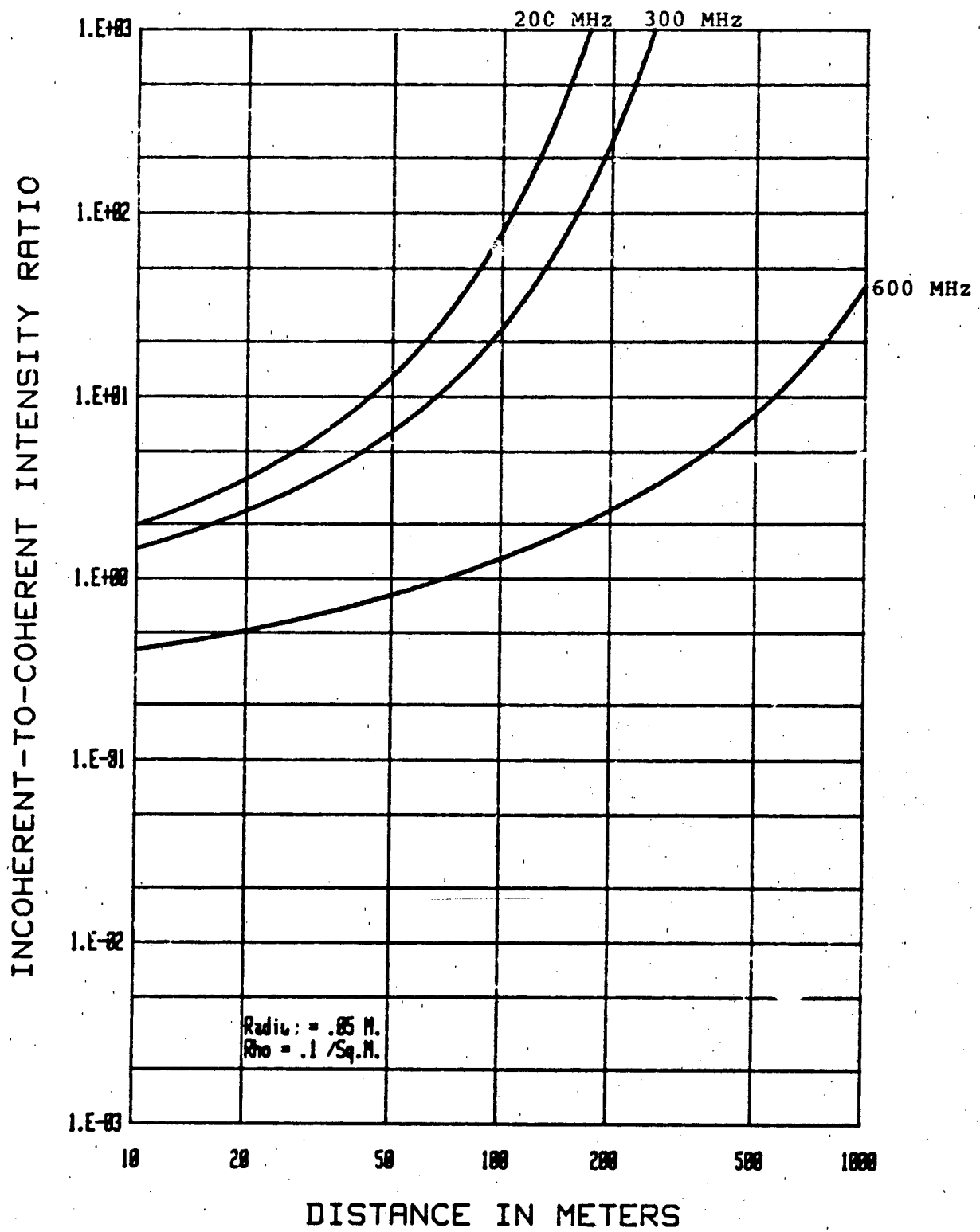
Figure 6A-17: Incoherent-to-Coherent Intensity Ratio Versus Distance
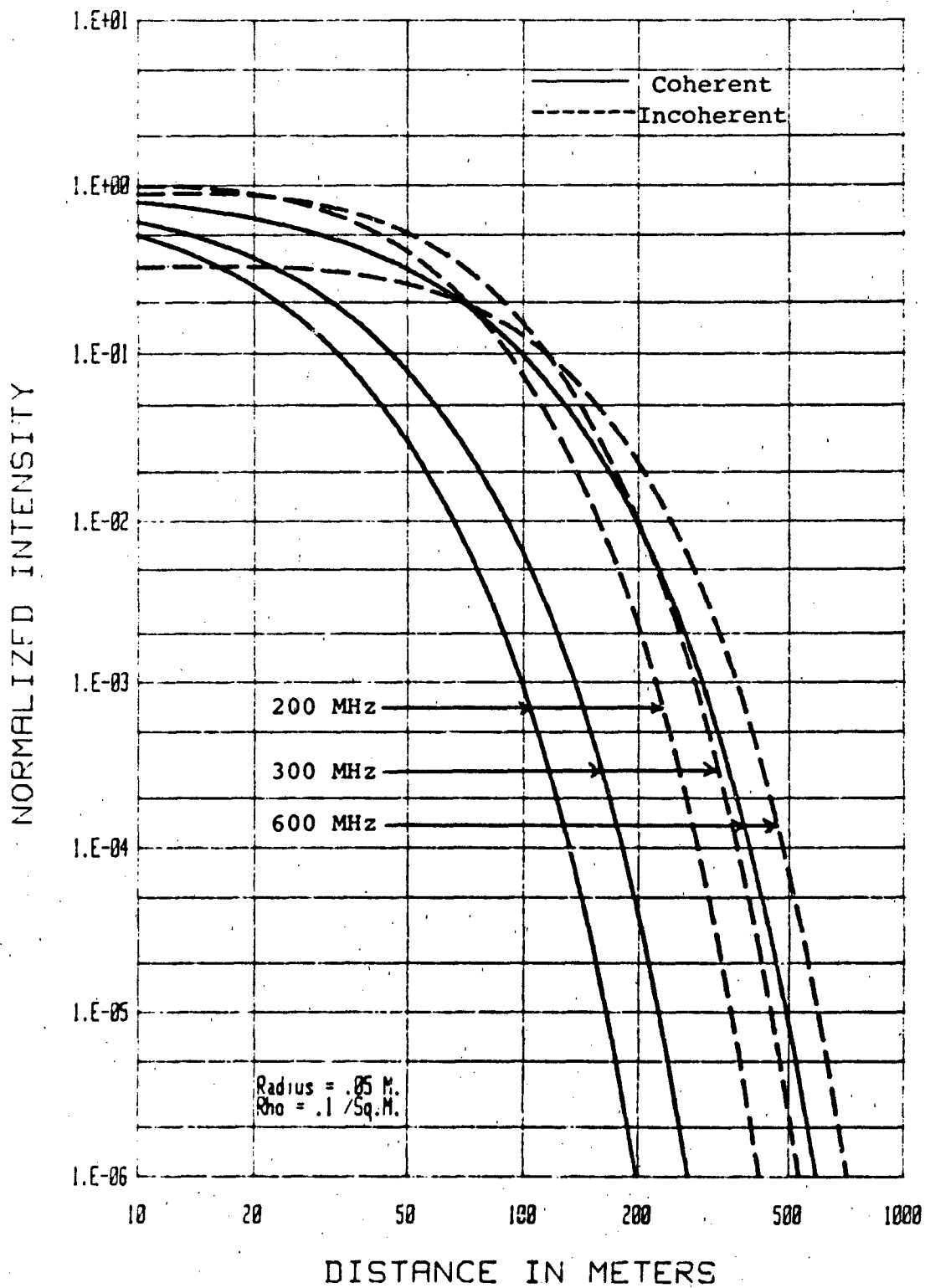
Figure 6A-18: Normalized Intensities Versus Distance
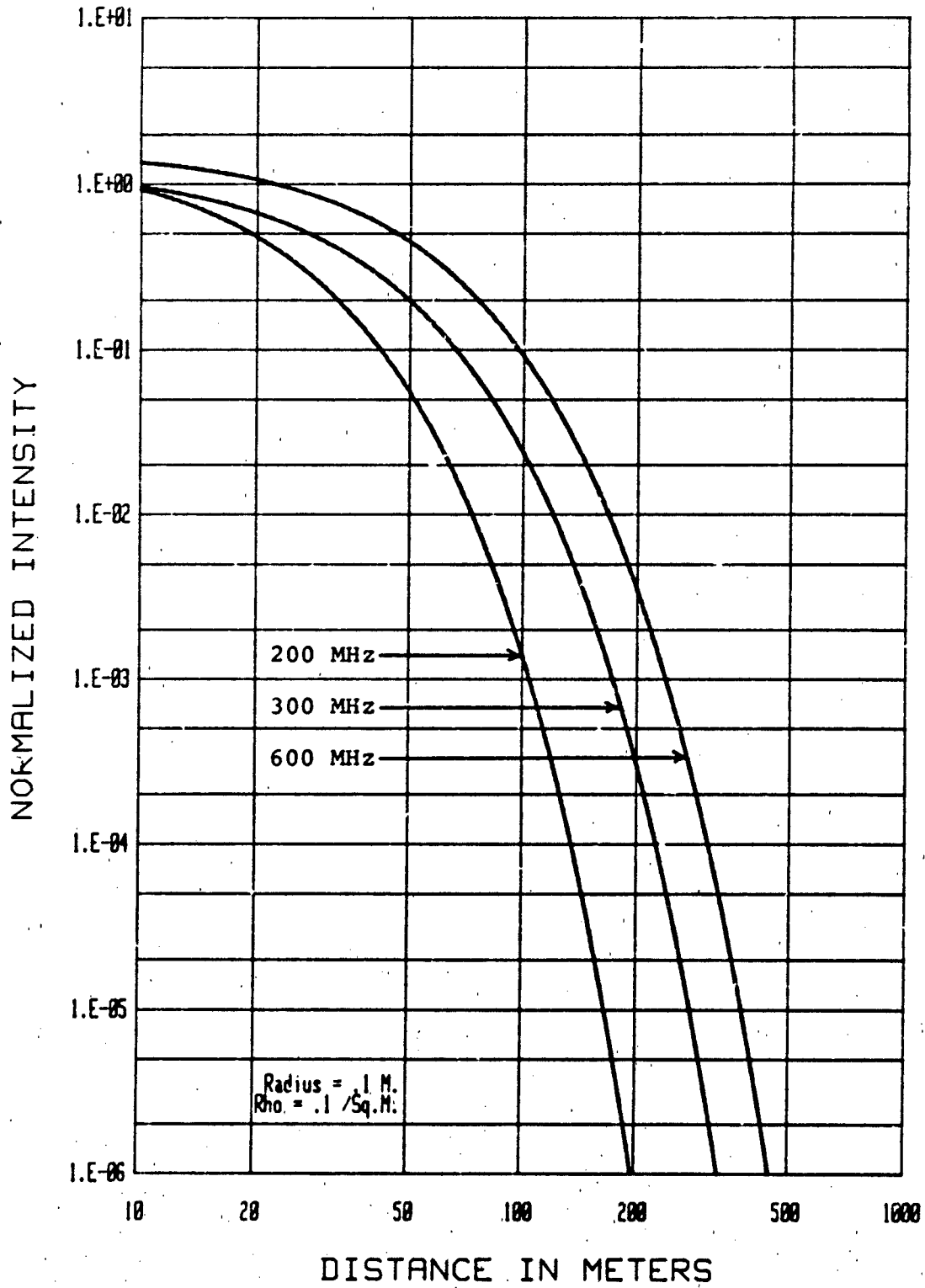
Figure 6A-19: Total Normalized Intensity Versus Distance
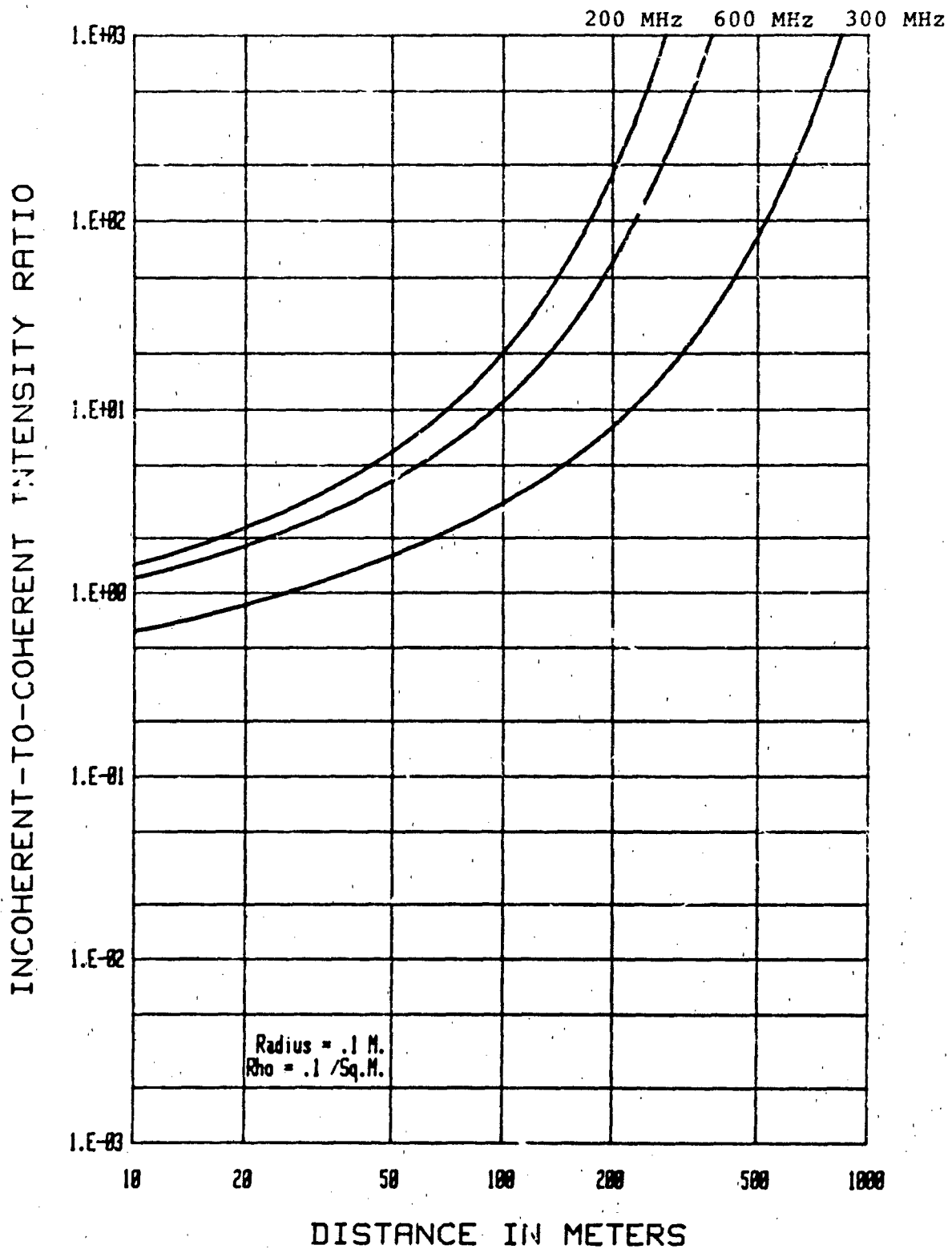
Figure 6A-20:  Incoherent-to-Coherent Intensity Ratio Versus Distance
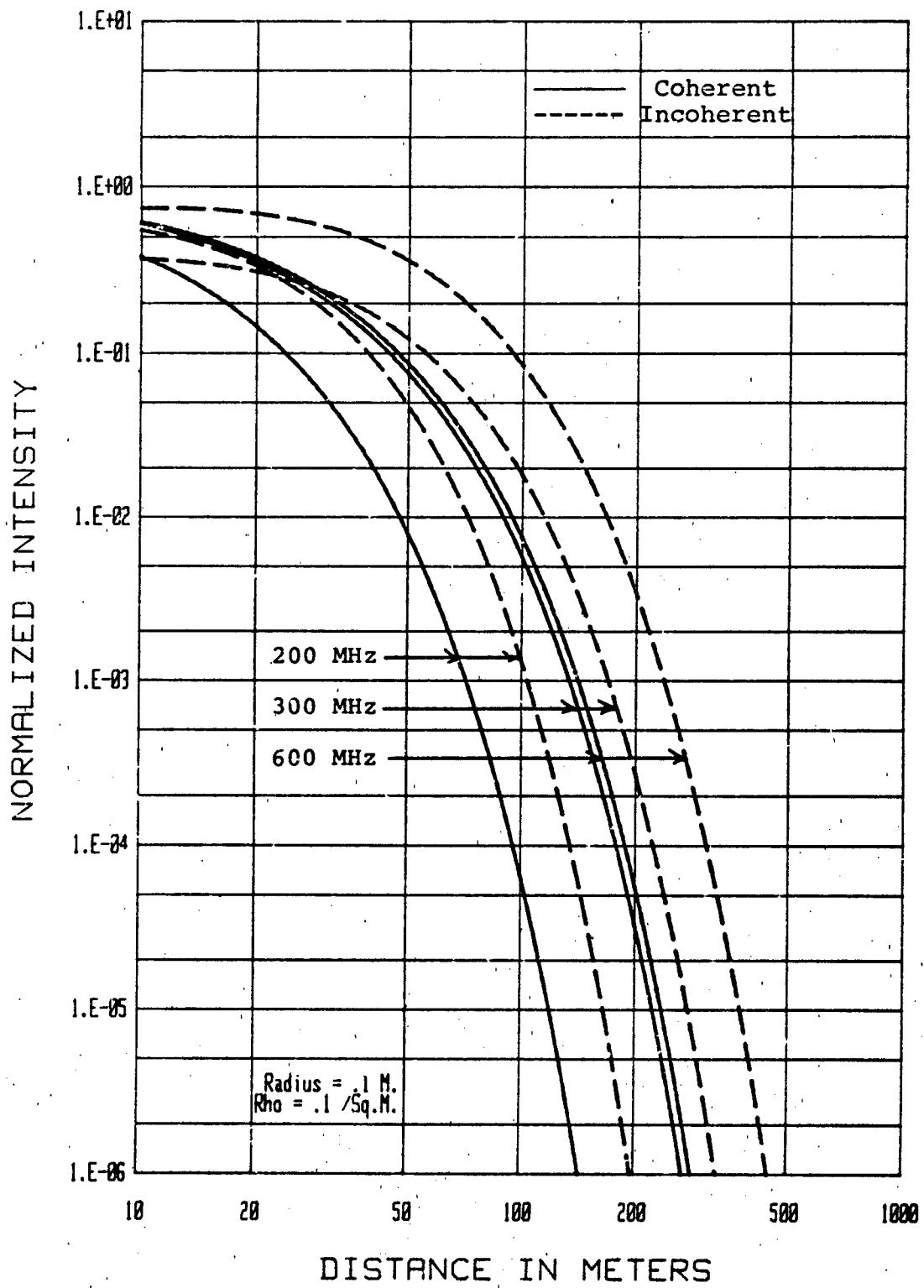
Figure 6A-21: Normalized Intensities Versus Distance

[This page intentionally left blank]

## 7.0 References

1. P.L. Altman and D.S. Dittmar, _Biology Data Book_, Vol. II (2nd edition). Fed. Amer. Soc. Exp. Biology (1972).

2. E.T. Assmann, _The Principles of Forest Yield Study_. New York: Pergamon (1970).

3. I.M. Besieris and W.E. Kohler, "Two-Frequency Radiative Transfer Equation for a Statistically Inhomogeneous and Anisotropic Absorptive Medium," In _Multiple Scattering and Waves in Random Media_, New York: North Holland (1981).

4. C.F. Bohren and D.R. Huffman, _Absorption and Scattering by Small Particles_, pp 194-212 Wiley-Interscience, New York 1983.

5. L.M. Brekhovskikh, _Waves in Layered Media_, New York: Academic Press (1960).

6. M.G. Broadhurst, "Complex Dielectric Constant and Dissipation Factor of Foliage," U.S. National Bureau of Standards Report 9592 (October, 1970).

7. G.S. Brown, "Coherent Wave Propagation Through A Sparse Concentration of Particles,' _Radio Science_, Vol. 15, No. 3, pp 705-510 (May-June, 1980).

8. G.S. Brown and W.J. Curry, "An Analytical Study of Wave Propagation through Foliage," Rome Air Development Center (RADC Final Technical Report RADC-TR-79-359 (January, 1980).

9. M.G. Cannell, _World Forest Biomass and Primary Production Data_. New York: Academic Press (1982).

10. N.L. Carlson, "Dielectric Constant of Vegetation at 8.5 GHz," Ohio State University, Electro-Science Laboratory, Technical Report 1903-5 (1967).

11. S.B. Carpenter and N.D. Smith, "Variation in Shade Leaf Thickness among Urban Trees Growing in Metropolitan Lexington, Kentucky," _Castanea_, Vol. 44, No. 2, pp 94-98 (January, 1979).

12. C.P. Cavalcante, D.P. Rogers and A.S. Giarola. "Radio Loss in Forests Using a Model with Four Layered Media," _Radio Science_, Vol 18, No. 5, pp 691-695 (September-October 1983).

13. G.P. Cavalcante and A.J. Giarola, "Optimization of Radio Communication in Media with Three Layers," _IEEE Transmission Antennas & Propagation_, Vol. AP-31, No.1, pp 141-145 (January, 1983).

14. Y.    Choc and L. Tsang, "A Mathematical Characterization of Vegetation Effect on Microwave Remote Sensing from the Earth," Texas A & M University, Remote Sensing Center, Technical Report RSC-139, August, 1983.

15. J.L.  Clutter et al, Timber Management: A Quantitative Approach. New York: Wiley (1983).

16. A.    Cohen "Scattering of a Linearly Polarized Incidence at Arbitrary Angle to Incident Plane of Infinite Tilted Cylinders," Optics Letters, Vol. 5, New York, pp 150-152 (April, 1980).

17. A.    Cohen and C. Acquista, "Light Scattering by Tilted Cylinders: Properties of Partial Wave Coefficients," Journal of the Optical Society of America, Vol 72, No. 5, pp 531-534, (May 1982).

18. R.E.  Collin and F.J. Zucker, Antenna Theory Part I. New York: McGraw-Hill (1969).

19. D.    Dence and T. Tamir, "Radio Loss of Lateral Waves in Forest Environments," Radio Science, Vol. 4, No. 4, pp 307-318 (April, 1969).

20. J.J.  Duderstadt and W.R. Martin. Transport Theory, Wiley-Interscience, New York (1979).

21. R.L.  Fante, "Relationship Between Radiative-Transfer Theory and Maxwell's Equations in Dielectric Media," Journal of the Optical Society of America, Vol. 21, No. 4 pp 460-468, (April, 1981).

22. E.L.  Feinberg, The Propagation of Radiowaves along the Earth's Surface. Moscow: USSR Academy of Sciences. (1961) [AD 660 951].

23. L.O.  Foldy, "The Multiple Scattering of Waves," Phys. Rev., Vol. 67, No. 3, pp 107-119 (March, 1945).

24. E.D.  Ford, "High Productivity in a Polestage Sitka Spruce Stand and its Relation to Canopy Structure," Forestry, Vol. 55, No. 1, pp 1-17 (1982).

25. R.M.  Frank et al, "A Silvicultural Guide for Spruce-Fir," USDA Forest Service General Technical Report NE-6 (1973).

26. A.K.  Fury and M.P. Chen, "Scattering from a Rayleigh Layer with an Irregular Interface." Radio Science, Vol. 16, No. 6, pp 1337-1347, (November-December 1981).

27. H.L.  Gary, "Crown Structure and Distribution of Biomass in a Lodgepole Pine Stand," USDA Forest Service Research Paper RM-165 (April, 1976).

28. S.F. Gingrich, "Measuring and Evaluating Stocking and Stand Density in Upland Hardwood Forests in the Central States," Forest Science, Vol. 13, No.1, pp 38-53 (1967).

29. G.H. Hagn, "VHF Radio System Performance Model for Predicting Communications Operational Ranges in Irregular Terrain," IEEE Trans. on Comm., Vol. COM-28, No. 9, pp 1637-1644 (September, 1980).

30. R.F. Hearmon and J.N. Burcham, "The Dielectric Properties of Wood," Forest Products Research, Special Report No. 8. London: Her Majesty's Stationery Office (1954).

31. F. Hildebrand, Introduction to Numerical Analysis, New York: McGraw-Hill, 2nd edition (1974).

32. S.T. Hong, I. Sreenivasiah and A. Ishimaru, "Plane Wave Pulse Propagation Through Random Media," IEEE-AP, Vol. 25, No. 6, pp 822-826, (November, 1977).

33. B.A. Hutchinson and D.R. Matt, "The Distribution of Solar Radiation within a Deciduous Forest," Ecological Monographs, Vol. 47, pp 185-207 (1977).

34. A. Ishimaru, Wave Propagation and Scattering in Random Media, (Vols. 1 & 2), New York: Academic Press (1978).

35. A. Ishimaru and J.T. Hong, "Multiple Scattering Effects on Coherent Bandwidth and Pulse Distortion of a Wave Propagating in a Random Distribution of Particles," Radio Science, Vol. 10, No. 6, pp 637-644, (June, 1975).

36. J.D. Jackson, Classical Electrodynamics, (2nd edition). New York: Wiley, (1975).

37. W.L. James and D. Hamill, "Dielectric Properties of Douglas Fir Measured at Microwave Frequencies," Forest Products J.,Vol. 15, No. 2, pg 57 (1957).

38. W.L. James, "Dielectric Properties of Wood and Hardboard," University of Wisconsin, Forest Products Laboratory, Madison, Wisconsin [AD-A015 654] (1975).

39. D.S. Kimes et al, "Extension of the Optical Diffraction Analysis Technique for Estimating Forest Canopy Geometry," Australian J. of Botany, Vol. 27, pp 575-588 (1979).

40. R. Kinerson and L.J. Fritschen, "Modeling a Coniferous Forest Canopy," Agricultural Meteorology, Vol. 8, pp 439-445 (1971).

41. D.L. Knepp, "Analytic Solution for the Two-Frequency Mutual Coherence Function for Spherical Wave Propagation," *Radio Science*, Vol. 18, No. 4, pp 535-549 (July-August, 1983).

42. R.H. Lang, A. Schneider, S. Seker and F.J. Altman, "UHF Radiowave Propagation through Forests," *CyberCom* Technical Report CTR-108-01 (September, 1982).

43. R.H. Lang, "Electromagnetic Backscattering from a Sparse Distribution of Lossy Dielectric Scatterers," *Radio Science*, Vol. 16, No. 1, pp 15-30 (January-February, 1981).

44. R.H. Lang and J. Sidhu, "Electromagnetic Backscattering from a Layer of Vegetation: A Discrete Approach," *IEEE Trans. Geoci. Electron.*, Vol. GE-21, No. 1, (January, 1983).

45. M. Lax, "Multiple Scattering of Waves," *Rev. Mod. Phys.*, Vol. 23, No. 4, pp 287-310 (1951).

46. E.L. Little, "Important Forest Trees of the U.S.," USDA Forestry Service Handbook HBN519 (June, 1978).

47. D. Ludwig, "The Radon Transform on Euclidean Space," *Communications on Pure and Applied Math.* Vol. 19, No. 1, pp 49-81 (February, 1966).

48. J.P. McClure et al, " Biomass in Southeastern Forests," USDA Forest Service Research Paper SE-227, (1981).

49. J.D. Murphy et al, "A Surface Wave Interpretation for the Resonances of a Dielectric Sphere," *IEEE Trans. Antennas & Propagation*, Vol. AP-28, No. 6, pp 924-927 (November, 1980).

50. J.F. Owen et al, "Internal Electric Field Distributions of a Dielectric Cylinder at Resonance Wavelengths," *Optics Letters*, Vol. 6, No. 11, pp 540-542 (November, 1981).

51. NATL Bureau of Standards, "Tables of the Bessel Functions $J_0(z)$ and $J_1(z)$ for Complex Arguments", 2nd ed., New York: Columbia University Press (1947).

52. NATL Bureau of Standards, "Tables of the Bessel Functions $Y_0(z)$ and $Y_1(z)$ for Complex Arguments", New York: Columbia University Press (1950).

53. C.L. Rino, V.H. Gonzalez and A.R. Hessing, "Coherence Bandwidth Loss in Trans-ionospheric Radio Propagation," *Radio Science*, Vol. 16, No. 2, p 245 (1981).

54. B.A. Roach, "A Stocking Guide for Allegheny Hardwoods and its Use in Controlling Intermediate Cuttings," USDA Forest Service Research Paper NE-373 (1977).

55. C.M. Rose and I.M. Besieris, "Nth Order Multifrequency Coherence Functions: A Functional Path Integral Approach," J. Math. Phys., Vol. 20, pp 1530-1538 (1979).

56. J.S. Rothacher, F.E. Blow and S.M. Potts, "Estimating the Quantity of Tree Foliage in Oak Stands in the Tennessee Valley," Journal of Forestry, pp 169-173 (March, 1954).

57. D.L. Sachs and P.J. Wyatt, "A Conducting-Slab Model for Electromagnetic Propagation Within a Jungle Medium," Radio Science, Vol. 3, No. 2, pp 125-134 (February, 1968).

58. F.K. Schwering, R.A. Johnson, N. Rokkos and G.M. Whitman, E.J. Violette and R.H. Espeland, "Effects of Vegetation and Battlefield Obscurants on Point-to-Point Transmission in the Lower Millimeter Wave Region," U.S. Army Science Conference, West Point (June, 1982).

59. S.S. Seker, "Resonant Backscattering from Sparsely Distributed Lossy Dielectric Scatterers," George Washington University, D. SC. Dissertation (1982).

60. J.A. Smith et al, "Thermal Vegetation Canopy Model Studies," Remote Sensing of the Environment, Vol. 11, pp 311-326 (1981).

61. I. Sreenivasiah, A. Ishimaru, and S.T. Hong, "Two-Frequency Mutual Coherence Function and Pulse Propagation in a Random Medium: An Analytic Solution to the Plane Wave Case," Radio Science, Vol. 11, pp 775-778 (1976).

62. D. Staiman and T. Tamir, "Nature and Optimization of the Ground (Lateral) Wave Excited by Submerged Antennas," Proc. IEE, Vol. 113, No. 8, pp 1299-1310 (August, 1966).

63. G.R. Stephens, "Productivity of Red Pine, I. Foliage Distribution in Tree Crown and Stand Canopy," Agricultural Meteorology, Vol. 6, pp 275-282 (1968).

64. T. Tamir, "On Radio Wave Propagation in Forest Environments," IEEE Trans. Antennas and Propagation, Vol. AP-15, No. 6, pp 806-817 (November, 1967).

65. T. Tamir and L.B. Felsen, "On Lateral Wave in Slab Configurations and Their Relation to Other Wave Types," IEEE Trans. Antennas and Propagation, Vol. AP-13, pp 410-422 (May, 1965).

66. V.W. Trapp and L. Pungs, "Einfluss von Temperatur und Feuchte auf das Dielectrische Verhalten von Naturholz im Grossen Frequenzbereich," <u>Holzforschung</u>, Vol. 10, No. 5, pp 144-150 (1956).

67. L. Tsang, J.A. Kong and R.T. Shin, "Radiative Transfer Theory for Active Remote Sensing of a Layer of Nonspherical Particles," <u>Radio Science</u>, Vol. 19, No. 2, pp 629-642 (March-April, 1984).

68. V. Twersky, "Multiple Scattering of Electromagnetic Waves by Arbitrary Configuration," <u>J. Math. Phys.</u>, Vol. 8, No. 3, pp 589-610 (1967).

69. B.J. Uscinski, "The Propagation and Broadening of Pulses in Weakly Irregular Media," <u>Proc. R. Soc. Lond.</u>, Vol. A336, pp 379-392 (1974).

70. USDA Forestry Service, <u>Wood Handbook</u> [HBN72]. Washington, D.C.: US Government Printing Office (1955).

71. E.J. Violette, R.H. Espeland and F. Schwering, "Vegetation Loss Measurements at 9.6, 28.8 and 57.6 GHz Through a Pecan Orchard in Texas," US Army, Research and Development Technical Report CECOM-83-2, Fort Monmouth, New Jersey (March, 1983).

72. J.R. Wait, <u>Electromagnetic Radiation from Cylindrical Structures</u>, New York: Pergamon (1959).

73. R.H. Waring et al, "Application of the Pipe Model Theory to Predict Canopy Leaf Area," <u>Canadian J. For. Res.</u>, Vol. 12, pp 556-560 (1982).

74. M.A. Weissberger et al, "Radio Wave Propagation: A Handbook of Practical Techniques for Computing Basic Transmission Loss and Field Strength," Electromagnetic Compatability Analysis Center (ECAC), Report No. ECAC-HDBK-82-049 (September, 1982).

75. G.M. Whitman, F. Schwering and L. Chen, "A Theory of Millimeter Wave Propagation in Vegetation," Fort Monmouth Report CECOM-TR-84-5 (July, 1984).

76. H.V. Wiant, "Diameter Distribution of the West Virginia University Forest," <u>West Virginia Agric. For.</u>, Vol. 7, No. 3, pp 16-18 (June, 1978).

77. K.C. Yeh, "Mutual Coherence Function and Intensities of Backscattered Signals in a Turbulent Medium," <u>Radio Science</u>, Vol. 18, No. 2, pp 159-165 (March-April, 1983).

78. K.C. Yeh and C.H. Lin, "An Investigation of Temporal Moments of Stochastic Waves," <u>Radio Science</u>, Vol. 12, pp 671-680 (1977).

## APPENDIX A

### Space-Frequency Correlation Equation

In this Appendix the approximate equation for the space-frequency correlation function will be derived. The methodology employed in the derivation will parallel the Foldy development for the mean equation.

Consider two fields $\psi(\underline{x}_t, \omega)$ and $\psi^*(\hat{\underline{x}}_t, \hat{\omega})$. The field $\psi(\underline{x}_t, \omega)$ is observed at point $\underline{x}_t$, at frequency $\omega$, while the field $\psi^*(\hat{\underline{x}}_t, \hat{\omega})$ is the conjugate of the field observed at point $\underline{x}_t$, at frequency $\omega$. In the remainder of the Appendix, the dependence of $\psi$ on $\underline{x}_t$ and $\omega$, and of $\psi^*$ on $\hat{\underline{x}}_t$ and $\hat{\omega}$ will be suppressed for convenience. All quantities without the conjugate sign will be assumed to be functions of unhatted variables, while conjugated quantities will be functions of hatted variables.

The total field $\psi$ can be decomposed into two parts: the incident field, $\psi_i$, and the various scattered fields from the individual particles, i.e.

$$\psi = \psi_i + \sum_{j=1}^{N} \psi_s^{(j)} \quad , \quad L\psi = g \tag{A-1}$$

where $\psi_s^{(j)}$ is the scattered field from the $j^{th}$ particle which is related to the transition operator $T_j$ of the $j^{th}$ particle as

$$L\psi_s^{(j)} = g_{eq}^{(j)} = T_j \psi^{(j)} \tag{A-2}$$

The quantity $\psi^{(j)}$ in (A-2) is the field at the location of the $j^{th}$ particle with the $j^{th}$ particle removed. Substituting (A-2) into (A-1) gives the following equation

$$\psi = \psi_i + \sum_{j=1}^{N} L^{-1} T_j \psi^{(j)} \quad , \quad L\psi_i = g \tag{A-3}$$

Similarly, the equation for the conjugate field $\psi^* = \psi^*(\hat{\underline{x}}_t, \hat{\omega})$ is obtained as

$$\psi^* = \psi_i^* + \sum_{j=1}^{N} L^{-1*} T_j^* \psi^{(j)*} \quad , \quad L^* \psi_i^* = g^*$$ (A-4)

Now, forming the product $\psi\psi^*$ and averaging yields

$$\langle\psi\psi^*\rangle = \psi_i\psi_i^* + \psi_i \sum_{j=1}^{N} L^{-1*} \langle T_j^* \psi^{(j)*}\rangle + \sum_{j=1}^{N} L^{-1} \langle T_j \psi^{(j)}\rangle \psi_i^*$$

$$+ \sum_{j=1}^{N} \sum_{k=1}^{N} L^{-1} L^{-1*} \langle T_j T_k^* \psi^{(j)} \psi^{(k)*}\rangle$$ (A-5)

The double sum appearing in the above equation can be broken into like terms (j=k) and unlike terms (j≠k) as follows

$$\langle\psi\psi^*\rangle = \psi_i\psi_i^* + \psi_i \sum_{j=1}^{N} L^{-1*} \langle T_j^* \psi^{(j)*}\rangle + \sum_{j=1}^{N} L^{-1} \langle T_j \psi^{(j)}\rangle \psi_i^* + \sum_{j=1}^{N} L^{-1} L^{-1*}$$

$$\cdot \langle T_j T_j^* \psi^{(j)} \psi^{(j)*}\rangle + \sum_{\substack{j=1 \\ j\neq k}}^{N} \sum_{k=1}^{N} L^{-1} L^{-1*} \langle T_j T_k^* \psi^{(j)} \psi^{(k)*}\rangle$$ (A-6)

To obtain an equation for the correlation function a closure approximation is employed. The approximation to be used is

$$\psi^{(j)} \approx \langle\psi\rangle$$

$$\psi^{(j)} \psi^{(j)*} \approx \langle\psi\psi^*\rangle$$ (A-7)

$$\psi^{(j)} \psi^{(k)*} \approx \langle\psi\rangle\langle\psi^*\rangle \quad , \quad j\neq k$$

This is a generalization of Foldy's closure approximation used to derive the mean equation. Using this approximation in (A-6) gives

$$\langle\psi\psi^*\rangle = \psi_i\psi_i^* + \psi_i \sum_{j=1}^{N} L^{-1*} \langle T_j^*\rangle\langle\psi^*\rangle + \sum_{j=1}^{N} L^{-1} \langle T_j\rangle\langle\psi\rangle \psi_i^*$$

$$+ \sum_{j=1}^{N} L^{-1} L^{-1*} \langle T_j T_j^*\rangle\langle\psi\psi^*\rangle + \sum_{\substack{j=1 \\ j\neq k}}^{N} \sum_{k=1}^{N} L^{-1} \langle T_j\rangle\langle\psi\rangle L^{-1*} \langle T_j^*\rangle\langle\psi^*\rangle$$ (A-8)

Since the particles are identically distributed, the statistics for all particles are the same, i.e.,

$$\sum_{j=1}^{N} \langle T_j \rangle = N \langle T \rangle \qquad (A-9)$$

$$\sum_{j=1}^{N} \langle T_j T_j^* \rangle = N \langle TT^* \rangle \qquad (A-10)$$

Employing these simplifications in (A-8) yields

$$\langle \psi \psi^* \rangle = \psi_i \psi_i^* + N\psi_i L^{-1*} \langle T^* \rangle \langle \psi^* \rangle + NL^{-1} \langle T \rangle \langle \psi \rangle \psi_i^*$$

$$\qquad (A-11)$$

$$+ NL^{-1} L^{-1*} \langle TT^* \rangle \langle \psi \psi^* \rangle + (N^2 - N) L^{-1} \langle T \rangle \langle \psi \rangle L^{-1*} \langle T^* \rangle \langle \psi^* \rangle$$

Notice that for $N \gg 1$, $N^2 - N = N^2(1 - \frac{1}{N}) \approx N^2$. Using this fact, Equation (A-11) can be put into the following form

$$\langle \psi \psi^* \rangle = (\psi_i + NL^{-1} \langle T \rangle \langle \psi \rangle) \cdot (\psi_i^* + NL^{-1*} \langle T^* \rangle \langle \psi^* \rangle)$$

$$+ NL^{-1} L^{-1*} \langle TT^* \rangle \langle \psi \psi^* \rangle \qquad (A-12)$$

Equation (A-12) can be simplified substantially by making use of the mean-wave equation.

The mean-wave equation is given in the text by Equation (2-2-48) as

$$\mathcal{L} \langle \psi \rangle = g \quad , \quad \mathcal{L} = L - N \langle T \rangle \qquad (A-13)$$

Multiply (A-13) by $L^{-1}$ from the left. This yields

$$\langle \psi \rangle = \psi_i + NL^{-1} \langle T \rangle \langle \psi \rangle \qquad (A-14)$$

A similar result for the conjugate field is also obtained by inspection

$$\langle \psi^* \rangle = \psi_i^* + NL^{-1*} \langle T^* \rangle \langle \psi^* \rangle \qquad (A-15)$$

Substituting Equations (A-14) and (A-15) into Equation (A-12) gives the desired equation for the space-frequency correlation function $\langle \psi\psi^* \rangle$

$$\langle \psi\psi^* \rangle = \langle \psi \rangle \langle \psi^* \rangle + NL^{-1}L^{-1*}\langle TT^* \rangle \langle \psi\psi^* \rangle \qquad (A-16)$$

Multiplying Equation (A-16) by $\mathcal{L}\mathcal{L}^*$ from the left, using the fact that $\mathcal{L}\langle\psi\rangle = g$, $\mathcal{L}^*\langle\psi^*\rangle = g^*$ and $\mathcal{L}\mathcal{L}^*L^{-1}L^{-1*} \approx 1$ yields

$$\mathcal{L}\mathcal{L}^*\langle \psi\psi^* \rangle - N\langle TT^* \rangle \langle \psi\psi^* \rangle = gg^* \qquad (A-17)$$

The above steps can be justified by scaling the problems with respect to the characteristic size of the particle, then N is replaced by the fractional volume which is small.

The final form of the correlation equation as it appears in Equation (2-2-44) is obtained by writing the spatial average of $TT^*$ out explicitly and by using Equation (2-2-38).

## APPENDIX B

### Radon Transform of the Mean Green's Function

The two-dimensional mean Green's equation is given in explicit form as follows

$$(\nabla_t^2 + k_o^2)G(\underline{x},\underline{x}_o) + \int d\underline{s}d\underline{x}'\rho(\underline{s})t(\underline{x} - \underline{s},\underline{x}' - \underline{s})G(\underline{x}',\underline{x}_o)$$
$$= -\delta(\underline{x} - \underline{x}_o) \qquad (B-1)$$

Employing the two-variables perturbation method, the mean Green's function $G(\underline{x},\underline{x}_o)$ is expanded as

$$G(\underline{x} - \underline{x}_o;\overline{\underline{x}},\overline{\underline{x}}_o;\epsilon) = \sum_{n=0}^{\infty} G^{(n)}(\underline{x} - \underline{x}_o;\overline{\underline{x}},\overline{\underline{x}}_o)\cdot\epsilon^n \qquad (B-2)$$

where the slow variables are defined as

$$\overline{\underline{x}} = \epsilon\underline{x} \quad, \quad \overline{\underline{x}}_o = \epsilon\underline{x}_o \quad, \quad \overline{\underline{s}} = \epsilon\underline{s} \quad, \quad \rho(\underline{s}) = \epsilon\overline{\rho}(\overline{\underline{s}}) \quad, \quad \epsilon \ll 1 \qquad (B-3)$$

Here $\epsilon$ is the fractional area and can be introduced into the Green's function equation by scaling variables. Setting $\rho = \epsilon\overline{\rho}$ is a more direct but less physical way of obtaining the correct $\epsilon$ dependence.

The Radon transform [ ] of $G^{(n)}$ (denoted by $\hat{G}^{(n)}$) with respect to $\underline{x} - \underline{x}_o$ is defined as

$$RG^{(n)} \equiv \hat{G}^{(n)}(\zeta,\underline{o};\overline{\underline{x}},\overline{\underline{x}}_o)$$

$$= \int d\underline{x}G^{(n)}(\underline{x} - \underline{x}_o;\overline{\underline{x}},\overline{\underline{x}}_o)\delta(\zeta - \underline{o}\cdot(\underline{x} - \underline{x}_o)) \qquad (B-4)$$

Thus the Radon transform of the mean Green's function is found to be

$$RG \equiv \hat{G}(\zeta,\underline{o};\overline{\underline{x}},\overline{\underline{x}}_o) = \sum_{n=0}^{\infty} \hat{G}^{(n)}(\zeta,\underline{o};\overline{\underline{x}},\overline{\underline{x}}_o)\cdot\epsilon^n \qquad (B-5)$$

In this Appendix the Radon transform of the mean Green's function is approximated to the first order only as

$$RG \approx \hat{G}^{(o)}(\zeta,\underline{o};\overline{\underline{x}},\overline{\underline{x}}_o) \qquad (B-6)$$

After inserting Equation (B-2) into (B-1) and equating coefficients of $\epsilon^o$ and $\epsilon'$, the following two equations in $G^{(o)}$ and $G^{(1)}$ are obtained respectively

$$(\nabla_t^2 + k_o^2)G^{(o)}(\underline{x} - \underline{x}_o; \overline{\underline{x}}, \overline{\underline{x}}_o) = -\delta(\underline{x} - \underline{x}_o) \qquad \text{(B-7a)}$$

$$(\nabla_t^2 + k_o^2)G^{(1)}(\underline{x} - \underline{x}_o; \overline{\underline{x}}, \overline{\underline{x}}_o) = h(\underline{x} - \underline{x}_o; \overline{\underline{x}}, \overline{\underline{x}}_o) \qquad \text{(B-7b)}$$

where

$$h(\underline{x} - \underline{x}_o; \overline{\underline{x}}, \overline{\underline{x}}_o) = -2\nabla_t \cdot \overline{\nabla}_t G^{(o)}(\underline{x} - \underline{x}_o; \overline{\underline{x}}, \overline{\underline{x}}_o)$$

$$-\overline{\rho}(\overline{\underline{x}}) \int d\underline{s}\, d\underline{x}'\, t(\underline{x}-\underline{s}, \underline{x}'-\underline{s}) G^{(o)}(\underline{x}-\underline{x}_o; \overline{\underline{x}}, \overline{\underline{x}}_o) \qquad \text{(B-8)}$$

$$\nabla_t = \partial_x \hat{\underline{x}} + \partial_y \hat{\underline{y}} \qquad ; \qquad \overline{\nabla}_t = \partial_{\overline{x}} \hat{\underline{x}} + \partial_{\overline{y}} \hat{\underline{y}} \qquad \text{(B-9)}$$

The Radon transform of Equation (B-7a) with respect to $\underline{x} - \underline{x}_o$ is found to be

$$\left(\frac{\partial^2}{\partial \zeta^2} + k_o^2\right)\hat{G}^{(o)}(\zeta, \underline{o}; \overline{\underline{x}}, \overline{\underline{x}}_o) = -\delta(\zeta) \qquad , \qquad -\infty < \zeta < \infty \qquad \text{(B-10)}$$

Since $G^{(o)}(-\zeta, -\underline{o}; \overline{\underline{x}}, \overline{\underline{x}}_o) = G^{(o)}(\zeta, \underline{o}; \overline{\underline{x}}, \overline{\underline{x}}_o)$, the solution of (B-10) has the following form

$$\hat{G}^{(o)}(\zeta, \underline{o}; \overline{\underline{x}}, \overline{\underline{x}}_o) = \begin{cases} A(\overline{\underline{x}}; \underline{o})\, e^{jk_o\zeta} & , \qquad \text{for } \zeta > 0 \\ \\ A(\overline{\underline{x}}; -\underline{o})\, e^{-jk_o\zeta} & , \qquad \text{for } \zeta < 0 \end{cases} \qquad \text{(B-11)}$$

where $A(\overline{\underline{x}}, \underline{o})$ is to be determined. Notice that the dependence of $A(\overline{\underline{x}}; \underline{o})$ upon $\underline{x}_o$ is suppressed for convenience and the solutions $e^{-jk_o\zeta}$ for $\zeta > 0$, $e^{jk_o\zeta}$ for $\zeta < 0$ have been excluded since there are no boundaries in free space.

The continuity of $\hat{G}^{(o)}$ at $\zeta = 0$ together with the jump condition of $\partial G^{(o)}/\partial \zeta$ at $\zeta = 0$ imply that

$$A(\overline{\underline{x}}_o; \underline{o}) = A(\overline{\underline{x}}_o; -\underline{o}) = -\frac{1}{2jk_o} \qquad \text{(B-12)}$$

The Radon transform of Equation (B-7b) with respect to $\underline{x} - \underline{x}_0$ is found to be

$$\left(\frac{\partial^2}{\partial \zeta^2} + k_o^2\right) \hat{G}^{(1)}(\zeta,\underline{o};\overline{\underline{x}},\overline{\underline{x}}_o) = \hat{h}(\zeta,\underline{o};\overline{\underline{x}},\overline{\underline{x}}_o) \tag{B-13}$$

where $\hat{h}(\zeta,\underline{o};\overline{\underline{x}},\overline{\underline{x}}_o)$ is the Radon transform of h given in Equation (B-8). The Radon transform $\hat{h}$ is computed for $\zeta > 0$ as

$$\hat{h}(\zeta,\underline{o};\overline{\underline{x}},\overline{\underline{x}}_o) = A(\overline{\underline{x}};\underline{o})e^{jk_o\zeta}$$

$$- 2\pi j \overline{\rho}(\overline{\underline{x}}) \int ds \tilde{t}(s\underline{o},s\underline{o}) f(\overline{\underline{x}};\underline{o},s) e^{js\zeta} \tag{B-14}$$

where

$$A(\overline{\underline{x}};\underline{o}) = - 2jk_o\underline{o}\cdot\overline{\nabla}_t A(\overline{\underline{x}};\underline{o})$$

$$- (2\pi)^2 \overline{\rho}(\overline{\underline{x}}) \tilde{t}(k_o\underline{o},k_o\underline{o}) A(\overline{\underline{x}};\underline{o}) \tag{B-15}$$

In Equations (B-14) and (B-15), $\tilde{t}$ is the Fourier transform of the transition kernal t of the scatterer, and the function $f(\overline{\underline{x}};\underline{o},s)$ is defined as

$$f(\overline{\underline{x}};\underline{o},s) = \frac{A(\overline{\underline{x}};\underline{o})}{s-k_o} + \frac{A(\overline{\underline{x}};-\underline{o})}{s+k_o} \tag{B-16}$$

To eliminate secular terms from the pertubation expansion of Equation (B-5), the following secular condition is required

$$\lim_{\substack{\zeta \to \infty \\ \underline{x} \text{ is fixed}}} \frac{G^{(1)}(\zeta,\underline{o};\overline{\underline{x}},\overline{\underline{x}}_o)}{\zeta} = 0 \tag{B-17}$$

This secular condition implies that

$$f(\overline{\underline{x}},\underline{o}) = 0 \tag{B-18}$$

Inserting Equations (B-14), (B-16) and (B-18) into (B-13) and defining $\underline{o}\cdot\overline{\underline{x}} = \overline{\zeta}$, $\underline{o}\cdot\overline{\underline{x}}_o = \overline{\zeta}_o$, the following differential equation in $A(\overline{\zeta};\underline{o})$ for $\zeta > 0$ is obtained

$$\frac{dA(\overline{\zeta};\underline{o})}{d\overline{\zeta}} = \frac{2\pi^2 j}{k_o} \, \overline{\rho}(\underline{x}(\overline{\zeta};\underline{o}))\tilde{t}(k_o\underline{o},k_o\underline{o})A(\overline{\zeta};\underline{o}) \qquad \text{(B-19)}$$

Solving Equation (B-19) with condition (B-12) yields the following

$$A(\overline{\zeta};\underline{o}) = -\frac{1}{2jk_o} \, e^{j\Delta\phi(\overline{\zeta};\overline{\zeta}_o;\underline{o})} \qquad \text{(B-20)}$$

where

$$\Delta\phi(\overline{\zeta},\overline{\zeta}_o;\underline{o}) = \frac{2\pi^2}{k_o} \int_{\overline{\zeta}_o}^{\overline{\zeta}} d\overline{\zeta}' \, \overline{\rho}\left(\underline{x}(\overline{\zeta}';\underline{o})\right)\tilde{t}(k_o\underline{o},k_o\underline{o}) \qquad \text{(B-21)}$$

Inserting Equation (B-20) into (B-11) and by Equation (B-6), the Radon transform of the mean Green's function is found as

$$RG \approx \hat{G}^{(o)}(\zeta,\underline{o};\overline{\underline{x}},\overline{\underline{x}}_o) = \begin{cases} -\dfrac{1}{2jk_o} \, \exp\left[jk_o\zeta + j\Delta\phi(\overline{\zeta},\overline{\zeta}_o;\underline{o})\right] \quad , \; \zeta > 0 \\[4mm] -\dfrac{1}{2jk_o} \, \exp\left[-jk_o\zeta - j\Delta\phi(\overline{\zeta},\overline{\zeta}_o;-\underline{o})\right] , \; \zeta < 0 \end{cases} \qquad \text{(B-22)}$$

## APPENDIX C

## Two-Dimensional Transport Equation

Starting from the correlation equation, the two-dimensional transport equation can be derived using the two-variable perturbation method and the Radon transform technique.

An approximate equation of the Bethe-Salpeter type for the correlation function,

$$\Gamma(\underline{x}_t, \hat{\underline{x}}_t) = \langle \psi(\underline{x}_t) \psi^*(\hat{\underline{x}}_t) \rangle \qquad \text{(C-1)}$$

is given by

$$\pounds \pounds^* \Gamma - \int ds_t \rho(\underline{s}_t) T(s_t) T^*(s_t) \Gamma = 0 \qquad \text{(C-2)}$$

where $\pounds$ is the mean field operator defined in Equation (6-1-16) and $T(s_t)$ is the transition operator defined in Equation (6-1-7). Equation (C-2) can be rewritten as

$$(\pounds - \pounds^*)\Gamma - (\pounds^{*-1} - \pounds) \int ds_t \rho(\underline{s}_t) T(s_t) T^*(\underline{s}_t) \Gamma = 0 \qquad \text{(C-3)}$$

where

$$(\pounds^{-1} \psi)(\underline{x}_t) = \int d\underline{x}_t' \, G(\underline{x}_t, \underline{x}_t') \psi(\underline{x}_t') \qquad \text{(C-4)}$$

Here $G(\underline{x}_t, \underline{x}_t')$ is the mean Green's function. It satisfies

$$\pounds G(\underline{x}_t, \underline{x}_t') = \delta(\underline{x}_t - \underline{x}_t') \qquad \text{(C-5)}$$

Equation (C-3) is now written in a more explicit form as

$$(\nabla_t^2 - \hat{\nabla}_t^2)\Gamma(\underline{x}_t, \hat{\underline{x}}_t) + M(\underline{x}_t, \hat{\underline{x}}_t) - M^*(\hat{\underline{x}}_t, \underline{x}_t) - N(\underline{x}_t, \hat{\underline{x}}_t) + N^*(\hat{\underline{x}}_t, \underline{x}_t) = 0 \qquad \text{(C-6)}$$

where

$$M(\underline{x}_t, \hat{\underline{x}}_t) = \int d\underline{x}_{t1} d\underline{s}_t \rho(\underline{s}_t) t(\underline{x}_t - \underline{s}_t, \underline{x}_{t1} - \underline{s}_t) \Gamma(\underline{x}_{t1}, \hat{\underline{x}}_t) \qquad \text{(C-7)}$$

and

$$N(\underline{x}_t, \hat{\underline{x}}_t) = \int d\underline{x}_{t1} d\underline{x}_{t2} d\hat{\underline{x}}_{t2} d\underline{s}_t \rho(\underline{s}_t) G(\underline{x}_t, \underline{x}_{t1})$$
$$\cdot t(\underline{x}_{t1} - \underline{s}_t, \underline{x}_{t2} - \underline{s}_t) t^*(\hat{\underline{x}}_{t1} - \underline{s}_t, \hat{\underline{x}}_{t2} - \underline{s}_t) \Gamma(\underline{x}_{t2}, \hat{\underline{x}}_{t2}) \qquad \text{(C-8)}$$

For small fractional volume $\varepsilon$, the solution of Equation (C-6) has two scales of variation in both $\underline{x}_t$ and $\underline{\hat{x}}_t$. A problem of this type can be treated by the two-variable perturbation technique. The small parameter $\varepsilon$ is introduced into Equation (C-6) by letting

$$\rho(\underline{s}_t) = \varepsilon\bar{\rho}(\underline{\bar{s}}_t) \quad , \quad \underline{\bar{s}}_t = \varepsilon\underline{s}_t \qquad (C-9)$$

where it has been assumed that $\bar{\rho}$ is a function of the slow variable $\underline{\bar{s}}_t$ only. This assumption implies that $\Gamma$, $G$, $M$ and $N$ are functions of not only $\underline{x}_t$, $\underline{\hat{x}}_t$ and $\varepsilon$ but also the slow variables $\underline{\bar{x}}_t$ and $\underline{\hat{\bar{x}}}_t$; thus

$$A(\underline{x}_t,\underline{\hat{x}}_t;\varepsilon) \equiv A(\underline{x}_t,\underline{\hat{x}}_t;\underline{\bar{x}}_t,\underline{\hat{\bar{x}}}_t;\varepsilon) \quad , \qquad (C-10)$$

$$A \in \{\Gamma,G,M,N\}$$

The function A is now expanded in a power series in $\varepsilon$:

$$A(\underline{x}_t,\underline{\hat{x}}_t;\underline{\bar{x}}_t,\underline{\hat{\bar{x}}}_t;\varepsilon) = \sum_{n=0}^{\infty} A^{(n)}(\underline{x}_t,\underline{\hat{x}}_t;\underline{\bar{x}}_t,\underline{\hat{\bar{x}}}_t)\varepsilon^n \quad , \qquad (C-11)$$

$$A \in \{\Gamma,G,M,N\}$$

Employing the chain rule the $\nabla_t^2$ and $\hat{\nabla}_t^2$ operators become

$$\nabla_t^2 \rightarrow \nabla_t^2 + 2\varepsilon\nabla_t \cdot \bar{\nabla}_t + \varepsilon^2\bar{\nabla}_t^2 \qquad (C-12)$$

$$\hat{\nabla}_t^2 \rightarrow \hat{\nabla}_t^2 + 2\varepsilon\hat{\nabla}_t \cdot \hat{\bar{\nabla}}_t + \varepsilon^2\hat{\bar{\nabla}}_t^2 \qquad (C-13)$$

where $\bar{\nabla}_t$ and $\hat{\bar{\nabla}}_t$ are the del operators with respect to the slow variables $\underline{\bar{x}}_t$ and $\underline{\hat{\bar{x}}}_t$ respectively.

Proceeding with the perturbation analysis, the expansion given in Equation (C-11) is used in Equation (C-6). Equating equal powers of $\varepsilon$ and using the fact that $M^{(o)} = N^{(o)} = 0$ gives equations for the $\Gamma^{(1)}$. The first two of these are:

$$(\nabla_t^2 - \hat{\nabla}_t^2)\Gamma^{(o)}(\underline{x}_t,\underline{\hat{x}}_t;\underline{\bar{x}}_t,\underline{\hat{\bar{x}}}_t) = 0 \qquad (C-14)$$

C-2

$$(\nabla_t^2 - \hat{\nabla}_t^2)\,\Gamma^{(1)}(\underline{x}_t,\underline{\hat{x}}_t;\underline{\bar{x}}_t,\underline{\hat{\bar{x}}}_t) + 2(\nabla_t\cdot\bar{\nabla}_t - \hat{\nabla}_t\cdot\hat{\bar{\nabla}}_t)\,\Gamma^{(0)}(\underline{x}_t,\underline{\hat{x}}_t;\underline{\bar{x}}_t,\underline{\hat{\bar{x}}}_t)$$

$$+\, M^{(1)}(\underline{x}_t,\underline{\hat{x}}_t;\underline{\bar{x}}_t,\underline{\hat{\bar{x}}}_t) - M^{(1)*}(\underline{\hat{x}}_t,\underline{x}_t;\underline{\hat{\bar{x}}}_t,\underline{\bar{x}}_t) - N^{(1)}(\underline{x}_t,\underline{\hat{x}}_t;\underline{\bar{x}}_t,\underline{\hat{\bar{x}}}_t)$$

$$+\, N^{(1)*}(\underline{\hat{x}}_t,\underline{x}_t;\underline{\hat{\bar{x}}}_t,\underline{\bar{x}}_t) = 0 \qquad\qquad\text{(C-15)}$$

Equations (C-14) and (C-15) are solved using the double Radon transformation defined as

$$RA = \hat{A}(\zeta,\hat{\zeta};\underline{o},\underline{\hat{o}};\underline{\bar{x}}_t,\underline{\hat{\bar{x}}}_t)$$

$$= \int d\underline{x}_t\, d\underline{\hat{x}}_t\, \delta(\zeta - \underline{o}\cdot\underline{x}_t)\,\delta(\hat{\zeta} - \underline{\hat{o}}\cdot\underline{\hat{x}}_t)\, A(\underline{x}_t,\underline{\hat{x}}_t;\underline{\bar{x}}_t,\underline{\hat{\bar{x}}}_t)$$

$$\text{(C-16)}$$
$$A\,\varepsilon\,\{\Gamma,M,N\}$$

Here $\underline{o}$ and $\underline{\hat{o}}$ are unit vectors. The solution of Equation (C-14) in terms of the Radon transform is given as

$$\hat{\Gamma}^{(0)}(\zeta,\hat{\zeta};\underline{o},\underline{\hat{o}};\underline{\bar{x}}_t,\underline{\hat{\bar{x}}}_t) = [J^+(\underline{\bar{x}}_t,\underline{\hat{\bar{x}}}_t;\underline{o})\,e^{ik(\zeta-\hat{\zeta})}$$

$$\text{(C-17)}$$

$$+\, J^-(\underline{\bar{x}}_t,\underline{\hat{\bar{x}}}_t;\underline{o})\,e^{-ik(\zeta-\hat{\zeta})}]\,\delta(\underline{o}-\underline{\hat{o}})$$

where $J^+$ and $J^-$ are still to be determined. The Radon Transform of Equation (C-15) is

$$\left(\frac{\partial^2}{\partial\zeta^2} - \frac{\partial^2}{\partial\hat{\zeta}^2}\right)\hat{\Gamma}^{(1)} = -2ik(\underline{o}\cdot\bar{\nabla}_t + \underline{\hat{o}}\cdot\hat{\bar{\nabla}})\,\hat{\Gamma}^{(0)}$$

$$+\, \hat{M}^{(1)} - \hat{M}^{(1)*} - \hat{N}^{(1)} + \hat{N}^{(1)*} \qquad\text{(C-18)}$$

where $\hat{M}^{(1)}$, $\hat{N}^{(1)}$ are the Radon transforms of $M^{(1)}$ and $N^{(1)}$.

To insure that $\hat{\Gamma}^{(1)}$ is a bounded function of $\zeta$ and $\hat{\zeta}$, the right hand side of Equation (C-18) must be orthogonal to the homogeneous solutions of $\hat{\Gamma}^{(1)}$. Applying this so-called secular condition results in the desired transport equation for the two point specific intensity $J(\underline{x}_t,\underline{\hat{x}}_t,\underline{o})$ where

$$J(\overline{\underline{x}}_t,\hat{\overline{\underline{x}}}_t;\underline{o}) = \begin{cases} J^+(\overline{\underline{x}}_t,\hat{\overline{\underline{x}}}_t;\underline{o}) & , \quad 0 < \theta \leq \pi \\ \\ J^-(\overline{\underline{x}}_t,\hat{\overline{\underline{x}}}_t;\underline{o}) & , \quad \pi < \theta \leq 2\pi \end{cases} \tag{C-19}$$

Here $J^+$ and $J^-$ are the unknown slowly varying coefficients appearing in Equation (C-17). The transport equation for $J(\overline{\underline{x}}_t,\hat{\overline{\underline{x}}}_t;\underline{o})$ is:

$$2ik\underline{o}\cdot(\overline{\nabla}_t + \hat{\overline{\nabla}}_t)J(\overline{\underline{x}}_t,\hat{\overline{\underline{x}}}_t;\underline{o}) + (2\pi)^2\overline{\rho}(\overline{\underline{x}}_t)\tilde{t}(k\underline{o},k\underline{o})J(\overline{\underline{x}}_t,\hat{\overline{\underline{x}}}_t;\underline{o}) - (2\pi)^2\overline{\rho}(\overline{\underline{x}}_t)$$

$$\cdot\tilde{t}^*(k\underline{o},k\underline{o})J(\overline{\underline{x}}_t,\hat{\overline{\underline{x}}}_t;\underline{o}) - 4i\pi^3\overline{\rho}(\hat{\overline{\underline{x}}}_t)\int_0^{2\pi}d\theta'|\tilde{t}(k\underline{o},k\underline{o}')|^2 J(\hat{\overline{\underline{x}}}_t,\hat{\overline{\underline{x}}}_t;\underline{o}')$$

$$\cdot A^+(\overline{\underline{x}}_t,\hat{\overline{\underline{x}}}_t;\underline{o})U[\underline{o}(\overline{\underline{x}}_t - \hat{\overline{\underline{x}}}_t)] - 4i\pi^3\overline{\rho}(\overline{\underline{x}}_t)\int_0^{2\pi}d\theta'|\tilde{t}(k\underline{o},k\underline{o}')|^2$$

$$\cdot J(\overline{\underline{x}}_t,\overline{\underline{x}}_t;\underline{o}')A^{+*}(\hat{\overline{\underline{x}}}_t,\overline{\underline{x}}_t;\underline{o})U[\underline{o}(\hat{\overline{\underline{x}}}_t - \overline{\underline{x}}_t)] = 0 \tag{C-20}$$

Here $\tilde{t}(\underline{k},\underline{k}')$ is the Fourier transform of $t(\underline{x},\underline{x}')$ as defined in Equation (6-1-12) and

$$A^\pm(\underline{x}_t,\hat{\overline{\underline{x}}};\underline{o}) = e^{i\Delta\phi^\pm(\overline{\underline{x}}_t,\hat{\overline{\underline{x}}}_t;\underline{o})} \tag{C-21}$$

with

$$\Delta\phi^\pm(\overline{\underline{x}}_t,\hat{\overline{\underline{x}}}_t;\underline{o}) = \pm\frac{2\pi^2}{k}\int_{\overline{\zeta}=\underline{o}\cdot\hat{\overline{\underline{x}}}_t}^{\overline{\zeta}=\underline{o}\cdot\overline{\underline{x}}_t}d\overline{\zeta}'\overline{\rho}(\overline{\zeta}';\underline{o})\tilde{t}(\pm k\underline{o};\pm k\underline{o}) \tag{C-22}$$

The unit step function is defined by $U(\zeta)$.

The correlation function $\Gamma^{(\circ)}(\underline{x},\hat{\underline{x}};\overline{\underline{x}},\hat{\overline{\underline{x}}})$ is found by taking the inverse Radon transform which is given by

$$\Gamma^{(\circ)}(\underline{x}_t,\hat{\underline{x}}_t;\overline{\underline{x}}_t,\hat{\overline{\underline{x}}}_t) = 4\int_0^\pi d\underline{o}\int_0^\pi d\hat{\underline{o}}(K\hat{K}\hat{\Gamma}^{(\circ)}(\zeta,\hat{\zeta};\underline{o},\hat{\underline{o}};\overline{\underline{x}}_t,\hat{\overline{\underline{x}}}_t) \tag{C-23}$$

where

$$\zeta = \underline{o}\cdot\underline{x} \quad , \quad \hat{\zeta} = \hat{\underline{o}}\cdot\hat{\underline{x}} \tag{C-24}$$

and

$$(K \hat{K} \hat{\Gamma}^{(0)})(\zeta, \hat{\zeta}; \underline{o}, \underline{\hat{o}}; \overline{\underline{x}}, \overline{\underline{\hat{x}}}) =$$

(C-25)

$$\left( \frac{1}{4\pi^2} P\int_{-\infty}^{+\infty} \frac{d\zeta'}{\zeta - \zeta'} \frac{\partial}{\partial \zeta'} \right) \left( \frac{1}{4\pi^2} P\int_{-\infty}^{+\infty} \frac{d\hat{\zeta}'}{\hat{\zeta} - \hat{\zeta}'} \frac{\partial}{\partial \hat{\zeta}'} \right) \Gamma^{(0)}(\zeta, \hat{\zeta}; \underline{o}, \underline{\hat{o}}; \overline{\underline{x}}_t, \overline{\underline{\hat{x}}}_t)$$

with $P\int$ being the principal value integral. Substituting Equation (C-17) into Equation (C-25), the correlation function can be obtained in terms of $J(\overline{\underline{x}}_t, \overline{\underline{\hat{x}}}_t; \underline{o})$ as

$$\Gamma^{(0)}(\underline{x}_t, \underline{\hat{x}}_t; \overline{\underline{x}}_t, \overline{\underline{\hat{x}}}_t) = \frac{k^2}{4\pi^2} \int_0^{2\pi} d\underline{o} \, J(\overline{\underline{x}}_t, \overline{\underline{\hat{x}}}_t; \underline{o}) e^{ik\underline{o} \cdot (\underline{x}_t - \underline{\hat{x}}_t)}$$

(C-26)

In summary, the correlation function is approximated by the first term in a two variable expansion

$$\Gamma(\underline{x}_t, \underline{\hat{x}}_t) = \Gamma^{(0)}(\underline{x}_t, \underline{\hat{x}}_t; \overline{\underline{x}}_t, \overline{\underline{\hat{x}}}_t) \epsilon^0 + O(\epsilon)$$

(C-27)

where $\Gamma^{(0)}(\underline{x}_t, \underline{\hat{x}}_t; \overline{\underline{x}}_t, \overline{\underline{\hat{x}}}_t)$ is given in terms of the two-point specific intensity, $J(\overline{\underline{x}}_t, \overline{\underline{\hat{x}}}_t; \underline{o})$, as expressed in Equation (C-26) and the two point specific intensity $J(\overline{\underline{x}}_t, \overline{\underline{\hat{x}}}_t; \underline{o})$ in turn satisfies the generalized transport Equation (C-20).

[This page intentionally left blank]

# Distribution List

Defense Technical Information Center                     12 copies
Cameron Station
Alexandria, VA   22314

US Dept of Commerce
Institute for Telecommunications Sciences/NTIA
Boulder, CO   80303

    Attn:  Dr. G. Hufford                          2 copies
           Mr. E. Violette                        1 copy

SRI International
333 Ravenswood Avenue
Menlo Park, CA   94025

    ATTN:  Dr. M. Frankel                          1 copy
           Dr. R. Nelson                          1 copy
           Dr. A. Spiridon                        1 copy

Prof. T. Tamir                                           1 copy
Dept of EE/Electrophysics
Polytechnic Institute of New York
333 Jay Street
Brooklyn, NY   11201

Mr. George Hagn                                          1 copy
SRI International
1611 N. Kent Street
Arlington, VA   22209

Prof. A. H. LaGrone                                      1 copy
Dept of EE
University of Texas
Austin, TX   78712

Dr. K. Chamberlin                                        1 copy
Dept of EE
Ohio University
Athens, OH   45701

Dr. R. Luebbers                                          1 copy
Lockheed Palo Alto Research Labs
3251 Hanover Street
Palo Alto, CA   94304

Dr.  G. S. Brown                                         1 copy
Applied Science Assoc., Inc.
105 East Chatham
Apex, NC   27502

Commander                                                1 copy
USA ERADCOM
EW Laboratory
ATTN:  DELEW-V (W. Barr)
Fort Monmouth, NJ   07703

Distribution List (cont.)

Commander                                         1 copy
USA CECOM
CENSEI
ATTN:  DRSEL-SEI-A (P. Major)
Fort Monmouth, NJ  07703

Commander                                         2 copies
USA CECOM
CENCOMS
ATTN: DRSEL-COM-RM-4 (F. Schwering)
Fort Monmouth, NJ  07703

Commander                                         1 copy
USA CECOM
CENCOMS
ATTN:  DRSEL-COM-RM-4 (G. Whitman)
Fort Monmouth, NJ  07703

IIT Research Institute                            1 copy
ATTN:  Mark Weissberger
c/o DOD ECAC
Annapolis, MD  21402

Commander                                         1 copy
USA CECOM
CENCOMS
ATTN:  DRSEL-COM-RM-4 (R. Johnson)
Fort Monmouth, NJ  07703

Commander                                         64 copies
USA CECOM
CENCOMS
ATTN:  DRSEL-COM-RF-2 (P. Sass)
Fort Monmouth, NJ  07703

Dr. J. Olsen                                      1 copy
Hughes Aircraft Company
Ground Systems Group
Fullerton, CA  92634

Dr. F. Amoroso                                    1 copy
Hughes Aircraft Company
Ground Systems Group
Fullerton, CA  92634

Mr. Richard Robertson                             1 copy
Atlantic Research Corp.
5390 Cherokee Avenue
Alexandria, VA  22314